COMPREHENSIVE MATHEMATICAL MODEL

FOR OXYGEN STEELMAKING

COMPREHENSIVE MATHEMATICAL MODEL FOR OXYGEN STEELMAKING

By

Ameya Kadrolkar, B.E., M.Tech.

A Thesis

Submitted to the School of Graduate Studies

In Partial Fulfilment of the Requirements

For the Degree

Doctor of Philosophy

McMaster University

DOCTOR OF PHILOSOPHY (2020) McMaster University
(Materials Science and Engineering) Hamilton, Ontario

Title: Comprehensive Mathematical Model for Oxygen Steelmaking

Author: Ameya Kadrolkar, M.Tech. (IIT Kharagpur)

Supervisor: Dr. Neslihan Dogan

Pages: xvii - 253

Abstract

The Oxygen Steelmaking process is used to refine pig iron produced in the blast furnace to produce liquid steel for further refining in secondary steelmaking processes. The main advantages of the process are its autogenous nature, wherein the heat is generated through the refining reactions itself, and the refining is completed in a relatively short time (typically 15-25 mins). Achieving the desired end-point composition of refined steel is essential to avoid re-blows, which lead to delays in downstream processes and an increase in steel production costs. Improving process control through regular monitoring and a better understanding of the process is thus very critical. Multiple reaction interfaces are formed between various phases (slag, metal, gas), at extremely high temperatures and this makes the monitoring of the process through sampling and observation difficult and expensive. Consequently, mathematical modelling has been used as a tool to improve the understanding of the process and propose developments in operation.

Numerous models have been developed in the past; however, these models do not address several open questions regarding the detailed reaction mechanisms and the contributions from different reaction zones inside the Basic Oxygen Furnace. The current work aimed to fill this gap. In this work, four prominent reaction zones, namely; impact, slag-metal bulk, cavity, and emulsion zones were identified. A more mechanistic approach involving process variables has been used to decrease the level of empiricism. With regards to the impact and the slag-metal bulk zones, the velocity of flow of metal (or surface-renewal) at the interfaces of these zones are calculated by taking into the momentum induced by the

top-jets and bottom-stirring plumes. This study found that these zones contribute negligibly to overall refining in the oxygen steelmaking process. In the case of the emulsion zone, a very rigorous description of all aspects (external and internal decarburization, bloating behavior, and trajectory) pertaining to the life cycle of a single metal droplet in slag has been achieved. The emulsion zone is found to contribute 5 to 75 % of decarburization during various times of blow. The cavity zone model represents the first reported effort to predict the refining behavior of metal droplets that are exposed to oxygen jets within the lance cavities. The model incorporated the mass transfer, reaction equilibria, and kinetics of the reactions. It is predicted that this zone plays a critical role in the removal of silicon and FeO formation in the early part of the blow and removal of carbon throughout the blow. Several significant insights with regards to improvement in the operation of the oxygen steelmaking process are derived from each sub-models. The integration of these models will guide the steelmaker to improve their practices so that they can achieve better consistency in the end-point composition of refined steel and reduce re-blows.

ACKNOWLEDGEMENTS

||श्री महालक्ष्मी चरणार्पणमस्तु||

||श्री सीतारामचंद्रार्पणमस्तु||

I express my sincere gratitude to Dr. Neslihan Dogan for giving me the opportunity to conduct Ph.D. studies with her. Her guidance has been invaluable and instrumental in this end result. I admire her open-mindedness in encouraging new ideas, even if some of them were contrary to her previous research. I thank Dr. Kenneth Coley for his insights, critical suggestions and encouragement that channeled the thesis in the right direction. Also, I would like to thank Dr. Christopher Swartz for his useful suggestions as a member of my supervisory committee. I thank Dr. Gordon Irons for insights into his previous research. I am grateful to the efforts of all previous students/researchers whose studies have directly or indirectly enriched my thesis.

I would like to thank staff members of Materials Science and Engineering Department Danielle Marcellin, Ed McCaffery and Dr. Xiaogang Li for their help at different stages of my graduate study. My special appreciation to Mary-Anne Bechamp for her very friendly and welcoming disposition as Graduate Administrative Assistant. I consider myself extremely fortunate to have worked as Teaching Assistant to Dr. Dmitri Malakhov. You

were a great leader who lead by example. I hope to emulate your qualities. I would like to thank McMaster Steel Research Center, Natural Science Engineering Research Council and McMaster University for the financial support.

A very special thanks to Anand *bhaiya* and Madhumanti *di* for their reassuring presence during this time. Dr. Anand Senguttuvan was an excellent friend, philosopher, and guide. I thank my good friends Yousef Tabatabaei and Rahul Sadavarte for always being there for me and for all the pleasant memories. Many thanks to Aliyeh Rafiei for her friendship and to colleagues in Materials Science and Engineering department for enriching this experience.

I would like to thank my wife Monica, for her love, understanding and encouragement during good and bad times. Lastly, I would like to express my deepest appreciation and gratitude to my brother Aditya and parents Krishna and Ajita Kadrolkar for their unconditional love, care, and support. I thank my parents for their sacrifices throughout my life and dedicate this thesis to them.

Table of contents

List of Figures

List of Tables

Chapter 1

Introduction

1.1 Overview

Modern steelmaking involves a range of unit operations and leads to the production of steel from iron-bearing raw materials and carbonaceous fuel. One such unit operation is broadly referred to as primary steelmaking consists of either oxygen or electric arc steelmaking. The basic oxygen steelmaking primarily converts pig-iron from blast furnace to liquid steel and has replaced its predecessors like the Open Hearth process owing to its high productivity[1,2]. Even though steelmakers have long operating experience, better understanding of BOF steelmaking is still required to prevent a range of issues such as failure to hit chemistry targets requiring a re-blow or slopping leading to delays and safety hazards. To overcome these issues and meet the growing demand in using more challenging raw materials, dynamic models are useful tools by optimizing current operations as well as suggesting suitable changes in the process variables such as the flux addition rates, lance height, and oxygen flow rate. While the dynamic models have been improving since their introduction in the 1970s, there has been a need to increase the reliability of the dynamic models. This can be achieved by incorporation of new insights pertaining to the kinetics and mechanisms of key refining reactions and the contribution of reaction zones to overall refining of liquid metal within the oxygen steelmaking process. For instance, there is still debate over the relative importance of carbon refining from bloated droplets within the emulsion versus directly at the point of oxygen jet impact with the metal bath. Further, the bloating behavior of metal droplets under various experimental conditions relevant to steelmaking operations was recently studied however was not included in the previous models. This work will build on these

recent advances in BOF modeling and on our understanding of the mechanisms and kinetics of all major refining reactions.

1.2 Objectives of This Study

The current research project aims to develop dynamic models based entirely on a mathematical formulation of kinetics and mechanisms of refining reactions from various reaction zones for enhancing the reliability of process models. The detailed objectives are as follows:

1. Develop a mathematical model to predict the refining rates of elements in the liquid metal at the impact zone and the slag-metal bulk zone and investigate the contribution of these zones to the overall refining of hot-metal.

2. Develop a mathematical model to predict the decarburization reactions in the slag-metal-gas emulsion. This model is based on the bloating behavior of droplets incorporating the CO gas generation (internal, external) and escape rates from metal droplets in the emulsion.

3. Develop a mathematical model to predict the refining rates of elements in the metal droplets splashed within the cavities and investigate the contribution of this zone to the overall refining of hot-metal.

4. Develop a dynamic flux dissolution model by coupling the existing thermodynamic tools (like FactSage, Cell Model and Thermo-Calc) with kinetic model. The thermodynamic tools would be used to calculate the saturation concentrations/solubility of CaO in slag.

Even though the specific focus of the sub-models on some specific refining reactions (silicon and manganese removal for impact and slag-metal bulk zones or decarburization for emulsion zone), the models address all the competing oxidation reactions.

1.3 Thesis Outline

This thesis is composed of seven chapters. Chapter 1 provides a background to the motivation for the current study, the research objectives and the thesis outline. Chapter 2 reviews relevant literature related to thermodynamics and kinetics of important refining reactions, related experimental studies, and models related to oxygen steelmaking.

Chapters 3 describes the kinetic models to estimate the refining reactions occurring at the surface of smooth lance-cavities and slag-metal bulk. The effect of operation parameters like oxygen supply rate, lance height and the bottom stirring rate are incorporated through the use of relevant correlations.

Chapter 4 provides another kinetic model to describe the refining reactions within the metal droplets in the emulsion zone. Various aspects involved in a critical refining reaction (decarburization) are included and described rigorously based on experimental information available in open literature.

Chapter 5 presents a model for competing oxidation reactions in droplets splashed in the oxidizing atmosphere of lance cavities. The contribution of the cavity zone to refining is quantified and the sensitivity of various process parameters (e.g. cavity gas composition, droplet residence time, and size distribution) to many refining reactions is examined.

Chapter 6 presents a modified flux dissolution model for oxygen steelmaking which couples the existing kinetic model and thermodynamic tools like Cell-Model, FactSage and Thermo-Calc. Chapter 7 brings together important findings from each of the earlier chapters illustrating how each one contributes to oxygen steelmaking. Lastly, some general conclusions and future work are offered.

Chapter 3 is published in Metals, while chapters 4 and 5 have been published in Metallurgical and Materials Transactions B, and Chapter 6 will be submitted for publication in the immediate future.

Chapter 2

Literature Review

The current chapter reviews the various essential aspects of steelmaking, which lead to the development of dynamic models for it. The definition of reaction zones critical to various refining reactions and relevant experimental and industrial studies undertaken to ascertain the contribution of each zone are reviewed. Significant refining reactions and the kinetics associated with them at different reaction interfaces are reviewed. The dynamics of fluid flow due to top-jets and bottom stirring are discussed. This chapter also includes the thermodynamic fundamentals of the slag and hot-metal phases. Finally, the importance of dynamic models, prevalent approaches and some of the previous dynamic models are discussed.

2.1 Overview of Oxygen Steelmaking

Oxygen steelmaking is a generic term encompassing the processes which involve the use of high purity oxygen to produce partially refined liquid steel from blast furnace hot-metal and scrap. The dissolved impurities such as carbon, silicon, and manganese react with oxygen. These refining reactions are relatively fast due to the creation of large reaction areas and heat generation [2,3]. This generated heat is consumed to melt the fluxes and scrap and to achieve the desired temperature of the steel product. These two factors have led to the commercial success of the process, which has mostly replaced the previously used Bessemer and Open Hearth processes[2]. The oxygen steelmaking process accounts for 50-

55 % of the steel produced despite the steady increase of electric arc furnace steelmaking as an alternative [2].

Several configurations of oxygen-hot-metal contact exist to achieve refining, as shown in Figure 2.1. The top-blown process involves blowing of the oxygen through supersonic jet(s) on a metal bath using a water-cooled lance from the top of the furnace. It was firstly introduced in the early ’50s for a 2-ton vessel at Linz and Donawitz in Austria, and the process named the ‘LD process’[3], which is alternatively referred to as Basic Oxygen Furnace (BOF) and Basic Oxygen Process (BOP). The advantages of this process involve the simplicity of the methodology of oxygen introduction through a lance that is separated from the metal bath and the ability to control the slag formation through variation of lance height[1]. However, the limitations include high losses of iron in slag, a high oxygen content of metal bath, high dust losses, and difficulties in producing low carbon steel[1].

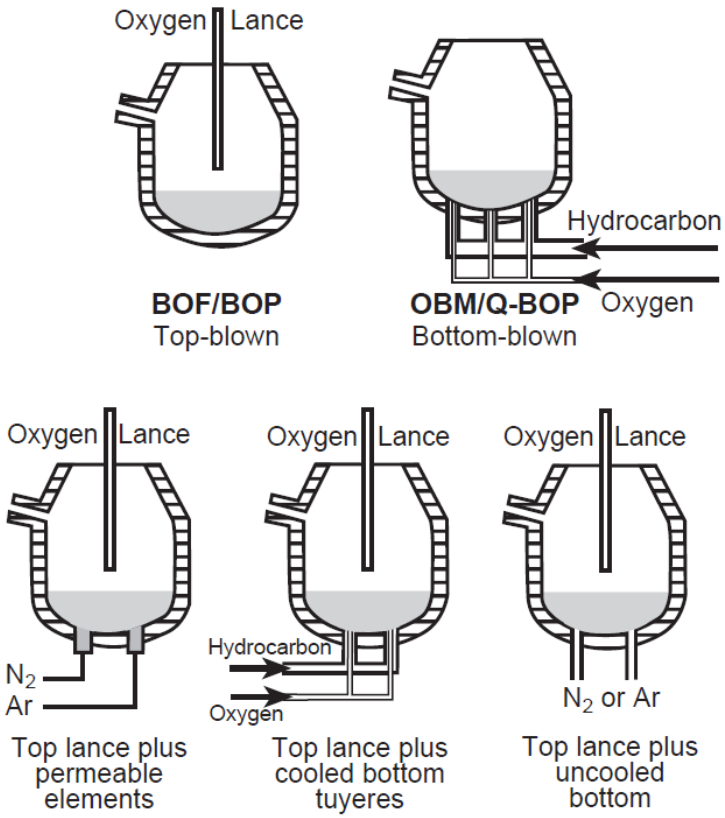

Figure 2.1: Various configurations of oxygen steelmaking process[2]

The bottom-blown process involves the introduction of the oxygen through the bottom of the bath using tuyeres and is referred to as OBM, Q-BOP, or LWS [3] depending on the tuyere design. The tuyere is made up of two concentric tubes, the inner nozzle and an outer annulus [2]. The burning of tuyeres and refractory wear due to excess exothermic reactions at the oxygen tip are prevented by introducing hydrocarbon gas through an outer annular section. The endothermic decomposition of the hydrocarbon chills the metal at the tuyere tip and creates localized cooling[2]. The bottom blown gas has a much more pronounced effect on the degree of mixing of the metal bath than that of the top-blown jet, as demonstrated by several studies [4,5]. Limitations of the bottom-blown process involve higher operational costs due to excessive wear of tuyeres and bottom refractories and a low

scrap melting capacity [6]. Based on the experiences of operations with the top and bottom blown processes, the combined-blown process was introduced, which involved both top oxygen blowing lance and injection of inert or oxidizing gas through tuyeres from the bottom of the furnace[2]. Considerable variations in the combined-blown process exist in terms of the bottom tuyeres/porous plugs/elements and stirring/oxidizing gas introduced from the bottom. The combined blown processes achieve a significant fraction of the stirring effect while reducing the wear rate of tuyeres and bottom refractories. The combined blown processes are advantageous over the LD process due to reducing excessive amount of slag formation thereby the advent of slopping[1].

2.2 Reaction Zones in Oxygen Steelmaking

A brief sequence of events occurring in top-blown oxygen steelmaking is as follows: weighing and charging of scrap and hot-metal, lowering of the lance into the furnace at a particular height from the bath and blowing of oxygen. The lance height and oxygen flow rate are adjusted during the blow to control the refining reactions. The lance height is generally high at the start of the blow to prevent the contact of lance-tip with the un-melted scrap in the melt [2]. Basic fluxes and other additives are added through hoppers or tuyeres to produce a basic slag during the blow. The primary aim of this process is to achieve the end-point composition and temperature of liquid metal close to that desired composition by the steelmaker. To better meet this aim, various means of monitoring and static and dynamic process models are used.

There are several reaction zones available in the oxygen steelmaking process, as stated by Deo and Boom[3]. They are namely, (1) Impact zone: It is the surface of cavities where the

oxygen jets impinge upon the bath. Since the temperature is relatively higher than other parts of the furnace, this zone is also called ‘hot-spot,’ (2) Slag-metal bulk zone: It is the interface between the metal bath and the slag, (3) Emulsion zone: It consists of liquid slag, metal droplets, and gas generated due to the reactions between slag and metal droplets. Large numbers of metal droplets are generated and ejected into the slag because of the impact of the oxygen jet on the metal bath. (4) Refractory wall: The heterogeneous nucleation of CO bubbles (leading to decarburization) as sufficient supersaturation can be achieved locally at the surface of refractory walls, (5) Oxygen jets/cavity zone: The refining reactions except dephosphorization can occur through the metal droplets entrained in the oxygen jets. (6) Unmelted scrap-metal bulk zone: The interface of un-melted scrap with metal can also contribute to the decarburization reaction in a similar way as the refractory wall. These reaction zones are represented in Figure 2.2.

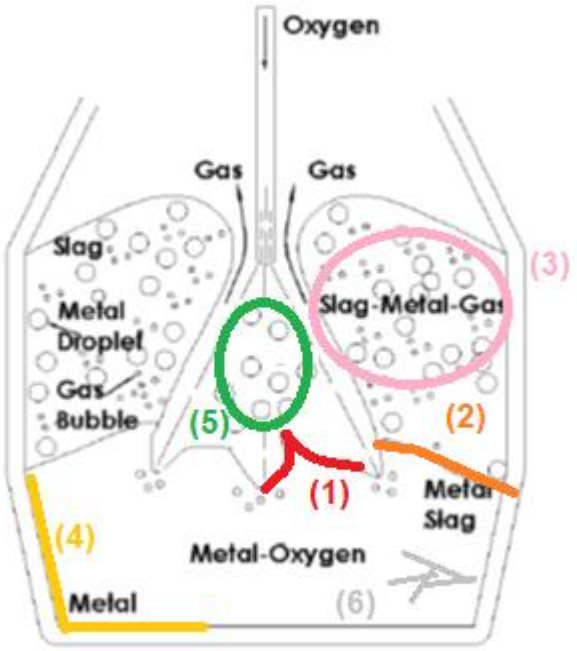

Figure 2.2: The schematic representation of reaction zones for oxygen steelmaking process[7] (1) Impact zone, (2) Slag-metal bulk zone, (3) Emulsion zone, (4) Refractory wall, (5) Oxygen jets/cavity zone, (6) Surface of un-melted scrap

2.2.1 Experimental and industrial evidence of the contribution of various reaction zones

Several attempts[8–17] were made to understand and quantify the contribution of each of the zones mentioned above to the overall refining in oxygen steelmaking even though it is a challenging task due to the limitations imposed by the high-temperature environment prevalent in the furnace.

The impact zone surface has been traditionally believed to be a contributor to the refining reactions. Precise measurements at the impact zone are specifically difficult due to extreme conditions, some modelling studies have suggested estimates of the extent of contribution. These include Dogan et al.'s[18] prediction for 200-t furnace, wherein 40 % of the

decarburization took place at the impact zone while Rout et al.[19] predicted the value to 24 % for the same furnace. Additionally, some validity for the contribution of the impact zone arose from the 'hot-spot theory', which claimed that the vast extent of refining occurs at the impact zone (despite relatively small reaction area) due to high temperature at the impact zone (500-800 ^{o}C) excess of that of the bath. Some experimental studies[8–13,17] were conducted to enhance the understanding of the region with regards to the temperature (thus ascertain the validity of the hot-spot theory) and fluid flow. Koch et al.[8,9] measured the impact zone temperature for hot-metal decarburization in a top blown, 50 kg furnace using a two-color pyrometer. They found that the temperature at the impact zone was in the range of 2000 to 2200°C, and the temperature increased with an increase in oxygen flow rate. The hot-spot theory has been disproven[10], as the prevalence of this high temperature within the bath could not be conclusively established. The optical pyrometry measurements were in the gas phase in the vicinity above the bath[11] rather than the impact zone itself, thus raising doubts over the contribution of the impact zone. In addition, the work by Ersson et al.[17] shows that the rate of decarburization at the impact zone is the same as that of the bath, also indicating a lesser contribution to the impact zone. Oeters[20] argued against a significant contribution of the impact zone, stating that the ratio of impact zone surface area to the bath volume was larger for experimental furnaces (~100 kg bath weight) like that of Koch et al.[21] than those for 100-300 t industrial furnaces. Thus, extensive refining (and especially decarburization) was possible at the impact zone in a 100-kg furnace, but not in industrial furnaces.

To understand the rate of circulation of hot-metal available for refining reactions at the impact zone, several experimental studies[10,12,13] were conducted. Chatterjee et al.[10] undertook a sampling study for a 6-t experimental furnace. Multiple samples were taken from the upper and lower parts of the bath during various times of the blow. For any time of the blow, the carbon content of 'upper' regions of the bath was lesser than that of 'lower' ones indicating at least some contribution of the impact zone to the overall refining of liquid metal. Sharma, Hlinka, and Kern[12] observed the flow behavior of metal due to the interaction of an oxygen jet in a 200-lb steel bath using an X-ray adjacent to a quartz window to establish the direction of fluid flow at the jet-metal impingement point. They found that the direction of metal flow was radially outward from the cavity, downwards from the wall, and upwards towards the bottom of the cavities. It is important to note that they didn't propose any correlation to predict the velocity of liquid using this technique. Davenport et al.[13] took images to track the circulation of plastic beads in water induced by the impinging gas jet. The density of plastic beads was equal to the water. They were able to observe liquid behavior at a rapid speed in a radially outward direction close to the surface of the bath. The momentum gained from the gas jets leads to the circulation of hot-metal (and in turn, the dissolved impurities) to the sides and back to the center, thus replenishing the hot-metal available for the reactions at the impact zone. A significant circulation rate of hot-metal around the impact zone would indicate a large amount of hot-metal coming in contact with oxygen. This would, in turn, imply a significant contribution of refining reactions at the impact zone.

Several industrial studies [14–16,22] focused on the sampling of emulsion and bath of the oxygen steelmaking process to quantify the contribution of the emulsion zone. Meyer *et al.*[14] applied splash sampling in a 230-t furnace wherein a shallow steel pan in line with the tap-hole was placed to collect the metal droplets ejected towards the hole. Even though the sampling was from the upper portion of the furnace, a significant fraction (6.8 to 35 %) of the metal was reported to be present in the emulsion during various times of blow, and an interfacial area was at least 70 m^2 /t hot-metal, as claimed by the authors. A similar conclusion was drawn by Urquhart and Davenport [16], who obtained samples from a scaled-down furnace ($1/50^{th}$) of an oxygen steelmaking process. Schoop *et al.*[15] utilized a bath sampling technique for a 200-t furnace and reported a large surface area ranging from 1000 to 3250 m^2, and the droplets to extensively dephosphorized as compared to the metal bath. Price *et al.*[22] carried out a sampling of the bath as well as emulsion using specially designed devices called bombs and measured the residence time of droplets using a radioactive gold isotope tracer technique in a 90-t oxygen steelmaking process. They measured the bath and sampled droplet compositions during various parts of the blow. Based on the estimation of total metal droplets present in the emulsion zone, they evaluated that the contribution of emulsion to decarburization was between 10 to 65 %, and the maximum contribution occurred during the peak decarburization period. Two significant indicators from sampling studies are namely high metal content in emulsion zone (or high interfacial area) and lower carbon contents in metal droplets (sampled from emulsion zone) as compared to bath[14,16,22], which indicated towards a significant contribution of emulsion zone to overall refining of liquid metal.

Although no specific experimental study was performed to identify the contribution of the slag-metal bulk zone, at least some refining is possible due to several reasons. Firstly, there is a difference in oxygen potential between the FeO rich slag and liquid metal, which would cause oxidation of impurities from liquid metal. Secondly, there is a continuous replenishment of hot-metal due to the momentum supplied by the top-jets and bottom stirring gas. Lastly, the entrainment of fine metal droplets into slag due to the passage of bottom stirring gas bubbles across the metal-slag interface is likely to increase the reaction area between the metal droplets and slag and increase the refining contribution of this zone.

Experimental studies[23,24] indicate that a thin film of metal is carried into the slag. In contrast, the passage of argon bubbles through liquid iron-slag interface and the drainage of this film causes suspension of metal droplets into slag. This phenomenon has been investigated using the in-situ X-ray transmission technique[23,24] and described by mathematical modelling [25]. It has been established that two distinct mechanisms of entrainment, namely film and jet cause entrainment of metal droplets in slag[23]. The film entrainment was caused by the rupture of the metal film (on the bubble) and interaction with the slag phase, while the jet entrainment was caused by the pull force exerted when the iron film drained into the slag due to upward motion of bubble[23].

In summary, refining reactions take place in various reaction zones. Since some of these zones have insufficient reaction volume or interfacial area to bring a considerable change in the bath composition, there is still a debate on the contribution of these zones.

2.3 Refining Reactions in Oxygen Steelmaking

Critical chemical reactions that determine the partitioning of oxygen amongst various metalloids and lead to slag formation are discussed below.

2.3.1 Decarburization reaction

The decarburization reaction is of prime importance in oxygen steelmaking because the oxygen blowing period is determined concerning the final carbon content and temperature of the steel within certain limits, before further processing [7]. It is believed that the overall decarburization reaction can be divided into three main regimes [3], as depicted in Figure 2.3. In the initial period of a blow (regime 1), the decarburization rate is low as the oxygen is consumed in other refining reactions, mainly desiliconization. The decarburization rate increases linearly as blow time progresses. During the main blow (regime 2), nearly all the oxygen is consumed by decarburization. Consequently, the overall decarburization rate increases with an increased oxygen flow rate, as shown in Figure 2.3. Towards the end of a blow, the overall decarburization rate decreases linearly as the carbon content reaches a critical level[3].

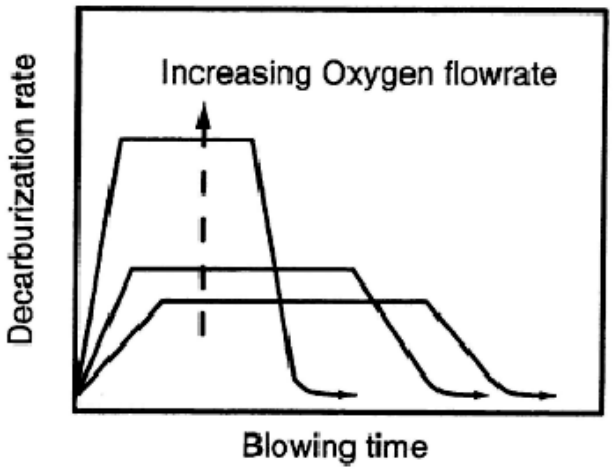

Figure 2.3: The evolution of decarburization rates as a function of the oxygen flow rate[3]

2.3.2 **Other refining reactions**

Other main reactions are desiliconization, demanganization, dephosphorization, and FeO formation. The silicon dissolved in the hot metal is oxidized to deficient levels (less than 0.05 wt.%) in the first three to five minutes of the blow (or early blow) due to its high affinity to oxygen and low activity of the reaction product (SiO_2) in slag [26–28]. Most of the silicon oxidation is likely to occur due to its direct reaction with oxygen, and a small fraction of silicon is removed by the reaction with FeO. These reactions are shown below[3,7]

$$[Si] + O_2 = (SiO_2) \quad (2.1)$$

$$[Si] + 2(FeO) = (SiO_2) + 2[Fe] \quad (2.2)$$

The oxidation of manganese in the first part of the blow follows the same trend as that of silicon and is oxidized through gaseous oxygen or FeO sourced oxygen[3,7].

$$[Mn] + ½\, O_2 = (MnO) \quad (2.3)$$

$$[Mn] + (FeO) = (MnO) + [Fe] \quad (2.4)$$

Besides, some of the oxidized Mn reacts with carbon in the middle of the blow and reverts to the metal bath through the reaction below[3,7].

$$(MnO) + [C] = CO + [Mn] \quad (2.5)$$

In the case of dephosphorization in a highly oxidizing atmosphere like oxygen steelmaking, through the formation of phosphate ion (PO_4^{3-}) in slag[29], the state of equilibrium of the phosphorus reaction between slag and hot metal has been expressed by Turkdogan[29] in equation 2.6. The concentration of dissolved oxygen $[O]$ is generally high, but the concentration of (O^{2-}) depends on the basicity of slag as the availability of free O^{2-} ions increases with an increase in the basicity of slag. Hence, the prevalence of a basic slag is vital for an effective dephosphorization.

$$[P] + \frac{5}{2}[O] + \frac{3}{2}(O^{2-}) = (PO_4^{3-}) \quad (2.6)$$

Other factors critical to dephosphorization are (FeO) content and temperature of slag[29]. An optimum (FeO) content and low temperature are crucial for the reaction mentioned above to move in forward reaction[30]. Low FeO level indicates a low oxygen supply, whereas excessive FeO level reduces the basicity of slag, hence increases the activity coefficient of P_2O_5 in slag[29].

Fe oxidation takes place throughout the blow. This reaction is a strong function of temperature, as well as the lance height[3]. The net FeO content in the slag is dependent on the difference between the rates of FeO formation and consumption due to other refining reactions. An optimum FeO formation is critical during the significant part of the blow[3,31]

to sustain the refining reactions in the emulsion zone, while not causing a loss in yield in steel because of an excessive amount of FeO in turndown slag. The FeO formation increases at the end of the blow as the rate of other refining reactions (mainly decarburization) decreases.[31]

2.3.3 Flux dissolution

The addition of flux into the slag is critical for increasing the basicity of slag and reducing the refractory wear of the furnace[32,33]. The rate of dissolution of fluxes into the slag has been extensively investigated through experiments[32–41] and described through models[42–45]. The dissolution of lime and dolomite into the slag can be described by the following two reactions.

$$CaO \rightarrow (CaO) \quad (2.7)$$

$$MgO \rightarrow (MgO) \quad (2.8)$$

The reactions 2.7 and 2.8 generally proceed through the formation of intermediate product at the flux particle-slag interface due to the reaction between flux particles and slag. These intermediate products are di and tricalcium silicates in the case of lime[39,46], whereas the solid solution of Fe and Mg is formed during dolomite dissolution[32]. The stability of the intermediate products is affected by the stirring conditions, temperature, and composition of the slag. Thus the intermediate products can retard the dissolution but do not stop the dissolution of fluxes altogether[7]. The dissolution is affected by both kinetic (stirring

conditions in slag) and thermodynamic factors (saturation limit, slag composition)[35]. Further discussion on this topic is provided in Chapter 6.

2.4 Dynamics of Fluid Flow

2.4.1 Oxygen jets

An adequately designed convergent-divergent nozzle, fitted at the end of the lance, can accelerate oxygen gas to supersonic velocity by converting pressure energy of the gas to kinetic energy[3]. The speed of the supersonic jets is higher than Mach 1. These jets are used to deliver oxygen to the metal bath to achieve its refining. The oxygen jets descending from the nozzle expand radially, and the velocity decreases (also referred to as jet decay) as they impinge upon the metal bath[3]. Employment of multi (typically 3 to 6)-hole lances with supersonic nozzles began so as more effectively deliver oxygen to a broad cross-section of the metal bath. The jets issuing from the nozzles might interfere before impinging upon the metal bath (also referred to as coalescence). This would result in a decrease in the velocity of the jets[47]. The nozzle inclination angle between 10 to 20^{o} with respect to the vertical axis is employed not only to achieve impingement of non-coalescing jets but also to avoid excessive splashing of metal on the wall of the furnace.

The oxygen jets impinging on the metal bath surface lead to the transfer of a fraction of jet-momentum, causing an oscillatory flow at impact zone and generation of metal droplets from the bath. In contrast, the residual fraction of momentum is transferred to bath and results in the formation of cavities[48]. This furthermore results in the displacement of liquid metal and leads to the continuous renewal of the reaction area. The nature of cavities formed

due to the impact of oxygen jets has been studied extensively through physical models[49–53] and mathematical models[5,54–56].

Banks and Chandrasekhara[49] developed a fundamental relationship between the momentum of a jet and cavity depth, assuming momentum as an independent variable based on water modelling.

$$\frac{\dot{M}}{\rho_l g n_o^3} = \dot{f}\left(\frac{n_o}{h}, \frac{d_t}{h}\right) \tag{2.9}$$

Using this analysis, Davenport et al.[13] further derived the correlation below

$$\frac{\dot{M}}{\rho_l g h^3} = \frac{\pi}{2K^2}\dot{\frac{n_o}{h}}\left(1 + \frac{n_o}{h}\right)^2 \tag{2.10}$$

where K=7.5 is turbulent jet constant, n_o is the depth of penetration of jet or depth of the cavity, g is the acceleration due to gravity, and h is the lance height. $\dot{M}$ is the momentum of the jet at the nozzle exit and is given by

$$\dot{M} = \frac{\pi}{4} d_t^2 v_e^2 \rho_g \tag{2.11}$$

Where v_e is the velocity of jet at the nozzle exit, d_t is the throat diameter at the nozzle. Banks and Chandrasekhara[49] arrived at a relation between cavity depth and diameter given by,

$$\frac{d_c}{n_o} = A\sqrt{\frac{\dot{M}}{\rho_l g n_o^3}} \tag{2.12}$$

Molloy[57] suggested three distinct flow patterns leading to the generation of metal droplets, namely: dimpling, splashing, and penetrating. The dimpling flow pattern occurs when there

is low jet velocity and/or a great distance between lance height and metal bath. A slight (and stable) surface depression is formed.[51] When the jet velocity increases and/or lance height is reduced, a shallow depression is formed and instability of the surface increases. This results in tearing of outwardly directed droplets from the edge of the depression, and it is referred to as the splashing mode[51]. With further increase in jet velocity and/or reduced lance height, greater penetration of the bath takes place, leading to deeper cavities. This results in an apparent reduction in the amount of outwardly directed 'splash' droplets and is referred to as the penetration mode[51]. The dimpling mode is rarely prevalent under oxygen steelmaking processing conditions. More details of the estimation of the droplet generation rate are presented in section 2.6.1.3.

Koria and Lange[50] performed a hot-model study involving impingement of the oxygen jet(s) on molten steel for top blowing and combined blowing processes. They employed both single and multi-nozzle jets. The study correlated the depth and diameter of the cavities with the dimensionless momentum of the jet(s). The dimensionless momentum is a function of the momentum of the jet (dependent upon oxygen supply pressure and the number and inclination angle of the nozzles) and the lance height. The correlation between the penetration depth (cavity depth, n_o) and parameters related to dimensionless momentum as proposed by Koria and Lange[50] is given by

$$n_o = 4.469 \times h \times \left(0.7854 \times 10^5 d_{th}^2 P_a \left(1.27 \frac{P_o}{P_a} - 1\right) \cos\alpha \frac{1}{g\rho_m h^3}\right)^{0.66} \quad (2.13)$$

The diameter of the jet at the impingement point or cavity diameter, d_c is given by,

$$d_c = 2.813 \times h \times \left(0.7854 \times 10^5 d_{th}^2 P_a \left(1.27\frac{P_o}{P_a} - 1\right)(1 + \sin\alpha)\frac{1}{g\rho_m h^3}\right)^{0.282} \quad (2.14)$$

where P_o is the supply pressure of oxygen, P_a is the ambient pressure inside the vessel, α is the inclination angle of a nozzle.

2.4.2 **Bottom stirring**

The bottom stirring plays an important role in the homogenization of the bath [1] and reducing the excessive oxidation of the metal bath[4,5] even though the volumetric flow rate of oxygen through the lance nozzles is much larger than bottom stirring gas in top-blown and mixed blown oxygen steelmaking processes. The introduction of bottom stirring gas in the top-blown oxygen steelmaking process increases the homogeneity of the bath, decreases mixing time and enhances the yield of liquid steel. This is demonstrated by the ranges of mixing times for various bottom stirring rates in oxygen steelmaking processes as shown in Figure 2.4 [1]. The range of mixing time decreases from left to right, i.e., it is maximum (90 -120 s) for the LD process and minimum (~ 20 s) for the OBM process. Many steelmakers chose to incorporate the benefits of bottom stirring while retaining the advantages of a top-blown configuration [1]. These include the LD-LBE, LD-CB, LD-KGC, LD-OTB, and involve a stirring gas (either N_2, Ar, CO, CO_2) in the range of 0.01 to 0.1 Nm^3/t.min (in contrast to oxygen rate of 2.5 to 4 Nm^3/t.min) [29]. This configuration is the most prevalent amongst other steelmaking processes[1]. Hence, the current study pertains to the modelling of refining reactions in such a combined process.

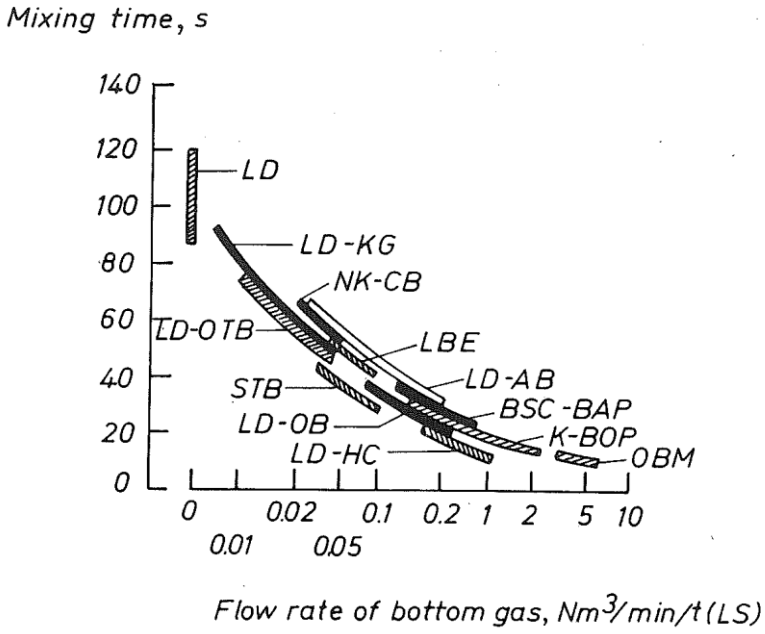

Figure 2.4: Mixing times of top, combined, and bottom-blown oxygen steelmaking processes[1].

Zhou et al.[5] studied fundamental kinetic energy transfer from top-jets and bottom stirring to bath in oxygen steelmaking. The energy transfer index (ETI) was defined to measure the efficiency of energy transfer to the bath from oxygen jets or bottom stirring. They calculated that the ETI increased when the bottom stirring gas flow rate is increased. On the contrary, the ETI decreased when the kinetic energy is supplied through oxygen jet (through a decrease in lance height or increase in gas flow rate). A physical model study by Fabritius et al.[58] investigated various overlap patterns between the bottom stirring plume and a wall jet. They found that the overlap between the bottom-stirring plume affected the cavity shape, droplet generation, and the droplet trajectory. Luomala et al.[59] conducted a physical modelling study. They varied bottom nozzle configurations to analyze the droplet generation, homogenization behavior of the bath. They concluded that the

droplet generation increases with an increase in the overlap between bottom stirring plumes and the top jets.

2.5 Thermodynamic Fundamentals

2.5.1 Thermodynamics of hot-metal

The hot-metal consists of mainly iron and relatively small concentrations of solutes such as carbon, silicon, manganese, and phosphorus[3,60]. According to Henry's law for 'dilute solutions,' the Henrian activity h_i of a solute, i is defined by[3]

$$h_i = f_i(wt\ \%)_i \tag{2.15}$$

where $(wt\ \%)_i$ is a solute concentration in wt % and the term f_i is the Henrian activity coefficient. The presence of other solutes has a marked effect on increasing/decreasing the activity of solute i. Under these circumstances, the activity coefficient for the solute i, in a multi-component system is defined as[60]

$$\log f_i = e_i^i(wt\ \%)_i + e_i^j(wt\ \%)_j + e_i^k(wt\ \%)_k \ldots \tag{2.16}$$

In general, e_i^k and e_i^j represent the effect of elements k and j on the Henrian activity coefficient of element i, respectively, when both i and k are present in dilute solution.[3] They are referred to as interaction parameters. The interaction parameters between various solutes in hot-metal have been measured experimentally by many researchers[60–62].

2.5.2 Thermodynamics of steelmaking slags

Liquid slag consists of a solution of ions or complex molecules derived from molten oxides[3]. Steelmaking slag originates from the oxides generated through oxidation of iron, impurities like silicon, manganese, and phosphorus, and dissolution of flux components

like calcium and magnesium oxides. The Raoultian activity of a slag component, i is expressed in the Raoultian standard state using the following equation

$$a_i = \gamma_i x_i \tag{2.17}$$

where x_i is the mole fraction of component in slag, γ_i is the Raoultian activity coefficient and a function of temperature and composition of slag. The activity coefficients of multi-component slag can be sourced from experimental data or can be evaluated from thermodynamic models.

The thermodynamic treatment of steelmaking slags can be described by considering either the molecular or the ionic nature of slag[3]. The molecular theory of slags assumes the liquid slag to be a solution of simple molecules such as $CaO, MgO, SiO_2,$ and P_2O_5 and complex molecules such as di, tricalcium silicates formed as a result of the chemical reactions between the simple molecules, and were assumed to be non-dissociated and non-reactive[3]. However, this led to a non-consideration of the role of these compounds in refining reactions like dephosphorization. Alternately, the ionic theory of slags assumes an ideal ionic behavior, whereby the oxides like CaO, MgO, and FeO completely dissociate and supply oxygen given by the following reactions[3]

$$CaO = Ca^2 + O^{2-} \tag{2.18}$$

$$MgO = Mg^2 + O^{2-} \tag{2.19}$$

$$FeO = Fe^2 + O^{2-} \tag{2.20}$$

The oxygen ions break up the polymeric structure of SiO_2 in slag, as described by the following reaction

$$SiO_2 + 2O^{2-} = SiO_4^{4-} \tag{2.21}$$

The silicate network successively breaks down to individual SiO_4^{4-} tetrahedra intermixed with cations Ca^{2+}, Mg^{2+} and some oxygen ions O^{2-} at high basicity, i.e $\frac{CaO}{SiO_2} > 2$ [29].

2.5.3 Thermodynamics of refining reactions

A reaction at constant temperature and pressure can be represented as below[29],

$$mM + nN = uU + vV \tag{2.22}$$

At equilibrium $\Delta G = 0$, therefore, in terms of the activities of reactants and products the standard free energy change accompanying the reaction is given by the difference of free energies of the products and the reactants [29]

$$\Delta G^o = (uG_U^o + vG_V^o) - (mG_M^o + nG_N^o) = -RT \ln \frac{(a_U)^u (a_V)^v}{(a_M)^m (a_N)^n} \tag{2.23}$$

The equilibrium constant is defined by

$$K = \frac{(a_U)^u (a_V)^v}{(a_M)^m (a_N)^n} \tag{2.24}$$

Inserting equation 2.24 into equation 2.23 leads to the following equation

$$\Delta G^o = -RTlnK \tag{2.25}$$

ΔG^o is solely a function of temperature, the equilibrium constant is also a function of temperature.

$$lnK = -\frac{\Delta H}{RT} + \frac{\Delta S}{R} \tag{2.26}$$

For an exothermic reaction (as is the case for the most of the refining reactions), the value of K would decrease with an increase in temperature; hence, the forward reaction rate would decrease if all other process conditions are identical and this leads to the formation of oxides. The thermodynamics of refining reactions has been extensively investigated, and the reaction equilibrium constants for the refining reactions in oxygen steelmaking are reported. These data are compiled in the open literature[60,63]. For example, the oxidation of silicon has the highest equilibrium rate constant followed by carbon, manganese, and iron such that $K_{Si} \gg K_C > K_{Mn} \approx K_{Fe}$.

2.6 Kinetics of Refining Reactions

2.6.1 Kinetics of decarburization reaction in the metal-slag interface (Emulsion zone and slag-metal bulk)

Even though the slag-metal interface is observed for both the emulsion and slag-metal bulk zone, the experimental studies[64–72] were primarily done with metal droplet in a slag for a more fundamental understanding of reaction kinetics between metal and slag. The insights on reaction kinetics developed from the droplet-slag experiments also apply to the slag-metal bulk. Mulholland *et al.*[64] adopted an X-ray fluoroscopy technique for in-situ observation of the behavior of a Fe-C-S metal droplet in slag. They employed a specially constructed vertical tube furnace that allowed X-rays to pass through without much absorption to observe and record a visual image of a metal droplet in slag. They found the

existence of a gas halo around the metal droplet, and the subsequent reactions proceed through gas as an intermediate layer, and the size of the droplet kept intact. They analyzed the effect of droplet size, slag composition, temperature, and metal composition on the size of the bubbles/foam formed. However, their observations were limited to being qualitative. Further quantitative measurements of this phenomenon were conducted by Gaye and Riboud [66] using a Constant Volume Pressure Increase (CVPI) technique. This technique involves the analysis of the pressure change in a sealed reaction vessel caused by the evolution of CO gas. One mole of CO produced equals one mole of FeO reduced from slag, as stated in equation 2.29. Hence, the rate of decarburization can be accounted for by measuring the pressure during the experiment. Gare and Hazeldean [65] firstly combined the CVPI method with the X-ray fluoroscopy technique. As a result, both qualitative and quantitative descriptions of the slag-metal interaction became possible. A similar configuration has been used by Fruehan et al. and Coley et al. The schematic representation of such an experimental set-up is shown in Figure 2.5[70]. These experiments were carried out at varying process conditions such as the temperature of slag, carbon and sulfur contents of droplet, and FeO content of slag.

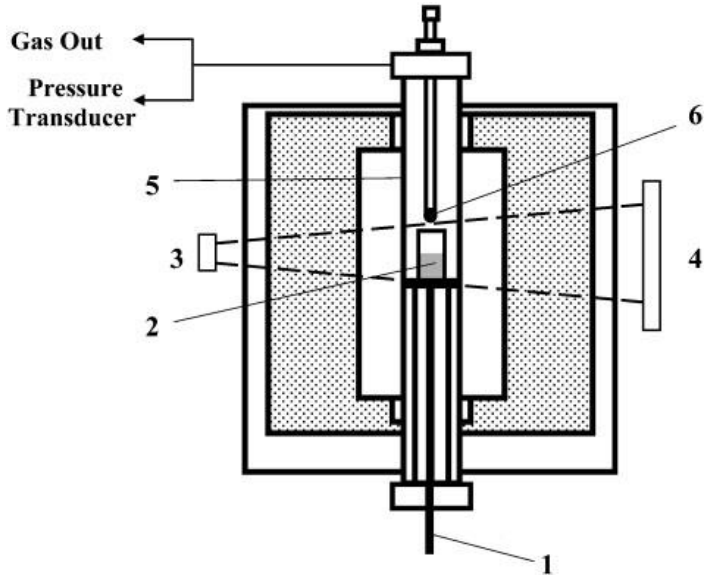

Figure 2.5: Schematic diagram of the experimental set up employing X-ray + CVPI method [70] *1: thermocouple; 2: slag; 3: X-ray generator; 4: image intensifier; 5: working tube; 6: iron pellet*

It is believed that the metal droplets react with FeO in the slag after they are ejected from the metal bath. FeO diffuses to the slag-gas interface towards a bubble on the metal-gas interface to supply oxygen. CO reduces FeO at the slag-gas interface, which is followed by a reaction at the metal-gas interface with CO_2 diffusion through a gas halo [67]. CO_2 provides oxygen to react with carbon in the melt. The schematic representation of metal droplet in slag is provided in Figure 2.6, and the proposed reactions involve the sequence [67]

$$CO_{(g)} + (FeO) = Fe + CO_{2(g)} \text{ (slag surface)} \quad (2.27)$$

$$CO_{2(g)} + [C] = 2CO_{(g)} \text{ (metal surface)} \quad (2.28)$$

The reduction of FeO in the slag by carbon in the metal droplet is described by the following overall reaction:

$$(FeO) + [C] = Fe + CO_{(g)} \quad (2.29)$$

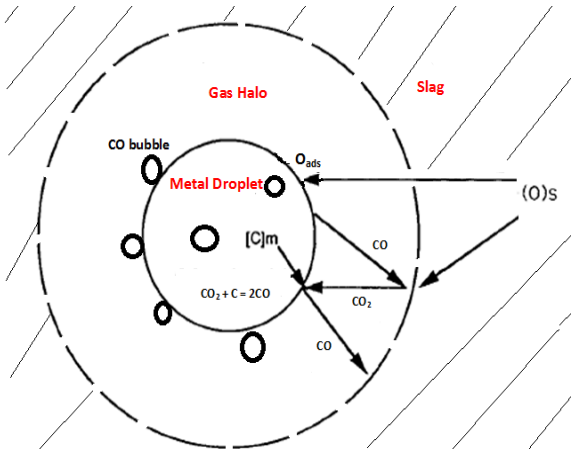

Figure 2.6: Schematic representation of a metal droplet in slag [67]

Based on these experiments, several authors suggested the various possible control mechanisms for the decarburization reaction occurring in the emulsion, as discussed below:

a. Oxygen mass transport in the slag

Paul et al.[73] experimentally studied the reduction of FeO by carbon in liquid iron. They suggested that the mass transport of FeO through the slag phase is the rate limiting step for decarburization reaction when the FeO content in the slag was less than 5 wt %. Experiments by Min and Fruehan [67] (for low FeO slags) and Molloseau and Fruehan[68] (for high FeO slags) confirmed that this control mechanism is prevalent when the FeO content in slags is below 10 wt %.

b. Gas-phase diffusion (through gas halo surrounding metal droplet)

A gas halo surrounds the carbon-containing metal droplets in contact with ferruginous slags due to CO formation[67,74]. The CO bubbles detach instantaneously or after a certain time. When the gas halo is stable the diffusion of CO_2 through gas halo towards the metal droplet can be slow and control overall decarburization reaction.

c. Gas-slag ($CO_2 - Fe$) reaction

The gas-slag reaction as described by equation 2.27, involves the dissociation of CO_2 gas in the presence of ferruginous slag. Barati and Coley[75] conducted a study of reaction kinetics of $CO - CO_2$ and ferruginous slags and found dependence of the rate of this reaction on the slag composition, oxidation state, and temperature. The dependence on the oxidation state suggested that the rate-controlling step is the formation of single charged CO_2 [69].

d. Gas-metal reaction (CO_2-C) reaction

The rate constant for this reaction is a strong function of sulfur content of metal droplets due to its being surface active element.[67,76–78] Low concentration of sulfur lowers the surface tension between metal and slag and promotes an increase in the surface area, thereby an increase in the rate of reaction [66]. On the other hand, a high concentration of sulfur in metal droplets may block the reaction sites of metal-gas reactions and cause it to be the rate limiting step.

e. Mass transport within the metal droplet

The mass transport of carbon from bulk metal to metal surface could influence the decarburization reaction. The control of reaction rate through this mechanism is also possible when the carbon content is very low making availability of carbon atoms at the interface lesser than the oxygen. Min and Fruehan[67] claimed that the decarburization rates calculated by assuming the mass transport of carbon within the metal droplet are higher than the measured rates, thus making its prevalence less probable.

f. CO nucleation inside/outside the metal droplet

Gare and Hazeldean[65] firstly proposed the CO nucleation in and around the metal droplet during the decarburization reaction based on the X-ray observations of the droplet-slag reaction, but their work did not specifically state any rate limiting step. CO nucleation within the metal droplet has been suggested to be the rate-controlling step by Chen and Coley[69,70]. The equation for homogenous nucleation, as described by classical nucleation theory, is stated as [70].

$$J_s = N_o \left(\frac{-\Delta H}{kT}\right)\left(\frac{3\sigma}{\pi m}\right)^{1/2} exp\left(\frac{-16\pi\sigma^3}{3kT(P_{ve}-P_L)^2}\right) \quad (2.30)$$

where N_o is the number concentration of CO embryos in the liquid, σ is the surface tension at the liquid-gas interface, ΔH is the heat of formation of one CO molecule, m is the mass of one molecule, T is temperature, k is the Boltzmann constant, P_{ve} is the pressure in the vapor bubble at equilibrium, and P_L is liquid pressure.

No homogenous nucleation of CO gas is predicted by equation 2.30[69,70] for the experimental conditions. However, experimental observations reported by Baker *et al.*[79,80] showed that iron droplet swelled and exploded due to CO nucleation inside the droplet when passing through a gas mixture of oxygen and helium. Many other studies[70,79–84] also indicated the presence of CO bubbles inside the metal droplet and the increase in the size of the metal droplet. The phenomenon was termed as "swelling" [70,81], "boiling"[79,80,82,83] or "bloating" [84]. The possibility of the formation of CO bubbles due to heterogeneous nucleation (e.g., on the surface of inclusion within the metal droplet) was unlikely as the experiments were carried out in a controlled atmosphere, which made the presence of

inclusion impossible. Thus the only explanation for these experimental observations is attributed to homogenous (or pseudo-homogeneous) nucleation within the droplet despite the theoretical impossibility indicated by equation 2.30[85].

Taking into account the possible control mechanisms for the decarburization reaction in the emulsion zone, some notable models[67–70,81,84] for emulsion zone decarburization were proposed. Fruehan and his co-workers [67,68] proposed a mixed control model involving control by the gas-metal interfacial reaction, mass transfer in gas film, and slag. The decarburization rate is primarily controlled by gas-metal interfacial reaction at high sulfur contents in the metal droplet, [S] and low FeO contents in the slag (FeO) because sulfur blocks surface sites for the reaction. In the case of low (FeO) and low [S], the rate is controlled by slag and gas-phase mass transfer. Finally, slag-phase mass transfer dominates the reaction rate for high (FeO) contents (> 10 wt %) as the droplet bloats, and the interfacial area increases.

Sun and Zhang [81,86] incorporated the reaction steps, namely mass transport within the metal droplet, within slag and reaction equilibria at the interface. The results of these models were validated against the experimentally measured decarburization rate for low FeO slag. However, this model did not consider the internal CO generation which was observed in several experimental studies. Brooks et al.[84] assumed that mass transport of carbon in the metal phase is the rate limiting step. Therefore, the 'effective rate constant' and the gradient between bulk and equilibrium carbon values determined the rate of decarburization in this model. The 'effective rate constant' evaluated using Higbie's penetration theory[87]. More details of this procedure are described in section 2.6.1.4. This

model was validated with the experimentally measured decarburization rate and residence time of Molloseau and Fruehan[68]. This model was employed by subsequent studies[7,88] to predict decarburization in the emulsion zone. However, as stated earlier, the mass transport of carbon in metal in less likely to be a rate limiting step. Chen and Coley's [69,70] model, on the contrary, described the CO generation within the metal droplet through modified homogenous nucleation theory, as described in the previous section. They observed the dependence of reaction rate on the droplet size and hence suggested the gas generation rate can be controlled by the nucleation of CO bubbles inside the droplet. The model was validated against experimentally measured CO generation rates.

Even though the experiments were focused on the investigation of the kinetics of decarburization of the emulsion zone, they equally apply to the slag-metal bulk. This is due to the similar nature (metal-slag) of the interface created in both reaction zones.

2.6.1.1 **Bloated droplet theory**

When the supply of oxygen from slag to the droplet-slag interface is larger than the consumption by decarburization and other reactions at the interface, then there is significant diffusion and build-up of oxygen inside the metal droplet. This leads to an increase in supersaturation and nucleation of CO bubbles within the metal droplet[69,70]. The rate of nucleation of CO gas depends on the concentration of carbon and oxygen, and the temperature and concentration of other impurities inside the metal droplet[83]. The nucleated CO bubbles then exert pressure on the metal droplet wall and escape from the metal droplet. Initially, the CO gas generated within the metal droplet is greater than the escape leading to retention of a significant fraction of CO gas. Due to this retention, the density of metal

droplets decreases, its volume increases, and the metal droplet becomes "bloated." The term 'bloating' was introduced by Brooks et al.[84], which was also referred to as 'swelling'[70,81] or 'carbon boil'[83,89] in other studies. The density of the bloated droplet is lower than the slag, which causes an increase in residence time of droplet in slag. Due to bloating, the surface area of a droplet and internal stirring within the droplet increase, leading to an increase in reaction rates of other refining reactions[90]. The formation of CO bubbles inside the metal droplet when it was reacted with FeO bearing slag or oxidizing gases has been observed in several studies [64,65,68–72,79,91–93].

Since decarburization kinetics in the emulsion are induced by the interfacial area, the reaction rate depends on (i) the number of metal droplets generated (ii) the droplet size distribution and (iii) the residence time of the metal droplets[94]. These parameters are discussed below.

2.6.1.2 **Generation of metal droplets**

He and Standish[95] defined a non-dimensional number, which expresses a ratio of the momentum intensity to the liquid properties, as a similarity criterion to predict the droplet generation rate through top gas blowing. This was termed as the Nominal Weber number and can be written as:

$$N_{NWe} = \frac{\rho_g u_j^2}{\sqrt{\sigma g \rho_L}} \tag{2.31}$$

where U_j is the free turbulent jet axial velocity, σ is the surface tension (kg/s^2), g is the gravitational constant (m/s^2), ρ_g and ρ_L are the density of gas and liquid (kg/m^3), respectively.

Li and Harris[96] presented the condition for the the onset of splashing based on Kelvin–Helmholtz instability criterion. They reported that splashing occurs when the following equation is satisfied.

$$\frac{\rho_g u_g^2}{2\sqrt{\sigma g \rho_L}} = 1.0 \tag{2.32}$$

where u_g is the critical gas velocity related to the free turbulent jet axial velocity, u_j. It can be shown by the following equation

$$u_g = \eta u_j \tag{2.33}$$

where η is constant. It is noteworthy that the terms in equation 2.31 and 2.32 are dimensionally similar. However Subagyo et al.[97] stated that the term in equation 2.32 relates to the physical condition of droplet generation, and is a direct measure of the number of times when the critical Kelvin–Helmholtz instability criterion is exceeded and hence it is more relevant. They introduced a dimensionless parameter, the "blowing number," N_B. It is stated in Equation 2.34 as follows,

$$N_B = \frac{\rho_g u_g^2}{2\sqrt{\sigma g \rho_L}} \tag{2.34}$$

Subagyo *et al.* [97] studied the behavior of metal droplets in the emulsion experimentally for a cast iron-slag-nitrogen system at high temperatures and developed a correlation between the blowing number and the rate of droplet generation per unit volume of the blown gas. The correlation is given in Equation 2.35.

$$\frac{R_B}{F_G} = \frac{(N_B)^{3.2}}{[2.6 \times 10^{-4} + (N_B)^{12}]^{0.2}} \quad (2.35)$$

where R_B is the droplet generation rate (kg/s), and F_G is the volumetric flow of blown gas (Nm^3/min). The predictions through Equation 2.35 agree well with those reported by He and Standish[94], which was undertaken at low temperatures. This equation can be used to predict the rate of droplet generation per unit volume of the blown gas. Rout et al.[98] modified the correlation suggested by Subagyo et al.[97] The authors re-evaluated the blowing number (at the impingement point of oxygen jet on bath) while taking into account the effect of temperature on the density and velocity of the gas jet. With increasing temperature, the density of gas jet decreases, and velocity increases and leads to an increase in the droplet generation rate. The authors predicted a droplet generation rate 3 to 8 times higher than that predicted by Subagyo et al.[97]. Sabah and Brooks[52] conducted a water modelling study and measured droplet generation in vertical and radial positions for varying lance heights. Based on readings of experiments, the authors proposed a new correlation for splashing mode (as described in section 2.4.1) which predicted a higher droplet generation than that of Subagyo et al[97]. They found that higher N_B does not necessarily indicate a higher droplet generation rate, and 'cavity mode' also affects the droplet generation. A recent study by Haas et al.[99] employed a direct measurement method to obtain a number of splashed droplets, droplet size, ejection velocity through water modelling, and digital image processing. Similar to Sabah and Brooks[52], they observed that the "number of detected droplets" decreases beyond a certain blowing number, which is contrary to equation 2.35. The authors speculated that this decrease was due to the change

in cavity mode. The splashing angle is found to become steeper while the lance height decreases, thus indicating that more droplets generated at the impact zone fall back into the cavity without reaching the emulsion zone.

2.6.1.3 **Size distribution of metal droplets**

The droplets ejected from the metal bath have varying sizes. Since the area to volume (A/V) ratio of the metal droplets varies with the droplet size, the size distribution of metal droplets could considerably influence the reaction kinetics in the emulsion zone.

Certain sampling studies involving hot-metal/liquid iron focused on the size of the droplets generated due to the impingement of an oxygen jet on a metal bath in the steelmaking process. These studies involved the collection of droplets from the tap-hole of the industrial furnace[14], sampling of droplets from the slag-gas-metal emulsion in industrial[22,100] and experimental [10,101] furnaces, analysis of over-flown slag from the shell of the furnace[102] and droplets splashed from a crucible[103]. Meyer et al.[14] reported the droplet size range of 0.15 to 3.32 mm for a 230-t furnace whereas Cicutti et al.[100] found that the size of the droplets ranged from 0.23 to 3.35 mm with a mean value of 1 to 2 mm for a 200-t oxygen steelmaking furnace. Chatterjee et al.[10] stated a size range of 'sprayed' droplets between 0.3 to 0.5 mm for a 6-t furnace, while Millman et al.[28] (also for a 6-t furnace) found the size range between 0.016 to 6 mm. Price et al.[22] reported a wide range of droplet size for a 90-t furnace, but the droplet size range of 1-2 mm was pre-dominant. Similarly, Trentini[102] found a wide range of droplet size in the quenched slag based on the droplets retained on various screen sizes. The greatest size was greater than 25.3 mm and the smallest size was less than 6.3 mm. The greatest variance in size distribution, however, was

reported by Koria and Lange[103] with the droplet size ranging between 0.04 and 70 mm. A few notable cold model studies[104,105] were also conducted. Peaslee[104] indicated a droplet size range between 0.2 to 3 mm whereas Standish and He[105] reported a range between 1-5 mm.

Pilot plant and industrial trials indicate that the size distribution of droplets ejected in top blown oxygen steelmaking process can be described using the Rosin-Rammler-Sperling (RRS) distribution function[95,100,103] given by the following equation

$$R = 100 \times e\left(-\left(\frac{d}{d'}\right)^{n}\right) \tag{2.36}$$

where R is the cumulative weight percent of droplets remaining on the sieve with diameter d. n and d' represent homogeneity of the distribution function and the measure of fineness, respectively[103]. The value of n is 1.26 for the steelmaking process[103]. d' represents the statistical drop size for $R = 36.8\,\%$ cumulative weight retained. d' is dependent on the blowing parameters and collection place.[103] Subagyo et al.[97] developed a correlation between d' and the dimensionless blowing number using the regression analysis technique combined with their experimental data and Koria and Lange's data[103].

$$d' = 12\,(N_B)^{0.82} \tag{2.37}$$

Haas et al.[99] reported that the droplet size correlation stated in equation 2.37 overestimates the droplet diameter based on the sampling in their water model study. However, they emphasized the need for further study to have a more comprehensive droplet property correlation with the lance design and profile. Thus as of now, the use of Koria and Lange's[103] correlation is reasonable for evaluation of droplet size distribution.

2.6.1.4 **Residence time of metal droplets**

Some industrial studies[15,22,106] through plant measurements, reported the residence time of metal droplets in the emulsion zone of oxygen steelmaking. Kozakevitch[106] predicted that the average residence times ranged between 60 to 120 seconds based on the carbon and phosphorus content in metal droplets. Price[22] employed the radioactive gold isotope tracer technique in a 90-t furnace to measure the residence time of droplets and found that it varies from 90 to 150 seconds. Schoop et al.[15] predicted the residence time to be between 0 to 59.9 seconds during various times of the blow based on the chemical analysis of droplets and kinetic model. Predictions of droplet residence time were also made through cold models[16,94]. Urquhart and Davenport[16] predicted that mean residence time is 0.25 s based on their cold model experiments. He and Standish[94] used a 3-D two-phase (mercury/glycerin) model and suggested that the average residence time of a droplet is between 2 and 40 s. Furthermore, many experimental studies[64,66–68] in which the droplet dropped from the top of a furnace into the liquid slag at steelmaking temperatures, were conducted. The droplet floated on the surface of the slag due to the formation of CO bubbles either within the droplet[66–68] or around the droplet (halo formation).[64] Therefore the density of the droplet is lower than the dense slag and the residence time of droplets would be extended from 0.2 seconds to 60 seconds. Brooks *et al.*[84] adopted this observation and developed a mathematical model based on both the ballistic motion and bloating of metal droplets to predict the residence time of a metal droplet in the slag-gas-metal emulsion. The ballistic motion model relied on the principles of mechanics and considered the balance of various forces acting on a metal droplet such as gravitational, buoyancy, drag and added

mass forces. For a certain period (due to swelling/bloating), the decarburization reaction within the metal droplet would decrease its apparent density and affect the ballistic motion of the droplet. Simultaneous analysis of the ballistic motion and the bloating phenomenon of the droplet would lead to a better description of the metal droplet behavior in an emulsion. Brooks *et al.*[84] described the "threshold decarburization rate, r_c^* " such that a droplet would bloat only when a threshold rate would be exceeded.

$$\rho_d = \rho_{do} \frac{r_c^*}{r_c} \qquad \text{for } r_c > r_c^* \tag{2.38}$$

$$\rho_d = \rho_{do} \qquad \text{for } r_c <= r_c^* \tag{2.39}$$

where ρ_{do} is initial droplet density, kg/m^3 and r_c is decarburization rate, wt %/s. Equation 2.39 implies that when the decarburization rate is lower than the threshold decarburization rate, there would be no bloating. In other words, the CO generation rate within the droplet would be equal to its escape rate, and the droplet would retain its original shape and density. The authors[84] noted that the threshold decarburization rate for bloating is a complex function of interfacial properties of droplet and slag. In the absence of better models, they evaluated the threshold rate based on the bloating behavior of a single droplet in slag observed by Molloseau and Fruehan [68]. They suggested a linear correlation between the threshold decarburization rate and FeO content in the slag for FeO content ranging between 5 and 20 wt %, as shown in the following equation[84]

$$r_c^* = 2.86 \times 10^{-4}(wt\%FeO) \tag{2.40}$$

The prediction of droplet residence time was approximately 11.5 seconds. This value was very close to that (about 11 seconds) experimentally observed by Molloseau and

Fruehan[68]. To predict the rate of decarburization in the single droplet, Brooks *et al.*[84] employed an equation based on the first-order reaction rate and assumed that mass transport of carbon within the metal droplet is the rate limiting step. The authors applied non-linear regression analysis to the decarburization data from Molloseau and Fruehan's[68] experiments and calculated the rate constant of the reaction. This approach did not address the various kinetic phenomena of the decarburization reaction in a droplet, as mass transport of carbon might only be one of the controlling steps, and other factors stated earlier would also control the rate of reaction to a varying degree, depending on the process condition. This approach was successfully incorporated by Dogan *et al.* [18] and later by Rout et al.[107,108] to predict the total decarburization rate of droplets in the emulsion.

2.6.2 Kinetics of decarburization reaction in the metal-gas interface (Impact zone and Oxygen jets /cavity zone)

Three distinct types of studies were performed to evaluate the reaction kinetics of carbon in liquid iron in contact with the gas phase. The first type included the study of the behavior of levitated[79,82,109–113] Fe-C and sessile[83,89] droplet in oxidizing gas atmospheres containing varying extents of CO_2 and O_2 and inert gases such as Ar and He. In these studies, the flow rate of the oxidizing gas was found to have the strongest influence, even with decreasing carbon contents. This indicated the presence of gas-phase mass transfer control. When the carbon content decreased to a very low level, the mass transfer in carbon towards the droplet-gas interface would control the reaction. Some of these studies[82,109] additionally employed high-speed photography (25 to 64 frames per second) during various times of experiments to further understand the reaction kinetics. Nucleation of CO bubbles and subsequent explosive disruption of the droplet (referred to as 'Carbon boil') were

observed in both these studies. While both studies observed the earlier onset of the boil, Jahanshahi[82] reported the nucleation of CO bubbles before the formation of an oxide phase and Distin et al.[109] reported that nucleation of the bubbles took place after the formation of an oxide phase on the surface. Sulfur was found to have an inhibitory effect on the decarburization rate as reported through various experiments for CO-CO_2 mixtures[111] and for O_2 gas mixtures[114]. The effect of sulfur on inhibition of decarburization has been found to reduce with an increase in temperature[83,114]. The chemical reaction control occurred due to presence of sulfur. However other conditions like low temperature (increases the adsorption coefficient of sulfur), high carbon content (increases the activity of sulfur, due to positive interaction coefficient) also aid in the prevalence of chemical reaction control. The sessile droplet studies[83,89] observed decarburization through the formation of CO gas within the droplet ('carbon boil'/ bloating) containing sulfur [S] contents between 0.005 and 0.4 wt % at 1583 and 1723 K. For oxidizing gas containing 40 vol% O_2, the onset of carbon boil was observed to be nearly constant for [S]≈ 0.2 wt %; however, the increase of [S] beyond this value decreased the onset time for bloating. This indicated that the effect of sulfur was not only in poisoning the reaction sites (decreasing surface decarburization) but also in decreasing the surface tension, which facilitated the nucleation of CO bubbles leading to carbon boil.

The second type of study included the study of the decarburization behavior of Fe-C melts in the oxidizing atmosphere[115]. Swisher and Turkdogan [115] studied the behavior of 80 g melt of Fe- 1wt % C exposed to CO-CO_2 gas mixtures of varying compositions at 1853 K. They postulated that the dissociation of CO_2 (i.e. interfacial reaction) on the surface of the

melt was rate limiting due to the poisoning effect of oxygen. The third type of study involved the sampling of droplets generated from the impact of oxygen jets on carbon-containing metal bath[21,116,117]. Koch et al.[21] conducted experiments involving blowing of an oxygen jet on a 50 kg molten Fe-C bath. The metal droplets generated due to the impact of jet on metal bath were sampled at various points of the cross-section of the metal sampler during a blow. The authors observed that the sampled droplets were significantly decarburized as compared to the bath. Also, the "inner" droplets (ejected into the jet) underwent greater decarburization as compared to the "outer" droplets (ejected into the emulsion zone in radially outward direction) indicating a significant contribution of gas-metal interface to decarburization in oxygen steelmaking. Kitamura et al.[116] sampled the splashed droplets due to oxygen and argon blowing in an 70 kg induction furnace . They observed that the splashed droplets due to oxygen blowing were finer than those splashed due to argon blowing. As expected, decarburization was observed due to oxygen and not due to argon. Nordquist et al.[117] conducted a sampling study in an induction furnace to investigate the behavior of generated droplets in an oxidizing atmosphere. The sampled droplets were analyzed using SEM-EDS and EPMA techniques. The carbon content of droplets was lower than the bulk of the bath at various times of the experiment. They found a strong influence of droplet size on the decarburization of droplets.

2.6.3 Effect of other impurities on decarburization at gas-metal and gas-slag interfaces

Several experimental studies were performed to analyze oxidation behavior of impurities such as Si and Mn in the presence of C in liquid iron with ferruginous slag[65,90] or oxidizing gases like O_2 and CO_2.[112,118] Gare and Hazeldean[65] conducted experiments to determine

the refining of Fe-C-(Mn, Si, S, P) metal droplets reacting with ferruginous slags at 1773 and 1813 K. They stated the elements Mn, Si, S, P did not significantly affect the decarburization reaction, especially if there was 'copious oxygen supply' from a high oxygen potential slag. The authors interpreted mass transfer control in metal and slag during different stages of their experiments. Similarly, Sun and Zhang[90] studied the reactions between droplets (3.45 wt % C, 1.85 wt % Si, 1.23 wt %Mn) and a slag containing 10 wt % FeO at 1713 K. They found that Si and Mn had a suppressing effect on the decarburization reaction, at least during the start of the experiment. This was primarily due to higher silicon and manganese composition as compared to previous study.[65] Additionally, silicon oxidation reaction was more favorable at 1713 K as compared to 1813 K. Thus decarburization was inhibited in this study. Sun and Zhang[90] also presented a kinetic model for this droplet-slag interaction. Based on this kinetic model, they predicted a decrease in the critical radius of nucleation or an increase in the supersaturation of CO formation due to a decrease in silicon content of metal droplets. The subsequent model by Sun[81] also came to a similar conclusion on the suppressing effect of silicon. Sun et al. in their model represented the limiting effect of mass transfer in metal and slag phases, but did not consider the effect of sulfur. Shibata et al.[119] measured the oxidation rates of carbon, phosphorus, and silicon through MnO from slag with low FeO contents (< 5 wt %) at temperatures between 1723 and 1823 K and presented a kinetic model for the system. They observed that MnO had a weaker oxidizing effect (the lower interfacial activity of oxygen) as compared to FeO, and silicon and phosphorus occurred preferentially over carbon. The rate of decarburization was found to be limited by the chemical reaction at the

slag-metal interface (a result of poisoning effect of sulfur). Jahanshahi[82] found a high emissivity oxide layer on the surface when silicon was present in the Fe-C-Si metal droplet. Also, the presence of silicon delayed the internal CO generation, even at concentrations of as low 0.015 wt.%.

Sun and Pehlke[112,113] investigated the simultaneous oxidation of silicon, manganese along with carbon levitated iron droplets in dilute (< 20 vol %) gaseous oxidizing atmospheres containing either O_2, CO_2 or a mixture. The oxidizing gas flow rates were low (500, 2000 mL/min) as compared to the those employed by Jahanshahi[82]. The resulting gas-phase mass transfer coefficients were low, and resistance to gas-phase mass transfer is high. They observed that decarburization preceded the oxidation of silicon, manganese, and iron. The onset of oxidation of Si, Mn, and Fe occurred only after carbon concentration decreases below 0.5 wt %. The gas richer in O_2 resulted in earlier onset of Si, Mn and Fe oxidation as every O_2 molecule supplies 2 atoms of oxygen, contrary to CO_2 gas, which supplies a single atom of oxygen. The poisoning effect of sulfur was not significant because of the higher temperatures of the experiments > 1873 K.

In summary, the decarburization at the metal-gas interface is found to be primarily controlled by mass transfer in the gas phase. At lower temperatures, the rate limiting step is the chemical reaction at the interface due to the poisoning effect of sulfur. Further, an impurity like silicon has a detrimental effect on decarburization.

2.6.4 **Kinetics of other refining reactions**

The other significant refining reactions include the removal of silicon, manganese and phosphorus. Experimental observations indicate that the rate of reactions is mostly limited

by mass transfer in either metal, slag or gas phases. Jahanshahi[82] found that the mass transfer of silicate ions in the slag was the rate limiting step when Fe-Si droplet was exposed to oxygen-bearing gas. Shibata et al. [119] found that refining reactions like those of silicon and manganese were controlled by the transport in slag and metal phases and not through a chemical reaction at interface. Gu et al.[85,120] observed that carbon played an important role in dephosphorization, and limited dephosphorization took place in the absence of carbon, even though the abundant supply of oxygen was available from slag.

2.7 Models of Oxygen Steelmaking

In oxygen steelmaking, the process parameters of significant interest to the operators are the endpoint carbon content and temperature of steel. However, it is very difficult to develop a process control technique based on visual observations and the operator's senses or manual sampling and other measurement techniques[3]. There are some limitations to the use of the monitoring tools as oxygen steelmaking involves nonlinear interconnected complex processes. For example, gas/liquid metal reactions depend on oxygen availability, while slag/metal reactions depend on physicochemical properties of slag and faster reaction rate induced by three-phase emulsion (gas-slag-metal droplets) and complex flow patterns at high temperatures. Control of the above processes for a given input of hot metal, scrap, flux, and the oxygen flow rate is required to produce steel with the desired chemistry and a minimum loss of iron into the slag. The defined difficulties can be addressed by developing process models, which make it possible to describe the complicated nature of the process and offer the potential to provide accurate predictive tools. The process models can be mainly classified into static models and dynamic models.

Static models comprise a set of energy and mass balance equations and determine the required amount of oxygen to be blown and flux and scrap to be added to the process for a given input and output values of the liquid metal composition[2]. The limitation of the static models is that they don't describe the intermediate process conditions or their sensitivity to variations of process parameters such as lance height, oxygen flow rate, and flux addition[121]. Therefore, steelmakers felt the need to develop a fundamental understanding of various aspects of oxygen steelmaking. This would enable in enforcing dynamic correction during the blow and optimize the process[108].

A dynamic model can explain the changes in the critical process parameters based on the events taking place in the furnace operation and lead to a better automatic control system of the process. Therefore, there has been an increasing focus on developing computer-based dynamic models. The development of dynamic models of oxygen steelmaking started in the 1970s.

Dynamic mathematical models can be classified into two categories: reaction interface models and reaction volume models[122]. In reaction interface models, an interface (gas-metal / slag-metal/ slag-gas) is defined, and the rate of reaction is assumed to be controlled by the resistance against mass transfer in the diffusion boundary layers at the interface[122]. Definition of the interfaces (along which refining reactions takes place) and the mass transfer coefficients is a critical part of this approach. It also adds to the complexity of this approach[122]. Further, the parallel rate-controlling reactions (e.g., the effect of sulfur in slowing chemical reaction and making it a rate limiting step) increases the complexity of this approach [122,123]. Contrarily, the reaction volume models consider 'passive' (bulk) and

active reaction volumes of a phase (e.g., metal bath or slag) separately[122,124]. The mass exchange between the two zones is pre-defined or determined through parameters like stirring energy[125]. The assumption of attainment of equilibrium in the active reaction volume at every time step is a significant assumption in such models. This makes possible integration of established thermodynamic softwares/tools for the evaluation of reaction equilibria in reaction volumes.[122,124]

2.7.1 Reaction interface models

In the case of the oxygen steelmaking process, the reaction interface models are more numerous than the latter. These involved single-zone mathematical models, which determine the overall refining rates of impurities in the furnace. The dynamic model developed by Asai *et al.*[126] was one of the earliest process models for oxygen steelmaking. They addressed the progress of refining reactions between oxygen and the metalloids (Fe, C, Si) at the impact zone. The impact zone was assumed to be the sole location of the reactions, and the formation of the emulsion was not considered. The rate constants (and their relative magnitudes) for these oxidation reactions were considered as input data to define their progress. Flux dissolution was calculated from an empirical equation obtained by the modification of the CaO-FeO phase diagram. A detailed heat balance model and dynamic prediction of bath temperature were presented. Later, scrap melting was introduced to the dynamic model by Muchi *et al.*[42]. Even though the model provided reasonably good predictions for the trends of refining reactions, flux dissolution, and bath temperature evolution, it did not address the refining in the emulsion zone, which was not

considered a significant contributor to refining reactions in those days. Notable attempts were made to present single-zone thermodynamic models.

Multi-component mixed transport control (MMTC)[127] theory was also employed to formulate reaction-interface models. The MMTC theory defines the mass transfer of components from both phases across a defined interface and also includes the reaction equilibria of the respective refining reactions. Deo et al.[128] presented the first example of such an application for the oxygen steelmaking process. They used identical mass transfer coefficients for C, Si, Mn, and Fe and a constant scrap melting rate. Knoop *et al*.[129] further modified this model to incorporate a slag-droplet model to describe the refining reactions in the emulsion zone. The refining reactions were assumed to occur in the emulsion zone, and the supply of oxygen and the formation of FeO were at the impact zone. The lime dissolution was described for both the presence of silicate layer (in the early part of the blow) and the absence of a silicate layer (in later part of the blow). Pahlevani *et al.*[130] attempted a multi-zone model based on MMTC theory, with an arbitrary distribution of the blown oxygen between direct decarburization (20%), the formation of FeO (70%), and post-combustion of CO (10%). Their model predictions showed a good agreement with the observed industrial values. The flux dissolution model is based on the equation presented by Matsushima *et al.*[39] The authors incorporated the dynamic properties such as slag viscosity, and density, flux particle settling velocity, radius and diffusion coefficient of CaO in slag in an actual process to calculate the mass transfer coefficient for flux dissolution in slag. Also, the solid fraction of the slag (which would increase the viscosity of the slag) was considered apart from the slag temperature for calculating the viscosity of

slag. The scrap dissolution model was absent and scrap was assumed to dissolve within 600 s of its addition. Lytvynyuk *et al.*[45,131] presented an improved version of Pahlevani's model by the addition of a scrap melting sub-model that incorporated both possible mechanisms (heat and mass transfer controlled) in scrap melting/dissolution and an improved heat balance sub-model. The model was validated against an industrial 70-t furnace. Also, the sensitivity of the process parameters to the addition of ore as coolants or FeSi as heating agents was analyzed.

The role of emulsion towards the refining reactions in the oxygen steelmaking process has been established with the progress of the industrial sampling trials and the experiments of the metal-droplet reaction. Recent models by Dogan *et al.*[18,132,133] and Sarkar *et al.*[134] studied the contribution of refining reactions in the emulsion zone on the overall process kinetics. Both the authors (Dogan and Sarkar) calculated the rate of droplet generation rate, thereby, the amount of metal in the emulsion zone using the work of He *et al.*[95] and Subagyo *et al.*[97]. Sarkar *et al.*[134] claimed that their calculations showed a lower quantity of hot-metal than expected in an actual emulsion zone, hence, their model predicted a lower rate of decarburization than that observed in the industry. Therefore they modified the predicted droplet generation rate by introducing a multiplication factor to correct the inconsistency. It is also worth noting that both these authors assumed a uniform size of metal droplets in the emulsion contrary to size distribution predicted from the work of He *et al.*[95] and Subagyo *et al.*[97].

The comprehensive model suggested by Dogan *et al.* [18,132,133,135] was the first model focused on the prediction of decarburization rate considering both the impact zone

as well as the emulsion zone. The rate of decarburization and the residence time of the droplets in the emulsion were calculated using the bloated droplet theory. However, for the decarburization, mass transport of carbon within the metal droplet was considered as the only rate-controlling mechanism, which is contrary to the experimental observations. Additionally, mathematical models for other sub-processes were either developed (flux dissolution model) or successfully adopted (scrap melting model) from literature. The flux dissolution model predicted the dissolution rate of both lime and dolomite and the sensitivity of particle size and the distribution of flux across the blow on the flux dissolution rate. A distinct advantage of the model was that the predictions of all the sub-modules of the model were validated against the industrial data of Cicutti *et al.*[27,100]. The shortcomings of the model were that it did not consider the other refining reactions hence lacked the prediction of slag evolution. Also, the heat balance model was absent, and the prediction of bath and slag temperatures was not included. Sarkar *et al.*[134] recently presented a three-zone model focusing on the refining reactions occurring in the emulsion zone. The oxygen steelmaking process is conceptualized as three Continuously Stirred Tank Reactors (CSTR's) with uniform temperature and concentration conditions within them. The three reactors represent the emulsion zone, the upper bath including the impact zone and the lower bath, respectively. A major contribution to the refining of hot-metal is attributed to the oxidation reactions in the emulsion zone while the residual oxidation occurs at the impact zone for the formation of slag (which acts as a source of oxygen to the emulsion zone). Simultaneous removal of elements has been modeled by Gibbs' free energy minimization at the slag–metal interface. The authors tried to incorporate the two distinct

control mechanisms for decarburization reactions in the emulsion zone. They are FeO transfer in slag and mass transfer of metalloid in the metal droplet. The slag evolution across the blow was predicted, but deviations from the measured values of FeO and CaO contents were observed. They believed that the disagreement in FeO was most likely due to the arbitrary distribution of the amount of the hot-metal at the impact zone, which is oxidized to produce FeO and lesser consumption of FeO in the emulsion zone at the end of the blow. The model did not consider the heat balance and the flux dissolution behavior in the process. There was a good agreement of predicted carbon content during the main part of the blow; however, the decarburization rate is predicted to be extremely low towards the end of the blow. The assumption on the reaction mechanism of the decarburization of low carbon droplets might be one of the reasons for this anomaly. The removal rates of Si and Mn are much slower than those observed in the actual process. Predictions for the first few minutes based on the emulsion model are poor, and further refinement of the model is necessary.

Rout et al.[19,88] further expanded the model framework by Dogan et al.[7,18,133] to incorporate the modified droplet generation rate and site blockage/poisoning effect of the surface activity of (SiO_2), (P_2O_5) and $[S]$ on the decarburization reaction. The formation of FeO was included based on the dynamic oxygen balance. They have incorporated the refining rates of other impurities, namely silicon, manganese, and phosphorus and have been able to predict the slag formation path during oxygen blowing process. The effect of droplet size distribution in the emulsion zone has been included. But the mechanism of the decarburization reaction is almost similar to that of Dogan et al[7,133]. Further the surface

blockage effect of (SiO_2) is likely to be over-estimated since the effect of (CaO) is not considered.

2.7.2 Reaction volume models

Jalkanen and his co-workers [125,136,137] proposed a model based on a single 'generalized reaction zone' where all the refining reactions took place. Distribution of oxygen between the competing refining reactions was determined by the magnitude of the thermodynamic reaction affinities of oxidation reactions. The supply of metal (and hence the impurities) to this reaction zone from the metal bath was determined by the stirring energy imparted by the oxygen jet and bottom stirring gas on the bath. Separate sub-modules were introduced for post-combustion of carbon monoxide, scrap melting and flux dissolution, and heat loss. Slag and bath temperatures were assumed to be equal. The model predictions indicated that the effects of fluid flow on the reaction kinetics require further investigation.

Kruskopf and Visuri[122] proposed a single zone/volume model that involved Gibbs free energy minimization approach. The refining reaction rates were determined by mass transfer between the slag and metal bath. The unified interaction parameter (UIP) model was used for liquid metal, while the modified quasichemical model (MQM) was used for the liquid slag. The amount of material and energy transported into the reaction zone is determined by indirect correlation as a function of bottom stirring. In addition, the scrap and flux dissolution and the temperature profile were predicted. The authors also expressed the possibility of adding new reaction zones to the existing model. The model under-predicted the silicon refining rate from the bath even though it is extremely favorable and equilibrium was assumed in the model. A possible reason might be the non-consideration

of the excess surface of metal droplets, which enhances the area to volume ratio, and hence the reaction rates.

Van Ende and Jung[138–140] presented another approach named 'Effective Equilibrium Reaction Zone (EERZ)' wherein the oxygen steelmaking process was divided into several reaction volumes/zones instead of a single reaction volume like the previously mentioned models[122,125]. Each reaction volume represented a reaction interface, and it is assumed that thermodynamic equilibrium is attained. The equilibrium was calculated employing "Macro processing" in FactSage[141], which enabled multiple calculations for thermodynamic equilibria without the need for frequent manual interference. The refining reactions were considered to be occurring in three zones, namely, impact zone, slag-metal bulk, and the emulsion zone. The model incorporated the kinetics of refining reactions by varying the reaction zone volumes, which in turn were claimed to be dependent on the process conditions (through empirical relations based on fluid dynamics). The reaction volume (or the amounts of reacting phase like slag/metal/gas) considered for each equilibrium calculation would affect the extent of refining reactions during each time instant. However, the exact details of the methodology to estimate the reaction volumes for various operating conditions are unavailable in open literature. Other aspects like scrap and flux dissolution were also incorporated by semi-empirical correlations in the model.

Chigwedu *et al.*[142] presented a model focused on a purely thermodynamic approach without consideration of mass transfer (of various elements) as done in either reaction interface or reaction model approaches. A hypothetical driving force for the oxidation of each element in the metal bath by oxygen was determined. The partition of the oxygen flow

to an element was equal to its fractional contribution to the total driving force. The only exception was phosphorus, as P_2O_5 formation was controlled by the rate of absorption by slag, hence only that requisite amount of oxygen was supplied to the phosphorus. An empirical equation describing the distribution of phosphorus between metal and slag was used. The model incorporated lime dissolution**,** scrap melting, and heat balance. Detailed mathematical description of various stages of scrap dissolution was discussed, and the sensitivity of the process to the selected scrap mix was studied. Ankit and Kundu[143,144] adopted 'Cellular automata' modelling to describe the decarburization of metal droplets in the emulsion zone of oxygen steelmaking. The associated elements in the emulsion zone namely C, Fe, and O, were distributed in grids. The change in the status of grids with respect to the neighbors was defined by the various models namely mass transfer, reaction, and replenishment, which involved their own unique rules. The salient features of the dynamic models discussed above are summarized in Table 2.1.

Table 2.1: Summary of dynamic models for the oxygen steelmaking process

	Decarburization	Other Refining reactions and Slag formation	Heat balance	Scrap melting	Flux dissolution	Validation
Reaction interface models						
Asai *et al.* (1970-74)	Single zone	Fe, Si, Mn, P		✓	✓	✓
Pahlevani *et al.* (2010)	Single Zone	Si, Mn, P			✓	✓
Shukla, Deo *et al.* (1987-2011)	Two Zone	Si			✓	
Dogan *et al.* (2010)	Two Zone			✓	✓	✓
Lytvynyuk *et al.* (2013)	Single zone	Si, Mn, P	✓	✓	✓	✓
Sarkar *et al.* (2015)	Two-zone	Si, Mn				✓
Rout *et al.* (2015-18)	Three-zone	Si, Mn, P		✓	✓	✓

Reaction volume models						
Jalkanen *et al.* CONSIM 5 (1998-06)	Single zone	Si, Mn, P, Ti, V	✓	✓	✓	✓
Van Ende and Jung (2014-17)	Three-zone	Si, Mn, P,	✓	✓	✓	✓
Kruskoff and Visuri (2017)	Single zone	Si	✓	✓	✓	✓
Other models						
Chigwedu *et al.* (2006)	Single zone	Si, Mn, P	✓	✓		
Ankit and Kundu (2016)	Single zone	C, P				

Review of various dynamic models reveals that varying degree of empiricism is adopted in certain aspects while a fundamental and mechanistic approach in others depends on the intended outcome. ‘Reaction volume models’ are limited by the lack of a clear correlation between operational parameters and the volume of various reaction zones. Contrary to that, various ‘Reaction interface models’ link the operational parameters with the calculation of mass-transfer coefficients. Some of the recent studies have modelled various phenomena

in multiple zones. Some fundamental kinetic and thermodynamic aspects of the phenomena have been accounted for in these models. The assumptions with regards to the sites of refining reactions (reaction zones) and other phenomena like flux and scrap dissolution were validated against industrial and experimental studies. However, definite new insights derived from the experiments have not been represented rigorously in the current models. One such example is the bloating behavior of droplets. The bloating behavior of droplets in the emulsion zone would, in turn, influence critical refining reactions like decarburization and dephosphorization. Another example is that the impact zone is assumed to be a high contributor to refining reactions under the high temperature, which is believed to be prevalent in this region. This assumption needs further verification using a more mechanistic approach to modelling. The incorporation of new sub-models is necessary to have a more reliable dynamic model and lead to process improvements.

Chapter 3

Model development for refining rates in oxygen steelmaking: Impact and slag-metal bulk zones

Chapter 3 is the pre-publication version of the article published in *Metals* 2019, vol. 9 (3), pp 309-331. https:// DOI:10.3390/met9030309. This chapter explains the details of the mathematical model developed to predict the refining reaction rates at the impact and slag-metal bulk zones and quantify the contribution of these zones to the overall refining of the metal bath during the oxygen steelmaking process under industrial conditions. This work aimed to propose a mechanistic approach to calculate the refining rates at these two zones, which would be an improvement over previous approaches that employed indirect methods (e.g., bath mixing intensity to evaluate mass transfer). This approach helped in achieving a more explicit use of process parameters in quantifying the refining rates. The important finding of this chapter is that the contribution of these two zones to the overall refining rates is insignificant. Bottom stirring is found to have a greater effect on the refining rates than the top-jets, although much higher momentum is imposed by the oxygen jets (on the bath) as compared to the bottom stirring plumes. The development of the model, its coding, data analysis against experimental and industrial data as well as manuscript drafting was carried out by the primary author. Dr. Neslihan Dogan provided extensive discussion during model development and proofread the manuscript. Drs. Gordon Irons and Anand Senguttuvan gave beneficial guidance.

Model development for refining rates in oxygen steelmaking: Impact and slag-metal bulk zones

Ameya Kadrolkar and Neslihan Dogan

McMaster Steel Research Centre, McMaster University, JHE 357, 1280 Main Street West, Hamilton, ON L8S 4L7, Canada. Contact

Abstract: A new approach has been adopted to predict the contribution of the impact and slag-metal bulk zones to the refining rates of impurities in a top blown oxygen steelmaking process. The knowledge pertaining to the behavior of top-jets and bottom stirring plumes (water model and industrial studies) was adapted. For the impact zone the surface renewal generated by the top jet as well as bottom stirring plumes is incorporated in the current model, whereas in case of the slag-metal bulk the surface renewal is caused solely by the bottom stirring plumes. This approach helped in achieving a more explicit use of process parameters in quantifying the slag formation. The results suggest a minor contribution of these two zones to the overall refining of impurities throughout the oxygen blow.

3.1 Introduction

The slag formation in oxygen steelmaking consists of oxidation reactions (Si, Mn, Fe, P) and the dissolution of flux additions such as CaO and MgO. At the start of the blow, there is rapid oxidation of Si and Mn due to thermodynamic favorability[1]. This is followed by main decarburization period, in which majority of carbon removal takes place. Deo and Boom[2] claimed that [Si] >0.05 wt % suppresses the CO formation/decarburization and the

effective estimation of desiliconization rate is essential to predict the start of main decarburization period. Phosphorus removal takes place primarily within the metal droplets in the emulsion zone. With the dissolution of fluxes the slag basicity increases and, the oxides of P and Mn are reduced to a certain extent in the emulsion zone. Therefore there is an increase in P and Mn contents in the bath in the middle of the blow and this phenomenon is termed as 'reversion'[2,3]. Although these reactions and their order of events are mostly understood through the sampling studies of the bath, the exact contribution of various reaction zones to these reactions has not been well understood.

Most oxidation reactions are extremely favorable at high temperatures and the thermodynamic aspect of these reactions is known under oxygen steelmaking conditions. The progress of these reactions are limited by the kinetics of the refining reactions within individual zones. The path of slag evolution has been reported based on plant trials[4–8] and previous modeling attempts[9–16] in literature. Early models developed by Asai and Muchi[9] and Jalkanen et al. [10] assumed that the reactions take place in a single zone. Asai and Muchi[9] suggested that slag is formed solely on the surface of the cavity, by incorporating the absorption of oxygen and simultaneous oxidation of carbon, silicon and manganese. The rate constants (and their relative magnitudes) for these oxidation reactions were considered as input data. The mean residence time of steel at the surface of the cavity was extremely small ~ 1e-5 s, which does not reflect the actual circulation of metal underneath the cavity. Jalkanen *et al.*[10,11] described refining with a generalized reaction zone. They incorporated the reaction affinities and diffusivity of the impurities, and the transport of the impurities to the reaction zone due to energy dissipation from top blown and bottom stirring

gases. An energy dissipation model developed by Nakanishi *et al.*[17] was applied. The mass transfer of impurities is correlated with top gas and bottom stirred gas flow rates by introducing two fitting parameters. Even though their approach is an effective way to describe the oxidation rate of impurities and slag formation phenomena, assessment of these two parameters is not available. These fitted parameters may vary from one vessel to another or with operational conditions. Therefore, it is difficult to further assess the significance of these parameters on the calculation of mass transfer rates.

Since the distinct role of impact and emulsion zones as reaction zones has been established[7,8,18], there are recent attempts to model refining reactions in these zones separately[12–16,19]. Sarkar et al[12] assumed that a stoichiometric equivalent quantity of hot-metal to the O_2 jet gets oxidised at the impact zone, which acts as a precursor for further refining in the emulsion zone. Their modeling predictions for [Si] and [Mn] did not correlate well with those reported by Cicutti *et al.*[4,5]. Rout *et al.*[13,14] presented a three zone model in which they applied first order rate equation to predict the refining rates of Si and Mn at the impact zone. Mass transfer of impurities in the metal phase was assumed to be the rate limiting step. The mass transfer coefficient was calculated using an empirical correlation suggested by Kitamura *et al.*[20] which incorporated induced stirring energy (by bottom stirring gas) in the bath and geometrical parameters of the furnace. As this correlation[20] was based on measuring oxidation rates of impurities in hot metal in contact with a layer of FeO containing slag for experimental and industrial ladles systems, the fluid flow dynamics of these systems are different from those applicable to the impact zone in an oxygen steelmaking furnace. At the impact zone intense turbulence is generated due to

impingement of oxygen jet and there is relatively small amount of slag in contact with the metal bath, as the slag is displaced by the O_2 jet in lateral direction. Some multi-zone models[15,16] provide a reasonable approach to predict slag formation, the details of this model are not available in open literature. Knoop et al.[15] presented a "slag-droplet model" based on multi-component mixed transport control (MMTC) theory[21]. It was assumed that FeO is formed in the impact zone, followed by FeO reduction with dissolved carbon in metal droplets. The refining reactions were assumed to occur in the emulsion zone, and oxygen was supplied through formation of FeO at the impact zone. Jung et al.[16] presented a thermodynamic model to represent various phenomena on the oxygen steelmaking like slag formation, scrap and flux dissolution. The eight phenomena were located in bulk metal bath (1.scrap dissolution and 2.metal homogenization), impact zone (3.surface and 4.hot-spot volume) and slag (5.slag-metal bulk reaction, 6.emulsion, 7.flux dissolution, 8.slag homogenization). The kinetics associated with these phenomena was incorporated by varying the volume of reaction zones as a function of the blowing conditions. At the impact zone, only the surface oxidation of metal is assumed to occur during the soft blow period, while during medium and hard blow period oxidation is assumed to occur at a depth beneath the impact zone. But the criterion for variation of reaction zone volume is unclear and the underlying empirical reactions used to determine the volume of the reaction zones were not described. Dogan et al.[19] developed a model to predict the decarburization rate at the impact and emulsion zones separately. This work was able to predict the end point carbon content of liquid metal however it does not include other important refining reactions. Further some recent findings on the bloating behavior of droplets were not included in these

models. Coley and coworkers[22–27] conducted numerous high temperature experiments using x-ray fluoroscopy technique to quantify the nucleation, growth and escape of CO gas bubbles within droplets and the interplay between decarburization and dephosphorization kinetics of bloated droplets in steelmaking slags. They studied the effect of temperature, metal chemistry and FeO content in slag. They concluded that the refining rates within droplets are extremely fast and droplet generation rate is limiting factor to extend the refining rates for oxygen steelmaking process. Developing a comprehensive model for top blown oxygen steelmaking that incorporates and critically investigates these new findings is currently the focus of a study by the authors of this paper. The central thesis of the model is that the kinetics of oxygen steelmaking is dominated by changes in the motion of iron droplets from the moment they are ejected from the surface of the metal bath to the moment they return to metal bath.

The process model focusses on the refining rates of major impurities such as carbon, silicon and manganese in different reaction zones to predict the metal and slag chemistry throughout the blow. The overarching aim of the current work is to provide better knowledge on the contribution of the refining rates at the impact zone and slag-metal bulk solely based on operational parameters using a mechanistic approach. This study is an attempt to use the theoretical findings from the experimental studies to the full-scale operating conditions by minimizing the use of empirical/fitting parameters. This would make the application of the model to different steelmaking furnaces straight-forward. The conceptual model developed by Dogan *et al.*[19,28–30] will be used in this work. This model consists of various sub-modules to describe scrap and flux dissolution, emulsion and impact

zone decarburization. In this study, two reaction zones are considered namely, reactions at the impact zone, and at the slag-bulk metal interface while the contribution of other reaction zones will be described in the subsequent work. Only few studies[4,5,31] have reported the path of slag evolution using industrial data. In the current study, the measured data of Cicutti et al.[4,5] is used to analyze the importance of refining rates for an industrial practice since the slag path was described based on the steel and slag samples taken at various times of the blow.

3.2 Model Development

The authors suggest that refining rates of impurities are controlled by the mass transfer of impurities in the metal at the gas-metal and the slag-metal interfaces. The refining rate of solutes [Si, Mn] can then be calculated using the following equation.

$$W_{[X]} = \frac{J_{[X]} M_X}{1000} = \left(\frac{k_{X-gm} A_{gm} \rho_m}{100} \{ [wt\ \%\ X]_b - [wt\ \%\ X]_{i-gm} \} \right) + \left(\frac{k_{X-sm} A_{sm} \rho_m}{100} \{ [wt\ \%\ X]_b - [wt\ \%\ X]_{i-sm} \} \right) \quad (3.1)$$

where $W_{[X]}$ is the weight of solute removed, (kg/s), X represents solutes such as Si and Mn in the liquid metal. $J_{[X]}$ is the moles of solute removed per unit time, (mol/s), M_X is the molecular weight of solute, the subscripts gm and sm represent the gas-metal and slag-metal interface, respectively, A is the contact area / interfacial area, ρ_m is the density of hot-metal, k_X is the mass transfer coefficient of solute (m/s), $[wt\ \%\ X]_b$ and $[wt\ \%X]_i$ are the solute contents in the bath and at interface, respectively. It is assumed that all silicon and manganese brought to the impact zone (gas-metal interface) are oxidized since oxidation of these elements is highly favorable at steelmaking temperatures, and

hence $[wt\ \%\ Si]_{i-gm} \approx 0$, whereas the interfacial equilibrium concentration at the slag-metal bulk is determined by the distribution coefficient between metal and slag.

$$[wt\ \%\ X]_{i-sm} = L_X(wt\ \%\ X) \tag{3.2}$$

where [] indicates the element dissolved in iron and ( ) indicates the compound dissolved in slag. L_X is the distribution coefficient of solute between metal and slag. The L_{Si} [32] and L_{Mn} [33] values are calculated through the approach adopted by Rout *et al.*[13,14,34].

3.2.1 Description of fluid flow at the impact zone and slag-metal bulk due to top-oxygen jet

Figure 3.1 schematically depicts phenomenon at the impact zone of the oxygen steelmaking furnace [3,35]. The top gas jet impinging on the metal bath surface forms a cavity and causes displacement of liquid metal and hence leading to continuous renewal of reaction area. The supersonic oxygen jet is obstructed by the metal bath and its velocity is reduced to impingement point velocity, u_j. The jet emerges in radially outward direction with a further reduced velocity called as tangential gas velocity, u_g. A major fraction of jet momentum is used to generate metal droplets from the bath while the residual jet momentum induces circular eddy flows in the bath, which bring the elements like C, Si and Mn to the surface of the cavity. The velocity of the bath underneath the cavity surface due to top-jets is termed as the surface renewal velocity, u_l.

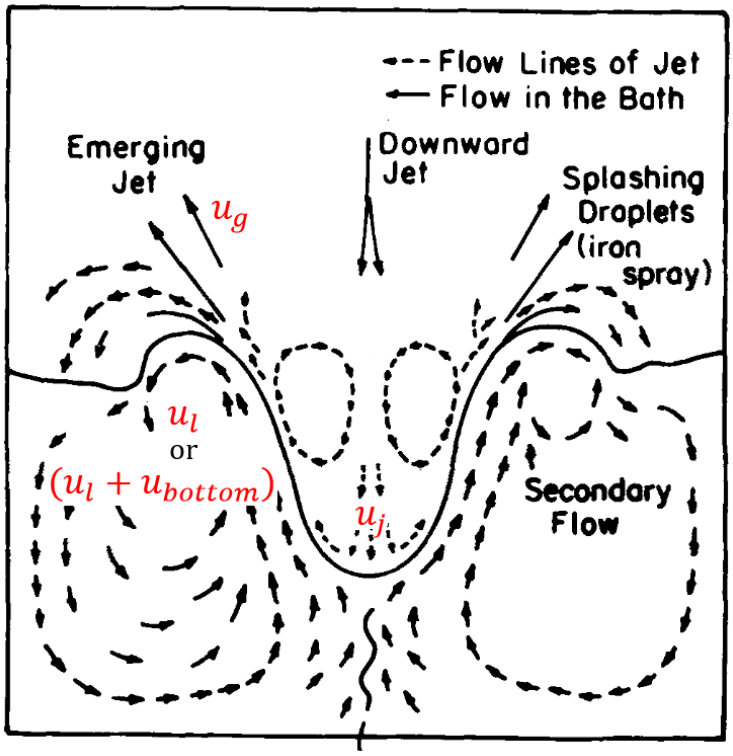

Figure 3.1: Fluid flow behavior at impact zone by gas jet impingement. [3,35] $u_j, u_g, u_l, u_{bottom}$ *are vertical velocity at the impingement point, tangential velocity of gas-jet, and surface renewal velocity of the metal bath due to oxygen jet and bottom stirring plumes, respectively.* $u_j > u_g >> u_l$ *.In current model the surface renewal velocity due to top jet bottom stirring plumes is* $(u_l + u_{bottom})$

Observation of actual fluid flow behavior in oxygen steelmaking furnace is impossible due to extreme conditions. Sharma, Hlinka and Kern[36] observed the flow behavior of metal due to interaction of an oxygen jet with a 200 lb steel bath using an X-ray adjacent to a quartz window in order to establish the direction of fluid flow at the jet-metal impingement point. It is important to note that they didn't propose any correlation to predict the velocity of liquid using this technique. Davenport et al.[37] took images to track circulation of plastic beads in water induced by the impinging gas jet. The density of plastic beads was equal to

the water. They were able to observe liquid behavior at a rapid speed in a radially outward direction close to the surface of the bath. They found that momentum gained from the gas jet was sufficient to carry this liquid metal stream down to the sides and back to the center. The evaluation of the surface velocity of liquid metal is very critical to the calculation of mass transfer coefficient. Even though previous studies[38–42] based on CFD simulations provide the values of surface velocity for a certain time step, a correlation incorporating the effects of blowing profile of oxygen steelmaking on surface velocity is necessary. Recently Hwang and Irons[43] performed water modelling studies to evaluate the velocity of surface renewal of a water bath due to the impinging gas jet. They measured the cavity dimensions using high speed imaging and local and bulk liquid velocities using Particle Image Velocimetry (PIV) technique as a function of various lance heights. They simplified stress balance and suggested the following correlation,

$$u_l = Au_g + B \tag{3.3}$$

where u_g and u_l are tangential velocities of gas and liquid (due to momentum of top-jet), respectively. A and B are constant values. Upon employment of the assumption that a linear relationship exists between the impact and tangential gas velocities i.e. $u_j = \eta . u_g$ and application of local modified Froude number similarity to the equation (3.3), the following correlation was obtained between liquid velocity and depth of cavity;

$$u_l = A'\sqrt{n_o} + B \tag{3.4}$$

where n_o is the depth of the cavity created due to impingement of the jet on the bath surface. Based upon their experimental observation they suggested that this correlation was valid for varying lance heights relevant to steelmaking conditions. The effect of cavity shape [43]:

$$\theta = tan^{-1}\left(\frac{d_c}{2n_o}\right) \quad (3.5)$$

where θ is the cavity angle (^{o}) and d_c is the cavity diameter. The contact distance (between jet and cavity) increases as the cavity angle θ increases. This correlation is given by[43],

$$u_l \times 100 \times cos\theta = \left((0.026 \pm 0.004) \times \sqrt{n_o \times 100}\right) - (0.02 \pm 0.006) \quad (3.6)$$

This correlation incorporates the cavity dimension: shape (θ) and depth n_o and explicitly correlates jet parameters with liquid metal velocity at the impact zone. In this study, the methodology by Dogan et al.[19] was adapted to calculate the diameter and depth of the cavity. Thus, the knowledge of cavity dimensions allows us to calculate the velocity of metal displaced underneath the cavity due to the impact of the oxygen jet.

3.2.2 Description of fluid flow at the impact zone and the slag-metal bulk interface due to bottom stirring

Bottom stirring by gases like Ar and N_2 is widely used to homogenize the metal bath in the oxygen steelmaking process[2]. As the stirring gas is introduced from the bottom of the vessel (through either porous plugs or tuyeres), gas-metal plumes are formed, and amount of metal reaching the surface of the metal bath increases. This increases splashing and the amount of metal in contact with the oxygen jet [44–47]. So the quantification of the amount of metal being brought to the impact zone is necessary. Krishnapishrody and Irons[48] developed a correlation between various plume parameters on a fundamental basis. They characterized the gas-metal plumes using scaled parameters to evaluate the operating variables such as metal and gas velocities in plume and metal circulation rate. Since their model results were validated against a wide variety of industrial data, this model was preferred in comparison to other models[49,50], and used in the current study to quantify

the amount of metal being brought to the impact zone. A brief description of the model is as follows:

Non-dimensional gas flow rate $Q^*$and height $z^*$are defined by the following two equations, respectively.

$$Q^* = \frac{Q}{g^{0.5}H^{2.5}} \tag{3.7}$$

$$z^* = \frac{z}{H} \tag{3.8}$$

The superscript * is used to indicate non-dimensional quantity. The functional relationship between the non-dimensional liquid velocity, u^*_{bottom} and $Q^*$and z^* is given by [48]

$$u^*_{bottom} = 1.16 \times (Q^*)^{0.32}(z^*)^{-0.28} \tag{3.9}$$

The actual liquid plume velocity, u_{bottom} can be calculated using the following non-dimensional relationship

$$u_{bottom} = u^*_{bottom}\sqrt{gH} \tag{3.10}$$

In ladles, single plumes are used to increase the mass transfer between slag and metal [51–53]. Contrary to a single gas-metal plume in a ladle, the emergence of bottom stirring plumes on a free surface is more complex. Based on locations of the bottom stirring plugs the plume may emerge to different locations on free surface. In this study, the bottom stirred plug configuration is applied based on the data reported by Bertezzolo et al.[54] for the 200-t oxygen steelmaking furnace. The top view of this interaction between 8-bottom stirring

plumes and 6-holed lance for a 200-t oxygen steelmaking furnace is shown in Figure 3.2(a) and (b). It should be noted that the intention of this figure is a schematic diagram to represent the assumption related to the plume-cavity interaction. The fluid flow profile is not computed by the authors. The interaction of the plumes with the cavities and the slag metal bulk is characterized on the basis of the following assumptions:

1. The eight plumes are represented by a sub-sector of 45 degree each. The downward circulating plumes do not affect the flow beyond their respective sub-sector.
2. Each plume has a significant momentum and by virtue of that, undergoes complete radial expansion in its subsector. This leads to surface renewal and supply of metal to the gas-metal interface (cavities) and slag-metal interface (slag-metal bulk).
3. Since only six cavities are created (by 6 holed lance), in contrast to the 8 bottom stirring plumes, the plumes are classified in two sets, namely
    a. (Plume set A) 4 Partial expanded plumes: Two plumes are responsible for bringing liquid metal in contact with cavity. This leads to surface renewal of single cavity as shown in Figure 3.2(a).
    b. (Plume set B) 4 Total expanded plumes: Each of the plume causes surface renewal of the single cavity, as shown in Figure 3.2(b)
4. The behavior of the plumes in the annular region surrounding the cavities is uniform in each sub-sector.
5. The instantaneous dimension of the cavities can be calculated as a function of the lance parameters and from that the width of the annulus is calculated. These values are used to calculate the instantaneous refining in the respective zones.

6. The metal flow resulting from the top-jet and the bottom stirring plumes is assumed to be additive, hence the surface renewal velocity is the sum of the top-jet and the bottom-stirring surface renewal velocities.

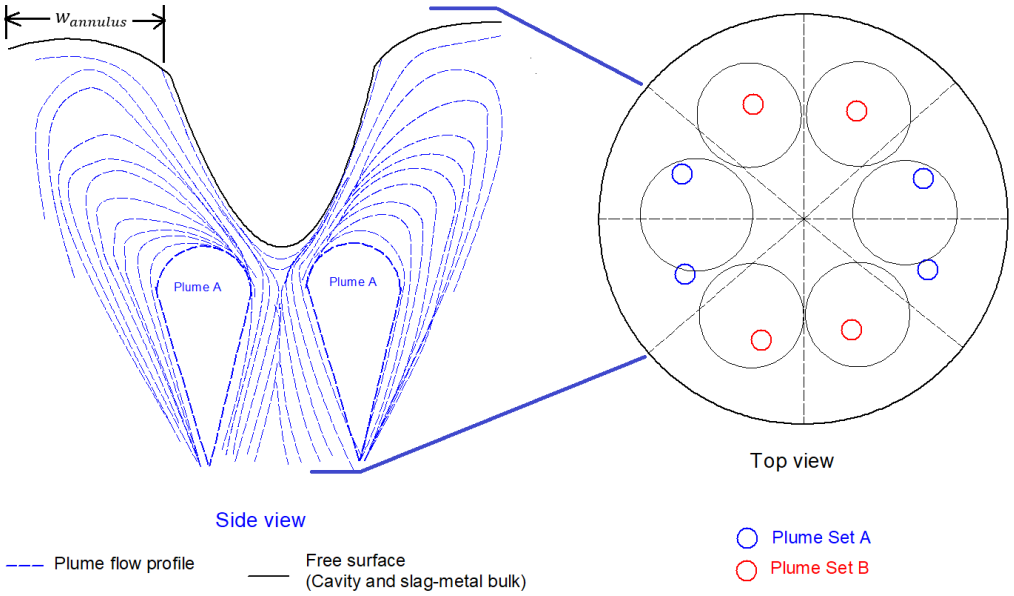

(a)

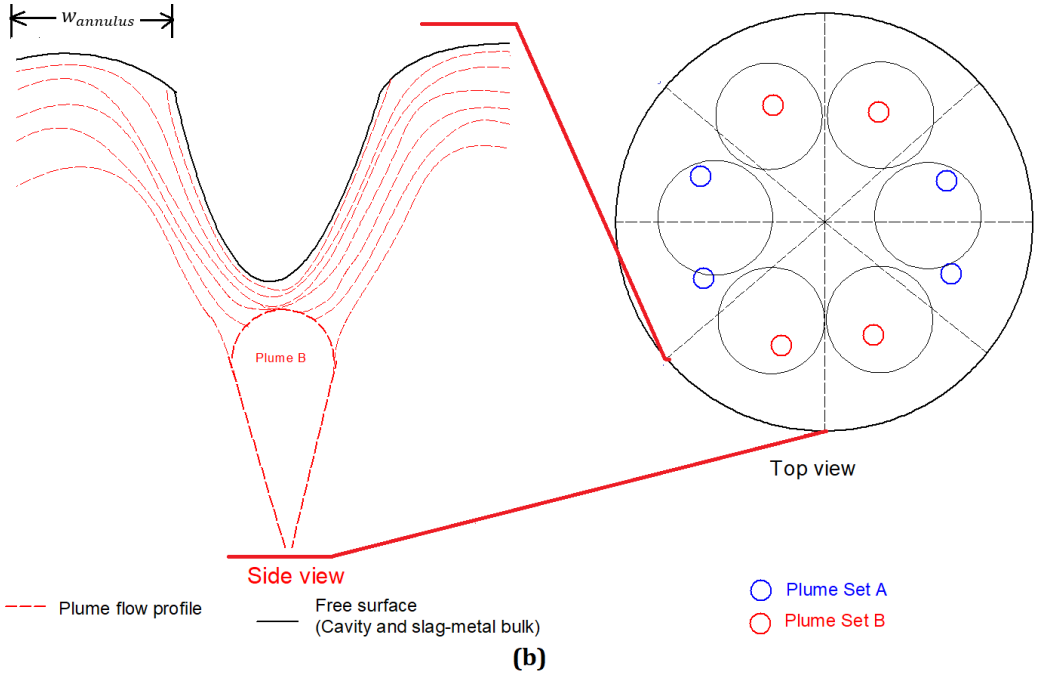

Figure 3.2: Schematic representation of interaction of cavities and plumes (a) Expansion of plume set A underneath cavities (Side view), (b) Expansion of plume set B underneath cavities (Side view). The solid lines in the figure represent the free surfaces (cavities, slag-metal bulk and vessel wall) whereas the dotted lines represent the plume flow profiles. Exact location of the porous plugs at bottom is currently unknown and is based on bottom stirring configuration of the 200-t furnace being modeled in the study of Bertezzolo et al.[53].

The instantaneous density and composition differences between upper and lower baths are quite possible, but large circulation of metal throughout the bath would reduce these gradients to significant extent. A high bath circulation rate of 126 t/min (refer Appendix: section 3.5) calculated in the current work for a 170-190 t bath indicates a high turnover of bath, thus decreasing these (density and composition) gradients and hence their effect on the metal flow behavior in a relatively short period of time. The circulation rate was mentioned in order to underline the relative homogeneity of the bath achieved by bottom stirring. The presence of scrap will reduce the circulation rate, but the bath inhomogeneity

will be reduced because of bottom stirring. The concentration and temperature gradients can be neglected under the defined stirring conditions.

3.2.3 Determination of mass transfer at the impact zone

The mass transfer coefficient, k, can be defined according to Higbie's penetration theory[55]

$$k = 2 \times \sqrt{\frac{D}{\pi t_c}} \tag{3.11}$$

where D is the diffusion coefficient of the reacting element X, t_c is the residence time of the reacting element at the impact zone/reaction interface and is defined by

$$t_c = \frac{l_c}{u} \tag{3.12}$$

where u is the velocity of surface renewal, l_c represents the '*characteristic length*' and it is the half of the circumference (i.e. arc length) of the paraboloid cavity, since the surface renewal is assumed to be symmetric about the axis of the cavity. Based on the above stated assumptions the mass transfer coefficients at the impact zone and slag-metal bulk are calculated as shown in Tables 3.1 and 3.2.

Table 3.1: Evaluation of mass transfer parameters at impact zone (gas-metal interface)

	Reaction area, m^2	Characteristic length, m	Time of contact, s	Mass transfer coefficient, m/s
Plume Set A	$\frac{1}{2} \times \left(\frac{A_{gm}}{n_{cav}}\right)$	$l_{c-gm} = \frac{1}{2} \times C_{cavity}$	$t_c = \frac{l_{c-gm}}{(u_l + u_{bottom})}$	$k_{gm} = 2 \times \sqrt{\frac{D}{\pi t_c}}$
Plume Set B	$\left(\frac{A_{gm}}{n_{cav}}\right)$			

where A_{gm}= Total area of cavities (gas-metal interfacial are), (A_{gm}/n_{cav}) represents area of a single cavity, m^2 and C_{cavity}= Circumference of the cavity. It should be noted that u_l and u_{bottom} are calculated using Equations 3.6 and 3.10.

Table 3.2: Evaluation of mass transfer parameters at slag-metal bulk (slag-metal interface)

Reaction area, m^2	Characteristic length, m	Time of contact , s	Mass Transfer coefficient, m/s
$A_{sm} = A_{vessel} - A_{gm}$	$l_{c-sm} = w_{annulus}$	$t_{c-sm} = \frac{l_{c-sm}}{(u_l + u_{bottom})}$	$k_{sm} = 2 \times \sqrt{\frac{D}{\pi t_{c-sm}}}$

where A_{sm}= Area of slag-metal bulk, m^2, $w_{annulus}$= Width of annulus between cavities and wall of vessel.

The values for diffusion coefficient of Si and Mn in the liquid iron, which are determined from experimental studies[56–58] and compiled by Kawai and Shiraishi[59], are used in the current study. They range from 4e-9 to 5e-9 m^2/s for Si (at 1550-1725 ^oC) and

1.77e-9 to 2.5e-9 m^2/s for Mn (at 1550-1700 ^oC). However another study by Grace and Derge [60] suggests that the values are ranging from 1.78e-8 to 2.11e-8 m^2/s for Si and 8.8e-9 to 1.05e-8 m^2/s for Mn in carbon saturated liquid iron. It is important to note that these values are one order magnitude higher than those obtained from Calderon et al.[56], Majdic et al.[57] and Kawai et al.[58]. Since these set of experimental values were arrived at independently, under different experimental conditions, the values were used in the calculations contrary to those suggested by Grace and Derge[60].

3.2.4 Determination of impact (reaction) area

In this study, the impact zone is defined as the smooth surface of the cavities formed by the supersonic jets from the lance, where the oxygen comes in contact with the metal bath. Previous studies[61–64] indicated that the cavity surface is rough, resulting in generation of 'splash sheets'[64] or 'metal-bath spraying effect'[61] . But the surface area enhancement due to splash sheet formation is difficult to estimate. Therefore, surface roughness is not included in the model development. In this study, the methodology by Dogan et al.[19] was adapted to calculate the impact area as follows,

The depth n_o and diameter d_c of the cavity are calculated using the correlation developed by Koria and Lange [65], for penetrability of impinging oxygen jets in molten pig-iron baths. They found that these parameters were mainly affected by the oxygen supply pressure, nozzle diameter and the lance height which contribute to the momentum of gas jet. The following equations are used to calculate the depth and diameter of the cavity.

$$n_o = 4.469 \times h \times \left(0.7854 \times 10^5 d_{th}^2 P_a \left(1.27\frac{P_o}{P_a} - 1\right)\cos\alpha \frac{1}{g\rho_m h^3}\right)^{0.66} \quad (3.13)$$

$$d_c = 2.813 \times h \times \left(0.7854 \times 10^5 d_{th}^2 P_a \left(1.27\frac{P_o}{P_a} - 1\right)(1+\sin\alpha) \frac{1}{g\rho_m h^3}\right)^{0.282} \quad (3.14)$$

where h is the lance height, d_t is the throat diameter of nozzle of lance, P_o is the supply pressure of oxygen, P_a is the ambient pressure inside the vessel, g is the acceleration due to gravity, α is the nozzle inclination angle. Then the area of single cavity, A_c is calculated using the correlation

$$A_c = \frac{\pi r_c}{6n_o^2}\left((r_c^2 + 4n_o^2)^{\frac{3}{2}} - r_c^3\right) \quad (3.15)$$

where r_c is the radius of cavity.

The total impact area of jets can be calculated by summation areas of individual cavities for multi-nozzle lance [2].

$$A_{gm} = \sum_{c=1}^{n_{cav}} A_c \quad (3.16)$$

The slag-metal bulk is defined by the interface between bath and slag at the annular region between the cavities and wall of the furnace. It is evaluated by subtracting the total area of cavities from the cross-sectional area of the vessel.

The sequence of calculation for the refining model at impact zone and slag-metal bulk is represented in Figure 3.3. For every time step, the data from hot metal and scrap composition such as manganese and silicon, metal-bath height, H, lance height, h and

bottom gas flow rate, Q_b with time are taken as inputs. The resultant cavity parameters and reaction areas (impact zone and slag-metal bulk) are then evaluated, followed by the calculation of the surface renewal velocities due to the top-jets and bottom-stirring separately as described in the previous section. The mass transfer coefficients at the two zones are calculated using equation 3.11 while the refining rate at the two zones is calculated using equation 3.1. Subsequently the composition of bath is updated by taking into account the instantaneous bath weight W_b , scrap dissolved scrap W_{sc} and the sequence of calculation is repeated for next time step.

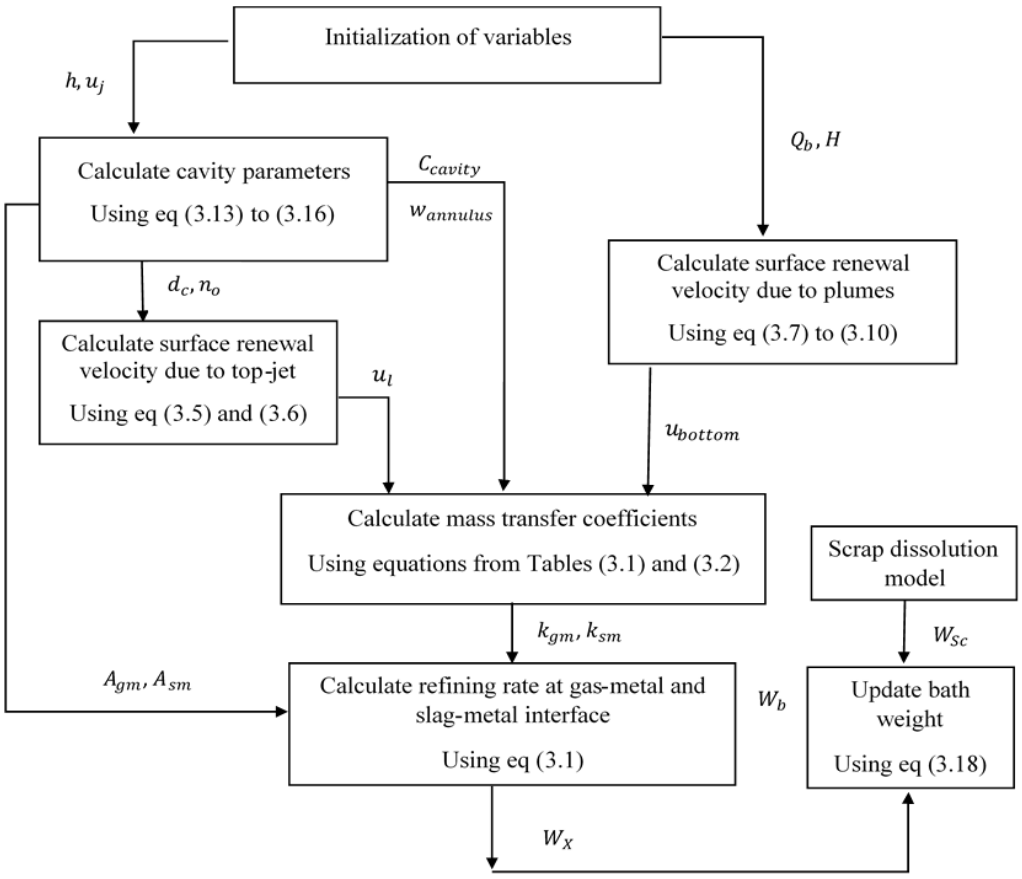

Figure 3.3: Schematic representation of calculation procedure for refining model. u_j is the velocity of the oxygen jet at the impact point, h is lance height, Q_b is bottom stirring gas flow rate, H is height of metal bath, C_{cavity} is the circumference of cavity, $w_{annulus}$ is the width of annular region between cavity and vessel walls, u_l is the velocity of surface renewal by top jet, u_{bottom} is the velocity of surface renewal by plumes, A_{gm}, A_{sm} are interfacial areas (cavities/Impact zone and slag metal bulk respectively), k_{gm}, k_{sm} are mass transfer coefficients at impact zone and slag-metal bulk., W_b is weight of bath, ,W_{sc} is the weight of melted scrap., W_X is weight of solute removed from hot-metal at a given instant.

3.3 Results and Discussion

3.3.1 Liquid velocity

The surface renewal velocities at the impact zone were calculated with respect to time, considering the instantaneous blowing parameters for the operation of Cicutti et al.[4,5]. Figure 3.4 illustrates the variation of the surface renewal velocity due to top-jet with respect

to cavity dimensions at various lance heights prevalent during the blow. The decrease in lance height decreases the surface renewal velocity whereas increases the cavity depth and radius. The decrease in lance height would increase the momentum transferred by oxygen jet to the cavity, which is expected, but this increased momentum supply is consumed in droplet generation and does not translate into an increase in surface renewal rate. This result is consistent with the literature. Hwang and Irons[43] also stated that the kinetic energy transfer (from the jet to the bath) was more efficient at higher lance heights based on their observation. The Energy Transfer Index (ETI) values for higher lance heights were higher than those for lower lance heights. The ETI is defined as a ratio between the kinetic energy of the bath and the input kinetic energy of the jet[43]. Similar observation was made in recent study by Zhou et al. [66] on kinetic energy dissipation by metal bath and slag in oxygen steelmaking vessel. For a 100-t oxygen steelmaking vessel they calculated the ETI value to decrease by 36 %, when lance height was lowered from 1.6 m to 1 m. (for O_2 flow rate of 3.76 Nm3/t.min).

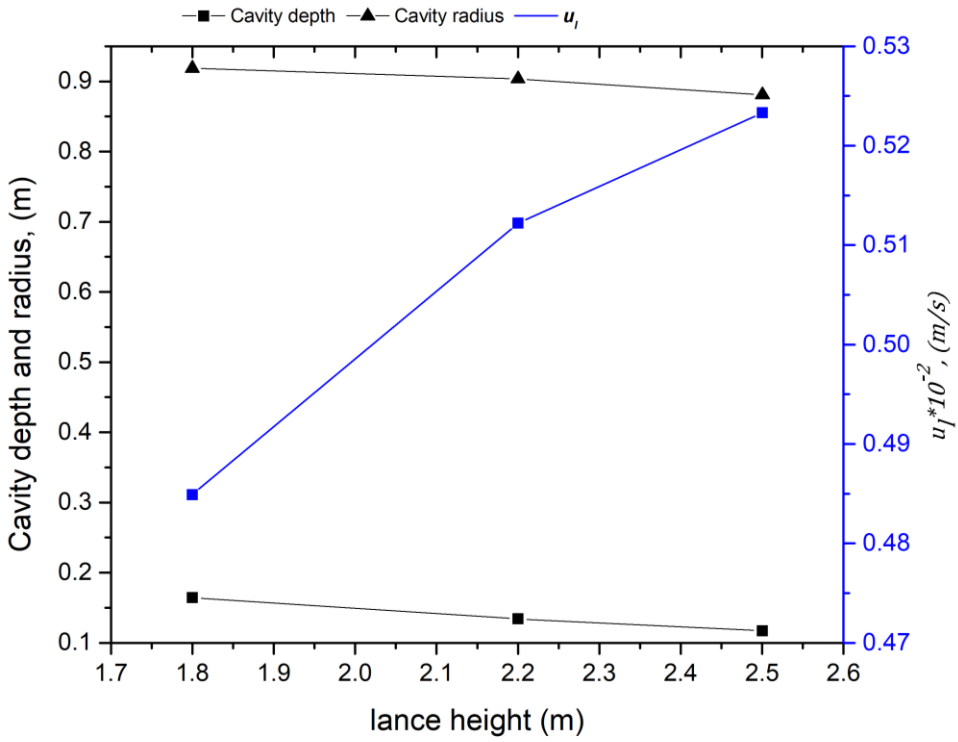

Figure 3.4: Change of cavity dimensions and surface velocity at various lance heights.

The surface renewal velocities due to top jet, u_l is compared with the surface renewal velocity due to bottom stirring, u_{bottom} in Figure 3.5. The velocity of the metal circulation due to top jet varies from 0.0048 to 0.0052 m/s and it is two orders magnitude lower than the metal velocity at the top of plume (0.45 to 0.64 m/s) Even though the characterization of metal flow is complex due to the overlap of the varying circulation patterns with respect to top-jet and plumes, this result shows that the plumes dominate the supply of metal to the cavities and the slag-metal bulk.

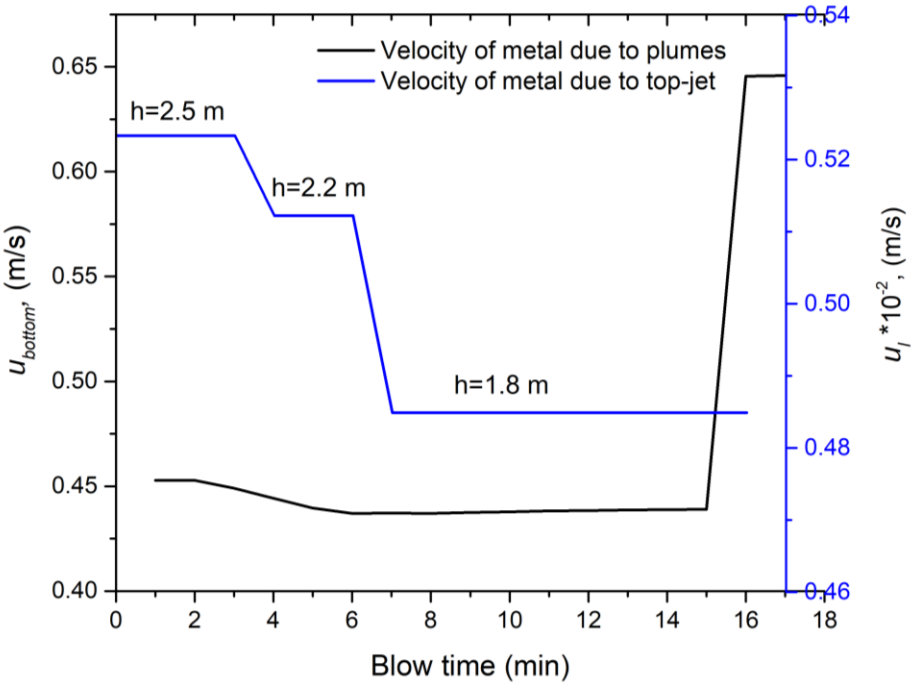

Figure 3.5: Comparison of surface renewal velocities due to top-jet and bottom stirring, (h= lance height, m)

It should be noted that this model predicts a large quantity of metal (~ 126 t/min: procedure for the calculation described in Appendix: section 3.5 is circulated by the bottom stirring plumes for a 200-t oxygen steelmaking furnace described by Cicutti et al.[4,5]. But it is worth considering exactly how much of this metal comes in contact with oxygen from the jet or the slag.

3.3.2 Mass transfer coefficients

The values of mass transfer coefficients are calculated with respect to the process parameters such as lance height and bottom stirring gas flow rate. These parameters affect the cavity dimensions, and the metal circulated coming in contact with the oxygen jet. The mass transfer coefficient at the cavities k_{cav}, related to liquid velocity due to top jet varies from 6.1e-6 to 5.8 e-6 m/s from start to end of the blow. If contribution of both top-jet and

bottom stirring plumes is considered, k_{gm} varies from 5.77e-5 to 6.70e-5 m/s. Similarly, the mass transfer coefficient at the slag-metal bulk due to top jet varies from 6.3e-6 to 6.5 e-6 m/s and for a combined contribution of top jet and bottom stirring plume it varies from 5.94e-5 to 7.45e-5 m/s. This study shows that the magnitude of the mass transfer coefficients for the top jet is considerably lower than combined effect of top blowing and bottom stirring. This finding is consistent with literature [17,53,67,68].

It should be noted that the magnitudes are lower as compared with those reported in the literature. The values of mass transfer coefficients which have been reported by Ohguchi et al. [21], k_m = 4e-4 m/s and k_s = 2e-4 m/s (metal and slag phase mass transfer coefficients respectively, for gas stirred mass transfer between the two phases).

In Figure 3.6 , the predictions of mass transfer coefficients at impact zone, k_{cav} from current study are compared with the values calculated though Kitamura et al's[20] approach for the Cicutti et al.'s steelmaking operation (wherein mass transfer coefficient varies as a function of stirring energy imparted on the bath through top-jet and bottom stirring gas). The mass transfer coefficients have been evaluated at two distinct bottom stirring flow rates namely the base case of 2.5 Nm^3/min and 5 Nm^3/min. The changes in the values reflected in both the cases represent the changes in lance heights (successively decreased during the blow from 2.5m/2.2m /1.8 m). If the bottom stirring rate is doubled, 11 % increase in mass transfer coefficient is observed whereas in Kitamura et al.'s case the increase is 23 %. The increase in bottom stirring rate would indeed increase the metal re-circulated per unit time (thus reducing the mixing time) but does not proportionately increase the metal reaching

the interface. There is a limit to the metal coming in contact with the interfaces which is discussed in section 3.3.3 .

The values predicted by Kitamura et al.'s[20] are at-least an order of magnitude higher than those predicted in the current study. In Kitamura et al.'s[20] case the decrease in lance height translates to increase in momentum transfer to the bath and corresponding increase in mass transfer coefficient is observed. In the current study the magnitude of mass transfer coefficient decreases due to decrease in lance height as discussed in the previous section. The increased supply of momentum is expended in droplet generation rather than agitation of bath. The sudden rise in mass transfer coefficients in the last 2 minutes of the blow is due to threefold increase in the bottom stirring rate (for bath homogenization).

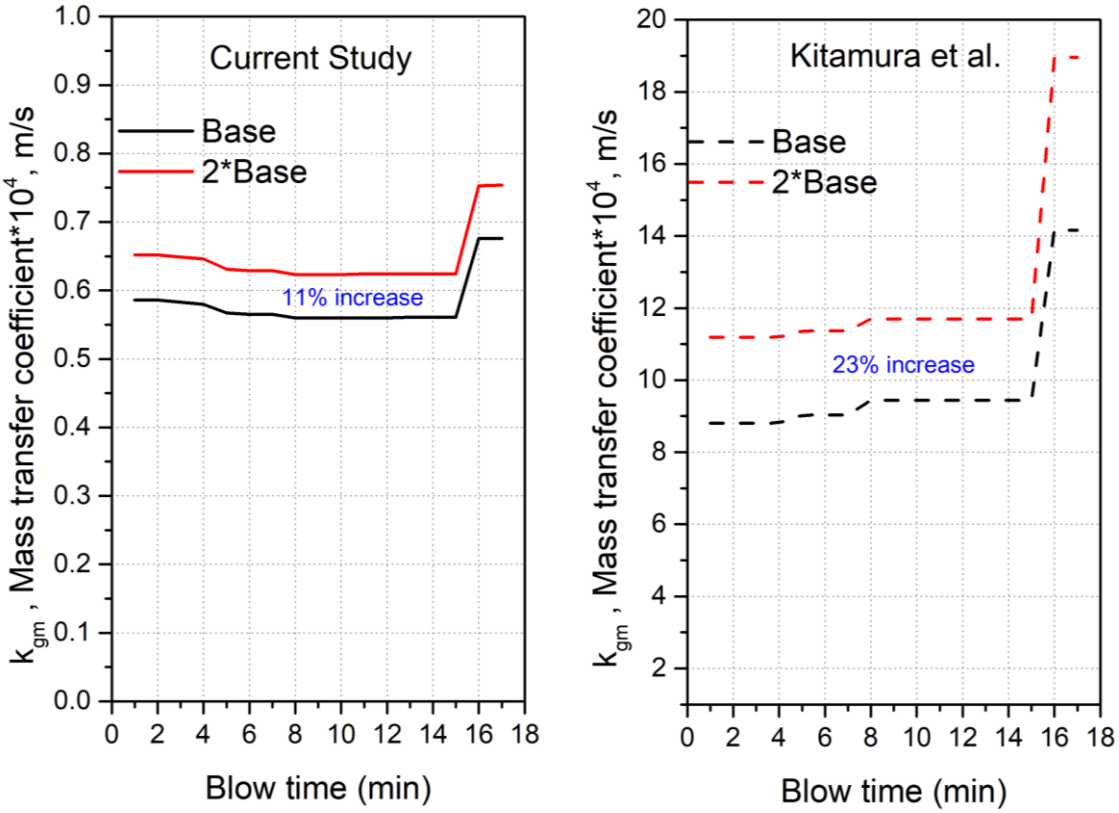

Figure 3.6: Comparison of metal phase mass transfer coefficients: (a) Current study and (b) Kitamura et al.[20]

3.3.3 Effect of lance height and bottom stirring on the metal circulation rate at the interfaces

As discussed in the previous section the metal circulating at the interfaces, MCRI, (cavities and slag-metal bulk) is calculated separately for each time step, based on the instantaneous mass transfer coefficient and areas and is given by the following equation.

$$\text{MCRI} = \{(k_{gm}A_{gm}\rho_{metal}) + (k_{sm}A_{sm}\rho_{metal})\} \quad (3.17)$$

Figure 3.7 (a) shows the variation of total metal circulating at the interfaces and the instantaneous lance height and bottom stirring rates. The metal circulation rate at interfaces (MCRI) varies between 388 to 468 kg/min. As expected the MCRI shows a similar dependence on the lance height as shown by the mass transfer coefficient. The bottom stirring rate affects this parameter significantly. The lowered lance height represents a harder blow as shown in Figure 3.7(b). This figure indicates that there is a marginal change as compared to the base case. On the other hand, doubling the bottom stirring rate increases the MCRI and it varies from 446 to 523 kg/min as shown in Figure 3.7 (c). The cross-sectional area of plume increases successively as it rises towards the top of the metal bath. But regardless of the mode of emergence of the plume on the free surface, the plume is able to circulate the metal across a larger area, where metal (and consequently the impurities like C, Si and Mn) comes in contact with oxygen from either the jet or FeO in slag.

It should be noted that the un-melted scrap most likely interacts with the plumes depending on scrap dimensions. Consequently, fluid flow at the impact and slag-metal bulk

zones may also be affected by the presence of un-melted scrap. However, to the best of authors' knowledge, there is no study available for the effects of un-melted scrap on the fluid flow behavior as well as mass transfer of solutes in the open literature. Therefore, the interaction of un-melted scrap with the rising plume is not considered in the current study.

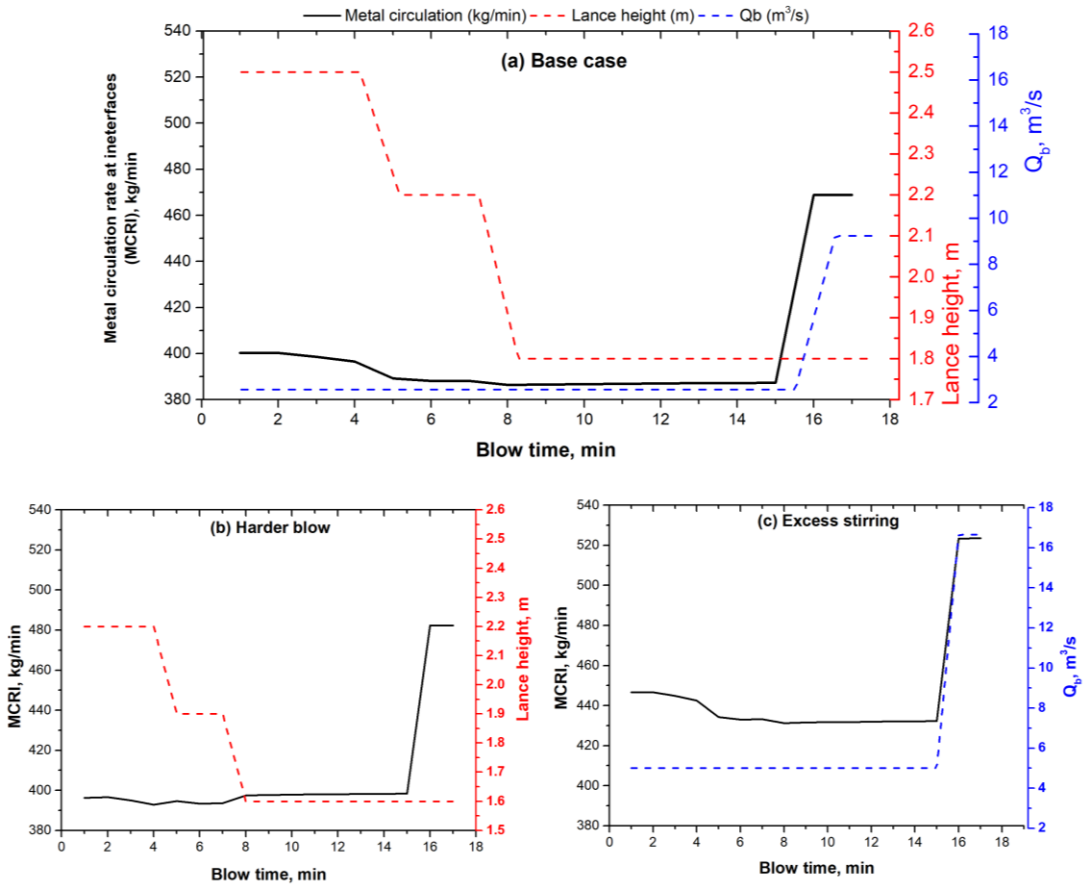

Figure 3.7: Effect of lance height and stirring rate on metal circulated at cavities and slag-metal bulk. (a) Base case (for operation of Cicutti et al., (b) Harder blow i.e consistently lower lance height (2.2 m/ 1.9 m / 1.6 m), (c) Excess stirring rate: 5 m^3/s (0-15 min), 16.66 m^3/s (16-17 min)

3.3.4 **Refining rates at the interface**

The change in bath weight during the blow was calculated by an approach previously suggested by Dogan et al.[28,29]. This involves accounting for the instantaneous amount of

scrap freezing/melting W_{sc}^{t}, droplet ejected $W_{md}^{ejection}$ and droplet returned W_{md}^{return} to the bath and metal consumed in slag formation W_{ox}, as indicated in equation 3.18

$$W_b^t = W_b^{t-\Delta t} + W_{sc}^t - W_{md}^{ejection} + W_{md}^{return} - W_{ox} \tag{3.18}$$

The change in bath and scrap masses for Cicutti et al.'s operation is shown in Figure 3.8. There is a minor decrease in metal bath weight in the first 2 minutes of the blow due to freezing of metal on the surface of cold scrap and a corresponding rise in scrap weight. Subsequently the scrap melts steadily and the bath weight increases linearly. There is a minor change in the bath weight after scrap is fully melted.

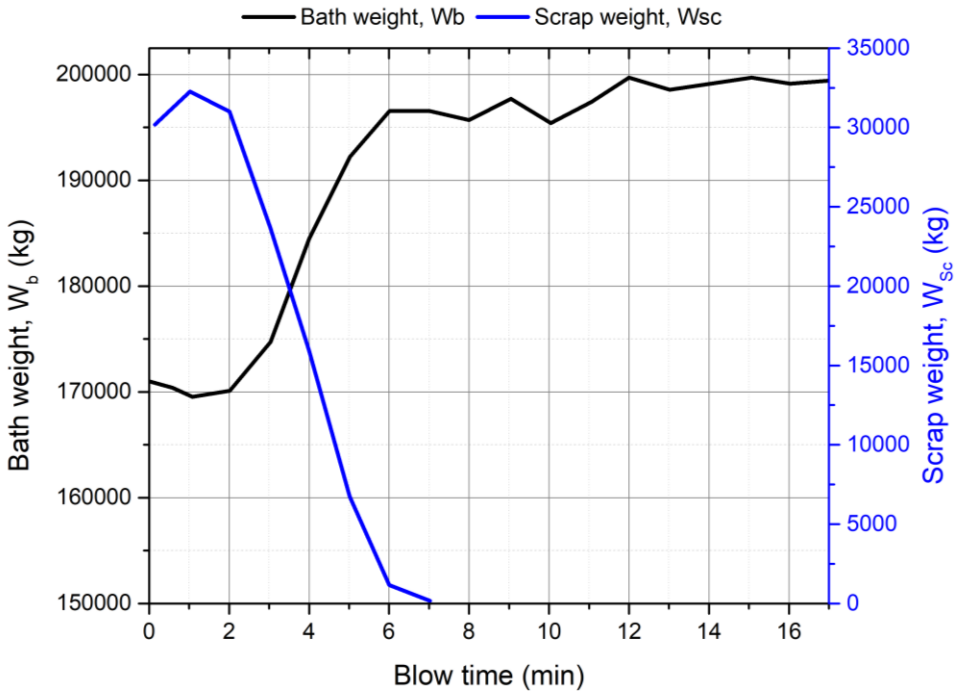

Figure 3.8: Bath and scrap weight changes for Cicutti et al.'s[4,5] operation

Figure 3.9 compares the effect of top oxygen jets and combined blow (top oxygen jets + bottom stirring plumes) on the oxidation rates of silicon and manganese in the liquid

metal at the cavities and the slag-metal bulk (as described in the combined refining model in Figure 3.3). Even though the refining model predicts oxidation throughout the blow, Si content in the metal is observed to decrease in the early part of the blow, primarily due to reduction in bath weight (due to freezing of metal on scrap). During later part of the blow, there is a negligible change due to increase in bath weight, even though oxidation continues to occur. Similar trend is observed for Mn content of liquid metal. There is hardly any oxidation of silicon and manganese taking place due to top oxygen jets. This is most likely due to the fact that surface renewal velocity is very small and hence only a marginal momentum of the oxygen jets is transferred to the bath.

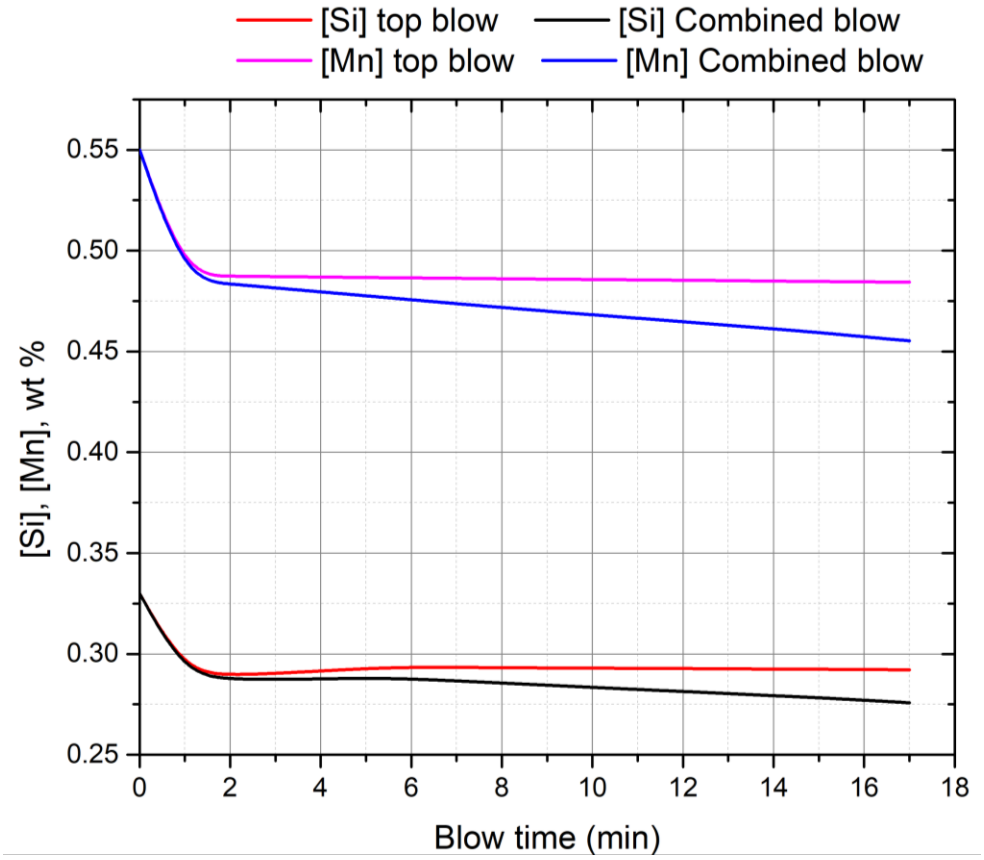

Figure 3.9: Effect of top and combined blows on the silicon and manganese oxidation rates during oxygen blow.

Figure 3.10 compares the predicted concentration of silicon and manganese in the metal to the measured values reported in the study of Cicutti et al[4,5]. The calculated values are significantly higher than measured values due to low refining rates at the impact and slag-metal bulk zones. The value of product of mass transfer coefficient and reaction area ($k * A$) should be 50-100 times higher if the impact zone and slag-metal bulk are considered as a major refining zones. This indicates that contribution of these reaction zones are insignificant. The authors are currently working on the calculation of refining rates in other possible reaction zones. It is still important to identify the possible sources of such a low prediction. It is worth considering how the selection of diffusion coefficient values from literature would affect the refining rate predictions. The lower diffusion coefficient values by Grace and Derge [54] (discussed in section 3.2.3) will affect the mass transfer coefficients to an extent, however the mass transfer rates don't increase significantly and there is no appreciable increase in the refining rates (the predicted final silicon content goes down from 0.2758 to 0.25 wt %).

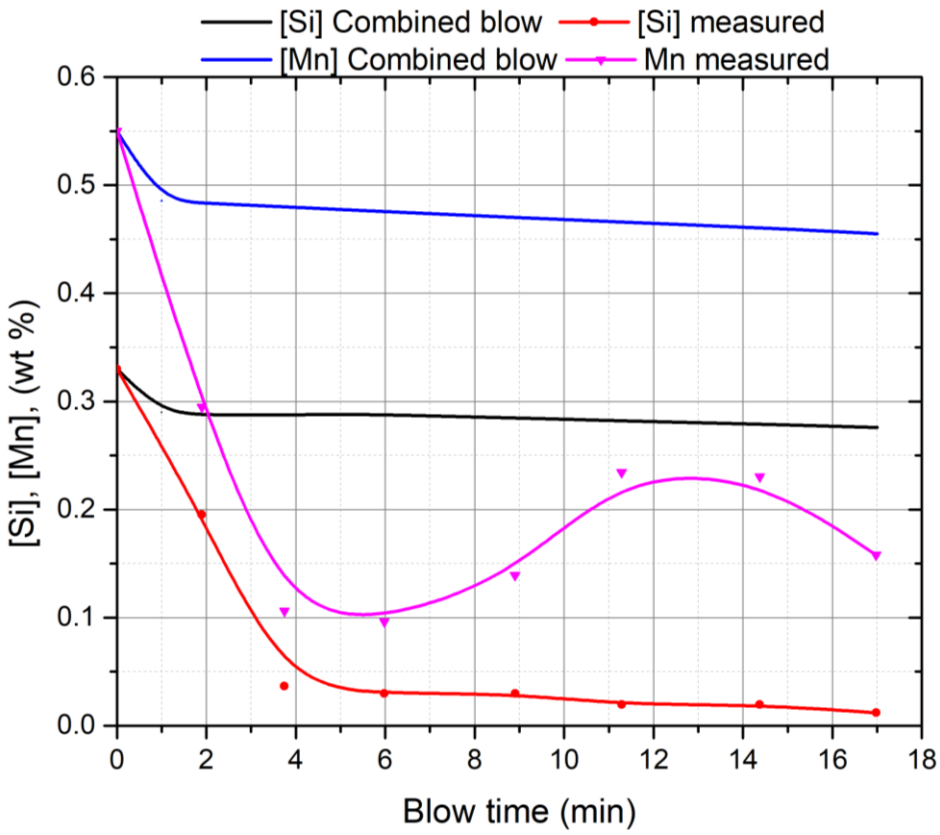

Figure 3.10: Comparison of measured and predictions for silicon and manganese in the liquid metal.

Figure 3.11 shows the variations in the area of impact zone and the slag-metal bulk zone and the individual contributions to the refining of silicon. The area of the impact zone increases as the lance height decreases. Therefore the slag-metal bulk area decreases. The refining rate of silicon is affected proportionately. The silicon refining rate falls between minutes 2 and 4 due to decrease in weight of metal bath. It can be inferred from this figure that change in lance height will vary the areas of cavities and slag-metal bulk, but this will not significantly increase the refining in the corresponding reaction zones.

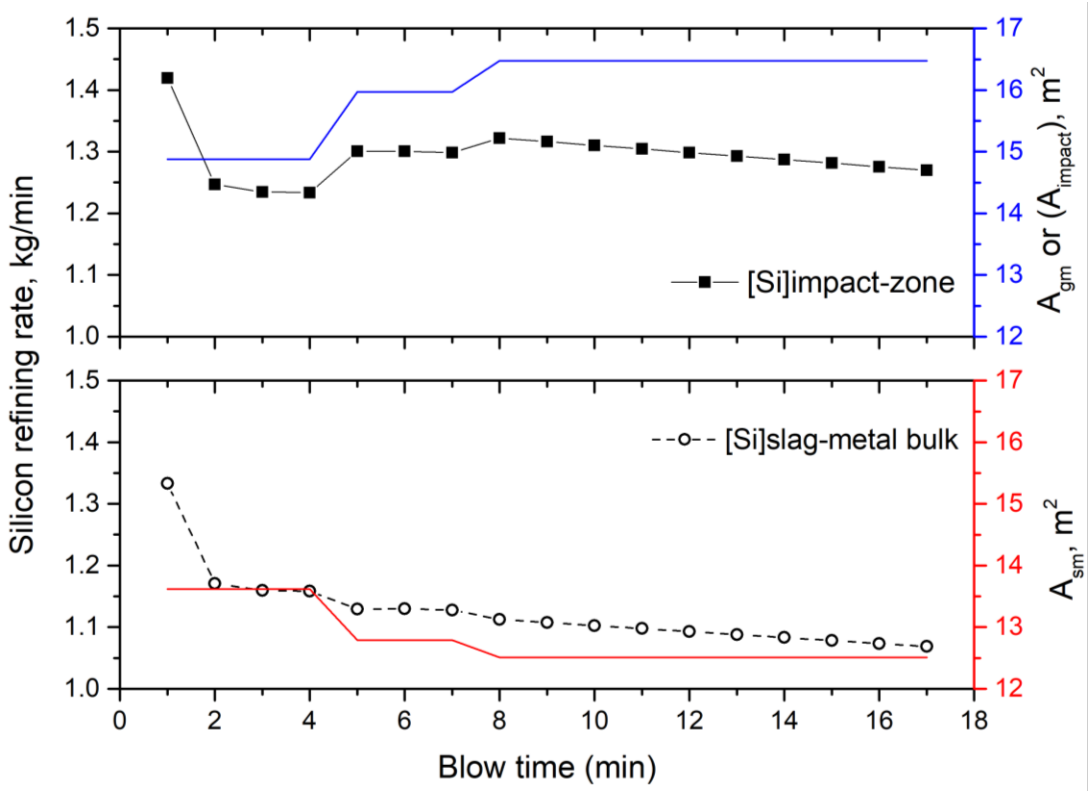

Figure 3.11: Variation of area and contribution to refining by impact and slag-metal bulk zones

Another possible reason for the low predictions might be small gas-metal reaction interface which is related to the assumption that the cavity surface is smooth (approximately 15 m^2). If the surface area of the impact zone rises by a factor of 10 (by assuming roughness due to splash sheet formation), the corresponding increase in the silicon refining rate is shown in Figure 3.12. The final silicon content goes down to 0.20 wt % if the surface roughness is considered, but it still cannot explain the rapid oxidation of silicon during the initial part of the blow. It is worth mentioning about the hot-model study by Koch et al.[61]. They conducted experiments which involved blowing of oxygen jet on a 50 kg molten Fe-C bath to simulate top-blown oxygen steelmaking process. The generated droplets due to *'metal-bath spraying'* at the cavity were sampled at various points of cross section of metal

sampler during a blow. The authors observed that at any given instant, the droplets had lower carbon content than the metal bath. Further the *'inner'* droplets (ejected into the jet) experienced much higher decarburization as compared to the *'outer'* droplets (ejected away from jet). This indicates a possibility of significant contribution of decarburization and other refining reactions via the gas-metal droplet interface rather than the smooth cavity surfaces.

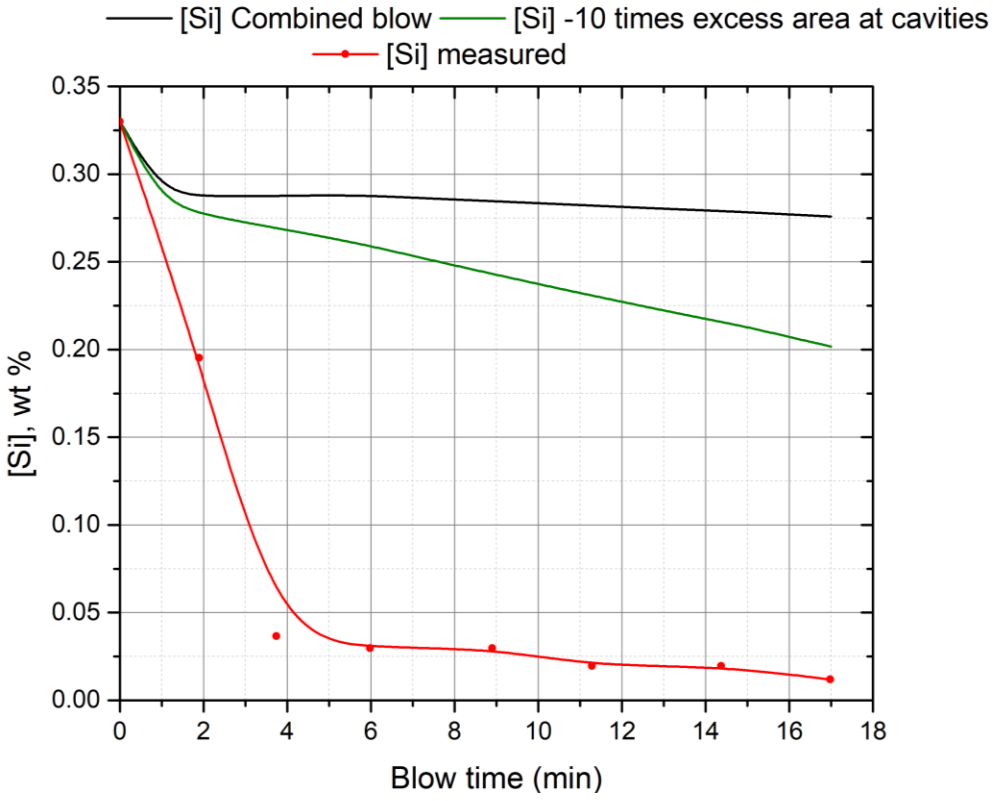

Figure 3.12: Effect of surface roughness on oxidation rate of silicon.

As discussed in the section above, the flow of bottom stirring plumes to the top causes circulation of metal, additionally there is escape of argon bubbles through the slag-metal interface as argon solubility in the metal is very low. While passage of the bubble into the slag, a thin film of metal is carried over, and the drainage of this film causes suspension of

metal droplets into slag. This phenomena of passage of argon bubbles through liquid iron-slag interface has been investigated using in-situ X-ray transmission technique[69,70] as well as mathematical modelling[71]. These studies described the effect of bubble size and interfacial tension between slag-metal on the metal suspended in slag. However typical observed[69] mass of ejection/entrainment of metal in slag phase was extremely low (0.0065 g/bubble for surface tension of 1.8 N/m and bubble diameter of 11.5 mm). This would entail an ejection of 2.55 kg metal/ min for Cicutti's et al.[4] bottom stirring rate of 2.5 Nm^3/min. This indicates a much lower contribution of refining through this mechanism.

3.4 Conclusions

A mechanistic description of the refining phenomena at the impact zone and the slag-metal bulk is presented. This includes the role of the oxygen jets and bottom stirring plumes in bringing the metal in contact with oxygen, through independent models for each.

1. Top-blown jets appear to cause negligible renewal of surface at the impact zone despite their high momentum. This leads to the conclusion that this momentum is expended in the generation of droplets.
2. The bottom stirring plumes cause a significant circulation of metal (~125 tonne/min for 2.5 m^3 stirring gas /min in 200-t furnace), but do not aid the refining reactions at the impact zone and the slag-metal bulk.
3. The contribution of the impact and slag-metal bulk appear to be negligible in the refining reactions the emulsion zone appears to be significant contributor to the refining reactions.

Funding: This research was funded by Natural Sciences and Engineering Research Council of Canada (NSERC), project number 20007117 and the McMaster Steel Research Centre (SRC).

Acknowledgments: The authors would like to thank Dr. Gordon Irons and Dr. Anand Senguttuvan for the valuable discussions regarding this work.

Conflicts of Interest: The authors declare no conflict of interest.

3.5 Appendix

The metal circulation for Cicutti et al. data is calculated as follows:

For 8 bottom stirring plug

Bottom stirring gas flow rate =150 Nm^3/h (for entire blow except last two minutes)

Bottom stirring gas flow rate, Q = 150/3600/8 = 0.005208 $Nm^3/s/plug$

Q, m^3/s	0.005208
H (height of metal bath), m	0.89

The value of the metal circulated by the plume (bottom stirred gas) is calculated by equations 3.7 through 3.10.

Q*	z*	U_l*	U_l, m/s	A_p, m2	Metal circulated by plume V_m, m^3/s	Metal circulated by single plume, kg/min
0.002225	1	0.1642	0.4854	0.0773	0.0375	$V_m\rho_m$ = 15774.98

So total metal circulated by 8 bottom stirring plumes = 15774×8 = 126199.8 kg/min

List of symbols and abbreviations

A_c	Area of single cavity , m^2
A_{gm}	Total area of cavities/impact zone, m^2
A_{sm}	Area between bulk slag and metal bath, m^2
C_{cavity}	Circumference of cavity, m
D	Diffusion coefficient of impurity in hot-metal, m^2/s
d_c	Diameter of cavity, m
d_{th}	Throat diameter of nozzle, m
H	Height of metal bath, m
h	Lance height, m
J_X	Moles of solute X transferred to interface, $\frac{moles}{s}$
k	Mass transfer coefficient, $\frac{m}{s}$
k_{X-gm}	Mass transfer coefficient of solute X at the impact zone/gas-metal interface, $\frac{m}{s}$
k_{X-sm}	Mass transfer coefficient of solute X at the slag-metal interface, $\frac{m}{s}$
L_X	Distribution coefficient of silicon between hot-metal and slag

l_{c-gm}	Characteristic length of cavity, m
l_{c-sm}	Characteristic length of slag-metal interface, m
$MCRI$	Metal circulating at the interfaces, $\frac{kg}{min}$
M_X	Molecular weight of solute X, $\frac{kg}{mole}$
n_{bse}	Number of bottom stirring elements i.e number of plumes
n_{cav}	Number of cavities
n_o	Depth of cavity, m
P_a	Ambient pressure inside vessel, $\frac{kg}{m.s^2}$
P_o	Oxygen supply pressure, $\frac{kg}{m.s^2}$
Q_b	Bottom stirring gas flow rate, $\frac{m3}{s}$
r_c	Radius of cavity, m
$t, \Delta t$	Time instant and time step, respectively
t_c	Residence time of an element at interface, m/s
u_{bottom}	surface renewal velocity due to bottom stirring, m/s
u_g	Tangential velocity of oxygen jet, m/s

u_j	Velocity of oxygen jet at impact point, m/s,
u_l	Surface renewal velocity of hot-metal due to oxygen jet, m/s
V_m	Volume of metal circulated, m^3
W_b	Weight of metal bath, kg
W_{sc}	Weight of melted scrap, kg
$W_{[X]}$	Weight of solute X (silicon and manganese) removed, kg/min
$W_{md}^{ejection}$	Weight of droplets ejected from the bath, kg
W_{md}^{return}	Weight of droplets returning to the bath, kg
W_{ox}	Weight of hot metal oxidized, kg
$w_{annulus}$	Width of annular region between cavity and vessel walls, m
X	Solute in hot-metal like Si or Mn
α	Inclination angle of the nozzle, (°)
θ	Cavity angle (cavity slope), (°)
ρ_m	Density of hot-metal , $\frac{kg}{m^3}$

3.6 References

1 T.W. Miller, J. Jimenez, A. Sharan, and D.A. Goldstein: *The Making, Shaping and Treating of Steel, 11th Edition Steelmaking and Refining Volume.*, 1998.

2 B. Deo and R. Boom: *Fundamentals of Steel Making Metallurgy*, Pretince Hall International, 1993.

3 R.D. Pehlke: *Metall. Trans. B*, 1980, vol. 11, pp. 539–62.

4 C. Cicutti, M. Valdez, T. Perez, J. Petroni, A. Gomez, R. Donayo, and L. Ferro: in *6th International Conference on Molten Slags, Fluxes and Salts*, Stockholm-Helsinki, 2000, p. 367.

5 C. Cicutti, M. Valdez, T. Pérez, R. Donayo, and J. Petroni: *Lat. Am. Appl. Res.*, 2002, vol. 32, pp. 237–40.

6 A.I. van Hoorn, J.T. van Konynenburg, and P.J. Kreyger: in *The role of slag in Basic oxygen steelmaking processes, McMaster Symposium on Iron and Steelmaking No.4*, W.-K. Lu, ed., Hamilton, Ontario, 1976, pp. 2: 1-26.

7 H.W. Meyer, W.F. Porter, G. Smith, and J. Szekely: *J. Met.*, 1968, vol. 20, pp. 35–42.

8 J. Schoop, W. Resch, and G. Mahn: *Ironmak. Steelmak.*, 1978, vol. 2, pp. 72–9.

9 S. Asai and I. Muchi: *Trans. ISIJ*, 1970, vol. 10, p. 250.

10 H. Jalkanen: *Sohn Int. Symp. Adv. Process. Met. Mater.*, 2006, vol. 2, pp. 541–54.

11 H. Jalkanen and L. Holappa: in *VII International Conference on Molten Slags Fluxes and Salts, The*, 2004, pp. 71–6.

12 R. Sarkar, P. Gupta, S. Basu, and N.B. Ballal: *Metall. Mater. Trans. B*, 2015, vol. 46, pp. 961–76.

13 B.K. Rout, G.A. Brooks, Z. Li, and A. Rhamdhani: in *AISTech 2017*, 2017, pp. 1315–26.

14 B.K. Rout, G.A. Brooks, Z. Li, and M.A. Rhamdhani: in *AISTech*, Pittsburgh, 2016, pp. 1019–26.

15 W. v. d. Knoop, B. Deo, A.B. Snoijer, G. v. Unen, and R. Boom: in *4th International Conference on Molten Slags and Fluxes*, Sendai, 1992, pp. 320–307.

16 I.H. Jung, P. Hudon, M.A. van Ende, and W.Y. Kim: in *AISTech Proceedings*, 2014, pp. 1257–68.

17 K. Nakanishi, K. Saito, T. Nozaki, Y. Kato, K. Suzuki, and T. Emi: in *65th Steelmaking Conference Proceedings*, 1982, pp. 101–8.

18 D.J. Price: in *Process Engineering of Pyrometallurgy Symposium*, The Institution of Mining and Metallurgy, London, 1974, pp. 8–15.

19 N. Dogan, G.A. Brooks, and M.A. Rhamdhani: *ISIJ Int.*, 2011, vol. 51, pp. 1102–9.

20 S. Kitamura, T. Kitamura, K. Shibata, Y. Mizukami, S. Mukawa, and J. Nakagawa: *ISIJ Int.*, 1991, vol. 31, pp. 1322–8.

21 S. Ohguchi, D.G. Robertson, B. Deo, P. Grieveson, and J.H.Jeffes: *Ironmak. Steelmak.*, 1984, vol. 11, pp. 202–13.

22 E. Chen: Ph.D thesis, McMaster University, 2011.

23 E. Chen and K.S. Coley: *Ironmak. Steelmak.*, 2010, vol. 37, pp. 541–5.

24 K.S. Coley, E. Chen, and M. Pomeroy: in *Proceedings of the Extraction and Processing Division Symposium on Pyrometallurgy in Honor of David G.C. Robertson*, P.J. Mackey, E.J. Grimsey, R.T. Jones, and G.A. Brooks, eds., 2014, pp. 289–302.

25 M.D. Pomeroy: MASc Thesis, McMaster University, 2011.

26 K. Gu, N. Dogan, and K.S. Coley: *Metall. Mater. Trans. B*, 2017, vol. 48, pp. 2343–53.

27 K. Gu, N. Dogan, and K.S. Coley: *Metall. Mater. Trans. B*, 2018, vol. 49, pp. 1119–35.

28 N. Dogan: Ph.D thesis, Swinburne University, 2011.

29 N. Dogan, G.A. Brooks, and M.A. Rhamdhani: *ISIJ Int.*, 2011, vol. 51, pp. 1086–92.

30 N. Dogan, G.A. Brooks, and M.A. Rhamdhani: *ISIJ Int.*, 2011, vol. 51, pp. 1093–101.

31 A. Masui, K. Yamada, and K. Takahashi: in *The role of slag in Basic oxygen steelmaking processes, McMaster Symposium on Iron and Steelmaking No.4*, 1976, pp. 3.1-3.28.

32 K. Narita, T. Makino, H. Matsumoto, A. Hikosaka, and J. Katsuda: *Tetsu-to-Hagane*, 1983, vol. 69, pp. 1722–33.

33 H. Suito and R. Inoue: *ISIJ Int.*, 1995, vol. 35, pp. 266–71.

34 B. Rout, G. Brooks, M.A. Rhamdhani, Z. Li, F.N. Schrama, and J. Sun: *Metall. Mater. Trans. B*, 2018, vol. 49, pp. 537–57.

35 T. Simotsuma and K. Sano: *Tetsu-to-Hagane*, 1965, vol. 51, p. 1909.

36 S.K. Sharma, J.W. Hlinka, and D.W. Kern: in *NOH-BOSC Proceedings*, 1977, pp. 187–97.

37 W.G. Davenport, D.Wakelin, and A.Bradshaw: in *Heat andMass Transfer in ProcessMetallurgy*, London, 1967, pp. 207–45.

38 H. Odenthal, U. Falkenreck, and J. Schlüter: in *European Conference on Computational Fluid Dynamics*, 2006, pp. 1–21.

39 H. Odenthal, J. Kempken, J. Schlüter, and W.H. Emling: *Iron Steel Technol.*, 2007, vol. 4, pp. 71–89.

40 H. Odenthal: in *6th International Congress on the Science and Technology of Steelmaking*, Beijing, 2015.

41 Y. Li, W.T. Lou, and M.Y. Zhu: *Ironmak. Steelmak.*, 2013, vol. 40, pp. 505–14.

42 M. Ersson, L. Höglund, A. Tilliander, L. Jonsson, and P. Jönsson: *ISIJ Int.*, 2008, vol. 48, pp. 147–53.

43 H.Y. Hwang and G.A. Irons: *Metall. Mater. Trans. B Process Metall. Mater. Process. Sci.*, 2012, vol. 43, pp. 302–15.

44 Q.L. He and N. Standish: *ISIJ Int.*, 1990, vol. 30, pp. 305–9.

45 M.J. Luomala, T.M.J. Fabritius, and J.J. Härkki: *ISIJ Int.*, 2004, vol. 44, pp. 809–16.

46 B.T. Maia, R.K. Imagawa, and R.P. Tavares: *AISTech 2016 Proc.*, 2016, vol. 55, pp. 1083–94.

47 B.T. Maia, C.N.A. Diniz, D.A. Carvalho, D.L.D. Souza, J.A. Guimarães, and S. Raissa: *AISTech 2017 Proc.*, 2017, pp. 1335–46.

48 K. Krishnapisharody and G.A. Irons: in *The Seetharaman Seminar-Materials Processing Towards Properties*, Sigtuna, Sweden, 2010, p. 317.

49 M. Sano and K. Mori: *Trans. Iron Steel Inst. Japan*, 1983, vol. 23, pp. 169–75.

50 G.G. Krishna Murthy, A. Ghosh, and S.P. Mehrotra: *Metall. Trans. B*, 1988, vol. 19, pp. 885–92.

51 J. Szekely, T. Lehner, and C. Chang: *Ironmak. Steelmak.*, 1979, vol. 6, p. 285.

52 C. Hsiao, T. Lehner, and Kjellberg: *Scand. J. Metall.*, 1980, vol. 9, pp. 105–10.

53 K. Nakanishi, T. Fujii, and J. Szekely: *Ironmak. Steelmak.*, 1975, vol. 2, p. 193.

54 U. Bertezzolo, R. Donayo, A. Gomez, G. Denier, and H. Stomp: in *2nd European Oxygen Steelmaking Congress; EOSC*, Taranta, 1997.

55 R. Higbie: *Trans. Am. Inst. Chem. Eng.*, 1935, vol. 35, pp. 36–60.

56 F. Calderon, N. Sano, and Matsushita: *Metall. Trans. B*, 1971, vol. 2, p. 3325.

57 A. Majdic, D. Graf, and J. Schenk: *Arch. für das Eisenhüttenwes.*, 1969, vol. 40, p. 627.

58 T. Saito, Y. Kawai, and K. Maruya: *Tohuku Daigaku Senk.*, 1960, vol. 16, p. 15.

59 Y. Kawai and Y. Shiraishi: *Handbook of Physico-Chemical Properties at High Temperatures*, 1988.

60 R. Grace and G. Derge: in *Transactions of the Metallurgical Society of AIME*, 1958, p. 331.

61 K. Koch, J. Falkus, and B. Ralf: *Steel Res. Int.*, 1993, vol. 64, pp. 15–21.

62 M. Lee, V. Whitney, and N. Molloy: *Scand. Jounal Metall.*, 2001, vol. 30, pp. 330–6.

63 M.S. Lee, L. O'Rourke, and N.A. Molloy: *Scand. J. Metall.*, 2003, vol. 32, pp. 281–8.

64 S. Sabah and G.A. Brooks: *Metall. Mater. Trans. B*, 2014, vol. 46, pp. 863–72.

65 S. Koria and K.W. Lange: *Steel Res.*, 1987, vol. 58, pp. 421–6.

66 X. Zhou, M. Ersson, L. Zhong, and P. Jönsson: *Metall. Mater. Trans. B Process Metall. Mater. Process. Sci.*, 2016, vol. 47, pp. 434–45.

67 S. Koria: *Can. Metall. Q.*, 1992, vol. 31, pp. 105–12.

68 S. Koria and S. Pal: *Steel Res.*, 1991, vol. 2, pp. 47–53.

69 Z. Han and L. Holappa: *Metall. Mater. Trans. B*, 2003, vol. 34, pp. 525–32.

70 Z. Han and L. Holappa: *ISIJ Int.*, 2003, vol. 43, pp. 292–7.

71 S. Kobayashi: *ISIJ Int.*, 1993, vol. 33, pp. 577–82.

Chapter 4

The decarburization kinetics of metal droplets in emulsion zone

Chapter 4 is a pre-publication version of the article published in *Metallurgical and Materials Transactions B.* vol. 50, (6), pp 2912-2929. DOI: 10.1007/s11663-019-01710-0. The following chapter presents a model to evaluate the decarburization behavior of the droplets in the emulsion zone of an oxygen steelmaking process. Recent experimental studies have established that CO generation inside the droplets dominates the decarburization of metal droplets in the emulsion zone. The CO generation leads to bloating and suspension of droplets in the emulsion zone, which is critical to other refining reactions. The previous models available in open literature do not incorporate new experimental insights and other aspects of the droplet-slag interaction in the emulsion zone. The current model has successfully integrated these features (like slag diffusion, internal and external CO generation, and bloating behavior) and validated them with the experimental data available in the literature. The model accomplishes a scientifically rigorous description of the bloating behavior of the metal droplets in the emulsion zone. The development of the model, its coding, data analysis against experimental and industrial data as well as manuscript drafting was carried out by the primary author. Dr. Neslihan Dogan provided extensive discussion during model development and proofread the manuscript. Dr. Coley, Kezhuan Gu, and Tai Xi Zhu provided useful insights during the model development.

The decarburization kinetics of metal droplets in emulsion zone

Ameya Kadrolkar and Neslihan Dogan

McMaster Steel Research Centre, McMaster University, JHE 357, 1280 Main Street West, Hamilton, ON L8S 4L7, Canada. Contact

Abstract

A mathematical model has been developed to predict the decarburization rate within individual droplets in the emulsion zone. All the chronological events pertaining to the life cycle of a metal droplet in the emulsion zone like oxygen supply (from slag), external and internal decarburization have been modelled dynamically and validated against experimental data available in open literature. The bloating behavior of metal droplets in the emulsion was represented theoretically by incorporating an escape function dependent on internal CO gas generation. The model is able to predict the onset of bloating and the residence time of metal droplets in the emulsion zone. The residence time of droplet containing 2.6 wt % C and 0.007 wt % S is in the range of 10-13 seconds. The contribution of decarburization rate in the emulsion zone to the overall decarburization rate is studied using the industrial data reported by Cicutti et al. The model predicts 5 to 75 % of total decarburization takes place in the emulsion zone. It is found that the extent of decarburization of a metal droplet depends on its initial carbon content rather than its oxygen content for slag containing FeO greater than 10 wt %.

4.1 Introduction

In oxygen steelmaking, large number of metal droplets are generated and ejected into the slag due to the high-speed oxygen jet impingement on the metal bath [1,2]. This leads to the formation of a large interfacial area between the metal droplets and the slag and enhances the kinetics of the refining reactions during oxygen blow. Few studies[1–6] investigated the contribution of refining reactions in the emulsion zone by sampling metal droplets from pilot plant trials. Meyer et al.[1] quantified the number of droplets generated in the emulsion zone and predicted the residence time of these droplets in order to investigate the refining rates in the emulsion zone. It was found that instantaneous carbon content of droplets in the emulsion were lower than that of bath[1] thus establishing the emulsion zone as a significant contributor to the decarburization reaction. Similar findings were reported by other researchers [3,6]. These industrial findings motivated several researchers[7–14] to study the behavior of a single metal droplet in a slag for a more fundamental understanding of reaction kinetics between metal and slag. Mulholland et al.[7] pioneered the use of X-ray fluoroscopy to study the effect of metal droplet size, metal and slag compositions and temperature on the decarburization behavior of droplets. The study provided valuable qualitative insight about formation of gas halo surrounding the metal droplet. Gaye and Riboud[9] firstly measured the reaction rate through measurement of flow rate of gas formed inside the chamber and came to be known as Constant Volume Pressure Increase (CVPI). The combination of X-ray fluroscopy and CVPI technique aided the in situ observation and quantitative measurement of decarburization reaction[10–12,14–16]. This combination was firstly employed by Min and Fruehan[10] for studying the decarburization rate of a metal

droplet reacting with slags containing less than 10 wt % FeO and suggested a 'mixed control model' for emulsion zone decarburization. Later, using similar set-up, Molloseau and Fruehan[11] observed that the decarburization rate of droplets ([C]= 2.9 wt %) in contact with slags with (FeO)> 10 wt % 'emulsified'. The CO evolution from the metal droplets (with similar carbon content) was found to be dependent on the FeO content in slag. Similar technique was used for Coley and his co-workers[12,14,17] to further study the decarburization kinetics under various conditions relevant to steelmaking operations. Chen and Coley[12] focussed on the effect of droplet size, FeO content in the slag and temperature on internal CO gas generation rates and bloating behavior. They proposed a model to predict the rate of internal CO gas generation. Homogeneous nucleation of CO gas bubbles within the metal droplet in ferruginous slag has been found to be responsible for bloating of droplets (leading to reduction of its density) and extending its residence time in the slag-gas-metal emulsion. Pomeroy and Coley[14] conducted further experimental study to identify the time for onset of bloating of the droplet due to internal CO gas generation. Recent study by Gu et al.[15] focussed on the dephosphorization kinetics using similar experimental set-up. They suggested that the internal stirring induced by the CO bubbles accelerates the refining of phosphorus and is expected to have similar effect on refining of silicon and manganese.

There are few proposed mathematical models[18–24] which incorporate the insights from experimental studies to predict the refining kinetics within metal droplets and its importance to the overall process kinetics. In the model proposed by Sun and Zhang[18], the effect of Si and Mn on the decarburization kinetics was included. However, the nucleation of CO bubbles is assumed to occur on the surface of a metal droplet and while the CO

nucleation within the metal droplet is not considered. Brooks et al.[24] developed a mathematical model to predict the trajectory of a metal droplet using ballistic motion. The rate determining mechanism of decarburization reaction was assumed to be mass transport carbon in a metal droplet. This model was applied by Dogan et al.[19,20] for quantifying the decarburization in the emulsion zone. This model was further expanded by Rout et al.[22,23] to incorporate the modified droplet generation rate and site blockage/poisoning effect of the surface activity of (SiO_2) , (P_2O_5) and $[S]$ on the decarburization reaction. They have incorporated the refining rates of other impurities and able to predict the slag formation path during oxygen blowing process. But the mechanism of the decarburization reaction is almost similar to that of Dogan et al[19,20]. Further the surface blockage effect of (SiO_2) is likely to be over-estimated since the effect of (CaO) is not considered. Sarkar et al.[21] quantified the refining rates within the emulsion zone by distributing the oxygen amongst decarburization and other refining reactions based on the free energy minimization technique. However, this methodology does not consider the CO generation inside the metal droplets. Additionally, the residence time of metal droplet is assumed to equal total time elapsed when the maximum possible decarburization of droplet takes place. This condition is not necessarily true as the decarburization might be interrupted by insufficient residence time of droplet in the emulsion.

Although these models have incorporated some insights from experimental data, a recent finding on bloating of droplet due to internal CO generation has not been successfully applied to describe the decarburization kinetics in the emulsion zone. The current work aims to provide better knowledge on the decarburization rate within the droplets under full

scale operating conditions at high temperatures. This model is based on a more mechanistic description of the droplet-slag behavior by incorporating the internal and external CO gas generation rate as well as its escape rate within metal droplets. The model was validated against available experimental studies and industrial data. In the present study, the effects of temperature and oxygen content of metal droplet on the decarburization rate in the emulsion zone are studied.

4.2 Model Development

The theoretical treatment suggested by Dogan et al.[20] is applied in this study to predict total decarburization rate in the emulsion zone. This rate can be calculated by the summation of decarburization rates of individual metal droplets for a given time using the following equation.

$$\frac{dW_C}{dt} = \frac{\sum_{i=1}^{n} \frac{m_d}{100} \left(C_i^{t+\Delta t_e} - C_i^{t}\right)}{\Delta t_e} \tag{4.1}$$

where C_i^t and $C_i^{t+\Delta t_e}$ are the carbon contents of a single metal droplet entering and leaving the emulsion zone (wt %), respectively. m_d is the mass of a single droplet (kg) and n is the total number of droplets generated at a defined time interval Δt_e. Time interval is chosen to be 1 second. In the model, the droplet generation rate is calculated using blowing number proposed by Subagyo et al.[25]. It should be noted that the calculation approach for residence time of droplets has been changed. The residence time of droplets is strongly dependent upon the apparent density of droplets in comparison to the density of slag-metal-gas emulsion. The dynamic changes in the droplets can be calculated when net CO gas within a single droplet is known. The modelling of aspects pertaining to the calculation of net CO

gas within the metal droplet, namely supply of oxygen (from slag), internal and external CO gas generation and escape of CO gas from the droplet are described below.

4.2.1 Oxygen supply

The supply of oxygen for the refining reactions in emulsion zone comes from FeO in the slag and described by the following reaction at the metal droplet surface,

$$(FeO) = [Fe] + [O] \tag{4.2}$$

The FeO flux, J_{FeO} (mol/s) through the slag due to the above reaction can be written as per the mass transfer model suggested by Min and Fruehan[10],

$$J_{FeO} = \frac{A_d k_s \rho_s}{100 M_{FeO}} (FeO - FeO^r) \tag{4.3}$$

where J_{FeO} is the oxygen atoms at the metal surface, moles/s, A_d is the area of a droplet, m^2, k_s is the slag phase mass transfer coefficient, $\frac{m}{s}$, and M is the molecular weight of individual component, $\frac{g}{mol}$, FeO and FeO^r are the concentrations of FeO in slag bulk and droplet-slag interface, respectively, in wt %.

This mass transfer model does not account for the non-equilibrium caused by the surface activity of sulfur. In order to include this effect, Min and Fruehan's model[10] is modified by considering non-equilibrium FeO dissociation reaction at the surface due to sulfur concentration, and the equation can be represented by difference between the forward $\vec{k}$ and backward $\overleftarrow{k}$ reaction for the FeO dissociation reaction (equation 4.2). This approach is originally suggested by Pomeroy[14] and applied in the current study.

$$J_{FeO} = A_d(1 - \theta_S)[\vec{k} a^r_{FeO} - \overleftarrow{k} h^r_O] \tag{4.4}$$

where a_{FeO}^{r} and h_{O}^{r} are the activities of FeO and O at the interface, respectively. θ_S is the fraction of surface area unavailable for reaction due to poisoning by sulfur and is calculated using the correlation suggested by Belton[26].

$$\theta_S = \frac{K_s h_s}{1 + K_s h_s} \tag{4.5}$$

where K_s is the adsorption coefficient of sulfur, and its evaluation is explained further in subsequent section.

The forward and backward reaction constants can be related to the equilibrium constant by the following relation,

$$K_{FeO} = \vec{k}/\overleftarrow{k} \tag{4.6}$$

where K_{FeO} is the equilibrium constant for FeO dissociation reaction (equation 4.2) and is given by the following equation[27]

$$K_{FeO} = 10\text{^}\left(\left(\frac{6150}{Td}\right) - 2.604\right) \tag{4.7}$$

The equations 4.4 and 4.6 can be combined to arrive at the following equation

$$J_{FeO} = \vec{k} A_d (1 - \theta_S)\left(a_{FeO}^{r} - \frac{h_O^r}{K_{FeO}}\right) \tag{4.8}$$

The equations 4.3 and 4.8 are combined to arrive at the following equation

$$\vec{k} A_d (1 - \theta_S)[a_{FeO}^{r} - \frac{h_O^r}{K_{FeO}}] = \frac{A_d k_s \rho_s}{100 M_{FeO}} (FeO - FeO^r) \tag{4.9}$$

The values of the three interfacial values in equation 4.9 (a_{FeO}^{r}, h_O^r and FeO^r) are obtained by the solving equation 4.9 and other non-linear equations 4.18 and 4.21 from subsequent section and Appendix : section 4.8 (4.A1 to 4.A6 and 4.A9). With the knowledge of value of FeO^r the net supply of oxygen can be calculated from equation 4.3 at each time step.

4.2.2 Decarburization reaction

The supplied oxygen reacts with carbon within the metal droplet and forms carbon monoxide (CO) gas,

$$[C] + [O] = CO \tag{4.10}$$

This reaction could either happen at the surface of the metal droplet (heterogeneous nucleation) or within the droplet (homogeneous nucleation/internal decarburization). The equilibrium constant, K_{CO} for this reaction is given by the following equation[28],

$$\log K_{CO} = \frac{1160}{T} + 2 \tag{4.11}$$

where,

$$K_{CO} = \frac{P_{CO}}{h_C h_O} \tag{4.12}$$

where P_{CO} is the supersaturation pressure of the CO bubble nucleated, h_C and h_O are the Henrian activities of carbon and oxygen in the metal droplet, respectively and calculated using the following equations[28].

$$h_C = f_c[C] \tag{4.13}$$

$$h_O = f_O[O] \tag{4.14}$$

The activity of elements is calculated from the activity coefficients by using the following equations.

$$log\ f_C = e_C^C[C] + e_C^O[O] + e_C^S[S] \quad (4.15)$$

$$log\ f_O = e_O^C[C] + e_O^O[O] + e_O^S[S] \quad (4.16)$$

where $e_O^C,\ e_O^O\ and\ e_O^S$ are the first order interaction parameters, and obtained from the literature[29]. [ ] represents the concentration of the element dissolved in the bulk metal droplet (wt %). The activities of elements are calculated as a function of instantaneous composition of metal droplet. This step is critical because change in the amount of a given metal component causes considerable change in the activities of other components. For instance, the activity of sulfur decreases as the carbon content of the droplet decreases because carbon has a positive interaction parameter with respect to sulfur. The activity of sulfur will further affect its surface tension and rate of the reactions at droplet-slag interface.

4.2.3 External decarburization

External decarburization was studied by few researchers[10,18]. In their high temperature experiments, they used low FeO containing slags in order to ensure that external decarburization occurred predominantly. Min and Fruehan[10] examined the effect of FeO content in the slag and sulfur content in metal droplet on the decarburization reaction and proposed a 'mixed control model'. They considered that mass transfer in the slag, mass transfer in the gas halo and chemical reaction at metal droplet-slag interface either partially or entirely controlled the decarburization reaction depending on the sulfur content of metal droplet. Similarly, Sun and Zhang[18] conducted experiments to predict the behavior of

single droplet in a slag containing 10 wt % FeO at 1773 K and further modelled the droplet-slag reactions by solving a set of non-linear equations pertaining to molar fluxes of components in metal and slag, interfacial activities of metal and slag components and interfacial reaction equilibria. This model incorporates possible control mechanisms except the poisoning effect of sulfur. In current study the external decarburization is calculated using the approach adapted from the work of Sun and Zhang[18] but the poisoning effect of sulfur on the metal-slag interfacial is also incorporated (based upon approach suggested by Pomeroy[14]). Accordingly the rate of external decarburization, J_{ext} can be stated as

$$J_{ext} = \frac{(1-\theta_S)k_{ext}A_d}{100M_C}\left(h_C^r h_O^r - \frac{P_{CO}^{ext}}{K_{CO}}\right) \tag{4.17}$$

where k_{ext} is the rate constant of decarburization reaction and equals 0.0136, $\left(\frac{kg}{m^2.s}\right)$. This value is taken from literature[14,30]. h_C^r and h_O^r are the activities of carbon and oxygen at the droplet-slag interface, respectively. P_{CO}^{ext} is the supersaturation pressure of the CO bubble nucleating on the surface of the droplet and was assumed to be equal to the pressure inside the furnace (1.5 atm).

The flux of carbon towards the slag-metal interface (J_C) (mol/s) is equal to the consumption of carbon by external decarburization

$$J_C = J_{ext} \tag{4.18}$$

where J_C is defined by Fick's first law as given in the following equation[18] :

$$J_C = \frac{A_d k_m \rho_m}{100M_C}([C] - [C]^r) \tag{4.19}$$

where k_m is the metal phase mass transfer coefficient of the elements (m/s). Its value is taken from the study of Shibata et al. [30] and equal to 1.5×10^{-4} m/s. ρ_m is the density of metal droplet ($\frac{kg}{m^3}$), $[\,]^r$ represents the interfacial concentration of the element. Similarly the flux of oxygen towards the slag-metal interface, J_O is given by

$$J_O = \frac{A_d k_m \rho_m}{100 M_O}([O] - [O]^r) \tag{4.20}$$

The supply of oxygen takes place from slag FeO of which a fraction is consumed by carbon and rest diffuses into the metal droplet to raise the oxygen concentration of the droplet, this balance is represented in the following equation:

$$J_O = J_C - J_{FeO} \tag{4.21}$$

4.2.4 **Internal decarburization**

Although internal/homogeneous CO gas generation has been observed for metal droplets exposed to oxidizing gases[31–35] and slags[11], only few studies[33,36–38]proposed a theoretical explanation for it. Recently, Chen and Coley[12,13] conducted X-ray fluoroscopy experiments at steelmaking temperatures and developed a mathematical model for internal nucleation rate of CO gas bubbles. Based on their experimental observations, Chen and Coley[12,13] modified the classical homogeneous nucleation rate equation by introducing a correction/modifying parameter 'ψ' to the surface tension of the metal droplet. This parameter physically represents the extent of decrease in energy barrier for homogeneous nucleation described differently by various authors[36–38]. Levine[36] suggested that this parameter accounted for the action of 'doubly charged oxygen ions' chemisorbed on CO

embryos in lowering the surface tension. The decrease in surface tension in turn lowers the energy barrier for the nucleation. Bowers et al.[37] proposed a theory which involved formation of a metastable blob phase before the bubble nucleation. The interfacial energy between the blob and the solvent is considerably less than that for a bubble, which a sharp interface (and hence higher interfacial energy). This makes the nucleation possible at lower supersaturation levels than predicted by classical nucleation theory. Similarly Lubetkin[38] used the surface activity of gases (oxygen in current system) which lead to bubble formation to describe nucleation occurring at lower supersaturation than predicted by theory. The nucleation rate of CO gas in a metal droplet is given by the following equation[12]

$$J_s = N_o \left(\frac{3\psi\sigma}{\pi m}\right)^{\frac{1}{2}} exp\left(-\frac{\Delta H}{kT}\right) exp\left(-\frac{16\pi(\psi\sigma)^3}{3kT\left(\Delta P_{CO}^{int}\right)^2}\right) \quad (4.22)$$

where J_s is the nucleation rate, number of nuclei$/m^3.s$, σ is the surface tension of metal droplet, '$\psi\sigma$' represents the surface tension at liquid metal- CO gas interface due to oxygen ions, (N/m), ΔH is the heat of formation of one CO molecule; m is the mass of one molecule of CO gas, kg, T is temperature, K, k is Boltzman constant, J/K. No is the number concentration of CO embryos in the liquid and its value is calculated using the following equation

$$N_o = N_A \times \frac{n_O}{V_o} \quad (4.23)$$

where n_O is the moles of oxygen present in a metal droplet, V_o is the initial volume of metal droplet. As an embryo of CO is formed from carbon and oxygen, the number of concentration of CO embryos would depend on the smaller value amongst the

concentrations of the two elements in liquid iron. In case of steelmaking, the activity of carbon in liquid iron is much higher than that of oxygen. Hence the value of N_o depends on oxygen concentration rather than that of carbon. ΔP_{CO}^{int} is the difference of CO vapor bubble pressure at equilibrium inside the metal droplet and pressure inside the furnace and can be calculated using equation 4.24.

$$\Delta P_{CO}^{int} = P_{CO} - P_{furnace} \tag{4.24}$$

The internal CO generation rate, J_{int} in mole/s can be represented as[12]

$$J_{int} = J_s \times \left(\frac{n_e}{N_A}\right) \times V_o \tag{4.25}$$

where n_e is the number of molecules in a CO embryo, N_A is Avogadro number, V_o is the initial volume of metal droplet, m^3. To the best of authors' knowledge, this model can predict the internal nucleation rate of CO bubbles satisfactorily under the relevant oxygen steelmaking conditions and it has been used in the current work.

4.2.5 **Surface tension of metal droplet**

The surface tension of the metal is a critical parameter affecting the instantaneous CO nucleation rate. The surface-active elements such as sulfur and oxygen, have a negative effect on surface tension, whereas carbon has a positive effect. Previous studies[39–43] have examined the individual and combined effects of these elements. The equation suggested by Chung and Cramb[44], is used in this study since it is the most comprehensive equation for calculating the surface tension of metal droplet incorporating effects of $[C], [S], [O]$ as well as temperature**,**

$$\sigma_{metal} = 1913 + (67.75 \times [C]) + \left(0.43 \times (1813 - T)\right) - (0.107 \times T \times ln\left(1 + (K_S h_S)\right)) - (0.153 \times T \times ln\left(1 + (K_O h_O)\right)) \quad (4.26)$$

where $K_O \; and \; K_S$ are the adsorption coefficients of the oxygen and sulfur and calculated as follows [44]

$$\log K_O = \left(\frac{11370}{T}\right) - 4.09 \quad (4.27)$$

$$\log K_S = \left(\frac{10013}{T}\right) - 2.87 \quad (4.28)$$

The instantaneous changes of composition of droplet due to CO nucleation and oxygen diffusion are accounted for while calculating the surface tension of metal droplet. The decrease in surface tension due to [S] and [O] are derived from their surface activity due to their selective adsorption at the interface. Initially as the concentration of surface-active elements increases the surface activities increase leading to decrease in surface tension, however beyond a certain concentration there is no increase in surface activity (or consequent decrease in surface tension). Halden and Kingery[45] firstly defined 'Excess surface concentrations' through use of Gibbs isotherm. They demonstrated that increase in excess surface concentration is observed with an increase in concentration of surface-active agent thus leading to decrease in surface tension. However beyond a particular activity/concentration excess surface concentration remains constant and the surface tension remains constant even if the concentration of surface-active agent is increased.

Several studies[41,43] focused on the effect of oxygen concentration on the surface tension of liquid metal. The values ranged from 0.04 to 0.1. Similarly, the concentration of sulfur ranged from 0.02 to 0.1. Accordingly, in current calculations the maximum concentrations of O and S are set as 0.07 and 0.02 wt % respectively.

4.2.6 **Escape rate of CO gas**

The model predictions of internal CO gas generation profile and the corresponding escape rate profile are illustrated in Figure 4.1(a) and Figure 4.1(b), respectively. These results are obtained for 1 g droplet reacting with slag at 1853 K from the study of Gu et al.[15]. It can be seen in Figure 4.1(a) that the internal decarburization started at 2 seconds, and at this instant total CO gas generated increased its peak value leading to significant accumulation of CO gas thereby bloating of the droplet. In the meantime, CO gas exerted significant pressure on the walls of the droplet and started to escape from the droplet. The escape of gas from the droplet started at 5 seconds and peaked at 11 seconds as seen in Figure 4.1 (b). The net outward force exerted on the CO bubbles at the droplet wall is a function of net CO gas present (or CO gas generation rate) inside the metal droplet as well as the surface tension of the metal droplet (a function of its composition). In the current work, a hyperbolic secant function was defined to generate the gas escape profile of a bloated droplet and is given by

$$J_{esc-t} = (\Delta t \times \sum J_{int}) \times \frac{1}{4} \times sech^2\left(\frac{t-\mu}{2}\right) \tag{4.29}$$

where J_{esc-t} is the net escaped moles of CO gas at time instant 't', μ is location parameter of the function and its value is proportional to droplet diameter /size, $\mu \propto d_d$. The value of μ lies between 2 and 9 for droplet size ranging from $0.5\ to\ 6 \times 10^{-3}$ m.

The function is based on the study by Zhu and Coley[46]. They found that the CO gas escape rate profile strongly depends on the internal CO gas generation profile. To the best of authors' knowledge, this is the only study available in literature to predict the escape rate of CO gas from a metal droplet reacting with slags and it is used as basis of the current predictions of CO gas escape profile.

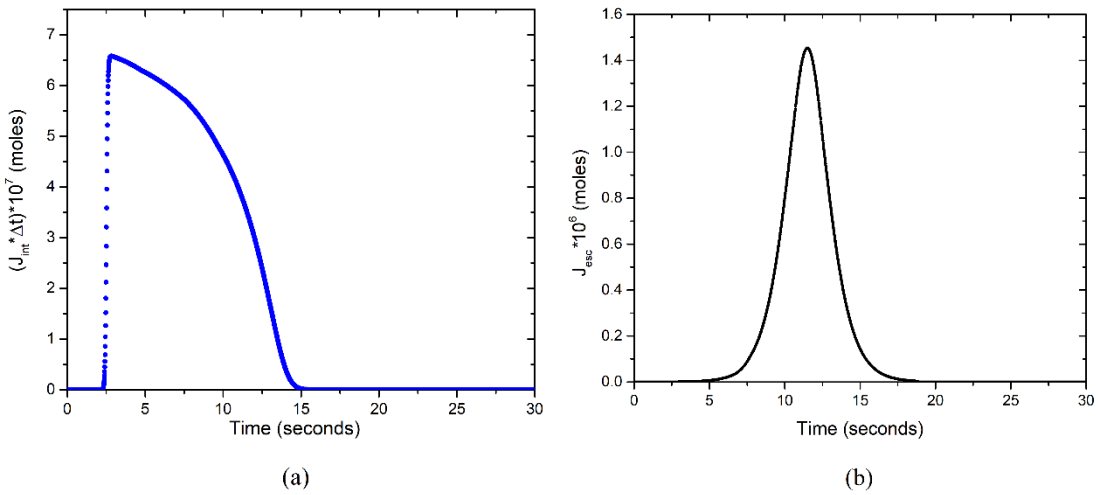

Figure 4.1 Prediction of (a) internal CO gas generation and (b) corresponding escape rate for a 1 g droplet at 1853.15 K in slag

The net escaped moles of CO gas, J_{esc-t} at a given time step are obtained from the escape rate profile and used to evaluate the net moles of CO gas retained inside a droplet, N_{CO-t} at a given time step. The equation to calculate the net retained moles of CO gas within a metal droplet can be written as

$$N_{CO-t} = (J_{int-t} \times \Delta t) - J_{esc-t} + N_{CO-(t-1)} \tag{4.30}$$

4.2.7 Residence time of metal droplet

In the current study, the residence time of a droplet is defined as the time interval between the arrival of a single metal droplet in the emulsion and sinking back into the metal bath. The residence time depends upon the change in density of the metal droplet due to the existing CO gas within the droplet. The net moles of CO gas within the droplet is calculated using Equation 4.30. The instantaneous density of a single droplet is calculated using the following equation,

$$\rho_t = \frac{m_{dt}}{\left(\frac{m_{dt}}{\rho_d}\right)+\left(\frac{N_{CO-t}*M_{CO}}{\rho_{CO}}\right)} \tag{4.31}$$

where m_{dt} is the weight of metal droplet at given time instant, kg, ρ_d and ρ_t are the initial and apparent density of a metal droplet, respectively, $\frac{kg}{m^3}$. ρ_{CO} is the density of nucleated CO at the temperature equal to that of metal droplet. If the apparent density of the droplet is less than the density of emulsion, then the droplet is assumed to be suspended in the emulsion, else the droplet sinks back into the bath. The density of emulsion can be calculated using the following correlation[24,47]

$$\rho_{s-g} = \rho_g \phi_g + \rho_s(1-\phi_g) \tag{4.32}$$

where ϕ_g is the volume fraction of CO gas in the emulsion and $\rho_g \; and \; \rho_s$ are the gas and slag densities, respectively. In the current work, the volume fraction of CO gas in the emulsion is assumed to be constant and the value is taken to be 0.8. The slag density[20] is calculated by considering the volume fractions and molar volumes of its components. The

density of emulsion formed by a typical slag in oxygen steelmaking conditions with ϕ_g = 0.8, is found to be 0.450 to 0.575 kg/m^3.

It should be noted that the trajectory of the droplets in the emulsion is included in the current work. This is done through ballistic droplet motion model[24] wherein trajectory of the ascending (into the emulsion zone) and descending (back into the metal bath) motion of metal droplets are predicted and the decarburization occurring during this time period is also accounted for in addition to the decarburization during the bloating period.

4.3 Model Assumptions

The residence time and decarburization rate of metal droplets are predicted using an industrial data reported by Cicutti et al.[6,48] for 200-t LD-LBE oxygen steelmaking process.

Table 4.1 shows the operating conditions of the process. Oxygen is blown through a six-nozzle lance with a flow rate of 10.33 Nm^3/s whereas inert gas mix of Ar/N_2 is blown with a flow rate of 0.0416 Nm^3/s. 30×10^3 kg of scrap is charged to the process. The composition of slag and hot-metal was analyzed by sampling them during the blow and at the end of blow. The following assumptions are made in the model based on this industrial data.

1. Time step Δt of 0.001 s is selected for simulations.
2. The temperature of metal droplet is equal to instantaneous bath temperature and it remains constant during its residence in the emulsion.
3. All the droplets ejected at each time step are assumed to have the same residence time for a defined droplet size.

4. The internal and external CO gas generation compete for oxygen, after the onset of internal gas generation. No constraint is imposed on either of these two reactions and the relative rates of the reactions are calculated separately at the same time.
5. The droplet size distribution is not included in the current work. The droplet size is assumed to be 2×10^{-3} m. This value is valid for industrial data[48] and similar assumption was also made by the previous models[20,22,49].
6. The initial carbon content of the metal droplet is equal to the bulk carbon content of the liquid metal. The measured values of bulk carbon content of the liquid metal and FeO content of slag were taken as input data for droplet and slag compositions at various times of the blow.
7. Metal droplets are dense and have oxygen concentration of 0.02 wt % (200 ppm) when they are initially ejected into the emulsion zone.
8. In the original model, correction factor (ψ) of 0.023 was used. Even though further work is required for a more rigorous theoretical explanation of the homogeneous nucleation, correction factor has been modified for a range of temperature applicable to oxygen steelmaking conditions. The values for correction factor varied between 0.021 and 0.026. This variation is determined based on model validation against experimental data which is discussed later in section 4.5.1. The value for correction factor equals 0.026 for bath temperatures up to 1813.15 K, whereas equals 0.024 when temperature ranges between 1813.15 K and 1853.15 K. It is 0.021 for temperatures greater than 1853.15 K. It should be noted that in the slags with low FeO content (<10 %), the value of (ψ) is expected to decrease[17]. This might be related to the lower nucleation barrier

for CO gas formed at the slag-metal interface. However, it is established that there is no bloating behavior of a droplet observed in slags with low FeO content. Therefore any potential effect of FeO content on the value of (ψ) is not included in this study.

9. The value of slag phase mass transfer coefficient k_s was taken to be $1.5\ \text{x}10^{-4}$ m/s considering a high basicity value of BOF slag (> 1.2) throughout the blow. This is a reasonable value since Gu et al.[15] have evaluated values ranging from 0.92 to 1.18×10^{-4} for slag basicity of 0.9. The value of mass transfer coefficient in slag could be higher with the progress of the blow, as temperature and the basicity of slag will increase due to increased flux dissolution. An increase in k_s would increase oxygen supply from slag to metal droplet and lead to earlier onset of internal nucleation, however there will be negligible effect of final carbon content. This is due to the fact that the internal nucleation ceases when the activity of carbon (h_C) decreases beyond a certain value.
10. The bloating behavior of droplets is not affected by the external decarburization because CO gas bubbles generated stays on the surface of the droplet for relatively short time and hence the contact time with the metal droplet is limited and these bubbles will negligibly contribute to the change of droplet density. Contrary to this, the internally nucleated CO gas bubbles which stay inside the metal droplet for a considerable time. Therefore, CO gas generated due to external decarburization is not considered in evaluation of the residence time and the internally generated CO bubbles are assumed to be only source of buoyancy of the metal droplet.

Table 4.1: The list of input data obtained from the study of Cicutti et al. [6,48].

Hot metal charged	170×10^3 kg
Scrap charged	30×10^3 kg
Oxygen flow rate	10.33 Nm^3/s
Number of nozzles	6
Lance height	1.8–2.5 m
Initial hot metal temperature	1623.15 K
Tapping temperature	1923.15 K

4.4 **Model Formulation**

The calculation procedure of the proposed model is provided in Figure. 4.2. The blowing conditions such as oxygen flow rate, presumed slag and metal composition that are entered as input data. The slag density and viscosity are then calculated as a function of composition and temperature. The number of droplets is then calculated as a function of blowing conditions as explained elsewhere[25]. Then the fluxes of oxygen and carbon are calculated, followed by the calculation of the instantaneous weight and surface area of metal droplet as well as activities of metal and slag components. At this point, the internal nucleation of CO is thermodynamically unfeasible. So, at this stage, CO formation takes place on the surface of droplet (termed as external decarburization). The non-linear equations for calculating interfacial concentration and activities of species at the metal droplet-slag interface are solved simultaneously. Due to supply of oxygen, depletion of carbon by CO gas generation, the weight and oxygen and carbon content of a metal droplet are updated.

After a certain time, the oxygen concentration inside the droplet rises due to oxygen flux from slag. Consequently, the threshold supersaturation pressure is exceeded (refer equation 4.12), so that homogeneous nucleation of CO bubbles becomes feasible. There is rapid generation of CO bubbles within the droplet leading to decrease in metal droplet density and suspension of metal droplets in the emulsion. With the increase in internal CO generation, there is a simultaneous escape of CO gas from the metal droplet. The instantaneous balance of CO generation and escape rates determines the apparent density of droplet and consequently the residence time of the metal droplet in the emulsion zone. With the knowledge of the residence time of droplet in the emulsion zone, the amount of carbon removed within an individual metal droplet as well as in the emulsion zone can be determined.

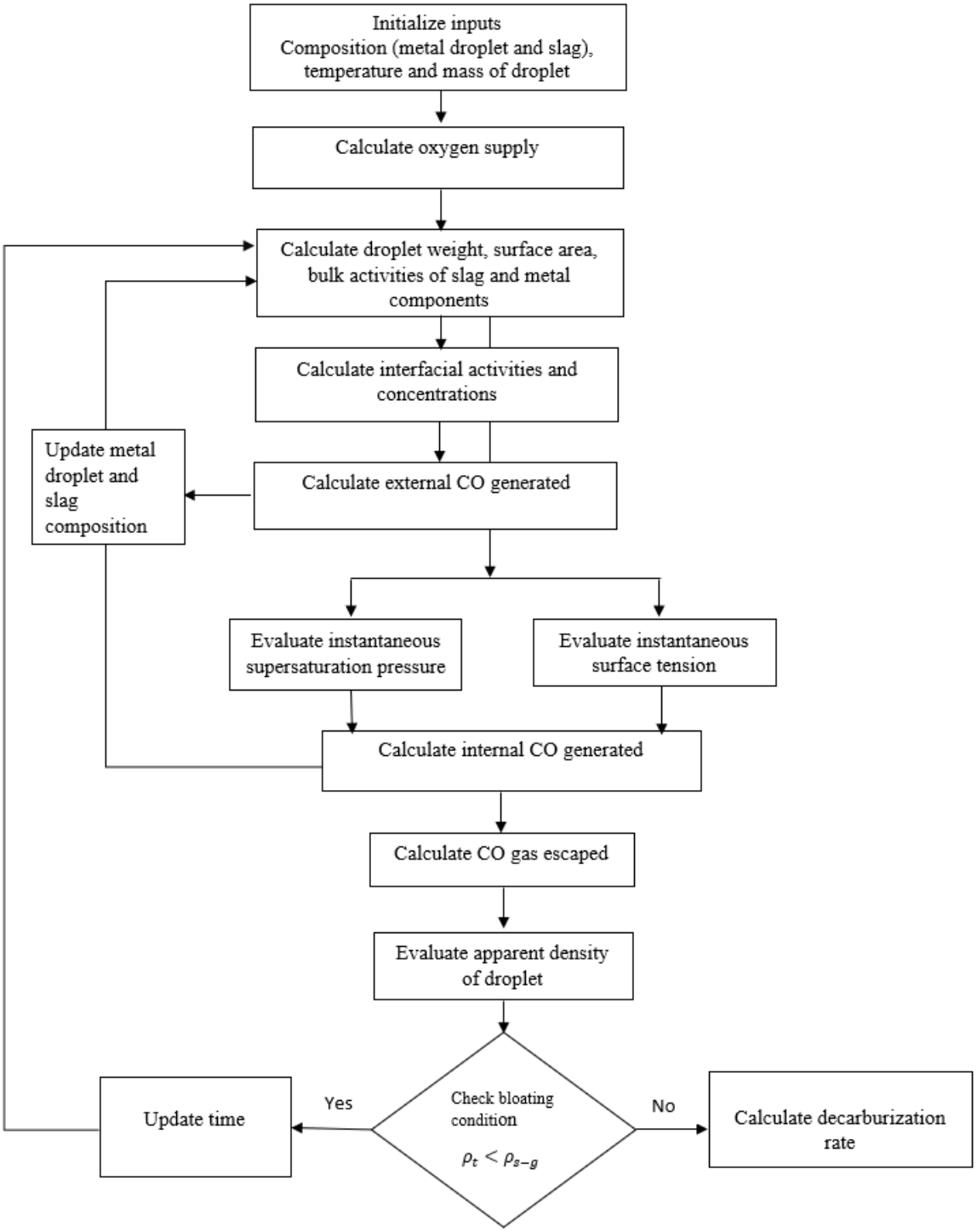

Figure. 4.2 : Algorithm of the decarburization in the emulsion zone model

4.5 Model Validation

4.5.1 CO gas generation

In oxygen steelmaking, dynamic changes in composition and temperature of slag and metal bath influence the decarburization rate. For example, when FeO content of slag is lower than 10 wt %, external decarburization most likely takes place[10,18] on the other hand, internal decarburization will occur for higher FeO contents. In order to explain decarburization reactions more thoroughly, the authors validated the proposed model under various experimental conditions such as FeO content, temperature and sulfur content.

In the first case, the model predictions for total CO gas generation are compared with the experimental data reported by Gu et al.[15]. They studied the dephosphorization kinetics of metal droplets in ferruginous slag as a function of temperature and sulfur during the decarburization period. The change in droplet size due to external and internal decarburization reactions was observed using X-ray fluoroscopy and the total CO gas evolution was measured by constant volume pressure change measurement technique. The slag composition for all experiments was 35 wt % SiO_2, 32 wt % CaO, 17 wt % Al_2O_3 and 16 wt % FeO. The carbon content of metal droplet was 2.62 wt %. The droplet weight was one gram.

Figure 4.3 shows the total amount of CO gas generated as a function of experimental temperature and time as well as sulfur content of metal droplets. In the current study, the total CO gas generated is predicted by using equations 4.17 and 4.25. The slag phase mass transfer coefficients were assumed to be 0.92, 1.01 and 1.18 x 10^{-4} m/s for experiments at 1813, 1853 and 1913 K, respectively. These values were reported by Gu et al.[15] and similar values were used in this study. The solid lines represent the model predictions whereas the

points represent the measured data. Total amount of CO gas generated increases with an increase in sulfur content of the droplet. The total CO gas generated for droplets with 0.007 and 0.014 wt % S are $9x10^{-4}$ and $1.2x10^{-3}$ moles, respectively. The model results are consistent with the experimental data reported by the previous researchers except towards the end of decarburization. The over-prediction by the current model is most likely related to local FeO depletion in the foamy slag. When the bloated droplet suspends in the foamy slag, the supply of oxygen would decrease and limit the CO gas generation. In this study, the FeO content in the slag remains constant during the reaction between metal droplet and slag and the dynamic change in FeO content is not included. However, it should be noted that FeO depletion is not expected to occur during oxygen steelmaking process therefore this discrepancy is unlikely to be an issue/limitation for model predictions under oxygen steelmaking conditions.

There are three regimes observed: (1) CO gas generation rate is limited in the first few seconds. During this time, there is insufficient oxygen inside the metal droplet and this leads to formation of CO gas surrounding the metal droplet. This regime is termed as incubation period. (2) There is a significant build-up of oxygen inside the metal droplet leading to substantial generation of CO gas inside the metal droplet. (3) The internal CO gas generation decreases due to a decrease in the activity of carbon. Total CO gas generated increases slightly with time. The contribution of the internal and external CO gas generated for a metal droplet containing 0.007 wt % S is compared in Figure 4.3(d). The model suggests that the external decarburization occurs during the incubation period. Its contribution reaches its maximum value and remains constant when the internal CO gas

generation starts. In regime 2, the internal CO gas generation is very rapid and reaches its peak value. As CO gas starts to escape from the metal droplet, the amount of CO gas generated within the droplet decreases. In regime 3, CO gas generation continues outside the metal droplet.

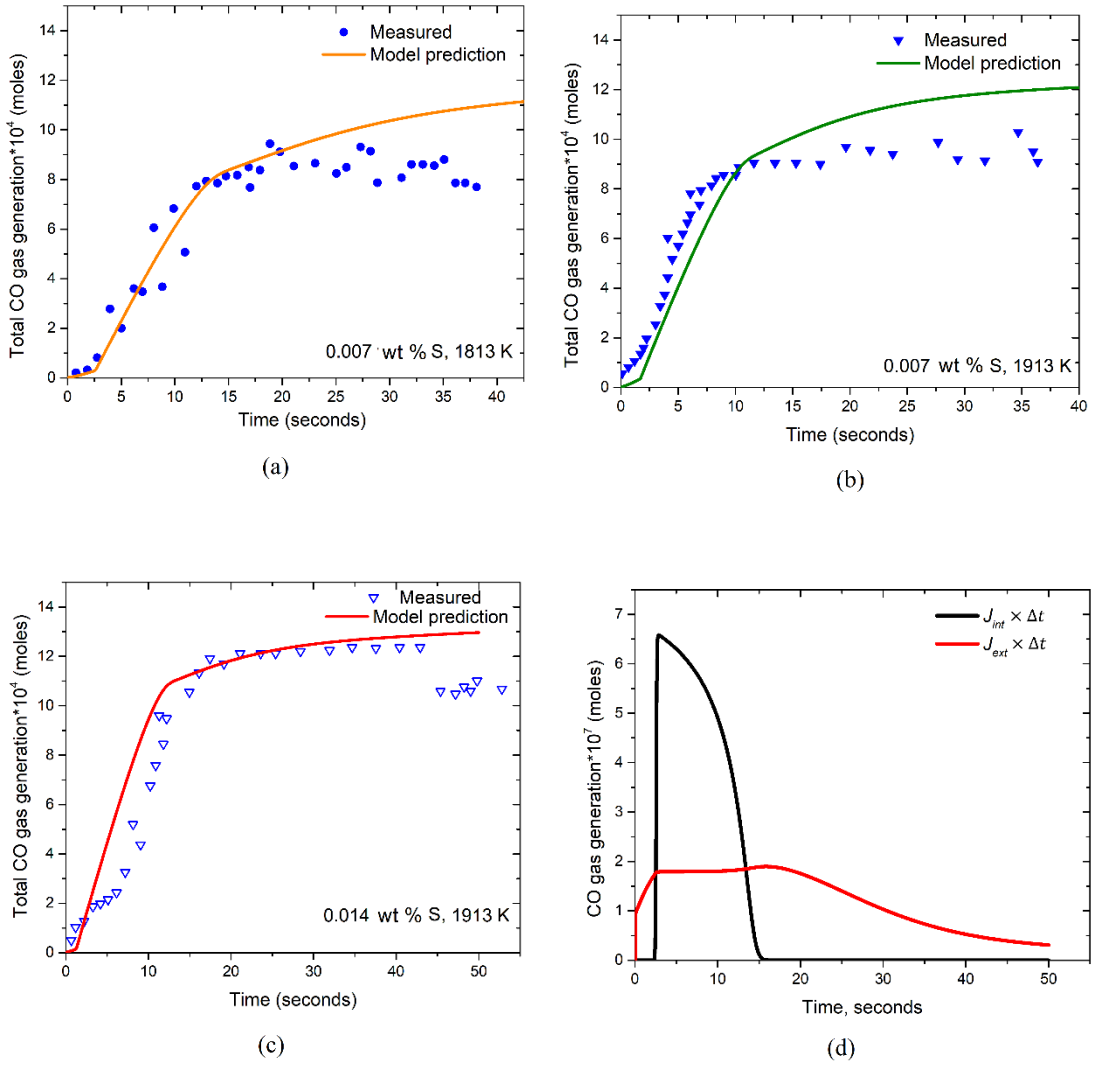

Fig. 4.3: Comparison of model results for total CO gas generated with measured data by Gu et al. [15] for a metal droplet containing (a) 0.007 wt % [S] content at 1813 K, (b) 0.007 wt % [S] at 1913 K, (c) 0.014 wt % [S] at 1913 K (d) Comparison of external and internal CO gas generated for a droplet with 0.007 wt % [S] content at 1813 K, as shown in Fig. 4.3 (a).

In the second case, the effect of low FeO content was studied. Model results were validated against experimental results of Min and Fruehan[10]. Similarly, their experimental set-up involved X-ray fluoroscopy and a mass flow meter for measuring the rate of gas generation. The metal droplets contained 4.2 wt % C and 0.001 wt % S whereas slags contained 7.5 wt % FeO and CaO/SiO_2 ratio of 1. Fig. 4.4 compares the model predictions for CO evolution with measured data as a function of droplet masses ($0.78, 1.28, 1.78 \times 10^{-3}$ kg). It should be noted the slag phase mass transfer coefficient used in these particular calculations was 3 x 10^{-5} m/s, and it is based on the work of Wei et al.[50]. Min and Fruehan didn't suggest any specific value in their work however they proposed that the slag phase mass transfer coefficient varied between 10^{-4} and 10^{-5} m/s. Further it is established that the mass transfer coefficient of FeO is low for slags with low FeO content at low temperatures[51]. It is observed that there is a constant increase in the amount of CO gas generated as a function of time. This finding agrees well with measured data for the first half of the experiments. Later, there is a disagreement between measured and calculated values. The authors believe that this discrepancy is related to local FeO depletion in the slag as explained for previous case study. The CO gas generated with time increases as the droplet mass increases. This is due to the high amount of carbon within the larger droplet. The contribution of the internal and external CO gas generated for a 1.78×10^{-3} kg metal droplet is compared in Fig. 4.4(d). The model suggests that the external decarburization is very rapid and reaches its peak value in few seconds. It decreases gradually toward the end of the experiment. It is important to note that no internal decarburization is predicted by the model under low FeO contents. This result is consistent with the previous researchers observation wherein

Min and Fruehan[10] claimed that the metal droplet was covered by the gas halo during the rapid reaction time, which ranged from 20 to 200 seconds.

Total CO gas generated was 2×10^{-3} moles for a larger metal droplet (1.78×10^{-3} kg). This value was slightly higher than that for a 1×10^{-3} kg metal droplet shown in Fig. 4.3. This is due to the high amount of carbon content of the metal droplet. Even though FeO content in these experiments was low (7 wt %) and the experimental temperature was 1673 K, the oxygen supply or low temperatures were not limiting factors for total CO gas generated.

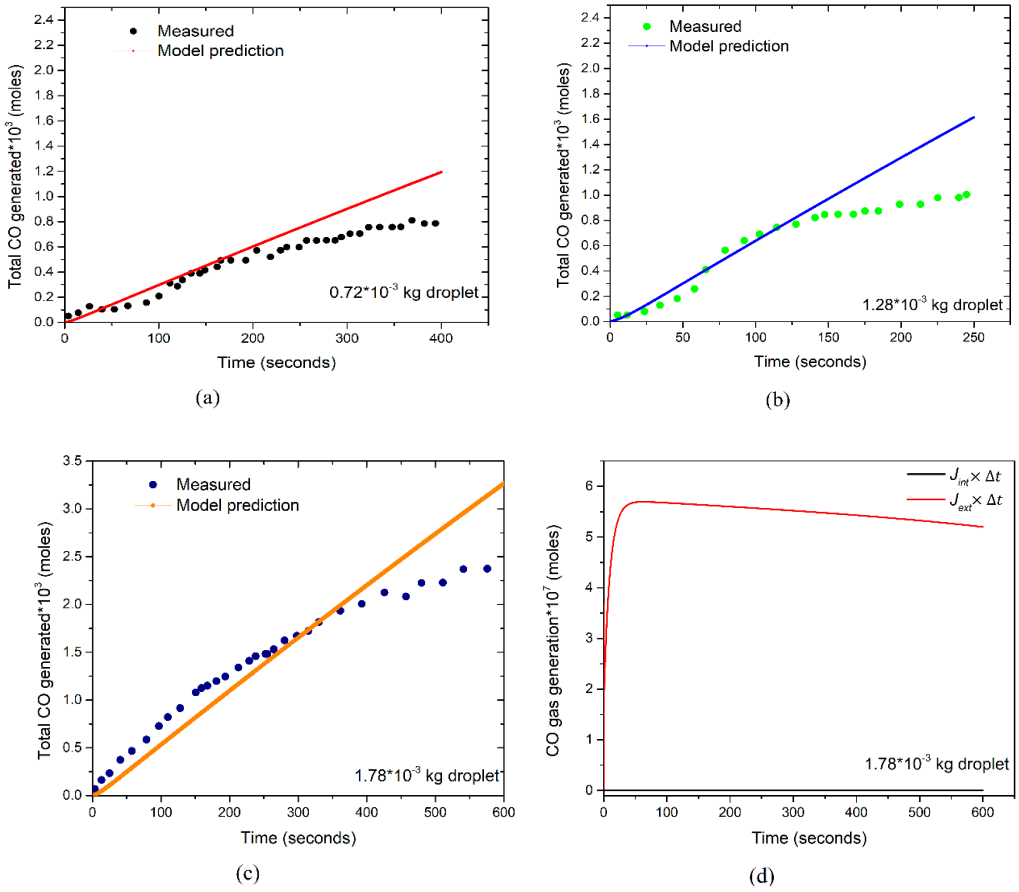

Fig. 4.4: Comparison of model results for total CO gas generated with experimental data by Min and Fruehan[10] for (a) 0.72×10^{-3} kg (b) 1.28×10^{-3} kg (c) 1.78×10^{-3} kg droplet containing 4.2 wt % [C] and 0.001 wt % [S] reacted with slag containing 7.5 wt % FeO, $(CaO)/(SiO_2)$ = 1 at 1673 K (d) comparison of external and internal CO gas generated for a 1.78×10^{-3} kg droplet, as shown in Fig. 4.4 (c).

4.5.2 Residence times of droplets

The residence time of droplets is calculated using Equations 4.30, 4.31 and 4.32 in the current study. The instantaneous amount of CO gas generated and escaped determines the volume change of a single metal droplet. Therefore, the apparent density of droplet can be calculated if the initial mass of the metal droplet is known. Fig. 4.5 illustrates the calculated apparent density of 1 g metal droplet containing 0.007 wt % S at 1853 K by the proposed model using experimental data reported by Gu et al.[15] (described in section 4.5.1). Based on the change in density of a metal droplet, the droplet behavior can be explained as follows: The apparent density of droplet, ρ_t, is more than that of foamy slag, ρ_{s-g} during incubation period. In regime 2, the apparent density of droplet decreases because of accumulation of CO gas inside it and the droplet suspends in the foamy slag ($\rho_t \leq \rho_{s-g}$). The metal droplet during this stage is termed as 'bloated'[24]. After a certain period of time, the droplet becomes devoid of CO gas as internal nucleation of CO gas ceases and the nucleated CO gas escapes. This leads to an increase in apparent density of droplet again ($\rho_t > \rho_{s-g}$) and the droplet sinks back from foamy slag to dense slag. For model validation against experimental data, the residence time of the droplet is equal to the time when the droplet resides in the foamy slag (regime 2).

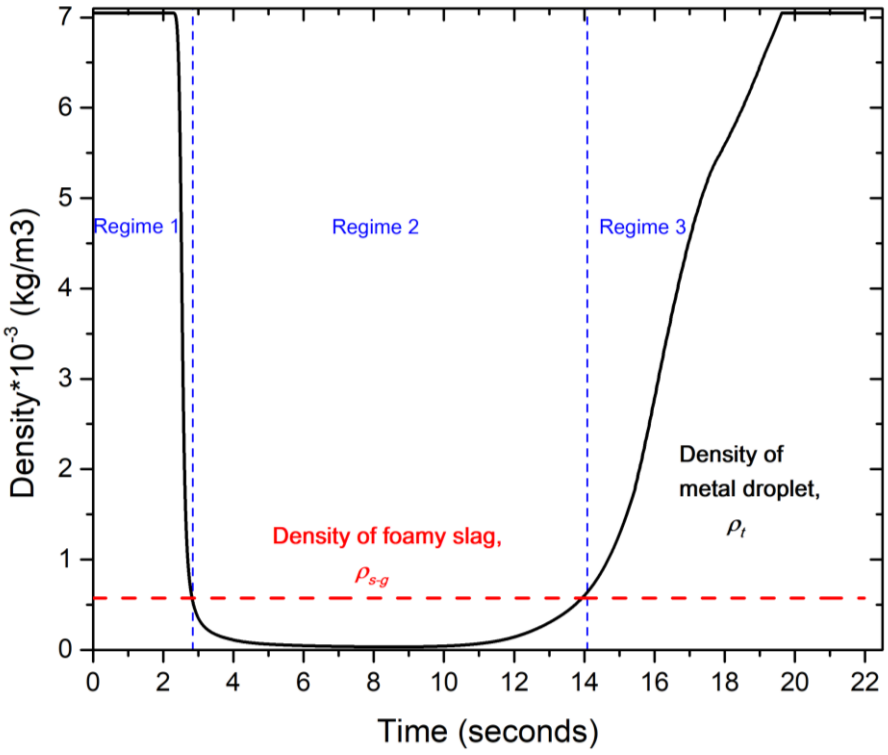

Fig. 4.5: Change in the apparent density of 1 g droplet containing 0.007 wt % [S] at 1853.15 K as a function of time

The model predictions for residence time of metal droplets are compared with measured data obtained by Gu et al.'s [15] experiments as shown in Fig. 4.6. The measured data is obtained from available X-ray videos of the experiments[15]. The authors assumed that the measured residence times is the time elapsed between the start of ascending of metal droplet in the dense slag (droplet rises from the bottom of crucible) and the start of descending of metal droplet (droplet reaches the interface between foamy and dense slag). The upper limit/maximum residence time represents the time elapsed between the ascending of the metal droplet and point when the droplet reaches the bottom of crucible. The lower limit/minimum residence time represents the time droplet stays in the foamy slag. The

predicted residence times varied between 10.5 to 13 seconds and these values are within the range of observed values.

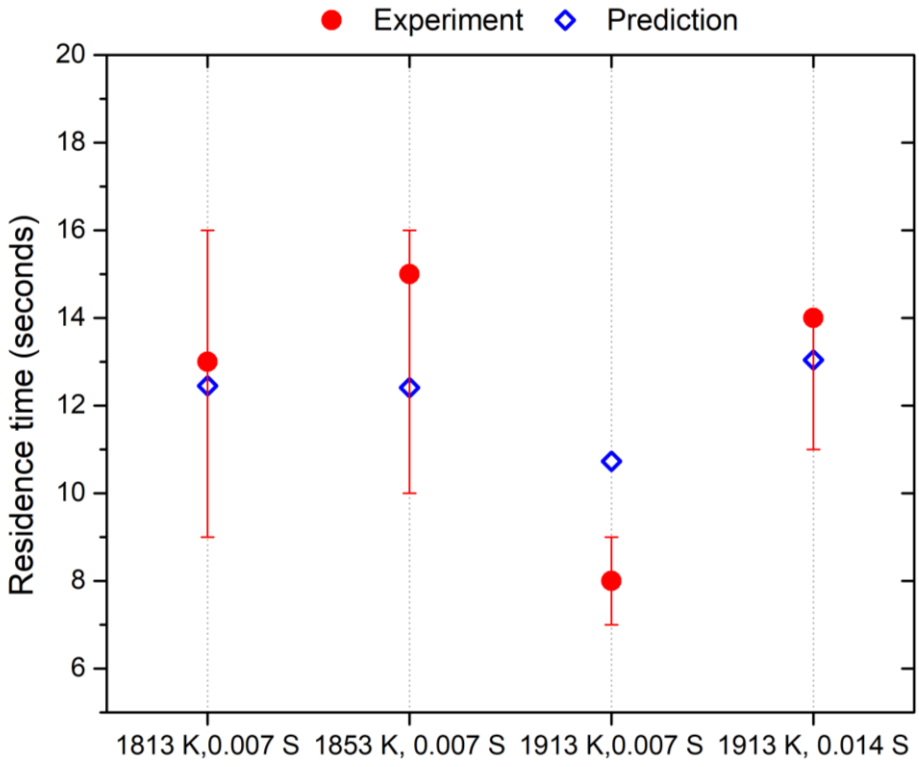

Fig. 4.6 : Comparison of model predictions for residence times with the experimental data reported by Gu et al.[15]

4.6 Results and Discussion

4.6.1 Residence time of droplets

The model was further studied using the industrial conditions reported by Cicutti et al. [48]. The residence time of the droplets is important with regards to the estimation of the extent of decarburization of the droplets. The predicted residence times of 2×10^{-3} m metal droplets during various parts of the blow are presented in Fig. 4.7. The corresponding carbon content of liquid metal [C] and FeO content of slag (FeO) are listed in Table 4.2. In the early part of the blow (0 to 6 mins), the residence time ranges from 6.4 to 7.25 seconds.

As the carbon content decreases further with time, the residence time of droplets decreases to 5 seconds and finally merely a second or less. This is due to the fact that the activity of carbon decreases due to the decrease in carbon content within the droplets. This leads to lesser CO gas generation inside the droplets, which is reason for their bloating and spending longer time in the emulsion. It is important to note that the decrease in FeO content does not influence decarburization rate because the oxygen supply from slag is sufficient throughout the oxygen blow. No bloating was predicted by the model for droplets generated beyond 14 mins, hence the residence time was negligible towards the end of blow. The overall trend of residence times and its dependence on [C] and (FeO) contents is similar to those predicted by previous researchers[2,4,5,19,24], however shorter residence times are predicted by the current model. The difference between the current model and previous models [19,24] is expected since the calculation procedure is completely changed. In the previous modeling attempts[19,20], the residence time of a single droplet was calculated based on a ballistic motion of a droplet at vertical and horizontal coordinates within the emulsion. In their attempts, they introduced a correlation to calculate the critical decarburization rate as a function of FeO content of slag. In order to explain the bloating behavior of droplets, they further calculated the apparent density of a single droplet as a function of initial density and the ratio between critical decarburization rate and decarburization rate at a given time step. On the other hand, the current model explains the bloating phenomenon more thoroughly from basic principles by incorporating the internal and external CO gas generation as well as CO gas escape with respect to oxygen supply for

any given time step. The current model reduces the empiricism for calculating the residence time of a single droplet.

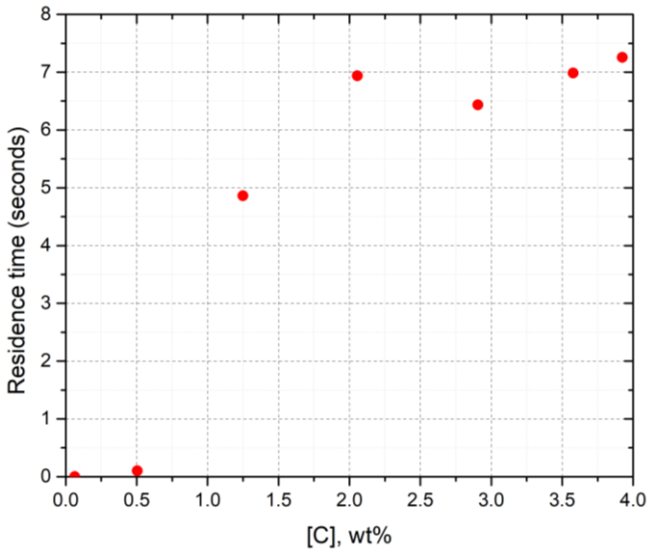

Fig. 4.7: Predicted residence times of metal droplets in the emulsion during the blow

Table 4.2: List of measured [C] and (FeO) contents as a function of blowing time[6,48]

Time, s	[C]	(FeO)
1.89	3.92	33
3.74	3.58	31
5.98	2.91	30
8.90	2.06	17.09
11.28	1.25	11.63
14.37	0.50	18.19
16.97	0.06	22.74

4.6.2 Carbon content of metal droplets

Changes in the carbon content of the metal droplets with respect to blow time are illustrated in Fig. 4.8. The black data points represent the initial carbon content of metal droplets ejected into the emulsion zone whereas red data points represent the final carbon content of metal droplets. This figure shows that the highest carbon removal takes place in the early part of the blow since the residence time of metal droplets is relatively long at this time. Later, it decreases gradually as residence times of metal droplets decrease. Accordingly, the final carbon content increases from 0.45 to 1.11 wt % during the first half of the blow. The predicted final carbon contents of the droplets in the emulsion are within the range of values (for sampled droplets) measured by Cicutti et al.[48] during various times of the blow.

The observations reported for various blows in an 6-t pilot plant converter[52] are similar, wherein the extent of decarburization (or the difference between carbon contents of the bath and emulsion droplets) decreases with the progress of the blow. This behavior stems from the fact that internal CO gas nucleation strongly depends on the activity of carbon, oxygen and sulfur (as inferable from equations 4.12, 4.22 and 4.26). The carbon content $[C]$ and activity h_C decrease during the blow as well as during the residence time of an individual droplet. Carbon being more abundant impurity in liquid metal affects the activities of oxygen and sulfur. During the early part of the blow, high carbon content leads to high activity of sulfur (h_S) as carbon and sulfur have highly positive interaction parameters with respect to each other. Higher values of h_S lead to a greater depression in surface tension of liquid metal thus leading to a higher CO gas nucleation as represented in equation 4.22, $J_s \propto \exp(-\sigma^3)$. This leads to a higher carbon removal in the early part of the blow and thus lower final carbon contents in metal droplets. Furthermore, the analysis of equation 4.22 shows that J_s is inversely proportional to the exponential of the supersaturation pressure squared, ΔP_{CO}^{int}. The activities of carbon (h_C) and oxygen (h_O) and equilibrium constant K_{CO} affect ΔP_{CO}^{int} (refer equation 4.12). Carbon and oxygen have negative interaction parameters with each other with the progress of blow so h_C decreases while h_O increases. There is a marginal change in the ΔP_{CO}^{int} for various times of the blow and hence a marginal effect on the nucleation of CO gas bubbles within a single droplet (refer equation 4.12). This indicates that decarburization reaction is mainly limited by the initial carbon content of metal droplet ejected into the emulsion zone.

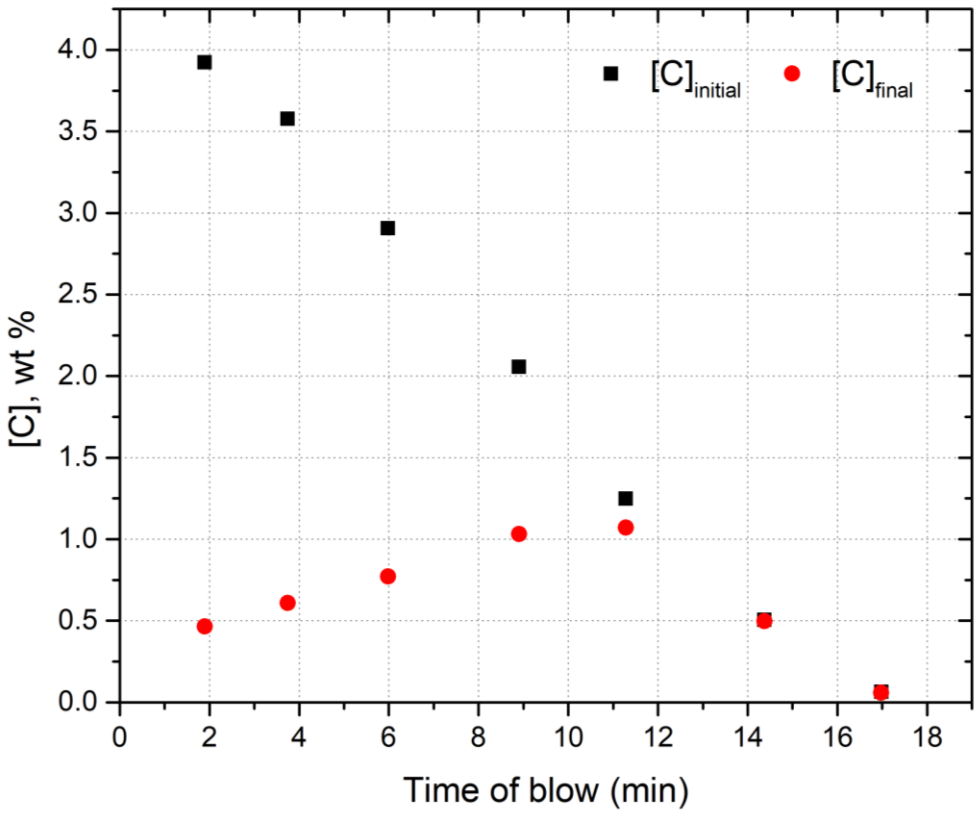

Fig. 4.8: Changes in the initial and final carbon contents of metal droplets in the emulsion with respect to blow time

The authors investigated the effect of droplet size distribution on the residence time of the droplets and decarburization rates. The model predicts that the residence time of droplets will decrease with a decrease in droplet size. However, the amount of carbon removed from a single droplet will be slightly affected. In the early part of the blow, the total decarburization rate in the emulsion will be similar regardless of droplet size and total amount of droplet generated would be more important than the size of the droplets. In the later part of the blow, the decarburization rate is expected to increase only for small droplets (< 0.001 m). This result implicates that controlling droplet size distribution as a function of oxygen blow practice can enhance the decarburization rates in the emulsion zone towards

the end of the blow. However, it is certain that greater silicon, manganese and phosphorus refining would occur in the case of smaller droplets as reported by a sampling study of 6-t experimental converter[52] . This is because the refining of these elements occurs at the droplet-slag interface (contrary to decarburization) and smaller droplets would have a larger interfacial area per unit volume. This model will be linked to the process model and the effect of size distribution of droplets will be further studied.

It is important to note that the current work is intended to provide a fundamental description of the bloating behavior and decarburization reaction of a single droplet in the emulsion zone. The effect of silicon and manganese is excluded in this study and would be discussed in subsequent publications. It is expected that the decarburization reaction continues despite the presence of silicon. This is due to the fact that the availability of silicon at interface is limited as compared to carbon even though silicon oxidation is extremely favorable as compared to that of carbon. Manganese will have a much smaller retarding effect on the kinetics of decarburization reaction.

4.6.3 **Decarburization rate in emulsion zone**

The contribution of decarburization rate in the emulsion zone to overall decarburization rate is studied by comparing model predictions for decarburization rates in the emulsion (kg/min) with the total decarburization rate under the operating conditions reported by Cicutti et al. as given in Figure 4.9. Total decarburization rate was calculated using the theoretical decarburization rate estimated by Cicutti et al[48] for a post combustion ratio of 0.10 whereas decarburization in emulsion is calculated using equation 4.1. In the early part of the blow, the decarburization rate is 174 kg/min followed by lower rates 150 to 159

kg/min during main blow (around 6-8 mins), and eventually falls down to 23 kg/min in the 11th minute of the blow. As discussed in the previous section, the presence of silicon during the early blow might decrease the predicted decarburization rate slightly, until the silicon content decreases to extremely low concentration (<0.05 wt %)[53]. However, this effect is not considered in the current model. In the early part of the blow, the decarburization rate in the emulsion zone contributes to 75 % of the total decarburization rate. Its contribution decreases to 5 % towards the end of the blow. It is notable that the decarburization per droplet decreases with the progress of the blow, as indicated by the [ΔC] wt % in Fig. 4.8. However this lower decarburization per droplet is compensated by high droplet generation (blowing time > 5.89 min) wherein droplet generation rises from 5033 to 7450 and 12843 kg/min as shown in Figure 4.9 and total decarburization does not fall sharply. No significant decarburization is predicted in the emulsion beyond 14 minutes as there is no occurrence of droplet bloating during that period due to low carbon content. It is important to note that the calculations are conducted for a fresh 'set of droplets' generated at each time-step and their refining behavior is tracked independently in the calculations. The authors believe that the decarburization rate is strongly dependent on the amount of carbon removed in a single droplet shown in Fig. 8 whereas it is slightly influenced by the residence time of the droplet. Therefore, the decarburization rate predictions would be affected slightly. Even though external decarburization continues to occur, the contribution of external decarburization to the overall decarburization is relatively small. This is due to the fact that the residence time of dense droplets is negligible (approximately 0.1s). This model enables to predict the carbon removal within dense and bloated droplets in the emulsion zone. These findings

indicate that bloating behavior of droplets is important for refining reactions in the emulsion zone and overall refining kinetics of the process.

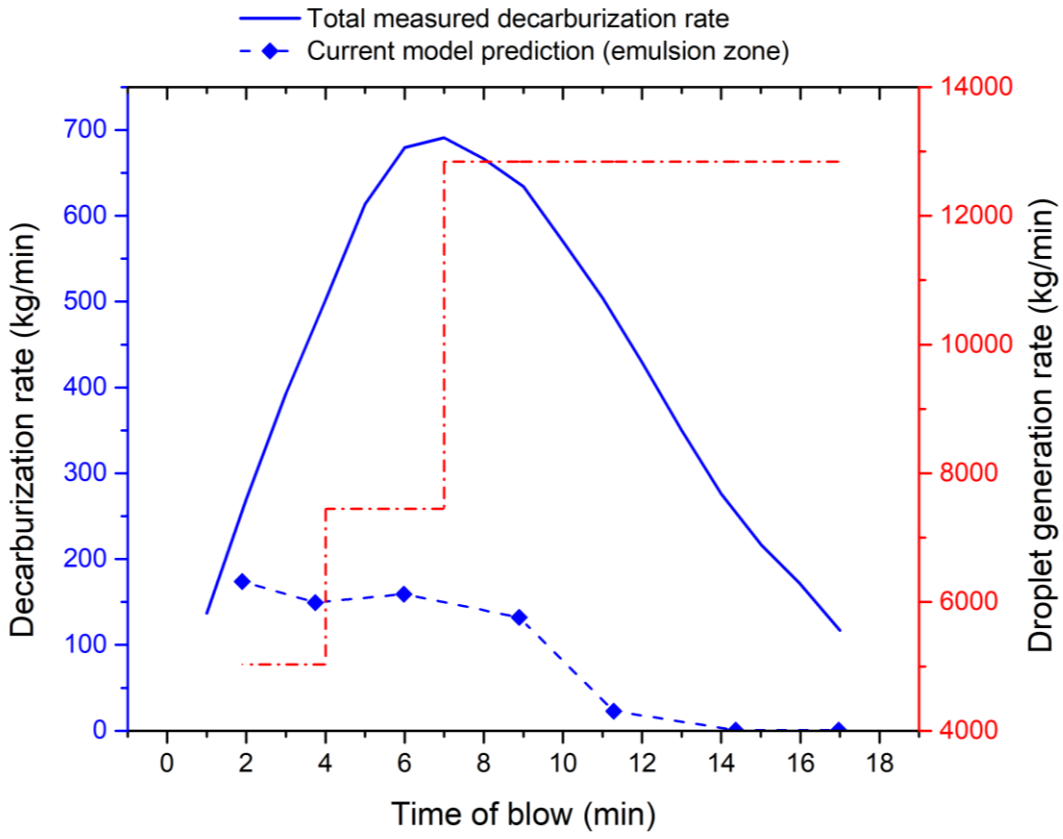

Figure. 4.9: Comparison of decarburization rate in the emulsion and overall decarburization rate as a function of droplet generation rate and blow time

The predicted decarburization rate in the emulsion zone shown in the above figure is based on the minimum droplet generation rate derived from the correlation of Subagyo et al.[25]. A more recent study by Rout et al.[54] suggests that droplet generation rate is almost five times higher than that of Subagyo et al. Further evaluation of droplet generation rate is required for better understanding of refining kinetics in oxygen steelmaking process. Application of such high droplet generation rate in the current work would increase the

decarburization rate in the emulsion zone to an extent that 100 % of decarburization reaction takes place in the emulsion zone particularly in the early part of the blow and such prediction doesn't reflect the reality. Beyond 11th minute, no significant bloating would be observed and an increase in the number of droplets in the emulsion zone would not lead to increase in any refining after this time. It is quite possible that a considerable fraction of the generated droplets would not reach the emulsion zone (considering their ejection angle and point of origin in cavity). These droplets are splashed within cavities (countercurrent to oxygen jets) and bring about significant refining including the decarburization as well as FeO generation necessary to sustain the emulsion zone refining. Experiments by Koch et al.[55] involving blowing of an oxygen jet on a 50 kg molten Fe-C bath support this claim. The metal droplets "sprayed" from the cavity were sampled at various points of the cross section of the metal sampler during a blow. The authors observed that the "inner" droplets (ejected into the jet) underwent higher refining as compared to the "outer" droplets (ejected into the emulsion zone in radially outward direction). This indicates a possibility of significant contribution of decarburization and other refining reactions in the cavity droplets. The authors believe that the decarburization occurring within the droplets residing in the cavities would be responsible for the residual decarburization which is unaccounted by emulsion zone.

4.6.4 Effect of initial oxygen content of droplet

The instantaneous oxygen content is a function of [Fe]-[O]-(FeO) and [C]-[O]-CO equilibrium and the degree of bottom stirring. The increase in turbulence of bath caused by bottom stirring improves the homogeneity of the bath and causes a fall in its oxygen content

(and hence the droplets). The oxygen content of metal bath rises during the initial part of the blow, is almost constant during the middle blow and rises significantly towards the end of the blow. The effect of initial dissolved oxygen content of a metal droplet of size 2×10^{-3}m on the onset of bloating is presented in Fig. 4.10. The initial oxygen content varied from 0.02 to 0.1wt %. The model predicts that an increase in initial oxygen content would reduce time for the onset of bloating (the time when $\rho_t \leq \rho_{s-g}$) slightly. This is due to the fact that supersaturation of CO gas is reached in a shorter time. However there is a negligible effect of initial oxygen content on the decarburization rate. This calculation is repeated for droplets ejected at different blow time. There is no noticeable change on the onset of bloating of droplets and total decarburization rate in the emulsion. This indicates that model assumption is suitable for predicting decarburization rates under oxygen steelmaking operating conditions and dissolved oxygen content within the metal droplet can be kept constant.

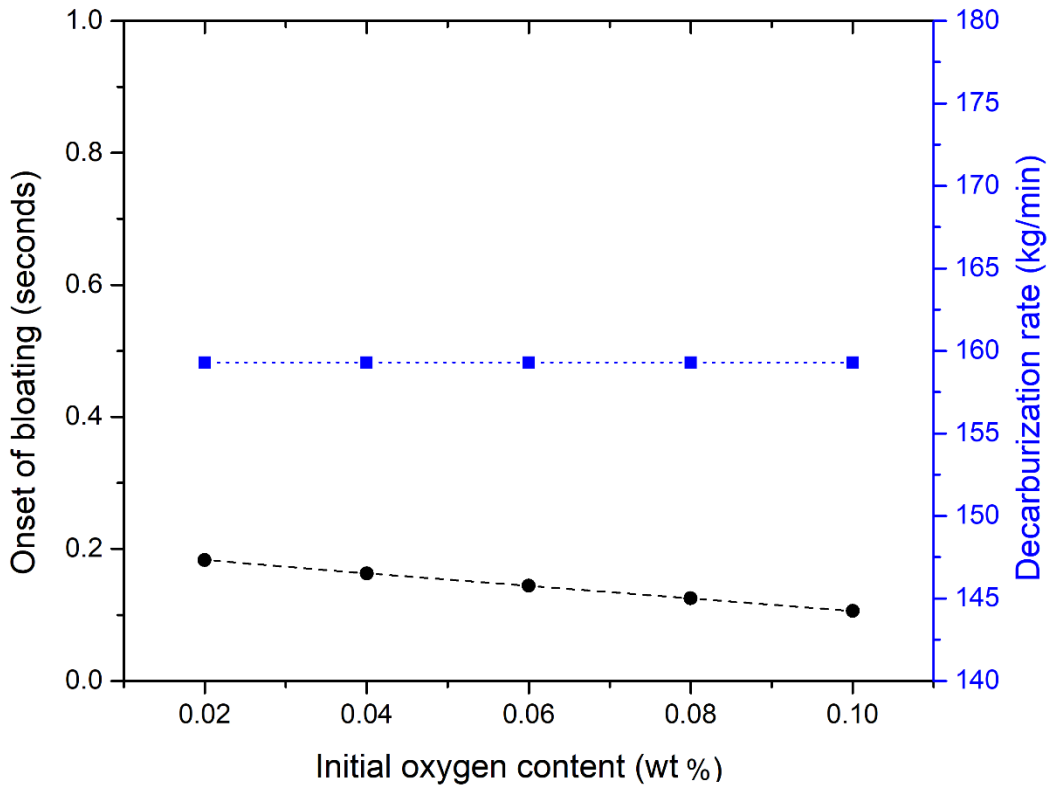

Fig. 4.10: Effect of initial dissolved oxygen content on onset of droplet bloating and decarburization rate (droplet size $2 \times 10^{-3} m$ *, ejection time: 5.89 min)*

4.6.5 Effect of temperature of droplet

In this work, the droplet temperature was assumed to be equal to the instantaneous bath temperature. The effect of droplet temperature (as compared to the bath temperature) on decarburization rates in the emulsion zone is presented as a function of ejection time of metal droplets in Fig. 4.11. The first prediction for each series is the value assumed as base case followed by an increase in temperature of 100 to 200 K. The predicted decarburization rates fall slightly with an increased in temperature up to 1813.15 K, but increase slightly with further decrease in temperature. The initial decrease is caused due to exothermic nature of the decarburization reaction. Thereafter (i.e above 1813.15 K) slight increase is

due the effect of change in value of correction factor ψ. It is constant and equal to 0.026 for calculations below 1813.15 K. Subsequently the value of ψ increases to 0.024 for temperatures up to 1853.15 K and 0.021 for higher droplet temperatures. As explained in the assumptions section, $'\psi'$ is surface tension modifying parameter. Hence a lower value of ψ entails a higher internal CO gas generation (refer equation 4.22).

Recent work by Rout et al.[23] attempted to predict the dynamic temperature of metal droplets by assuming the droplet temperature to be equal to impact zone temperature, and it being cooled to temperatures between 1800 to 2000 K. In their work, the impact zone temperature was approximately 2300 K. Even though droplet temperature would be higher than the instantaneous bath temperature when it enters the emulsion zone, the extent of absorption of heat by the metal droplet during the short period is difficult to measure and not available in the open literature. Therefore, a detailed phenomenological heat transfer model incorporated with high temperature experiments will be beneficial for better prediction of droplet temperature thereby decarburization rates in the emulsion zone. It should be important to mention that these calculations are done with same values of slag phase mass transfer coefficient ($1.5\ x10^{-4}$ m/s). However this value is likely to increase with an increase in temperature which would counteract the decrease in decarburization. The authors believed that the assumption of droplet temperature is reasonable for the current knowledge. Further studies are required to evaluate the temperature of droplet.

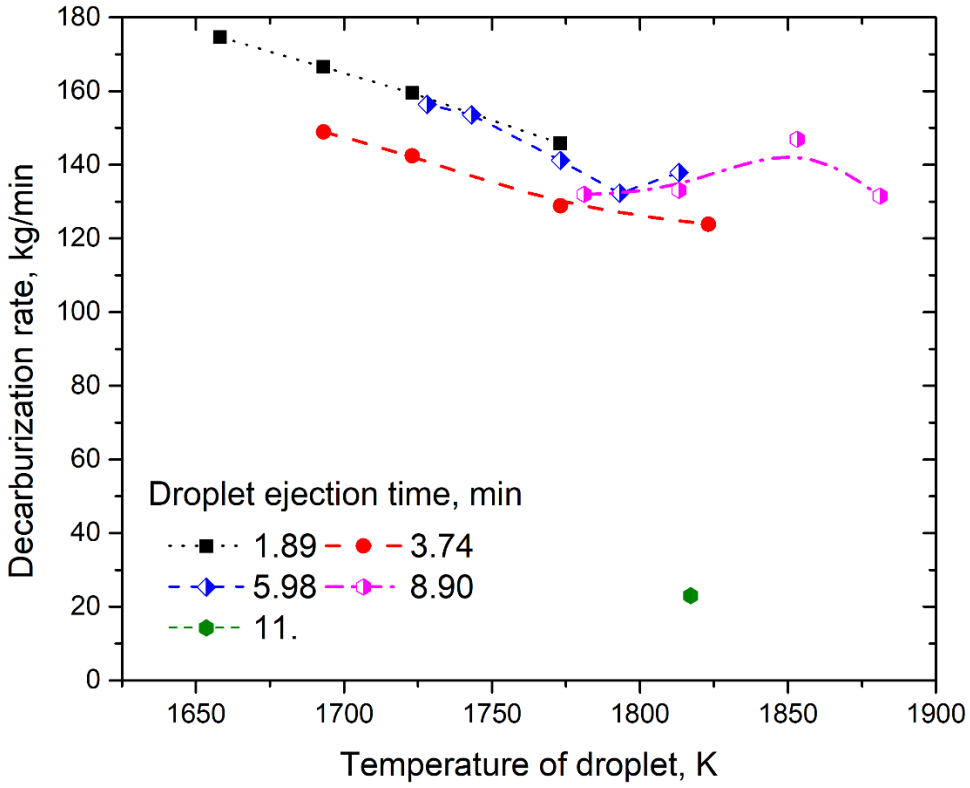

Fig. 4.11: Effect of droplet temperature on the total decarburization rate in the emulsion zone as a function of blow time

4.7 **Conclusions**

A mathematical model is developed to study the decarburization reaction within a single droplet and validated against experimental data available in open literature. Then the residence time and decarburization rate of a single droplet and total decarburization rate in the emulsion are predicted using industrial data reported by Cicutti et al.[6,48]. Some significant conclusions of the current model are as follows:

- The bloating behavior of metal droplets in the emulsion was represented theoretically by incorporating internal CO gas generation and CO gas escape. The

authors believe that this study is the most scientifically rigorous treatment of bloating behavior of droplets in open literature.

- This model enables to predict the carbon removal within dense and bloated droplets in the emulsion zone. In the first half of the blow, the droplets become bloated and their residence times range between 6 to 7.5 s as the initial carbon content of metal droplets is relatively high. Later in the blow, there is limited bloating (hence small residence time) when carbon content is below 1 wt % as the activity of carbon decreases. Therefore, droplets remain dense. These results indicate that the residence time of droplets in emulsion is more dependent on the carbon content of droplets as long as FeO content in the slag is not excessively low (below 8-10 wt %).
- The predicted decarburization rate in the emulsion zone is approximately 5 % (end blow) to 75 % (early blow) of total decarburization for the industrial operation of Cicutti et al.[6,48]. This represents a contribution of 20 % of total carbon removal using a defined droplet generation rate prescribed by Subagyo et al.'s [25] approach. The decarburization rate decreases with the progress of the blow and the increase in droplet generation does not adequately compensate for low decarburization per droplet. It is negligible towards the end of the blow (> 14 minutes).
- The current model provides a better understanding of decarburization reaction and confirms the importance of the bloated droplets presence in the emulsion zone. However the effect of variations in lance height and oxygen flow rate on the decarburization rate in cavity and emulsion zones remains as future work. These

parameters have significant influence on the droplet generation rate, droplet size distribution thereby decarburization rate. Incorporation of this model into the process model and validation of the process model is essential to help steelmakers gain a better understanding of the process and further optimize/control the industrial operations.

- The initial oxygen content of metal droplets has a minor effect on the onset of internal decarburization and a negligible effect on the decarburization rate. This makes employment of a higher bottom stirring rate favorable rather than an impediment to decarburization in emulsion zone.
- The increase in temperature of droplet reduces the decarburization rate.

Acknowledgements

The authors would like to thank Prof. Kenneth Coley, Dr. Kezhuan Gu and Mr. Tai Xi Zhu for fruitful discussions related to bloated droplet theory. This research was funded by the Natural Sciences and Engineering Research Council of Canada (NSERC), project number 20007117 and the McMaster Steel Research Centre (SRC).

4.8 Appendix

a. Calculation of interfacial activities of metal droplet components

The activity coefficients for carbon and oxygen can be calculated by taking into account the interaction parameters of carbon, oxygen and sulfur.

$$log\ f_C^r = e_C^C[wt\ pct\ C]^r + e_C^O[wt\ pct\ O]^r + e_C^S[wt\ pct\ S]^r \quad (4.A1)$$

$$log\ f_O^r = e_O^C[wt\ pct\ C]^r + e_O^O[wt\ pct\ O]^r + e_O^S[wt\ pct\ S]^r \quad (4.A2)$$

The Henrian activities of carbon and oxygen are defined by,

$$h_C^r = f_C^r [wt\ pct\ C]^r \quad (4.A3)$$

$$h_O^r = f_O^r [wt\ pct\ O]^r \quad (4.A4)$$

b. Evaluation of mole fraction and activity of (FeO)

The mole fraction of FeO at the droplet-slag interface is defined by the following equation

$$X_{FeO}^r = \frac{(wt\ pct\ FeO)^r}{M_{FeO}\left(\frac{wt\ pct\ FeO^r}{M_{FeO}} + \frac{wt\ pct\ SiO_2^r}{M_{SiO_2}} + \frac{wt\ pctMnO^r}{M_{MnO}}\right)} \quad (4.A5)$$

The Raoultian activity of FeO at the interface can be defined by,

$$a_{FeO}^r = \gamma_{FeO} X_{FeO}^r \quad (4.A6)$$

c. Balance of supply and consumption of oxygen at the interface.

The equilibrium constant for decarburization reaction is defined as

$$K_{CO} = \frac{P_{CO}^{ext}}{h_C^r h_O^r} \quad (4.A7)$$

The value of P_{CO}^{ext} is taken to be equal to 1.5 atm (equal to the pressure of the furnace).

$$K_{FeO} = \frac{a_{FeO}^r}{h_O^r} \quad (4.A8)$$

The equations 4.A7 and 4.A8 can be rearranged in terms of h_O^r and combined to arrive at the following equation

$$\frac{K_{FeO}}{a_{FeO}^r} = \frac{K_C h_C^r}{P_{CO}} \quad (4.A9)$$

NOMENCLATURE

A_d	Surface area of a metal droplet, (m^2) M_{FeO} is the
a_{FeO}	Raoultian activity of FeO in slag $(-)$
e_j^i	First order interaction parameter, of solute j on i
f_C, f_O, f_S	Henrian activity coefficients of carbon, oxygen and sulfur respectively.
h_C, h_O, h_S	Henrian activities of carbon, oxygen and sulfur respectively.
J_C, J_{FeO}, J_O	Flux of carbon, oxygen and FeO towards metal droplet-slag surface, $(\frac{moles}{s})$
J_{ext}, J_{int}	External and internal CO generation rates respectively, $(\frac{moles}{s})$
J_{esc}	Net escaped moles of CO gas at a given time step, $(moles)$
J_s	Nucleation rate, $(\frac{nuclei}{m^3.s})$
K_{CO}, K_{FeO}	Equilibrium constants for CO formation and FeO dissociation reaction
K_O, K_S	Adsorption coefficients of the oxygen and sulfur $(-)$
k_s, k_m	Slag and metal phase mass transfer coefficient, $(\frac{m}{s})$
$\vec{k}, \overleftarrow{k}$	Forward and backward reaction constants of FeO dissociation reaction $(-)$
m_d	Mass of metal droplet, (kg)
N_{CO}	Net retained moles of CO gas within a metal droplet, $(moles)$
$P_{CO}^{ext}, \Delta P_{CO}^{int}$	Supersaturation pressure for external(droplet surface) and internal CO gas generation (atm)
$t_{inst}, t_{res}, \Delta t$	Instantaneous time, residence time, time step respectively $(seconds)$
Δt_e	Time interval during which the emulsion zone decarburization is being evaluated
V_o	Initial volume of metal droplet, (m^3)

GREEK SYMBOLS

θ_S	Fraction of surface area poisoned by sulfur $(-)$
ρ_t, ρ_d	Apparent and initial density of metal droplet $(\frac{kg}{m^3})$
$\rho_g, \rho_s, \rho_{s-g}$	Densities of gas, slag and emulsion respectively $(\frac{kg}{m^3})$

σ, σ_{metal}	Surface tension of metal, $(\frac{N}{m})$
ϕ_g	Volume fraction of CO gas in the emulsion
ψ	Correction factor to the surface tension of the metal $(-)$

SUBSCRIPTS/SUPERSCRIPTS

r	Slag-metal interface
$s-g$	Emulsion

4.9 References

1 H.W. Meyer, W.F. Porter, G. Smith, and J. Szekely: *J. Met.*, 1968, vol. 20, pp. 35–42.

2 J. Schoop, W. Resch, and G. Mahn: *Ironmak. Steelmak.*, 1978, vol. 2, pp. 72–9.

3 R.C. Urquhart and W.G. Davenport: *Can. Metall. Q.*, 1973, vol. 12, pp. 507–16.

4 P. Kozakevitch: *J. Miner. Met. Metarials Soc.*, 1969, vol. 22, pp. 57–68.

5 D.J. Price: in *Process Engineering of Pyrometallurgy Symposium*, The Institution of Mining and Metallurgy, London, 1974, pp. 8–15.

6 C. Cicutti, M. Valdez, T. Pérez, R. Donayo, and J. Petroni: *Lat. Am. Appl. Res.*, 2002, vol. 32, pp. 237–40.

7 E.W. Mulholland, G.S. Hazeldean, and M. Davies: *J. Iron Steel Inst.*, 1973, vol. 211, pp. 632–9.

8 T. Gare and G.S. Hazeldean: *Ironmak. Steelmak.*, 1981, vol. 4, pp. 169–81.

9 H. Gaye and Riboud.P.V: *Metall. Trans. B*, 1977, vol. 8, pp. 409–15.

10 D.J. Min and R.J. Fruehan: *Metall. Trans. B*, 1992, vol. 23, pp. 29–37.

11 C.L. Molloseau and R.J. Fruehan: *Metall. Mater. Trans. B*, 2002, vol. 33, pp. 335–44.

12 E. Chen: Ph.D thesis, McMaster University, 2011.

13 E. Chen and K.S. Coley: *Ironmak. Steelmak.*, 2010, vol. 37, pp. 541–5.

14 M.D. Pomeroy: MASc Thesis, McMaster University, 2011.

15 K. Gu, N. Dogan, and K.S. Coley: *Metall. Mater. Trans. B Process Metall. Mater. Process. Sci.*, 2017, pp. 1–18.

16 K. Gu, N. Dogan, and K.S. Coley: *Metall. Mater. Trans. B*, 2017, vol. 48, pp. 2343–53.

17 K.S. Coley, E. Chen, and M. Pomeroy: in *Proceedings of the Extraction and Processing Division Symposium on Pyrometallurgy in Honor of David G.C. Robertson*, P.J. Mackey, E.J. Grimsey, R.T. Jones, and G.A. Brooks, eds., 2014, pp. 289–302.

18 H. Sun and G. Zhang: in *3rd International Congress on Science ans Technology of Steelmaking*, 2005, pp. 257–68.

19 N. Dogan, G.A. Brooks, and M.A. Rhamdhani: *ISIJ Int.*, 2011, vol. 51, pp. 1093–101.

20 N. Dogan: Ph.D thesis, Swinburne University, 2011.

21 R. Sarkar, P. Gupta, S. Basu, and N.B. Ballal: *Metall. Mater. Trans. B*, 2015, vol. 46, pp. 961–76.

22 B. Rout, G. Brooks, M.A. Rhamdhani, Z. Li, F.N. Schrama, and J. Sun: *Metall. Mater. Trans. B*, 2018, vol. 49, pp. 537–57.

23 B.K. Rout, G. Brooks, M. Akbar Rhamdhani, Z. Li, F.N.H. Schrama, and A. Overbosch: *Metall. Mater. Trans. B*, 2018, vol. 49, pp. 1022–33.

24 G. Brooks, Y. Pan, Subagyo, and K.S. Coley: *Metall. Mater. Trans. B*, 2005, vol. 36, pp. 525–35.

25 Subagyo, G. a. Brooks, K.S. Coley, and G. a. Irons: *ISIJ Int.*, 2003, vol. 43, pp. 983–9.

26 G.R. Belton: *Met.Trans.B*, 1976, vol. 7, pp. 35–42.

27 Y. Kawai and Y. Shiraishi: *Handbook of Physico-Chemical Properties at High Temperatures*, 1988.

28 M. Hino and K. Ito, eds.: *Thermodynamic Data for Steelmaking*, Tohoku University Press, Sendai, 2010.

29 G.K. Sigworth and J.F. Elliot: *Met. Sci.*, 1974, vol. 3, pp. 298–310.

30 E. Shibata, H. Sun, and K. Mori: *Metall. Mater. Trans. B Process Metall. Mater. Process. Sci.*, 1999, vol. 30, pp. 279–86.

31 L.A. Baker, N.A. Warner, and A.E. Jenkins: *Trans. Metall. Soc. AIME*, 1967, vol. 239, pp. 857–64.

32 P.A.A. Distin, G.D.D. Hallett, and F. D. Richardson: *J. Iron Steel Inst.*, 1968, vol. August, pp. 821–33.

33 N. El Kaddah and D.G. Robertson: *J. Colloid Interface Sci.*, 1977, vol. 60, pp. 349–60.

34 K. Mor, H. Sun, K. Ga, V. Sahajwalla, and R.D. Pehlke: *ISIJ Int.*, 1999, vol. 39, pp. 25–33.

35 K. Gao, V. Sahajwalla, H. Sun, C. Wheatley, and R. Dry: *ISIJ Int.*, 2000, vol. 40, pp. 301–8.

36 H.S. Levine: *Metall. Trans. B*, 1973, vol. 4, pp. 777–82.

37 P.G. Bowers, K. Bar-eli, and R.M. Noyes: *J. Chem. Soc. Faraday Trans.*, 1996, vol. 92, pp. 2843–9.

38 S.D. Lubetkin: *Langmuir*, 2003, vol. 19, pp. 2575–87.

39 C. A.W. and I. Jimbo: *Steel Res.*, 1989, vol. 60, pp. 157–65.

40 W. Cramb, W.R. Graham, and G.R. Belton: *Metall. Trans. B*.

41 K. Ogino, S. Hara, T. Miwa, and S. Kimoto: *Trans. ISIJ*, 1984, vol. 24, pp. 522–31.

42 R. Hongbin, M. Suzuk, D.R. Poirier, H. Yin, M. Suzuki, and T. Emi: *ISIJ Int.*, 1998, vol. 38, pp. 229–38.

43 P. Sahoo, T. Debroy, and M.J. McNallan: *Metall. Trans. B*, 1988, vol. 19, pp. 483–91.

44 Y. Chung and A.W. Cramb: *Metall. Mater. Trans. B*, 2000, vol. 31, pp. 957–71.

45 F.A. Halden and W.D. Kingery: *J. Phys. Chem.*, 1955, vol. 59, pp. 557–9.

46 K.S. Coley and T.X. Zhu: *Private Communication*, Hamilton, Ontario, 2018.

47 Subagyo and G.A. Brooks: *ISIJ Int.*, 2002, vol. 42, pp. 1182–4.

48 C. Cicutti, M. Valdez, T. Perez, J. Petroni, A. Gomez, R. Donayo, and L. Ferro: in *6th International Conference on Molten Slags, Fluxes and Salts*, Stockholm- Helsinki, 2000, p. 367.

49 N. Dogan, G.A. Brooks, and M.A. Rhamdhani: *ISIJ Int.*, 2011, vol. 51, pp. 1086–92.

50 P. Wei, M. Sano, M. Hirasawa, and K. Mori: *ISIJ Int.*, 1993, vol. 33, pp. 479–87.

51 M. Barati and K.S. Coley: *Metall. Mater. Trans. B*, 2006, vol. 37, pp. 41–9.

52 M.S. Millman, A. Kapilashrami, M. Bramming, and D. Malmberg: *Imphos : Improving Phosphorus Refining*, Luxemborg, 2011.

53 B. Deo and R. Boom: *Fundamentals of Steel Making Metallurgy*, Pretince Hall International, 1993.

54 B.K. Rout, G. Brooks, Subagyo, M.A. Rhamdhani, and Z. Li: *Metall. Mater. Trans. B*, 2016, vol. 47, pp. 3350–61.

55 K. Koch, J. Falkus, and R. Bruckhaus: *Steel Res. Int.*, 1993, vol. 64, pp. 15–21.

Chapter 5

Model development for refining rates in oxygen steelmaking: Cavity zone

Chapter 5 is the draft version of the article to be submitted for publication in immediate future. It is observed that during the early blow in oxygen steelmaking, desiliconization and FeO formation proceed at a rapid rate. The surface of the smooth cavities (impact zone) formed due to impact of jets on the bath surface was believed to be a significant contributor to these reactions. However, it has been found that impact zone contributes negligibly to these reactions as shown in Chapter 3. This finding leads to the possibility of these refining reactions thereby early slag formation occurring on the surface of droplets exposed to the oxidizing atmosphere of the jets. The chapter presents a model to explain the refining behavior of such 'cavity' droplets, which are splashed within the cavity zone and do not reach the emulsion zone. The model quantifies the contribution of the cavity zone to the overall refining in oxygen steelmaking and represents first such work reported in open literature. The original concept of this reaction zone was suggested by Dr. Kenneth Coley. The development of model, its coding, data analysis against industrial data as well as manuscript drafting was carried out by the primary author. Dr. Neslihan Dogan provided extensive discussion during model development. Dr. Wangzhong Mu, Dr. Dogan and Dr. Coley provided suggestions for improving the manuscript to its final form.

Abstract:

The prediction of early slag formation and refining in the oxygen steelmaking is critical to the progress of the blow and consistently achieving the target end-point composition. In the current study, a new reaction zone is proposed, which describes the competing oxidizing reactions within the metal droplets splashed in the cavity zone. The model is validated against experimental data. The predictions have been made for the refining of droplets in the cavity zone of a 200-t industrial oxygen steelmaking furnace. The sensitivity of various relevant parameters to cavity zone refining such as gas composition, size distribution, and the residence time of droplets has been investigated. The model explains the rapid slag generation due to FeO formation during the early blow. The cavity zone has been found to be a significant contributor to carbon refining particularly in the end-blow when the emulsion zone ceases to be an effective contributor to the overall refining. The model predicts that the cavity zone contribution ranges from 20 to 40 % for silicon, manganese, and 20 to 70 % for carbon during various times of blow.

5.1 Introduction

In the oxygen steelmaking process, the refining of liquid iron into steel of the desired composition takes place in a relatively short time. The refining reactions occur in several reaction zones[1] with each of the reaction zone having its unique characteristics. The impact zone is one such zone where the oxygen jets impinge upon the metal bath surface, thereby creating a number of cavities. This zone has been assumed to be a significant refining zone, and a few models have been presented to explain the refining reactions occurring at this zone[2–5]. However, in the authors' earlier work[6], it was demonstrated that

a small fraction of the overall refining reactions takes place in this zone during the oxygen steelmaking process. This leads one to question the source of the observed rapid refining of silicon and FeO formation, in other words, early slag formation, which is critical to the progress of subsequent refining reactions in the emulsion zone. A possible source of silicon removal and the FeO formation could be the surface of droplets splashed in the cavities (subsequently referred to as cavity droplets). To the best of authors' knowledge, the possibility of this phenomenon was first discussed in the study of Hammer et al.[7]. Later the experimental study by Koch et al.[8] sampled the 'sprayed' droplets generated due to the impact of oxygen jet on a hot-metal bath in an induction furnace. They observed that these droplets were significantly decarburized as compared to the metal bath. A recent laboratory study by Nordquist et al.[9] found that a decrease in droplet size increased the extent of decarburization and desiliconization and suggested that the refining would increase when the interfacial area between droplets and jets was generated. In the previous multi-zone models[3,5,10–13], the contribution of the cavity droplets to refining was not considered. This study proposes a mathematical model to quantify the contribution to refining of reactions involving droplets in the cavity. The effects of the droplet size distribution and the gas composition on the various refining reactions and FeO formation have been analyzed.

5.2 Experimental Studies on Droplet Behavior

To date, high temperature experiments have been carried out to study the refining behavior of Fe alloy liquid droplets in gaseous atmospheres[14–20]. In most of these studies, the droplets were levitated in the gaseous atmosphere[14–19] or suspended on a stationary metal plate[20]. Baker et al.[15] studied the decarburization rates of levitated Fe-C droplets (carbon

contents up to 5.5 wt %) in $O_2 - He$ gas mixtures at 1600°C. Based on the experimental measurements and calculations involving the effects of natural and forced convection, they concluded that the decarburization is entirely controlled by mass transport of O_2 in gas phase at high carbon contents (>1 wt%). Distin et al.[16] used a similar experimental set-up and investigated the effect of various gas atmospheres on the decarburization rate at approximately 1760°C. They measured the decarburization rate and the onset of FeO formation for droplets in pure O_2 and CO_2 over a range of flow rates. The reaction rate increased with increasing gas flow rate indicating that the reaction was controlled by mass transport in the gas phase. At approximately the same time as the FeO formation, these workers reported the occurrence of 'carbon boil,' which involved vigorous CO generation inside the metal droplet.

Some other researchers[14,18,19,21] focussed on the competing oxidizing reactions in levitated droplets. Robertson and Jenkins[14] studied the behavior of levitated Fe-Si, Fe-C and Fe-C-Si droplets in O_2 atmospheres at 1600°C. Further, the quenched droplets were analyzed using electron microscopy and chemical analyses. They observed that blobs of FeO rich slag nucleated on the surface, grew and coalesced and accumulated underneath the droplet. Sun and Pehlke[18,19] carried out an extensive experimental investigation of the oxidation behavior of levitated Fe-C-Si-Mn liquid alloy droplets in $CO \ / \ CO_2 \ / \ O_2 - N_2$ atmospheres for temperatures between 1575 and 1720 $°C$. They observed a preferential oxidation of carbon over silicon and manganese. The silicon and manganese oxidation reactions proceeded only after a significant carbon removal occurred. Their observations were fairly consistent over a range of temperature and composition of gas stream. They proposed that

the mass transport of oxidizing gas species in the gas phase is the rate limiting step during the major part of the experiment. The metal phase transfer of impurities such as C, Mn, and Si also contributed to rate control towards the end of the experiment when the concentration of the impurities decreased to values close to respective equilibrium values. They also presented a 'system reaction model' which involved description of fluxes in the metal, gas and iron oxide/slag phases as well as the chemical reaction at the droplet-gas interface. The model predictions agreed well with their experimental data. Sano and Matsushita[22] studied the desiliconization behavior of Fe-Si droplets with O_2 and CO_2 diluted with He. The controlling mechanism of the desiliconization reaction was attributed to the mass transport in the gas film surrounding the droplet. They observed a formation of FeO and SiO_2 deposits on the reaction tube. Widlund et al.[21] analyzed the behavior of the Fe-C-Si droplets in a He atmosphere with 10 and 20 % O_2 at temperatures of 1400 and 1660 $°C$. The compositions of the droplets were similar to the initial C (4 wt %) and Si (0.37- 0.71 wt %) contents in the oxygen steelmaking process. They observed that the onset of silicon oxidation only after the carbon content was below 0.6 wt % (20 % O_2) and 0.35 wt % (10 % O_2), respectively. These authors noted that the measured decarburization rates were lower than those predicted by their equilibrium calculations using ThermoCalc. These authors employed SEM to analyze the quenched droplets and reported that there was no visible oxide/slag layer surrounding the droplets. But they reported that a higher oxygen concentration up to 0.02 to 0.24 wt% at depths 0.5 to 1 μm through EDS analysis thus indicating the possibility of a thin oxide layer.

Apart from single droplet experiments, some researchers [8,9,23] sampled and analyzed the droplets generated under top blown oxygen jet on a metal bath. Kitamura et al.[23] injected inert gas and oxygen through the top lance and collected 'splash particles' (i.e., cavity droplets) generated in a 70 kg metal bath at 1823 K. The cavity droplets under oxygen blowing were found to be of a lower size and have undergone greater decarburization as compared the droplets generated under argon blowing conditions. Koch et al.[8] conducted a sampling study of droplets generated by blowing an oxygen jet on a 50 kg molten Fe-C bath. The metal droplets "sprayed" from the cavity were sampled at various points of the cross-section of the metal sampler during a blow. The analysis of sampled droplets showed lower carbon contents as compared to the bath. Nordquist et al.[9] sampled droplets generated from blowing oxygen jet on a 15 kg steel bath containing only C as well as both C and Si. They studied the degree of refining as a function of the size distribution of metal droplets. It should be noted that a slag layer was surrounding the droplets in both cases.

Both single droplet and sampling studies indicate that there is a considerable contribution to the refining of droplets exposed to oxidizing gases. In the current work, a mathematical model has been developed to quantify the refining behavior of the cavity droplets.

5.3 Model Description

The model framework suggested by Sun and Pehlke[18] was further modified in the current work. In the original model, mixed mass transport control was applied to the droplet-gas interface. The flux of metal and gas components and reaction rates at the interface were defined. The interfacial quantities were determined by solving these equations, followed

by updating the composition of the droplets. The kinetic model framework for the cavity droplet oxidation calculations is described in detail in sections 5.3.1- 5.3.4.

5.3.1 Reaction equilibria at the droplet-gas interface

The various reactions occurring at the cavity droplet-gas interface and their respective rate constants are presented in Table 5.1[18,24–26]. All the reactions below are considered in this study.

Table 5.1: Summary of reactions and respective equilibria at droplet-gas interface[18,24–26].

Reaction	**Equilibrium constant**	
Reactions for oxygen supply		
Oxygen decomposition $O_2 \leftrightharpoons 2[O]$	$ln\, K_O = ln\frac{a_O^{r\,2}}{p_{O_2}^r} = \frac{28171}{T} + 0.815$	(5.1)
Carbon dioxide decomposition $CO_2 \leftrightharpoons [O] + CO$	$\log K_{CO_2} = \log\frac{p_{CO}^r a_O^r}{p_{CO_2}^r} = -\frac{8718}{T} + 4.762$	(5.2)
Reactions for oxygen consumption		
Silicon oxidation $2[O] + Si \leftrightharpoons SiO_2$	$\log K_{Si} = \log\frac{\gamma_{SiO_2} X_{SiO_2}}{(a_O^r)^2 a_{Si}^r} = \frac{30110}{T} - 11.4$	(5.3)
Manganese oxidation $[O] + [Mn] \leftrightharpoons MnO$	$\log K_{Mn} = \log\frac{\gamma_{MnO} X_{MnO}}{a_O^r a_{Mn}^r} = \frac{12760}{T} - 5.62$	(5.4)
Iron oxidation $[O] + [Fe] \leftrightharpoons FeO$	$\log K_{Fe} = \log\frac{\gamma_{FeO} X_{FeO}}{a_O^r a_{Fe}^r} = \frac{6150}{T} - 2.604$	(5.5)

where K represents the equilibrium constant of the respective reaction, 'a' represents the activity of the slag or metal component, and the superscript 'r' represents the gas-metal interface.

5.3.2 **Metal phase mass transfer**

The fluxes of metal impurities and iron (mol/s) towards the gas-metal interface are defined by Fick's first law as follows:

Table 5.2: A list of flux equations for solutes within a metal droplet

$J_O = \frac{A_d k_m \rho_m}{100 M_O}([O] - [O]^r)$			(5.6)
$J_C = \frac{A_d k_m \rho_m}{100 M_C}([C] - [C]^r)$			(5.7)
J_{Si}	$= 0$	$if\ [O]^r \leq [O]_{Si}$	(5.8)
	$= \frac{A_d k_m \rho_m}{100 M_{Si}}([Si] - [Si]^r)$	$if\ [O]^r > [O]_{Si}$	
J_{Mn}	$= 0$	$if\ [O]^r \leq [O]_{Mn}$	(5.9)
	$= \frac{A_d k_m \rho_m}{100 M_{Mn}}([Mn] - [Mn]^r)$	$if\ [O]^r > [O]_{Mn}$	
J_{Fe}	$= 0$	$if\ [O]^r \leq [O]_{Fe}$	(5.10)
	$= J_{FeO}$	$if\ [O]^r > [O]_{Fe}$	

where J_O, J_C, J_{Mn}, J_{Si} and J_{Fe} are the flux of O, C, Mn, Si, and Fe (mol/s), respectively. k_m is the metal phase mass transfer coefficient of the elements (cm/s), ρ_m is the density of metal droplet ($\frac{g}{cm^3}$), A_d is the area of a droplet (cm^2), [ ] represents the concentration of an element in the metal droplet (wt %), $[\,]^r$ represents the interfacial concentration of a component, M represents the atomic weight of the individual components.

Constraints are imposed on the oxidation of silicon, manganese, and iron wherein the elements oxidize only when the interfacial concentration of oxygen $[O]^r$ is higher than the oxygen concentration in equilibrium with the respective elements such as

$[O]_{Si}, [O]_{Mn}, [O]_{Fe}$ and their oxides. Their values are calculated from the equilibrium equations (Eqs. 5.3, 5.4 and 5.5) using the metal composition. If the interfacial oxygen content obtained from Eq. 5.14 is smaller than the equilibrium oxygen content of the component, the oxidation of the element does not occur, and the flux of the element across the metal-gas interface is zero, as seen in Eqs. 5.8 through 5.10.

The thermodynamic activities of the metal components at the droplet-slag interface are defined through the following equations[1] :

$$h_C^r = f_C^r [wt\ \%C]^r \quad (5.11)$$

$$h_{Si}^r = f_{Si}^r [wt\ \%Si]^r \quad (5.12)$$

$$h_{Mn}^r = f_{Mn}^r [wt\ \%Mn]^r \quad (5.13)$$

$$h_O^r = f_O^r [wt\ \%O]^r \quad (5.14)$$

where the activity coefficient of the component 'X' at the interface, f_X^r is calculated using the equations[1], described in Appendix 5.9A.

5.3.3 Gas phase mass transfer

The transfer of gas species through a gas film surrounding the metal droplet can be described using the following equations.

$$J_{O_2} = \frac{A_d k_{O_2}}{RT}\left(p_{O_2} - p_{O_2}^r\right) \quad (5.15)$$

$$J_{CO} = \frac{A_d k_{CO}}{RT}\left(p_{CO}^r - p_{CO}\right) \quad (5.16)$$

$$J_{CO_2} = \frac{A_d k_{CO_2}}{RT}\left(p_{CO_2} - p_{CO_2}^r\right) \quad (5.17)$$

where $k_{O_2}, k_{CO}, k_{CO_2}$ are the gas phase mass transfer coefficients for individual gas species. The methodology[18] for the calculation of the mass transfer coefficient for oxygen is explained in the section 5.4.1. $p^r_{O_2}, p^r_{CO_2}, p^r_{CO}$ are the partial pressures of the gas species at the interface and evaluated through solution of non-linear equations as described at the end of section 5.3.5. The terms $p_{O_2}, p_{CO_2}, p_{CO}$ represent the partial pressures of the respective gas species in the cavity. The methodology of calculation is explained in Appendix 5.9B.

5.3.4 Slag formation

In this study, it is assumed that a thin slag layer is formed surrounding a metal droplet and followed by trickling down underneath the droplet, as stated in section 5.5. In this layer, the slag components are FeO, MnO and SiO_2. If an insignificant barrier to mass transport in the slag layer is assumed then the rate of oxidation of iron, silicon, and manganese (mol/s) is equal to the formation of corresponding oxides

$$J_{Si} = J_{SiO_2} \tag{5.18}$$

$$J_{Mn} = J_{MnO} \tag{5.19}$$

It is important to note that no composition gradient is considered within the slag layer. The moles of FeO formed at each time instant 't' is evaluated from the solution of the equation below

$$M_{FeO}(t) = (1 - H) * J_{FeO} * t_{step} \tag{5.20}$$

where H is the hindrance factor which limits the FeO formation and is explained in the assumptions section. The total slag formed (moles) (on a single droplet) is updated at each time step as given by,

$$m_{slag}(t) = m_{slag}(t-1) + M_{FeO}(t) + M_{SiO_2}(t) + M_{MnO}(t) \quad (5.21)$$

The total slag generated in the cavity zone will be a sum of slag formed on all the droplets of various sizes. In addition, the total amount of slag components formed is calculated for each time step through the following equations.

$$T_{FeO} = T_{FeO} + M_{FeO}(t) \quad (5.22)$$

$$T_{SiO_2} = T_{SiO_2} + M_{SiO_2}(t) \quad (5.23)$$

$$T_{MnO} = T_{MnO} + M_{MnO}(t) \quad (5.24)$$

The mole fractions $X_{FeO}, X_{SiO_2}, X_{MnO}$ are calculated at each time step as follows:

$$X_{FeO} = \frac{T_{FeO}}{m_{slag}(t)} \quad (5.25)$$

$$X_{SiO_2} = \frac{T_{SiO_2}}{m_{slag}(t)} \quad (5.26)$$

$$X_{MnO} = \frac{T_{MnO}}{m_{slag}(t)} \quad (5.27)$$

The values of $X_{SiO_2}, X_{MnO}, X_{FeO}$ evaluated at a given time instant are used for the calculation of respective equilibria in equations 5.3, 5.4 and 5.5, respectively.

5.3.5 Mass balance equations

Apart from mass balances for silicon and manganese at the droplet-gas interface, the balances for oxygen and carbon can be described as follows:

Oxygen balance

The supply of oxygen occurs through dissociation of gas species O_2 and CO_2 at the droplet surface (given by equations 5.1 and 5.2, respectively) producing atomic oxygen. This atomic oxygen is then consumed for the oxidation of C, Si, Mn, and Fe. In addition, some of the oxygen gets dissolved in the metal droplet. The oxygen balance at the metal droplet surface can be written as follows,

$$2J_{O_2} + 2J_{CO_2} = J_O + J_{CO} + J_{Mn} + J_{FeO} + 2J_{Si} \tag{5.28}$$

Carbon balance

Similarly, the supply of carbon at the droplet surface takes place through the flux of carbon from the bulk of metal droplet and flux of CO_2 through a gas film surrounding the metal droplet (given by equation 5.17) and consumption of this carbon to produce CO gas (moles/s).

$$J_{CO_2} + J_C = J_r \tag{5.29}$$

where J_r is the CO gas formed due to the consumption of carbon (moles/s), such that

$$J_r = J_{CO} \tag{5.30}$$

The rate of oxidation of carbon (moles/s) is equal to

$$J_r = k_a A_d (pO_2 + pCO_2) \tag{5.31}$$

The overall rate constant, k_a ($\frac{mol}{cm^2.s.atm}$) for carbon oxidation is given by [12],

$$k_a = \frac{1}{\frac{1}{k_{fa}} + \frac{1}{k_{O_2}}} \tag{5.32}$$

where k_{fa} is the rate constant for the reaction of carbon in liquid iron[27] with oxidizing gases like O_2 and CO_2 is given by,

$$k_{fa} = \frac{k_f}{1 + K_S[S]} \tag{5.33}$$

where k_f is the chemical rate constant for pure iron and K_S is the adsorption coefficient of

$$\log K_S = \frac{3870}{T} + 0.51 \tag{5.34}$$

sulfur, which is a function of temperature given by the following relationship.

The sixteen interfacial quantities $[\%C]^r, [\%Si]^r, [\%Mn]^r, [\%O]^r, h_C^r, h_{Si}^r, h_{Mn}^r, h_O^r, \log f_C^r$, $\log f_{Si}^r$, $\log f_{Mn}^r$, $\log f_O^r, pCO_2^r, pO_2^r, pCO^r, J_{FeO}$ are determined through solution of 16 non-linear equations, namely, equilibrium relations (5.1), (5.2), (5.3) through (5.5), mass balance equations (5.28) and (5.29), activity relations (5.11) through (5.14) and relationship for activity coefficients (5.A1) through (5.A4) and carbon oxidation relation (5.30). With the knowledge of these interfacial quantities, the extent of refining and slag formation at every time step can be evaluated.

5.4 Evaluation of Mass Transfer Coefficients

5.4.1 Gas phase mass transfer coefficient[18]

The mass transfer coefficient of oxygen in the gas phase can be calculated using the Sherwood number correlation proposed by Ranz and Marshall.[28] The correlation is valid for forced convection around a sphere

$$Sh_{O_2} = 2 + 0.6Re^{0.6}Sc^{0.33} \tag{5.35}$$

$$k_{O_2} = \frac{D_{O_2-O_2}Sh_{O_2}}{d_d} \tag{5.36}$$

where d_d is the droplet diameter, (cm).

5.4.2 Metal phase mass transfer coefficient

The metal phase mass transfer coefficient is calculated using Higbie's penetration theory[29] as employed by Brooks et al.[30] for droplets suspended in the emulsion phase. The mass transfer coefficient k_i for an element $i = Si,\ Mn$ and C in a droplet is given by,

$$k_i = 2\sqrt{\frac{D_i v_d}{\pi d_d}} \tag{5.37}$$

where v_d is the ejection velocity of the droplet (m/s), and D_i is the diffusion coefficient of element i in liquid iron.

5.5 Model Assumptions

Based on the experimentally observed behavior of droplets in various studies, the following assumptions are made.

1. A cavity droplet is assumed to begin life with the instantaneous composition of the metal bath.
2. For a given time instant, every droplet of a given size undergoes similar refining behavior.
3. Every droplet is devoid of slag cover when it is first splashed in the cavity.
4. Initially, the slag layer is formed across the interface of the droplet exposed to the oxidizing gases. It consists of FeO, MnO and SiO_2. The activities of SiO_2 and MnO are calculated based on assumed mole fractions X_{SiO_2} = 0.05 and X_{MnO} = 0.05 since the relative amount of silicon and manganese as compared to iron in the hot-metal is tiny. At the next time instant, the individual component activities are calculated based on the respective mole fractions in the slag layer and the activity coefficients.

Later the slag trickles down across the surface droplet thus, hindering only a fraction of the gas-metal droplet interface and preventing further contact with gas at that limited area. The effect of this partial hindrance of the slag layer is considered only for FeO formation. The reason for this is that FeO is a significant component of the slag layer surrounding the droplet. Other gas-metal reactions are not affected by the hindrance as they are sustained by the oxygen supply from FeO formed on the surface of the droplet. The hindrance factors increase as the droplet size decreases as the A/V ratio for smaller droplets is higher as compared to larger droplets and thus entail more significant slag formation. The proposed hindrance factors are as follows

Table 5.3: Hinderance factors for various droplet sizes

Droplet size, mm	4	3	2	1	0.5
Hinderance factor, H, (-)	0.05	0.15	0.3	0.4	0.65

5. Depending upon the ejection angles and velocities of the droplet, the residence of droplets in cavities can be calculated using the ballistic motion model proposed by Brooks et al.[30]. For an ejection velocity of 1.2 m/s, the change of residence times is calculated as shown in the following figure. The residence time of cavity droplets decreases with a decrease in the droplet size and an increase in the ejection angle. However, a negligible difference in residence time with a variation of droplet size is found.

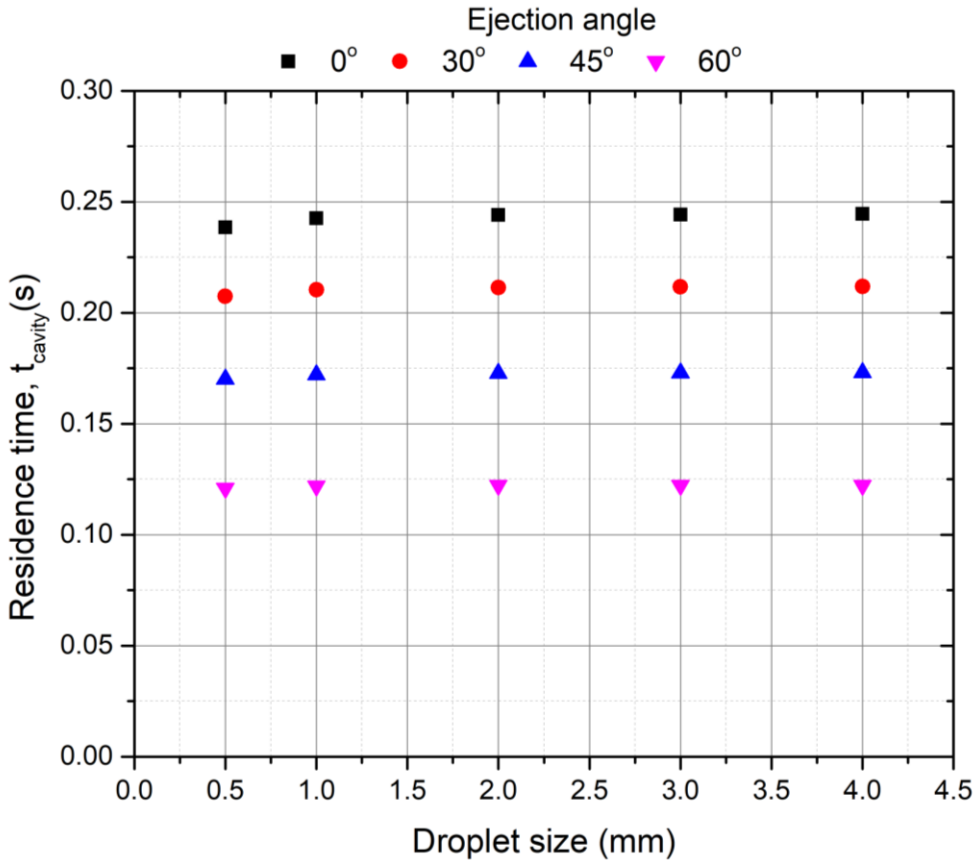

Figure 5.1: Variation of residence times of cavity droplets as a function of ejection angle and droplet sizes calculated using a ballistic droplet motion model

Considering the predictions for Figure 5.1, a uniform residence time of 0.15 seconds is assumed for all the droplets in the current study. The time step is chosen to be 0.01 seconds for the calculations.

6. The droplet generation rate in the cavity is taken to be 15000 kg/min during the first 5 minutes of the blow and 30000 kg/min during the subsequent part of the blow when the lance height is lowered. A decrease in lance height would lead to an increase in droplet generation. The proposed droplet generation rate is greater than that originally predicted by Subagyo et al.[31]. In recent studies, it is found that the droplet generation rate should

be greater to predict the refining rates in the oxygen steelmaking process. These studies were validated against an industrial practice.

7. The size distribution of droplets is calculated from the RRS (Rosin-Rambler-Sperling) distribution based on the analysis of the size distribution of droplets sampled in the pilot plant and industrial trials[32–34]. For Cicutti et al. operations,[34,35] a droplet size ranging between 0.5 and 4 mm is considered in the current study.
8. At the start of the blow, the initial gas composition in the cavity is taken as pure oxygen and subsequently with the progress of decarburization reaction, CO and CO_2 are introduced into the gaseous atmosphere. While the oxygen flow rate through the lance nozzles is known, the amount of entrained $CO\ and\ CO_2$ gases can only be estimated. It would be a function of lance height, as the degree of jet expansion would decrease with a decrease in lance height. Based on the prevailing post-combustion ratio ($\frac{pCO_2}{pCO+pCO_2}$) of 0.15, the cavity gas composition for various degrees of entrainments can be calculated. The sample calculation of gas composition in the cavity is provided in Appendix B. Hence, pO_2 can range from 0.45 to 0.77 while pCO varies between 0.2 and 0.4 and pCO_2 varies between 0.03 and 0.08.

5.6 Results and Discussion

5.6.1 Validation

The proposed model was validated against the results of Sun and Pehlke[18] based on the levitated droplet experiments for different oxidizing gas mixtures and a gas flow rate of 500 mL/min. The reaction time ranged from 60 to 80 seconds. The carbon content of metal droplets varied from 3.10 to 3.39 wt %, whereas silicon content ranged between 0 and 2 wt

%, manganese content was from 0 to 0.36 wt %, and sulfur content was from 0.002 to 0.5 wt %. The weight of the liquid iron droplets varied between 1.0 and 1.6 gram. The simultaneous oxidation of [C], [Si], and [Mn] was measured during various times of the experiments under different PO_2 and PCO_2 mixtures. In the case of levitated droplet for validation, the value of the mass transfer coefficient suggested by Mori et al.[36] and employed by Pehlke et al.[19] was used. The experimental results were compared with model predictions in Figure 5.2 Figure 5.2 . The data points represent experimental results where dash lines represent model predictions. In the experiments, the authors observed that silicon and manganese oxidations started only after the carbon content decreased below 0.5 wt %. Similar results were predicted by the current model. This is due to the condition (explained in section 5.3.2) for the oxidation of silicon, manganese and iron (equations 5.8 and 5.10). The model predictions for decarburization agree well with the experimental results. Further, the onset of silicon and manganese oxidations is predicted reasonably well except for medium carbon droplet (Figure 5.2 d). This comparison indicates that the proposed model can predict reasonably well for competing oxidation reactions under various oxidizing atmospheres. The accurate predictions particularly for the initial part of the experiment suggests that the model is suited for application in oxygen steelmaking wherein the droplet will be in contact with the gas atmospheres for a fraction of a second.

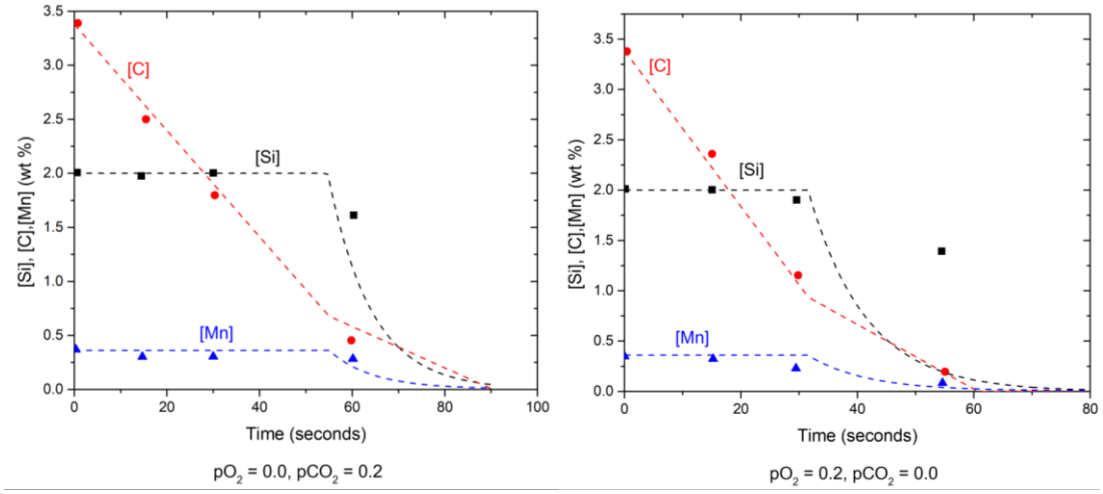

(a) (b)

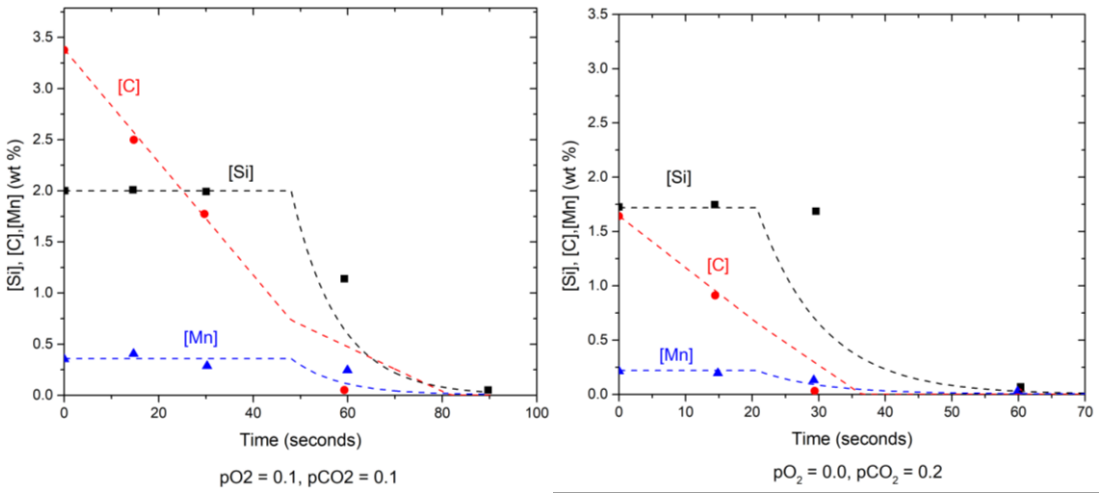

(c) (d)

Figure 5.2 : Comparison of metal droplet composition predicted by the proposed model and experimental data[18] as a function of time and different gas atmospheres, (a) $pO_2 = 0, pCO_2 = 0.2$, *(b)* $pO_2 = 0.2, pCO_2 = 0.0$, *(c))* $pO_2 = 0.1, pCO_2 = 0.1$, *(d))* $pO_2 = 0, pCO_2 = 0.2$.

5.6.2 **Refining behavior of single droplet**

The refining behavior of droplet is sensitive to droplet size as the smaller droplets have a higher area to volume (A/V) ratio, and a greater surface area for refining reactions is generated for the same volume (or mass) of metal. The refining behavior of the cavity droplets of different sizes ejected during different times of the operation reported by Cicutti et al.[27,100] are presented in Figure 5.3, 5.4, and 5.5. The initial and final temperatures of the bath are taken from the reported values of Cicutti et al., and the temperatures for the intermediate blow are calculated through linear extrapolation between the initial and final temperatures.

It is observed that the final concentrations of carbon, silicon, and manganese decrease with a decrease in droplet size even for the short residence time of 0.15 seconds. This indicates that the refining of metal droplets increases with a reduction in droplet size. The term 'refining percentage' is introduced to quantify the extent of the refining of various elements in the droplets. It is defined as

$$Refining\ percentage = 100 * \left(\frac{X_i - X_f}{X_i}\right) \tag{5.38}$$

where X_i and X_f are respectively the initial and final contents (wt %) of an element $X = C, Si, Mn$ in a droplet. The 'refining percentage' (wt %) increases with the decrease in size and an increase in (A/V) ratio of the droplet. As seen in Figure 5.3, the refining of carbon is lower compared to silicon and manganese due to the poisoning effect of sulfur. The refining percentage of carbon increases from 1.67 % for the largest droplet (4 mm) to 14.60 % for the smallest droplet (0.5 mm), as seen in Figure 5.3(d). The silicon refining in a single

droplet is shown in Figure 5.3 (b) at the start of the blow, with the initial content of droplets being 0.33 wt %. The refining percentage rate of silicon is approximately 15 % for the largest droplet, whereas it is significantly higher (~80%) for 1mm droplets and almost complete refining (~99 %) for 0.5 mm droplets. As seen in Figure 5.3(c), similar refining behavior and refining percentages are observed for manganese as for silicon with respect to droplet sizes. A near-complete removal (refining percentage> 99 %) of manganese is found even before the completion of residence time by 0.5 mm droplet, whereas a refining rate of 15 % is seen for the 4 mm droplet. The predicted refining behavior of the droplets generated in the cavity is different from those measured by Sun and Pehlke[18]. Their predictions were shown in Figure 5.2. Simultaneous oxidation of carbon, silicon, manganese, and iron is observed for droplets in the cavity zone, whereas Sun and Pehlke[18] observed that only after the carbon concentration is decreased to a low level, the oxidation of other elements commences. The origin of this anomaly lies in the different process conditions, firstly the gas flow rate is much higher in oxygen steelmaking conditions ($< 620 \frac{Nm^3}{s}$) than in the experiment ($0.5\ to\ 2 \times 10^{-3}\ \frac{Nm^3}{s}$). This results in higher (two order) gas phase mass transfer coefficients in the converter than in the experiment. Secondly, the oxidizing power of the gas in oxygen steelmaking is much higher $(pO_2 + pCO_2) \geq 0.54$ compared to the experimental condition $(pO_2 + pCO_2) = 0.2$. This leads to a higher oxygen concentration at the droplet-gas interface leading to a prediction of rapid oxidation of all the elements in the metal droplet as compared to the experiments.

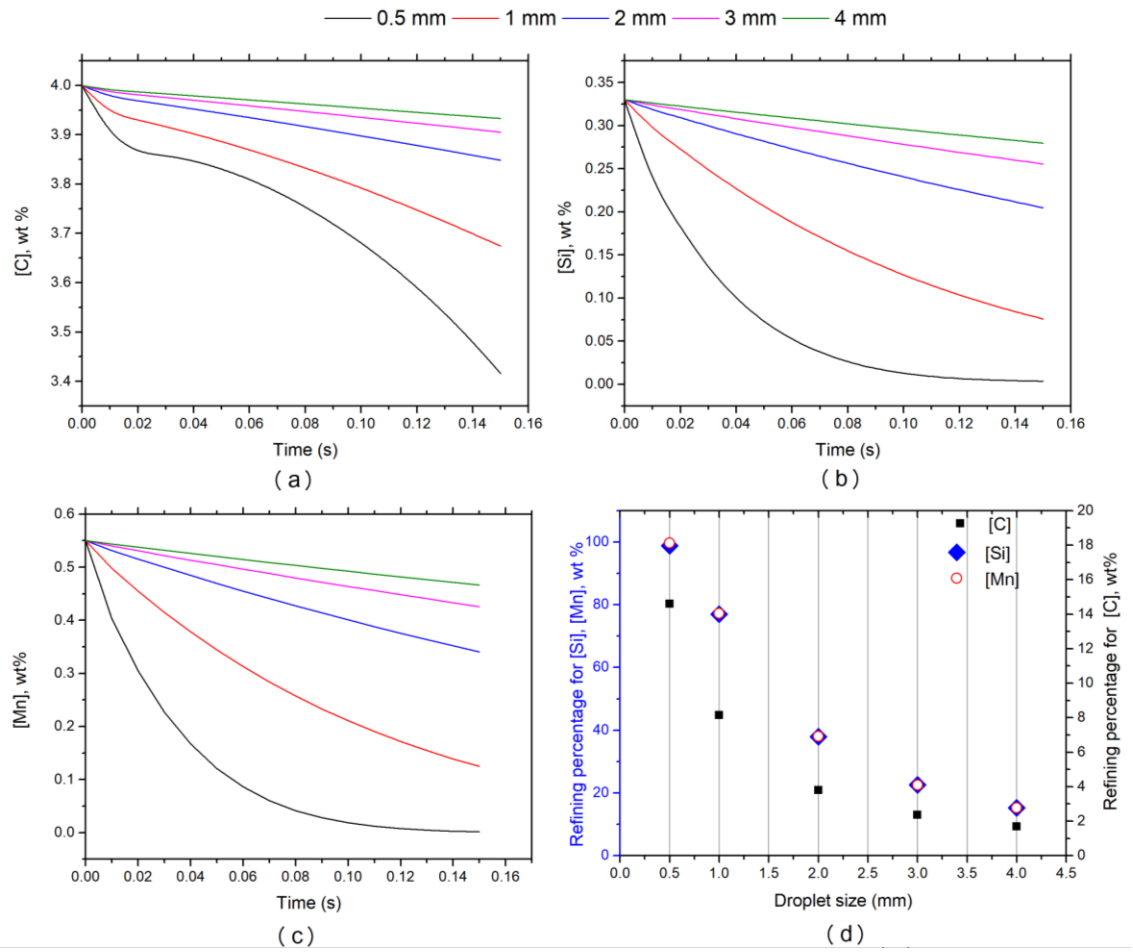

Figure 5.3: Refining of cavity-droplets of various sizes at the start of the blow of Cicutti et al. (t = 0 min, T = 1350 °C) for (a) Carbon, (b) Silicon and (c) Manganese (d) 'Percentage refining' achieved by droplets of various sizes.

The refining behavior of the carbon as a function of cavity-droplet size in the middle and end of the blow is shown in

Figure 5.4. The droplets show greater refining than that observed in the early blow, as seen in Figure 5.3(a). This is due to the effect of temperature on the poisoning effect of sulfur. The adsorption coefficient of sulfur decreases with an increase in temperature as the blow

progresses (refer eq. 5.34). This leads to a decrease in the poisoning effect and a corresponding increase in the decarburization of droplets. The extent of refining increases with the reduction in the size of droplets. In the case of a droplet size of 0.5 mm ejected in the middle of the blow, the carbon content decreases to a negligible value. At the same time, larger droplets also show higher carbon refining than the droplets of similar size at the start of the blow (refer Figure 5.2 (d)). As seen in Figure 5.3(b), the refining percentages for the middle blow are higher than that of a respective sized droplet at the start of the blow. The refining percentage of 0.5 mm droplet is nearly 100 %. As seen in Figure 5.3(c), near-complete refining is predicted for ejected cavity-droplets of all sizes at the end of the blow. The carbon is reduced to a negligible level even before the end of residence time.

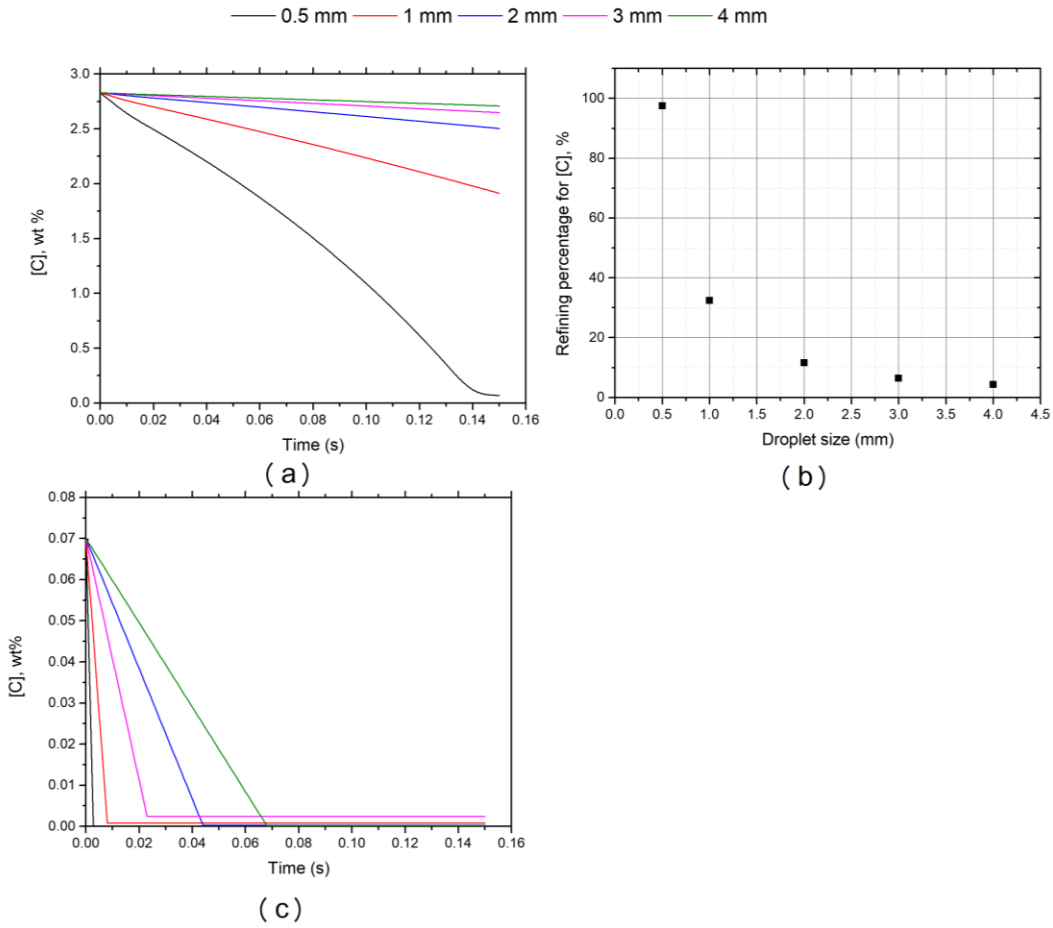

Figure 5.4: (a) Carbon refining in the middle of the blow (t = 6 min, T = 1455 °C), (b) Refining percentage of carbon as a function of cavity-droplet size in the middle of the blow (c) Carbon refining in the end of the blow (t = 16 min, T = 1630 °C)

As reported by Cicutti et al., silicon and manganese are removed by 5 min into the blow. Hence the refining behavior of silicon and manganese is not considered. Manganese reversion occurs towards the end of the blow. Therefore manganese refining is regarded at the end of the blow, as shown in Figure 5.5. It is observed that the manganese content of the droplets decreases with decreasing droplet size, and complete refining is observed for

a 0.5 mm droplet. The refining percentage of droplets for manganese is nearly the same as that of the same sized droplets in the early part of the blow.

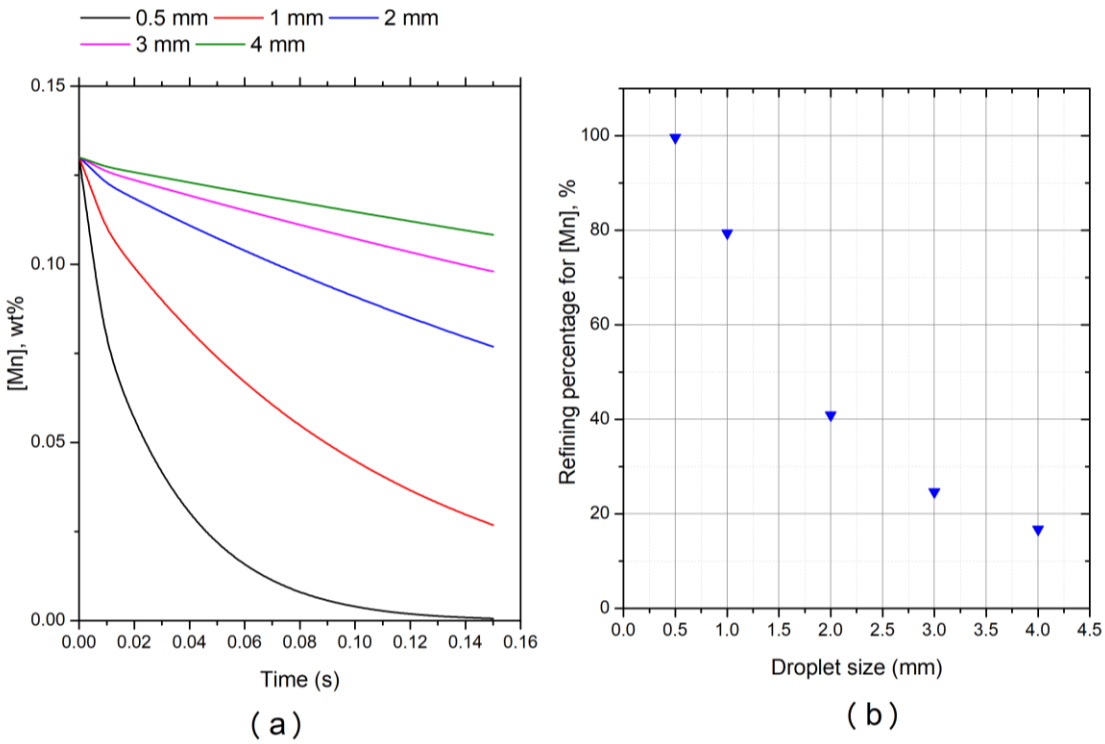

Figure 5.5: (a)Manganese refining of a cavity-droplet, and (b) Refining percentage of manganese at the end of the blow (t = 16 min, T = 1630 ^{o}C)

Another important aspect of metal droplet refining in a cavity zone is the formation of the iron oxide. An optimum FeO formation is important from the perspective of steelmakers to sustain the sufficient decarburization and dephosphorization in the emulsion zone, particularly in the early part of the blow. It is also vital to early slag formation, which is important to phosphorus refining. However, in the middle and end of the blow, the decarburization in the emulsion zone subsides, and the excessive amount of FeO formation leads to a loss in the yield of the liquid steel and excessive refractory wear. Figure 5.6

compares the amount of FeO formed per unit droplet mass in the cavity as a function of blow time and droplet size. F_d represents the ratio between FeO formed and the initial mass of a single droplet in gram during the residence time of a droplet. The value of F_d rises with a decrease in droplet size because the (A/V) ratio of the smaller droplets is higher, as stated earlier. One significant point to be noted is that the values of F_d for the same droplet size at the end blow are significantly smaller than those in early and middle blows. This is because of the effect of increasing temperature with the progress of the blow, causing a decrease in the equilibrium constant, K_{Fe} (refer Equation 5.5).

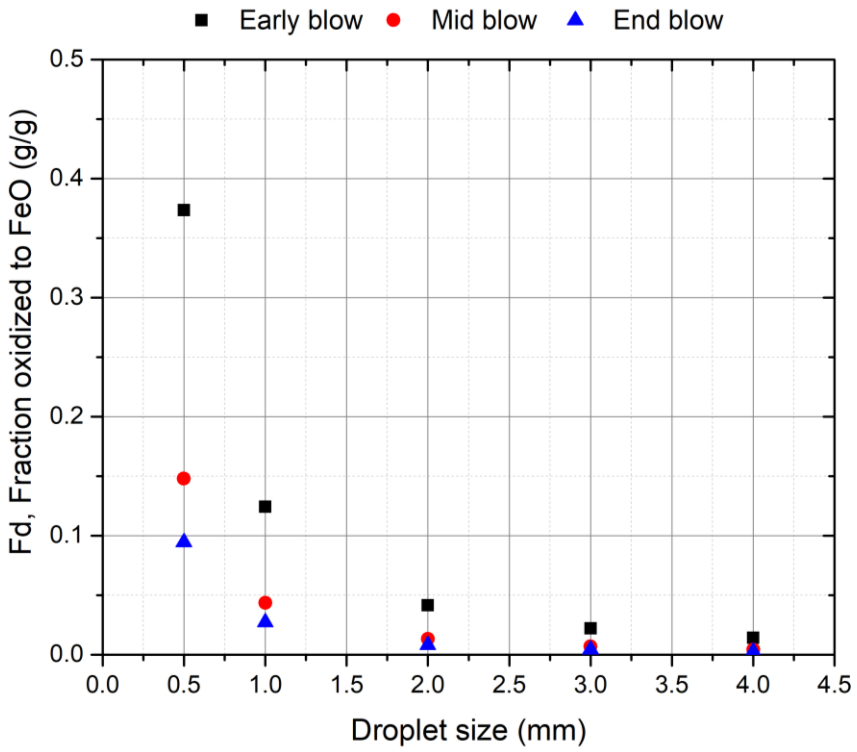

Figure 5.6: FeO formation ratio, F_d, (g/g) for various cavity-droplet sizes as a function of start of the blow (t = 0 min , T = 1350 °C) , middle of the blow (t = 6 min , T = 1455 °C), and end of the blow (t = 16 min, T = 1633 °C)

5.6.3 Contribution of Cavity Zone to Overall Refining of BOF operation

The amount of an impurity $X(C, Si, Mn)$ (in kg) in the cavity zone through the droplets of various sizes ejected between time instants $'t-1'$and 't' is given by

$$\left(X_{refined}\right)_t = \sum_{i=1}^{5}\left(n_{droplets}\right)_i \sum_{t-1}^{t}(wtX)_{i,t_{cav},} \tag{5.39}$$

Where the $(wtX)_{i,t_{cav},}$ (in kg) represents the amount of impurity X refined in a single droplet of size $'i'$ during its residence time t_{cavity} in cavity zone and $\left(n_{droplets}\right)_i$ represents the number of droplets of size 'i' between the time instants. The number '5' represents the five distinct sizes of droplets (from 0.5, 1, 2, 3, and 4 mm) considered in the current study.

The residual amount of impurity in the bath $(X_{bath})_t$ (kgs) due to refining is given by

$$(X_{bath})_t = (X_{bath})_{t-1} - \left(X_{refined}\right)_t \tag{5.40}$$

The new composition of X in the bath (wt % due to refining in the cavity at time $'t-1'$ and $'t'$ of the blow is given by

$$X_t = \frac{(X_{bath})_t}{(W_{bath})_t} \times 100 \tag{5.41}$$

When the value of X_t(represents the bath composition brought about by the refining cavity zone) is evaluated, the net contribution of the cavity zone for the refining of C, Si, and Mn between time instants '$t-1$' and 't' of the blow, can be calculated using the following equation. For this purpose, the industrial data reported by Cicutti et al.[27,100] is used.

$$Contribution\ of\ cavity\ (\%)\ = 100 \times \frac{(X_{t-1} - X_t)}{(X_{t-1} - X_{measured-t})} \tag{5.42}$$

The values of X_{t-1} and $X_{measured-t}$ are derived from the extrapolation of measured data of Cicutti et al.[34]. Figure 5.7 compares the change in the silicon content of cavity droplets with those reported by Cicutti et al. along with the contribution of the cavity to the overall refining of silicon. The silicon refining in the cavity zone increases with time. However, the decrease in total Si content is steeper than that in the cavity zone. In other words, the contribution of the cavity zone is 30 % in the first min of the blow, followed by a decrease to 10% at the 4th min of the blow. After this point, the silicon refining is completed. This finding indicates that the contribution of other zones becomes more critical. In previous work[37] of the authors, it was demonstrated that the emulsion zone has sufficient oxygen (through slag FeO) to sustain refining reactions of other elements like silicon and manganese in addition to that of carbon. These droplets get suspended in the emulsion zone due to bloating, and this allows for the refining reactions to proceed. Also, in other work by the authors[6], a specific contribution of the impact zone (smooth cavity surfaces) and the interface between metal bath and slag (slag-metal bulk zone) was also shown to contribute to the refining of silicon and manganese.

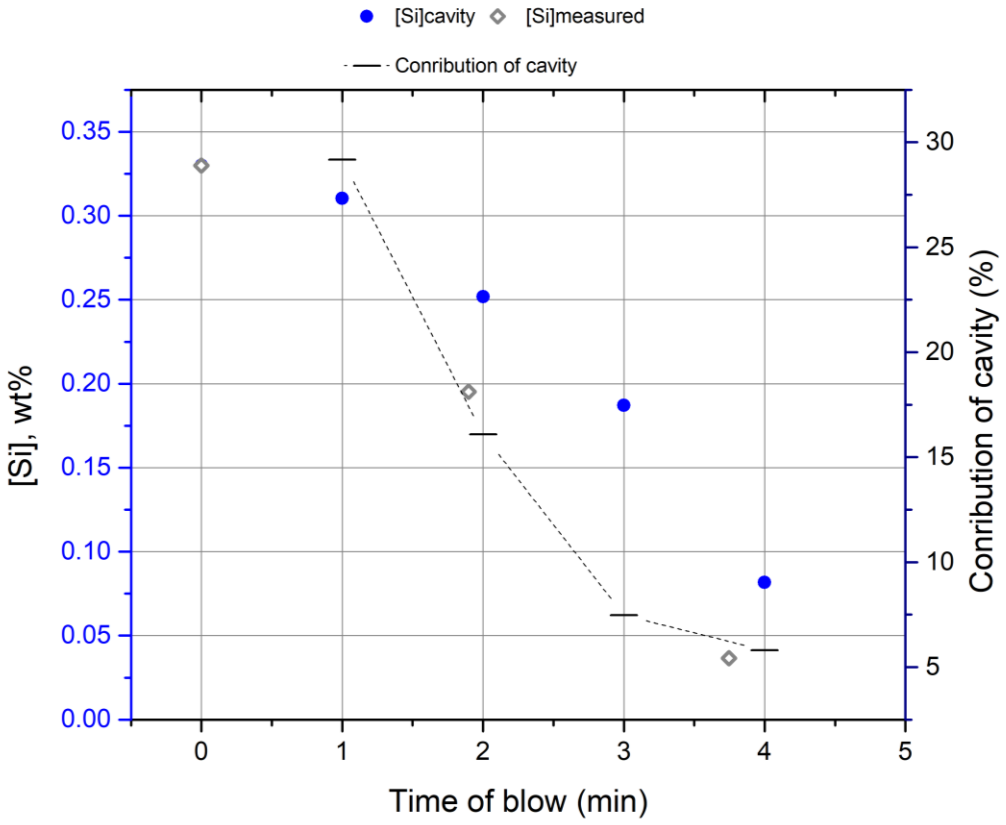

Figure 5.7: Silicon refining in the cavity zone and contribution of cavity zone to the overall refining of Si.

Figure 5.8 compares the calculated change in the manganese content of cavity droplets with those reported by Cicutti et al., which include a contribution from both cavity and emulsion refining. The cavity zone is predicted to contribute to 10 to 30 % of the total refining of manganese in the early part of the blow. The measured data shows that [Mn] content is reduced to ~0.08 wt %.

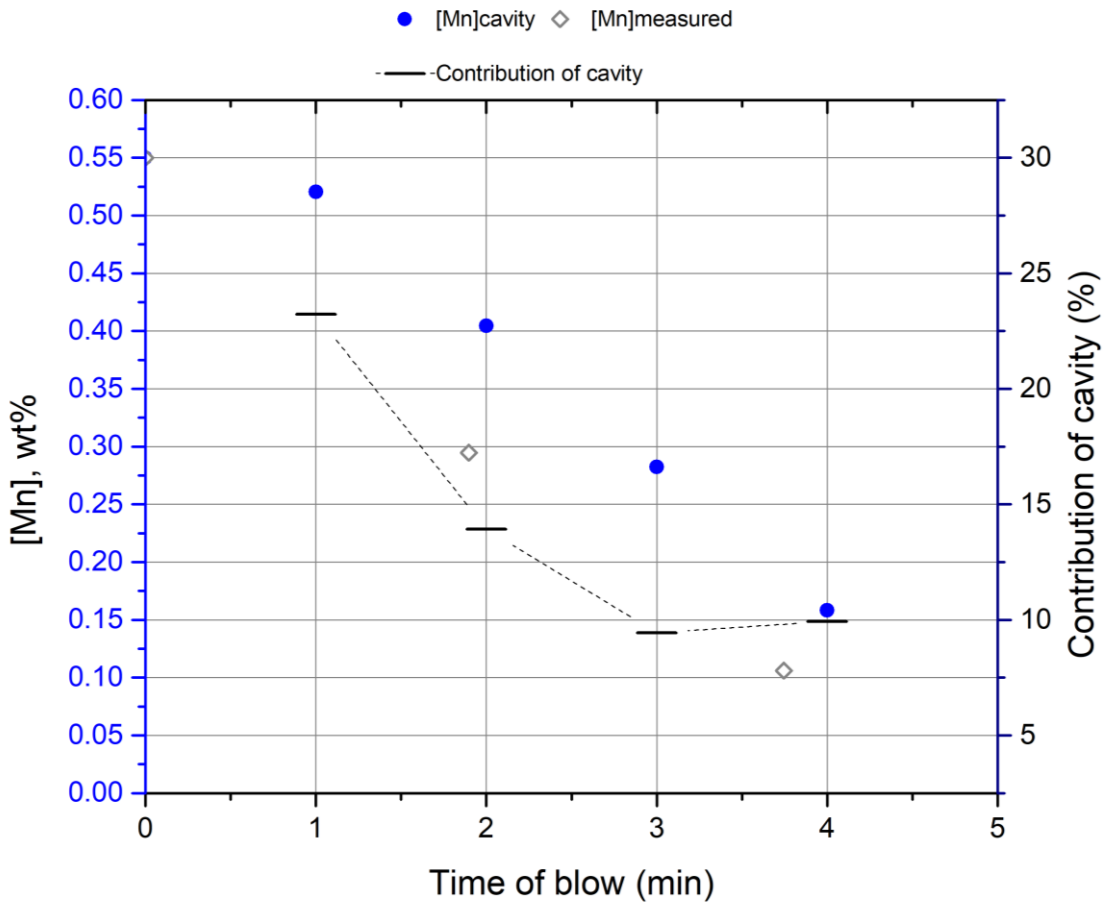

Figure 5.8: Manganese refining in the cavity zone and contribution of cavity zone to the overall refining of Mn.

Figure 5.9 shows the contribution of decarburization in the cavity zone to the total decarburization. The contribution of the cavity is high in the first two min of the blow when the overall decarburization is low. Followed by a significant decrease in the decarburization, and the contribution of the cavity is calculated (using equation 5.42) to be between 40 and 70 % during the main blow. Towards the end of the blow (t > 14 min), the decarburization is increased again up to 90 %. This finding coincides with the authors' predictions for the contribution of the emulsion zone, which was decreasing due to the

absence of bloating towards the end of the blow[37] .The increase in the contribution of cavity occurs due to a decrease in silicon and manganese contents of the bath. Also, the effect of temperature rise with the progress of the blow is significant on carbon, leading to an increase in carbon removal.

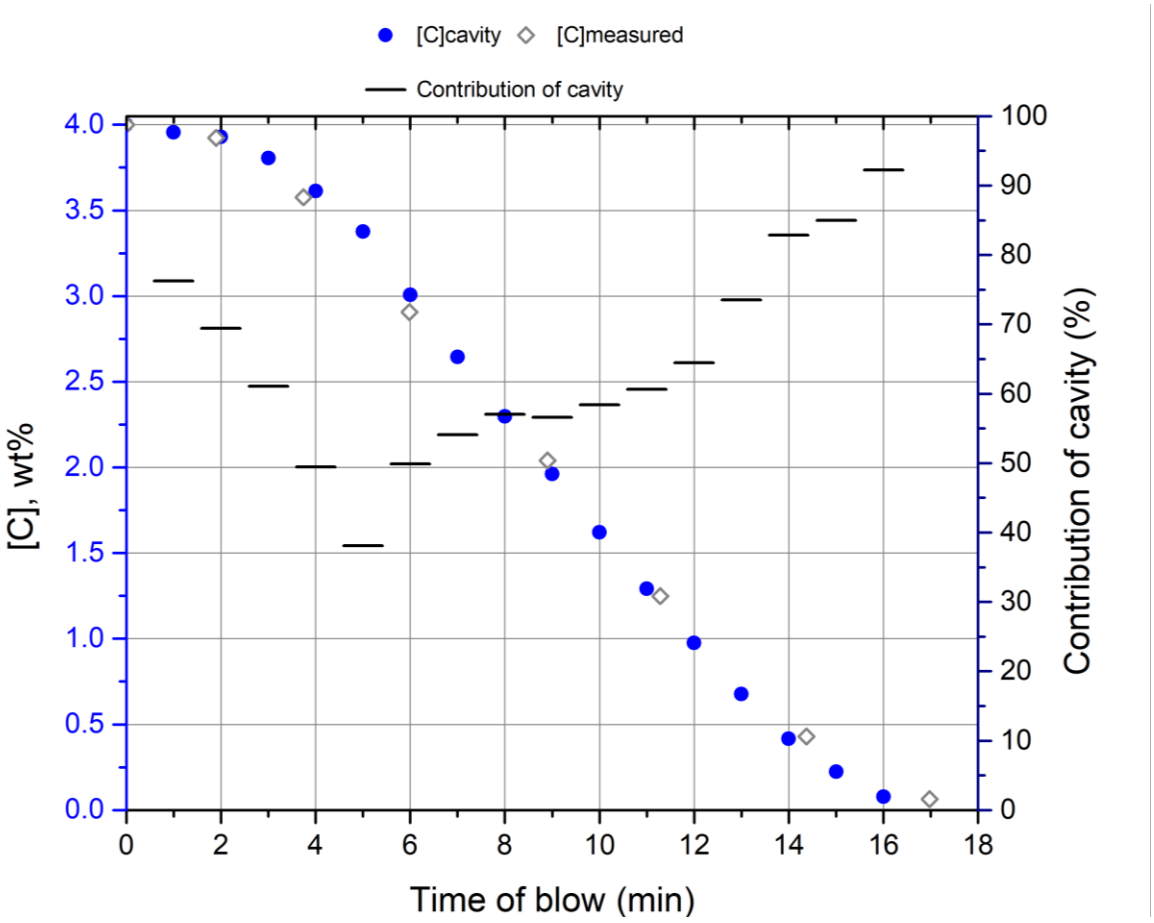

Figure 5.9: Carbon refining in the cavity zone and contribution of cavity zone to the overall refining of C.

Figure 5.10(a) presents the prediction for the FeO formation along with the droplet generation rate considered during various times of the blow, while Figure 5.10(b) compares the values for %(FeO) reported by Cicutti et al. and predicted by the model. As seen in Figure 5.10(a), the droplet generation is assumed to be 15000 kg/min for the first 5 minutes

of the blow and 30000 kg/min for the remaining part of the blow. For a constant droplet generation rate, the FeO formation decreases with the progress of the blow because of an increase in the liquid metal temperature.

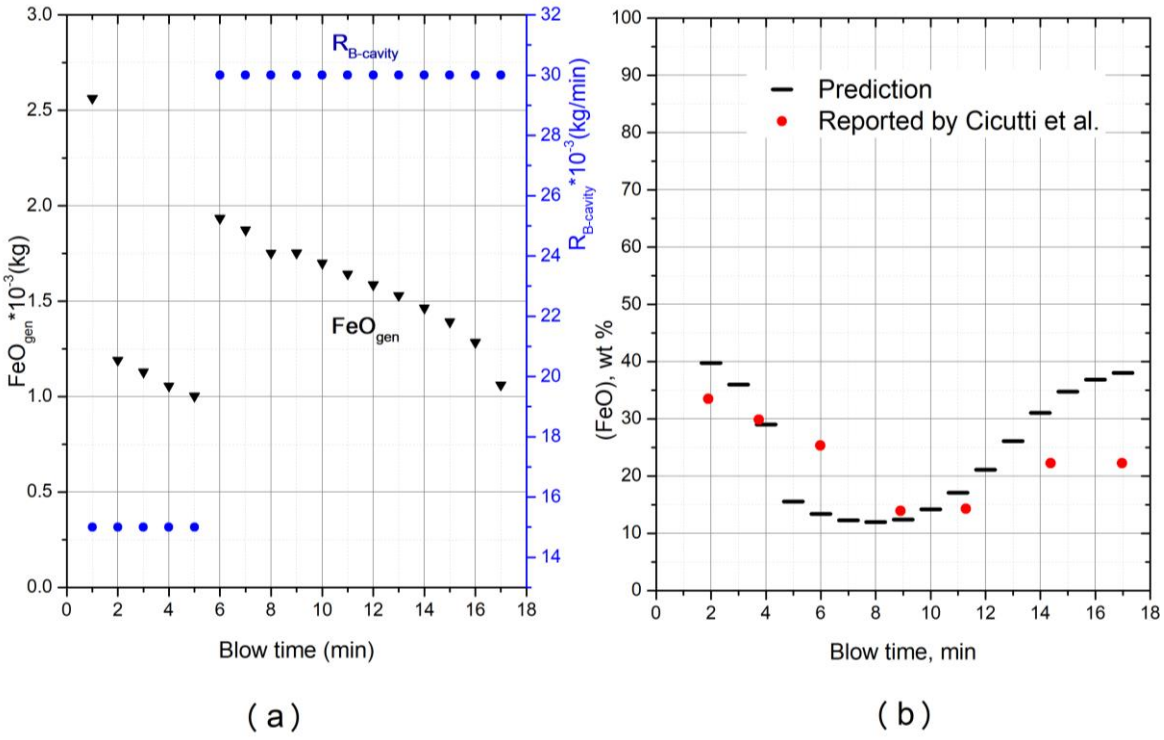

Figure 5.10: (a) Prediction of FeO formation and assumed droplet generation rate in the cavity during the blow (b) Comparison of predicted and reported FeO content of slag

In the model, it is assumed that FeO is formed only in the cavity zone. Then it is consumed in the emulsion zone by the decarburization reaction. So, the accumulated FeO, FeO_{acc} (kg) is calculated by the summation of accumulated FeO from the previous time step and the difference in the amount of generated and consumed FeO, as given by the following equation.

$$(FeO_{acc})_t = \left(FeO_{gen}\right)_t - (FeO_{con})_t + (FeO_{acc})_{t-1} \quad (5.43)$$

The FeO content of slag is then calculated through following equation

$$(FeO), wt\% = \frac{(FeO)_{acc-t}}{W_{slag-t}} \quad (5.44)$$

where W_{slag-t} is the total weight of slag in kg at the given time instant t.

It can be seen in Figure 5.10(b) that the model predicts the FeO content of slag in the early blow (from 2 mins onwards) and middle blow (up to 12-13 mins) reasonably well. However, slight over-prediction is observed beyond 13 mins of the blow.

5.7 Sensitivity Analysis

Certain simplifying assumptions were considered in the current model for parameters that can't be accurately ascertained because of the chaotic nature of the cavity zone.

5.7.1 Residence time

The residence time of droplets would depend upon the size and the point of origin of the cavity (either lip or base of the cavity) and it is expected that the extent of refining will be affected. However, it is difficult to ascertain the number of droplets generated from different locations of the cavity and their ejection velocities. In the current study, a constant residence time for droplets of all sizes is assumed. Figure 5.11 presents the final compositions of droplets as a function of droplet size and residence time. An increase in residence time implies an additional exposure to the oxidizing gas. Therefore, it is observed that the increase in residence time increases the refining of the silicon and manganese,

whereas the refining of carbon is mostly unaffected for larger droplets (2, 3 and 4 mm droplet diameter) because of poisoning effect of sulfur. This effect is countered in the case of smaller droplets (0.5, 1 mm) due to their higher (A/V) ratio leading to lower final carbon content. It is important to note that the poisoning effect of sulfur is diminished in the latter part of the blow, and the variation of refining with droplet size is observed for all droplet sizes. The value of F_d i.e the fraction of droplet oxidized to FeO, increases with the increase in residence time from 0.15 to 0.25 s, but the effect is more pronounced for smaller droplet sizes (0.5 and 1 mm). However, it should be noted that even a slight increase in the value of F_d corresponds to a considerable increase in total FeO generation as the droplets generated during the blow are relatively large (10^6 to 10^7). This leads to the conclusion that for a given droplet generation rate, the increase in residence time of droplets in the cavity will increase the refining of droplets. But it also leads to an increase in the FeO formation and decreases the yield of liquid steel at the end of the blow if finer droplets are produced in higher proportion.

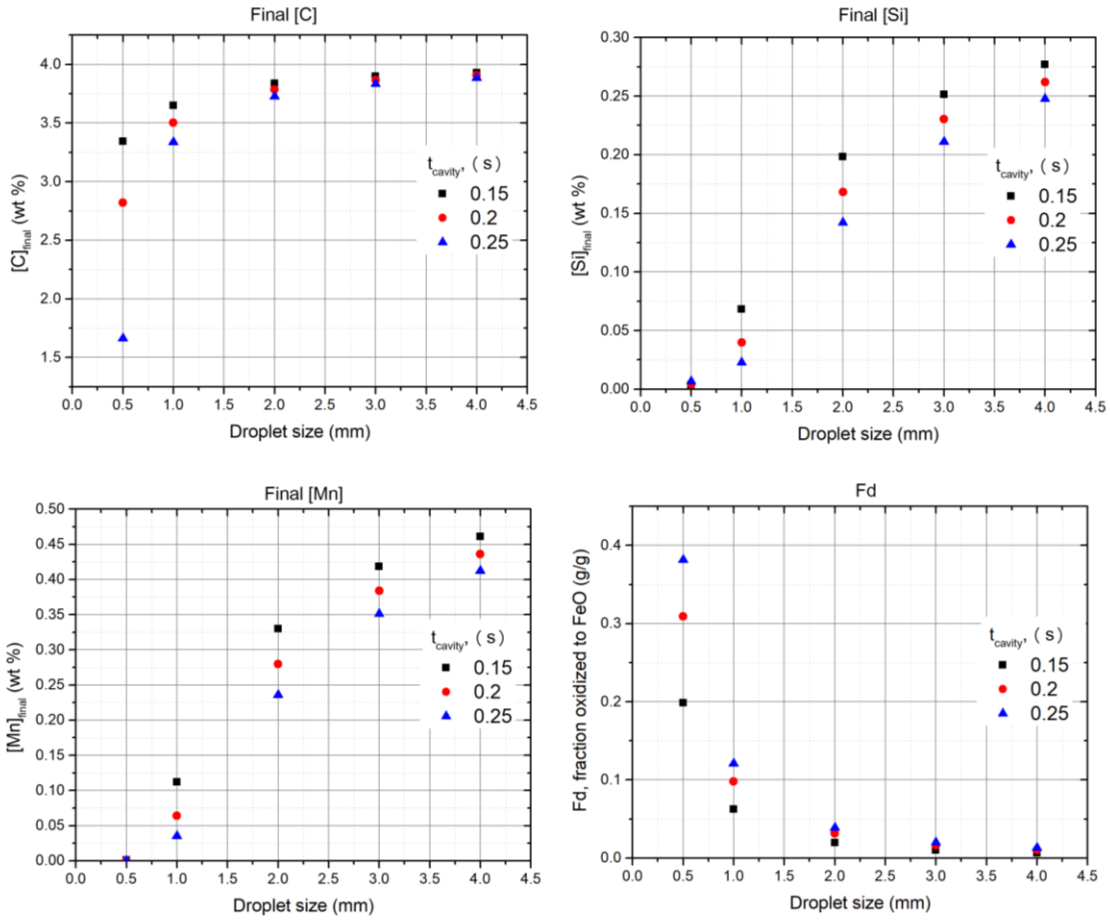

Figure 5.11: Effect of residence times on the final (a) carbon, (b) silicon, (c) manganese contents of cavity droplets and (d) F_d as a function of droplet diameter. These predictions are made for the droplets ejected at the start of the blow, T = 1350 °C, [C]initial = 4, [Si]initial = 0.33, [Mn]initial = 0.55.

5.7.2 **Gas composition**

Highly oxidizing nature of the gas atmosphere and high surface to volume ratio from these droplets are the factors that possibly contribute to a high refining rate. In the current study, the gas composition of $\mathrm{pO_2} = 0.53, \mathrm{pCO} = 0.4, \mathrm{pCO_2} = 0.07$ is assumed, as explained in earlier sections. However, if the ratio of oxidizing gases (pO_2, pCO_2) increases, change in the refining behavior might be observed as a higher ratio of oxidizing gases would entail a

greater oxygen concentration, $[O]^r$ at the interface. Figure 5.12 presents the effect of cavity gas compositions based on three entrainment rates 200, 300, 400 kg/min (as described in section 5.5) for droplet ejected at the start of the blow. The gas compositions corresponding to these entrainment rates are presented in Table 5.4 and the calculation procedure given in Appendix 5.9.B.

Table 5.4: Composition of cavity gas for different entrainments (in terms of decarburization rates)

Decarburization rate causing equivalent entrainment of gas, kg/min	pO_2	pCO	pCO_2	Net oxidizing gas ratio $\frac{(pO_2 + pCO_2)}{(pO_2 + pCO_2 + pCO)}$
100	0.77	0.2	0.03	0.8
200	0.62	0.32	0.06	0.68
300	0.53	0.4	0.07	0.6
400	0.45	0.46	0.09	0.54

The oxidizing capacity of cavity gas decreases with an increase in entrainment rate from 200 to 400 kg/min, however, no significant increase in the refining of carbon, silicon, and manganese is observed. Since the droplets under consideration are from the start of the blow, the chemical reaction control (due to the poisoning effect of sulfur) is dominant on the carbon refining. The additional oxygen supply at the interface (due to lower entrainment of CO and CO_2) is found to result in an increase in the refining of carbon for smaller droplets (0.5 mm). A similar effect is observed for F_d wherein, F_d changes for the 0.5 mm size droplets due to a combined effect of the high surface area of droplets and an additional oxygen supply at the interface. The impact of extra oxygen is not observed for silicon and

manganese refining, as they present in smaller quantities in the metal droplet (0.33 and 0.55 wt %, respectively), and their oxidation is limited by their availability at the interface. This indicates that variation of the gas composition (or the oxygen availability at the interface) strongly affects the oxidation/refining of elements present in significant quantity at the interface (e.g., carbon and iron) rather than elements present in smaller amounts like silicon or manganese. It is essential to mention that this statement is valid for small droplets.

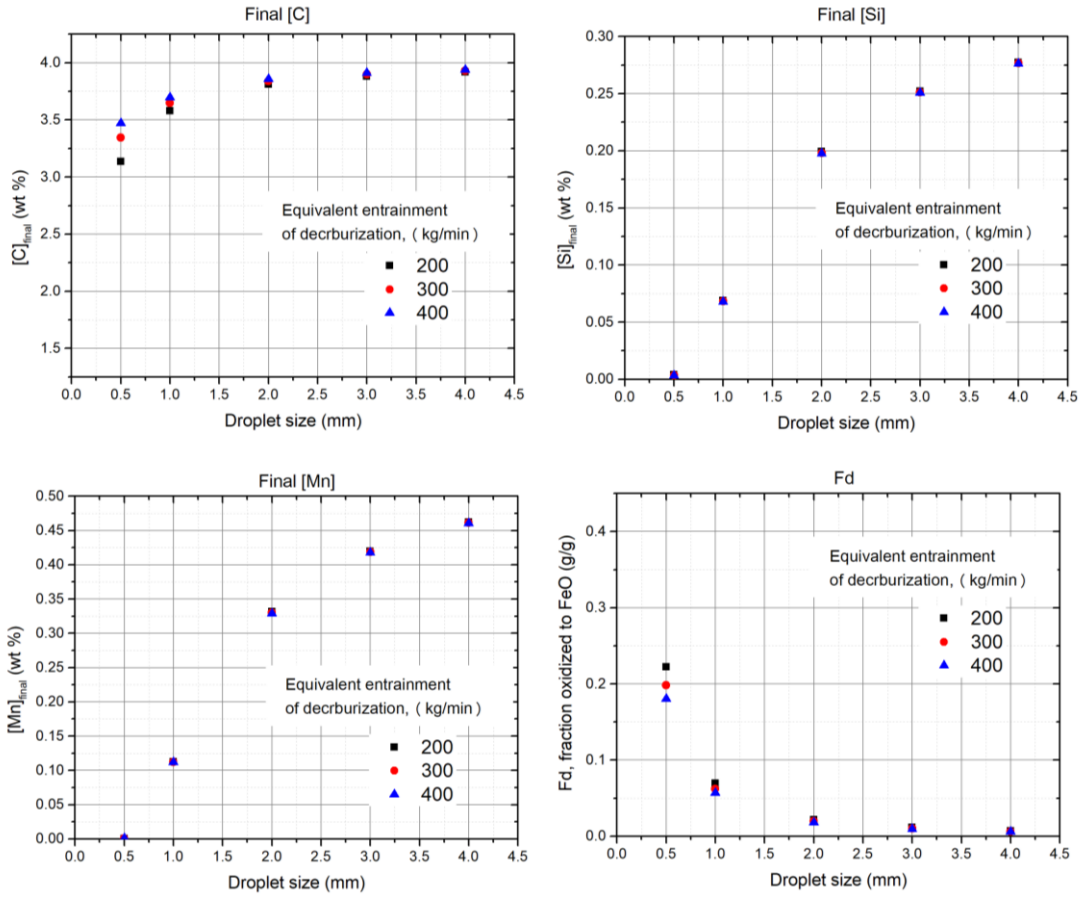

Figure 5.12: Effect of varying cavity gas composition on the final (a) carbon, (b) silicon, (c) manganese contents of cavity droplets and (d) F_d of droplets of different sizes for residence time = 0.15 seconds. These predictions are given for the droplets ejected at the start of the blow, T = 1350 ^oC, [C]initial = 4, [Si]initial = 0.33, [Mn]initial = 0.55 in wt %

5.7.3 Size distribution

In the current study, the coarse size distribution of droplets based on one of the prescribed values of Cicutti et al. is taken to be the base case. This size distribution is compared with a finer size distribution of droplets. Both the size distributions are shown in Table 5.5. n and d' represent homogeneity of the distribution function and the measure of fineness, respectively[32]

Table 5.5: Size fractions of the droplet sizes for coarse and fine size distributions.

Size of the droplet, (mm) →	4	3	2	1	0.5
Coarse (d' = 1.418, n = 1.764)	0.02	0.13	0.42	0.27	0.15
Fine (d' = 1.232, n = 1.7)	0.01	0.09	0.39	0.31	0.19

The effect of size distribution on refining and FeO formation, as shown in Figure 5.13. It is observed that the fine size distribution does not affect the impurity refining significantly, especially for silicon and manganese. Still, it leads to a significant increase in FeO formation throughout the blow, as seen in Figure 5.13(d). A previous study[31] has presented a function relation between droplet size distribution and lance height. This leads to the conclusion that the size distribution of cavity droplets needs to be controlled carefully, particularly for the FeO formation so that the refining in the emulsion zone is sustained, and the excessive loss of production yield is prevented.

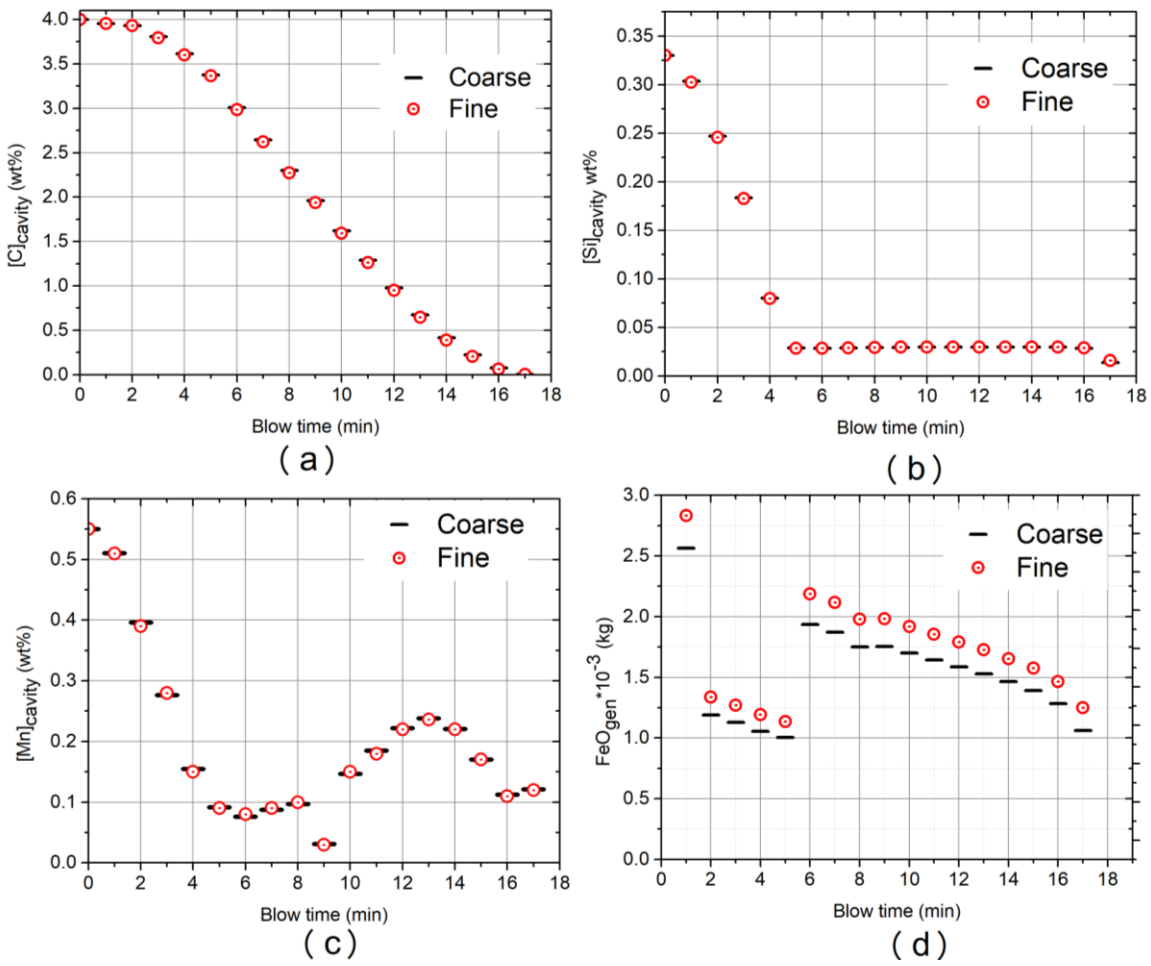

Figure 5.13: Effect of size distribution on (a) carbon, (b) silicon, (c) manganese contents of metal bath brought to cavity refining and (d) the amount of FeO formed during the blow for residence time = 0.15 seconds.

5.8 Conclusion

A model is presented to quantify the refining of elements within the cavity droplets generated in the oxygen steelmaking furnace. The authors believe that this is the first attempt that considers and explains the refining path in this zone. The model incorporates the knowledge of various insights on droplet-gas interaction available from experimental studies. Some of the significant conclusions of the current model are as follows

1. The model can explain the simultaneous oxidation of impurities and iron through the incorporation of the thermodynamic equilibria of several reactions at the metal droplet-gas interface and mass transfer in the metal and gas phases.
2. The model explains the rapid formation of FeO during the early part of the blow, which is critical to sustaining the refining reactions in the emulsion zone. But there is an over-prediction of FeO formation towards the end of the blow.
3. The contribution of the cavity zone towards silicon and manganese refining is between 20 to 40 % during the early blow.
4. In the case of refining carbon, the contribution ranges from 20 to 70 %, and the contribution rises steadily with the progress of the blow.
5. Further investigation is required to find a connection between parameters that are critical to model predictions (e.g., residence time of droplets, droplet generation rate) with the operational parameters.

5.9 Appendix

Appendix A

The activity coefficient of the metal droplet components at the interface is calculated through the following equations.

$$log\ f_C^r = e_C^C[wt\ \%C]^r + e_C^O[wt\ \%O]^r + e_C^{Si}[wt\ \%Si]^r + e_C^{Mn}[wt\ \%Mn]^r + e_C^S[wt\ \%S]^r \quad (5.A1)$$

$$log\ f_{Si}^r = e_{Si}^C[wt\ \%C]^r + e_{Si}^O[wt\ \%O]^r + e_{Si}^{Si}[wt\ \%Si]^r + e_{Si}^{Mn}[wt\ \%Mn]^r + e_{Si}^S[wt\ \%S]^r \quad (5.A2)$$

$$log\ f_{Mn}^r = e_{Mn}^C[wt\ \%C]^r + e_{Mn}^O[wt\ \%O]^r + e_{Mn}^{Si}[wt\ \%Si]^r + e_{Mn}^{Mn}[wt\ \%Mn]^r + e_{Mn}^S[wt\ \%S]^r \quad (5.A3)$$

$$log\ f_O^r = e_O^C[wt\ \%C]^r + e_O^O[wt\ \%O]^r + e_O^{Si}[wt\ \%Si]^r + e_O^{Mn}[wt\ \%Mn]^r + e_O^S[wt\ \%S]^r \quad (5.A4)$$

where e_j^i is an interaction parameter and represents the effect of solute i on the activity coefficient of solute j. The values for interaction parameters are obtained from the work of Sigworth and Elliot[38].

Appendix B

It is known that the oxygen flow rate from lance nozzles is 620 $\frac{m^3}{min}$ using the industrial data by Cicutti et al.[34,35]. In the current study, it is assumed that an equivalent gas from 300 kg/min decarburization is entrained by the oxygen jets. Therefore equivalent carbon in gas = 300*1000/12 = 25000 moles/min = 25000*0.0224 = 560 $\frac{m^3}{min}$

If the post-combustion ratio is 0.15, then $volume\ of\ CO_2\ gas,\ V_{CO_2}$ = 0.15*560 = 84 $\frac{m^3}{min}$

$volume\ of\ CO\ gas,\quad V_{CO}$= 0.85*560 = 476 $\frac{m^3}{min}$

$$pO_2 = \frac{V_{O_2}}{V_{O_2} + V_{CO_2} + V_{CO}} = 0.53 \quad (5.B1)$$

$$pCO = \frac{V_{CO}}{V_{O_2} + V_{CO_2} + V_{CO}} = 0.4 \quad (5.B2)$$

$$pCO_2 = \frac{V_{CO_2}}{V_{O_2} + V_{CO_2} + V_{CO}} = 0.07 \quad (5.B3)$$

5.10 References

1 B. Deo and R. Boom: *Fundamentals of Steel Making Metallurgy*, Pretince Hall International, 1993.

2 H. Jalkanen: *Sohn Int. Symp. Adv. Process. Met. Mater.*, 2006, vol. 2, pp. 541–54.

3 B. Rout, G. Brooks, M.A. Rhamdhani, Z. Li, F.N. Schrama, and J. Sun: *Metall. Mater. Trans. B*, 2018, vol. 49, pp. 537–57.

4 B.K. Rout, G.A. Brooks, Z. Li, and M.A. Rhamdhani: in *AISTech*, Pittsburgh, 2016, pp. 1019–26.

5 R. Sarkar, P. Gupta, S. Basu, and N.B. Ballal: *Metall. Mater. Trans. B*, 2015, vol. 46, pp. 961–76.

6 A. Kadrolkar and N. Dogan: *Metals (Basel).*, 2019, vol. 9, pp. 1–26.

7 Hammer.R: *Stahl und Eisen*, 1957, vol. 77, pp. 1303–8.

8 K. Koch, J. Falkus, and R. Bruckhaus: *Steel Res. Int.*, 1993, vol. 64, pp. 15–21.

9 A. Nordqvist, A. Tilliander, K. Grönlund, G. Runnsjö, and P. Jönsson: *Ironmak. Steelmak.*, 2009, vol. 36, pp. 421–31.

10 N. Dogan: Ph.D thesis, Swinburne University, 2011.

11 N. Dogan, G.A. Brooks, and M.A. Rhamdhani: *ISIJ Int.*, 2011, vol. 51, pp. 1093–101.

12 N. Dogan, G.A. Brooks, and M.A. Rhamdhani: *ISIJ Int.*, 2011, vol. 51, pp. 1102–9.

13 B.K. Rout: Ph.D Thesis, Swinburne University, 2018.

14 D.G. Robertson and A.E. Jenkins: in *Heterogenous Kinetics at Elevated Temperatures, Proceedings of International conference in Materials and Process Metallurgy*, G.R. Belton and W. Worell, eds., Philadelphia, 1969, pp. 393–408.

15 L.A. Baker, N.A. Warner, and A.E. Jenkins: *Trans. Metall. Soc. AIME*, 1967, vol. 239, pp. 857–64.

16 P.A.A. Distin, G.D.D. Hallett, and F. D. Richardson: *J. Iron Steel Inst.*, 1968, vol. August, pp. 821–33.

17 S. Jahanshahi: Ph.D Thesis, Imperial College of Science and Technology, 1980.

18 H. Sun and R.D. Pehlke: *Metall. Trans. B*, 1996, vol. 27, pp. 854–64.

19 H. Sun and R.D. Pehlke: *Metall. Mater. Trans. B*, 1995, vol. 26, pp. 335–44.

20 K. Mor, H. Sun, K. Ga, V. Sahajwalla, and R.D. Pehlke: *ISIJ Int.*, 1999, vol. 39, pp. 25–33.

21 D. Widlund, D.S. Sarma, and P.G. Jönsson: *ISIJ Int.*, 2006, vol. 46, pp. 1149–57.

22 N. Sano and Y. Matsushita: *Trans. ISIJ*, 1971, vol. 11, pp. 232–9.

23 S. Kitamura and K. Okohira: *Tetsu-to-Hagane*, 1990, vol. 76, pp. 199–206.

24 C.R. Taylor and J. Chipman: *Trans. AIME*, 1943, vol. 154, pp. 228–47.

25 H. Sakao and T. Fujisawa: *Recommended Equilibrium Value of Steel-Making, 19th Committee, No. 1059*, 5th edn., Japan Society for Promotion of Science and Technology, Tokyo, 1982.

26 S. Ban-ya and S. Matoba.: *Tetsu-to-Hagane*, 1962, vol. 48, pp. 925–32.

27 D.R. Sain and G.R. Belton: *Metall. Trans. B*, 1976, vol. 7, pp. 235–34.

28 W.E. Ranz and M.R. Marshall: *Chem. Eng. Prog.*, 1952, vol. 48, pp. 173–80.

29 R. Higbie: *Trans. Am. Inst. Chem. Eng.*, 1935, vol. 35, pp. 36–60.

30 G. Brooks, Y. Pan, Subagyo, and K.S. Coley: *Metall. Mater. Trans. B*, 2005, vol. 36, pp. 525–35.

31 Subagyo, G. a. Brooks, K.S. Coley, and G. a. Irons: *ISIJ Int.*, 2003, vol. 43, pp. 983–9.

32 S.C. Koria and K.W. Lange: *Metall. Trans. B*, 1984, vol. 15, pp. 109–16.

33 N. Standish and Q.L. He: *ISIJ Int.*, 1989, vol. 29, pp. 455–61.

34 C. Cicutti, M. Valdez, T. Perez, J. Petroni, A. Gomez, R. Donayo, and L. Ferro: in *6th International Conference on Molten Slags, Fluxes and Salts*, Stockholm- Helsinki, 2000, p. 367.

35 C. Cicutti, M. Valdez, T. Pérez, R. Donayo, and J. Petroni: *Lat. Am. Appl. Res.*, 2002, vol. 32, pp. 237–40.

36 K. Mori, Y. Fukami, and Y. Kawai: *Trans ISIJ*, 1988, vol. 28, pp. 315–8.

37 A. Kadrolkar and N. Dogan: *Metall. Mater. Trans. B*, 2019, vol. 50, pp. 2912–29.

38 G.K. Sigworth and J.F. Elliot: *Met. Sci.*, 1974, vol. 3, pp. 298–310.

Chapter 6

A Dynamic Flux Dissolution Model for Oxygen Steelmaking

Chapter 6 is a pre-publication version of the article published in *Metallurgical and Materials Transactions B*. vol. 48B (1), pp. 99-112. DOI: 10.1007/s11663-016-0777-8. The following chapter introduces a procedure for simulating the amount of dissolved lime in the oxygen steelmaking process, by coupling of the existing thermodynamic tools and kinetic models simultaneously. The procedure is developed to calculate the saturation concentrations/solubility of CaO in slag using thermodynamic tools, namely FactSage, Cell Model, and Thermo-Calc. The total amount of dissolved lime is evaluated by integrating solubility values in the rate equation of lime dissolution over time, taking into account the effects of physical properties and temperature of slag and particle size of flux additions and validated against industrial data available in the literature. Furthermore, the existence of two distinct control mechanisms in lime dissolution in slag is discussed. The development of the model, its coding, data analysis against industrial data as well as manuscript drafting was carried out by the primary author. Dr. Neslihan Dogan provided extensive discussion during model development and proofread the manuscript. Dr. Andersson performed the calculations pertaining to ThermoCalc and reviewed the final version of the manuscript while Alan Galindo helped with Cell Model calculations.

A Dynamic Flux Dissolution Model for Oxygen Steelmaking

Ameya Kadrolkar[1], Nils Å.I. Andersson[2] and Neslihan Dogan[1]

[1]McMaster Steel Research Centre, McMaster University, JHE 357, 1280 Main Street West, Hamilton, ON L8S 4L7, Canada.

[2]Royal Institute of Technology (KTH), Brinellvägen 23, Stockholm, Sweden, SE-10044

Abstract

A modified model for prediction of flux dissolution in oxygen steelmaking process is presented in this study. The aim of this paper is to introduce a procedure for simulating the amount of dissolved lime with respect to the saturation concentration of CaO by coupling the existing thermodynamic and kinetic models simultaneously. The procedure is developed to calculate the saturation concentrations/solubility of CaO in slag using thermodynamic models namely FactSage, Cell Model, and Thermo-Calc. Total amount of dissolved lime is evaluated by integrating solubility values in the rate equation of lime dissolution over time taking into account the effects of physical properties and temperature of slag and particle size of flux additions and validated against industrial data available in literature. Comparison between measured and calculated undissolved lime shows a good agreement between them using any thermodynamic models even though there are some differences in the predictions of saturation concentration of CaO in slag. It has been shown

that two distinct control mechanisms for lime dissolution in BOF slags exist and consideration of the free lime-controlled mechanism is essential for accurate prediction of dissolution rate of lime in slag.

Keywords: lime, dissolution rate, mass transfer, thermodynamic modeling, oxygen steelmaking

6.1 Introduction

In oxygen steelmaking, flux is added in a solid form to the process to form a basic slag that will limit the degradation of the refractory lining and will remove oxidation products such as phosphorus and silicon. The progress of flux dissolution determines the efficiency of fluxing of impurities and prolongs contact time with refractory lining. Since top blowing process takes only 15–20 min to refine impurities from the steel, full utilization of flux added requires rapid flux dissolution in the slag. Therefore, the degree of flux dissolution is of crucial interest for understanding the progress of slag–metal reactions in the oxygen steelmaking system.

There have been several experimental studies[1,2,11,12,3–10] on the mechanism and kinetics of flux dissolution into stirred and stagnant slag baths at high temperatures. However, these are generally limited studies with experimental conditions, such as the stirring intensity, composition and temperature of molten slag system, which can be practically studied at laboratory scale. Although these studies provide qualitative information on flux dissolution, it is difficult to apply the findings to predict the kinetics of flux dissolution under full-scale operating conditions. In order to close this knowledge gap, there have been few modeling attempts [13–16] made.

Asai *et al.*[13], Graveland-Gisolf *et al.*[17], Dogan *et al.*[14] and Lytvynyuk *et al.*[16] developed a process model for oxygen steelmaking process and they incorporated a flux dissolution sub-model as a part of their process model. In all models, rate of lime dissolution is assumed to be controlled by CaO diffusion through boundary layer and is a function of difference between the CaO content in slag phase and saturation concentration. Asai *et al.*[13] expressed the saturation concentration of CaO in slag as a polynomial expression (derived from a simplified ternary phase diagram of FeO-SiO_2–CaO system) of slag and bath temperature. They were able to predict the amount of lime dissolved as a function of lime addition and blow time however the validation of this model against industrial operations wasn't provided in their study. Graveland-Gisolf *et al.*[15] took into account the silicate layer formation around the lime particles. However detailed description of the model is not available in open literature. Dogan *et al.*[14] calculated the saturation limit of CaO in slag using the ternary phase diagram FeO–SiO_2–CaO, considering intersections between the liquidus line with a straight line connecting the point with $2CaO{\cdot}SiO_2$ (further referred to C_2S). This represents the equilibrium between C_2S and dissolved CaO in the slag.

Lytvynyuk *et al.*[16] applied a flux dissolution model which was originally suggested by Kitamura *et al.*[12]. The phase diagram calculations were made to predict the saturation concentration of CaO and the fraction of C_2S by applying lever rule to the FeO–SiO_2–CaO slag system. They applied two values for mass transfer coefficient of CaO in different regions. The value of mass transfer coefficient for the dissolution in the C_2S saturated region was assumed to be $1/10^{th}$ of that in the liquid slag region. Even though previous studies provided insight to predict the dissolution of flux, the application of the proposed

models is currently limited. In order to develop more robust and accurate model, it is important to investigate an approach to predict the saturation level of metal oxides under various slag compositions.

The aim of the present study is to provide better predictions on the rate of flux dissolution under full-scale operating conditions at high temperatures with the aid of thermodynamic modeling. In the present study, the effectiveness of thermodynamic models to evaluate the saturation concentration of CaO will be assessed and optimum model will be suggested for industrial applications. In this study, the flux dissolution model developed by Dogan *et al.*[18] is used as it involves the most rigorous treatment of flux dissolution, while taking into account the kinetic and thermodynamic phenomena involved, with description of the effects of flux addition rate and particle size on the rate of dissolution.

6.2 Model Development

Dogan *et al.*[18] developed a process model for a top-blown oxygen steelmaking process. The model for flux dissolution was built as a sub-model of the proposed process model and incorporates the effect of temperature, stirring intensity and slag composition throughout the blow.

In the flux dissolution model, the dissolution rate of fluxes into slag system was expressed by a decrease in the radius of solid flux particles. The number of particles dissolved in the slag is proportional to particle concentration in the slag. The calculations for different individual particle size were carried out separately and the results were then added. The amount of lime dissolved in the slag phase as a function of time was determined using equation 6.1

$$\frac{dW_L}{dt} = \rho_L S \frac{dr}{dt} n_L \quad (6.1)$$

where W_L is the mass of dissolved lime (kg), ρ_L is density of lime (kg/m^3), n_L is the number of lime particles, S is the surface area of particle (m^2), r is the average radius of lime particles (m) and t is time (min). The dissolution of refractory into the slag phase was a complicated and very slow process. It was very difficult to predict the amount of refractory dissolved during one heat. For simplicity, it was not included in this study.

It has been established that the rate of lime dissolution is controlled by diffusion of CaO through boundary layer[19]. The equation for the dissolution rate was adopted from the study of Matsushima *et al.*[8]. The decrease in the radius of spherical flux particles is calculated as a function of time assuming spherical geometry, as shown in equation 6.2.

$$\frac{dr}{dt} = k \frac{\rho_s}{100\rho_L} \left(CaO_{sat} - CaO_{slag}\right) \quad (6.2)$$

where k is the mass transfer coefficient of CaO in the slag (m/min), CaO_{sat} is the solubility/saturation of CaO in the slag phase (in mass %) and CaO_{slag} is the concentration of CaO in the slag phase (in mass %). The density of slag, ρ_s is calculated as the ratio of the average molecular weight and the volume of the slag (evaluated through the partial molar volumes of the slag components) at a given time step. The data for the molar volume of oxides in slag was taken from the work of Keene and Mills[20].

Dogan *et al.*[18] proposed a modified correlation to calculate the mass transfer coefficient, k that can better represent the dual flow regimes (namely, the turbulent impact zone at the

center and the stagnant zone close to the refractory lining) during oxygen steelmaking operations. The oxygen steelmaking process has heterogeneous mixing characteristics. In the beginning, solid particles exist in a transient regime with regard to their size and velocities. As the particles decrease in size, those that remain in the turbulent regime become faster. Therefore, it is difficult to predict the dissolution rate of solid flux particles using one simple equation. Dogan et al. applied a correlation for rigid spheres proposed by Clift *et al.*[21]. This correlation is valid for high Schmidt number (Sc>200) and 100<Re<2000 as shown in equation 6.3.

$$Sh = 1 + 0.724(Re)^{0.48}(Sc)^{0.33} \tag{6.3}$$

Reynolds number (Re) is a function of settling velocity of particles moving in a fluid. The settling velocity of a lime particle in slag, up, is calculated from the equation suggested by Oeters [18] for 0.5 <Re<1000 as shown in equation 6.4 .

$$u_p = \left[\frac{(\rho_s - \rho_L)g}{9\sqrt{\mu_s \rho_s}}\right]^{\frac{2}{3}} d_p \tag{6.4}$$

Dogan et al.[18] modified the settling velocity of particles by introducing factor β, to represent the varying dynamic conditions in the oxygen steelmaking process as follows

$$Re' = \frac{(\beta \mu_p) d_p \rho_s}{\mu_s} \tag{6.5}$$

where d_p is the diameter of a solid particle, ρ_s and μ_s are density and viscosity of slag, respectively. The resultant modified equation was represented as follows

$$Sh = 1 + 0.724(Re')^{0.48}(Sc)^{0.33} \tag{6.6}$$

Dogan *et al.*[18] found that the predicted lime dissolution agreed well with that reported by Cicutti *et al.*[22] when the value of β was equal to 10. The same value is used in the current study.

6.2.1 Dissolution Mechanism of Fluxes

a. Lime:

Previous studies[1–3,8,19,23] have revealed that lime does not directly dissolve in silica containing slag and a film of di-calcium silicate (C_2S) or tri-calcium silicate (C_3S) are most likely to be formed. In oxygen steelmaking system, the dissolution mechanism of lime is influenced by the composition of slag and controlled by the saturation level of lime, C_2S or C_3S depending on the ratio of CaO to SiO_2. As the temperature of slag rises with the progress of the blow, the silicate layers become unstable and CaO is directly absorbed in the slag. Matsushima *et al.*[8] suggested that the thickness of silicate layers is affected by the FeO content of the slag. A thicker film forms when the concentration of FeO in slag is less than 20 mass%. Above this level the film formation discontinues and the dissolution of lime progresses[8].

b. Dolomite

MgO from the dolomite reacts with FeO in steelmaking slag to form magnesiowustite on the surface of the dolomite particle[1]. Umakoshi *et al.*[23] measured the dissolution rate of sintered burnt dolomite in a stirred Fe_xO–CaO–SiO_2 slags containing FeO from 20 to 65 mass% (%CaO/%SiO_2=1) at temperatures of 1623K (1350 ^oC) to 1698K (1425 ^oC). They suggested that diffusion of MgO through a boundary layer is the rate limiting step when the FeO content of slag phase is above 20 mass% while diffusion of CaO through boundary

layer is rate limiting for small FeO concentrations (mass% FeO<20). They also observed that $2CaO \cdot SiO_2$ film layer disappears under forced convection conditions and the formation of (Fe,Mg)O is hardly affected by the intensity of stirring[23].

6.2.2 Determination of Saturation Concentration

Computational thermodynamics models are used to understand the limits of the system and portioning of the impurities among the phases. In this study thermodynamics models namely FactSage™, Thermo-Calc™ and Cell Model are applied to calculate the saturation concentration of CaO in the slag as a function of slag composition and temperature. These models provide the limits for the dissolution rate of lime particles in the slag. In this study, FactSage™ and Thermo-Calc™ are selected because they provide one of the most comprehensive database and solution models for oxygen steelmaking slags and the authors have an access to both models.

In developing thermodynamic models, the phases and possible species within the system need to be defined carefully. In this study, there are two phases defined in each thermodynamic model. Molten oxide phase consists of major slag components: SiO_2, MgO, CaO, FeO and MnO. It is known that Fe_2O_3 would also be present in addition to FeO. However it is hard to predict FeO/Fe_2O_3 ratio and there is no industrial data available for comparison. Since only FeO composition of BOF slags were reported by both Cicutti et al.[22,24] and Millman et al.[25,26], FeO was considered as the only Fe containing specie in the slag. Various possible solid oxide phases which are likely to be formed in the current system are included as a part of the calculations. They are pure CaO, MgO and SiO_2 and silicates such as di-calcium silicate (C_2S), tri-calcium silicate (C_3S), and $MgSiO_3$, $CaSiO_3$, Ca_2SiO_4,

$Ca_2MgSi_2O_7$, $Ca_3MgSi_2O_8$. The appropriate solution models for each phase also need to be evaluated based on solution structure and behavior. The specific details of each thermodynamic model are described below.

a. FactSage™:

The saturation concentration of CaO is calculated using the "Phase Diagram" module in FactSage 6.4™. A pseudo ternary diagram is plotted for representing the slag composition at the temperature of each time step, with the composition/weight fraction of MgO and MnO being defined as constants, while the variation of composition of the major components namely, SiO_2, CaO and FeO is represented on the three axes of the ternary diagram.

FToxid solution database and FToxid compound database are selected for describing both solution (slag) and solid oxides pertaining to the oxygen steelmaking operations. The database is based on Quasi-chemical solution models for various binary, ternary and quaternary sub-systems of SiO_2, CaO, FeO, MgO and MnO which have been validated with the experimental data available in literature[27–29] and further optimized and evaluated together at all compositions[30].

b. Thermo-Calc™:

The saturation concentration of CaO is computed directly for a given slag composition and temperature using the SLAG2 database in Thermo-Calc™, where the Kapoor-Frohberg-Gaye Quasi-chemical Cell Model[31] is used to describe the liquid slag phase. The temperature, pressure (assumed constant, 1 Bar) and fractions of slag are first defined whilst leaving CaO as a free condition, thus leaving one degree of freedom. The last condition is

set to fix the phase $3CaO\text{-}SiO_2$ to zero, if this calculation fails a switch to CaO is made to account for the alternate mechanism described below. This is whether the liquid is in equilibrium with the tri-calcium silicate phase or the CaO phase at the saturation limit.

c. Cell Model:

The Cell model is also based on the Quasi-chemical solution model. Kapoor and Frohberg[32] suggested the cell model where oxides are described by two sub-lattices. Gaye and Wilfringer[33] modified this model to include polyanionic and multi-component melts and Graham[34] suggested a numerical approach to the model.

In the cell model, slag is described as a mixture of components having molecular formulae (Mi)ui(O)vi and (Mi)ui(S)vi using a two sub-lattice thermodynamic approach. An anionic vacancy free sub-lattice occupied by oxygen ions and a cationic sub-lattice occupied by cations and cationic entities exists according to the order of their decreasing electrical charge. Cationic entity is defined as cations doubly bonded to one oxygen atom. This extension is helpful to describe the behavior of some oxides which do not release all their oxygen to anionic sub-lattice, such as P_2O_5[35]. A change in the state of oxygen ions polarization can be written as:

$$O^0 + O^{2-} = 2O^- \tag{6.7}$$

Conservation of charge is maintained using cationic and anionic mass balance equations[34]:

$$Cations: \quad \sum_{k=1}^{p} R_{ii}^{k} + \sum_{k=1}^{m} \sum_{\substack{j=1 \\ j \neq 1}}^{p} R_{ij}^{k} = \sum_{k=1}^{p} v_{ik} x_{ik} \tag{6.8}$$

$$Anions: \qquad \sum_{k=1}^{m} R_{ii}^{k} + \sum_{\substack{j=1 \\ j\neq 1}}^{m} R_{ij}^{k} = \sum_{i=1}^{p} v_{ik} x_{ik} \tag{6.9}$$

where R_{ii}^{k} and R_{ij}^{k} represent the number of symmetric (i-k-i) and asymmetric (i-k-j) cells, v_{ik} the anion stoichiometric index of the component, x_{ik} the mole fraction of cation-i and anion-k and m, p are the number of cations and anions, respectively. For a given system, Gaye et al.[33] assumed that: (i) each cation appears in two cells, (ii) each symmetrical cell contains two cations, and (iii) that there are two asymmetrical cells.

There are two types of energy parameters required to describe the formation of cells to determine the activity coefficients of metal oxides in slag as a function of composition and temperature, (i) the formation energy W_{ij}, of the asymmetric cells corresponding to the reaction between two symmetric cells M_iOM_i and M_jOM_j : (ii) interaction energies limited to one parameter per couple of cations, Eij describing the binary interaction energy between symmetric and asymmetric cells. For the calculations the values of the energy parameters were referred from the work of Gaye and coworkers [35,36] .The calculation procedure for saturation concentration of CaO in the slag using Cell Model[34] is provided in Appendix: section 6.7 .

A pseudo ternary diagram is plotted for representing the slag composition, at the temperature of each time step, with the composition/weight fraction of MgO and MnO being defined as constants, while the variation of composition of the major components namely, SiO_2, CaO and FeO is represented on the three axes of the ternary diagram. Then the activities of various compounds along the locus of points with constant SiO_2/FeO ratio

of the slag are monitored. The change in activity of a phase indicates a precipitated compound (C_2S or C_3S or CaO) due to addition of lime in slag.

The predicted saturation concentration of CaO using various thermodynamic models is entered to the Equation 6.2 to calculate the dissolution rate of lime particles. The computational coupling of thermodynamic and kinetic models is explained later.

The saturation concentration of MgO was calculated using a correlation suggested by Chen *et al.*[37]. This correlation is based on the phase diagram CaO–MgO–FeO–SiO_2 slag saturated with magnesiowustite at 1873K (1600 ^oC) reported in literature and is function of slag composition and temperature. Since the results for the saturation concentration of MgO was consistent with the values reported in the literature[37], the same correlation was used in this study.

6.2.3 **Temperature Profile**

It is known that the temperature of metal bath (T_b) increases linearly during the oxygen blow with regard to the previous studies[38,39]. The metal temperature can be approximated using;

$$T_b = z.t_i + T_{b,0} \tag{6.10}$$

Where z is a constant varying from one practice to another, t_i is the time of the blow in min and T_b is the bath temperature in K.

On the other hand, there is limited information available about the slag temperature. Dogan *et al.*[18] assumed that slag temperature is 100K higher than the bath temperature. Alternatively, Bardenhuer *et al.*[40] suggested that it is 250K higher than bath temperature during the early part of the blow, decreasing to 50K higher at the end of the blow. In this

study, slag temperature is calculated based on two assumptions made in literature. The effects of these assumptions on the predictions of saturation concentrations and dissolution rates of fluxes are discussed later.

Temperature profile 1 is given by the following equation 6.11.

$$T_s = T_b + 100 \tag{6.11}$$

Temperature profile 2 explained by the following equation 6.12 .

$$T_s = T_b - 12.95.\, t_i + 263.51 \tag{6.12}$$

Where T_s is the slag temperature in K. As shown in Figure 6.1, the temperature profile 1 is steeper than temperature profile 2.

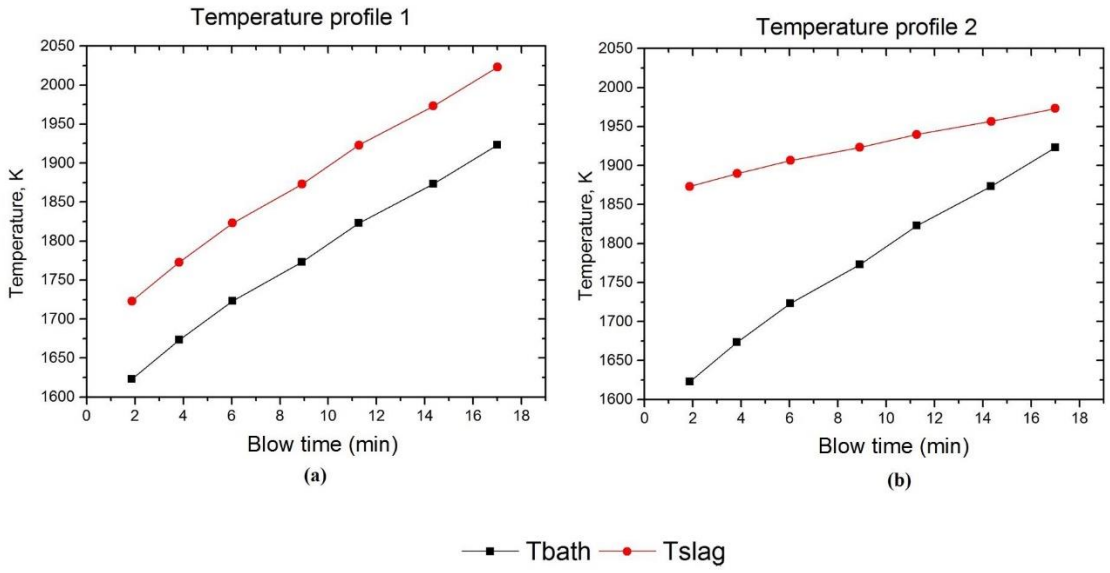

Figure 6.1: Slag temperature profiles.

6.3 Formulation of the Model

The computational solution is based on a stepwise calculation of the flux dissolution and it allows for a continuous calculation of the change in the radius of flux particles throughout the oxygen steelmaking process. The basis of this model was a central sub-model where the change in the amount of flux dissolved was calculated as a function of the process variables and parameters considered by the initiation of data required, and a calculation of crucial parts of the kinetics of this process.

Initially, global parameters such as the gas constant, molecular weight of metal oxides and density of lime, lance dynamics, oxygen blowing conditions and furnace charges such as hot metal, and scrap and flux additions were entered into the central sub-model as input data. The bath and slag temperatures were calculated to obtain the physical properties of slag and gas phases such as density and viscosity. Flux dissolution was calculated as a function of composition, temperature, and the physical properties of slag. The sequence of calculation procedure was explained elsewhere[18].

In this model, a time step of 1 min was selected to be consistent with the input data available in literature[22,24,25] to calculate the amount of CaO and MgO dissolved at the end of each time step. For dynamic calculation of the saturation concentration of CaO in the slag, a custom program interface was created using the Thermo-Calc™ Software Developers Kit (SDK)TQ, which made it possible to interface Thermo-Calc™ to the kinetic model[18] directly in Scilab. Similar approach could be applied to couple FactSage™ with Scilab. The Cell-model was originally developed using MATLAB and was converted to SCILAB for this study.

6.4 Input Data

The flux dissolution model was compared with the industrial data published in the literature[22,24–26]. The data-set from Cicutti *et al.*[22] at Siderar Steel, Argentina was obtained from a 200-t BOF converter while three distinct data-sets representing unique slag paths from Millman *et al.*[25] were based on pilot-plant trials in a 6-t BOF converter. The details of the operating parameters are summarized in Table 6.1.

In the case of operating conditions reported by Cicutti *et al.* [22,24], 1000 kg of lime was added to the system before the blow and the remaining amount of lime was added during the first seven minutes of the blow at a constant rate. It was assumed that 1200 kg of lime dissolved into the process at the end of first minute to be consistent with the industrial data. In case of the operating conditions for three heats reported by Millman *et al.*[26], there was no flux addition before the start of the blow and all lime was added during the first two minutes of the blow. In this study it was assumed that 40 kg of lime to be dissolved in the slag during the end of first minute. The remaining/undissolved lime and the rest of the lime added in the second minute were assumed to dissolve together.

In this study, it was assumed that the initial particle diameter of flux additions for Cicutti *et al.*[22,24] is same for every addition at various times and an initial particle diameter equals to be 30 mm, whereas it is taken to be 2.88 mm for the calculations pertaining to plant data reported by Millman *et al.*[26]

Table 6.1: Operating conditions of three oxygen steelmaking process trials[22,24–26]

<table>
<tr><td></td><td>Cicutti et al.[22,24]</td><td colspan="3">Millman et al.[25,26]</td></tr>
<tr><td>Amount of hot metal charged , kg</td><td>170000</td><td colspan="3">~4600- 5200</td></tr>
<tr><td>Amount of scrap charged , kg</td><td>30000</td><td colspan="3">500-700</td></tr>
<tr><td rowspan="2">Lime addition, kg</td><td rowspan="2">7600</td><td>S1835</td><td>S1840</td><td>S1845</td></tr>
<tr><td>350</td><td>300</td><td>250</td></tr>
<tr><td>Dolomite addition, kg</td><td>2800</td><td colspan="3">No addition</td></tr>
<tr><td>Initial hot metal temperature, K (°C)</td><td>1623K (1350 °C)</td><td colspan="3">1573K (1300 °C)</td></tr>
<tr><td>Tapping temperature, K (°C)</td><td>1923K (1650 °C)</td><td colspan="3">2023K (1750 °C)</td></tr>
<tr><td>Oxygen blow</td><td>620 m^3/min, 6 hole lance</td><td colspan="3">17 m^3/min, 1 hole lance</td></tr>
<tr><td>Inert gas (Ar/N_2), m^3/h through the bottom</td><td>150-500</td><td colspan="3">30</td></tr>
<tr><td rowspan="3">Lance height, m</td><td rowspan="3">2.5m/ 2.2m/ 1.8m</td><td>S1835</td><td colspan="2">0.17 m (0-6 min)/
0.16 m (6-16 min)</td></tr>
<tr><td>S1840</td><td colspan="2">0.18 m (0-2 min) /
0.17 m (2-4 min)/
0.16 m (4-16 min)</td></tr>
<tr><td>S1845</td><td colspan="2">0.17 m (0-2 min)/
0.16 m (2-4 min)/
0.15 m (4-16 min)</td></tr>
</table>

6.5 Results and Discussion

6.5.1 Control mechanism of flux dissolution

The addition of lime to the oxygen steelmaking slag would lead to saturation by precipitation of silicate or by presence of free lime as discussed in section 6.2.1.

Accordingly, two control mechanisms for lime dissolution in oxygen steelmaking slags are proposed based on the evaluation of the phase equilibria for slag-lime system under various operating conditions using different thermodynamic models. In this work, the first precipitated product at the saturation would indicate the controlling mechanism for the lime dissolution.

Figure 6.2 shows the evaluation of phase equilibria assuming temperature profile 1 and using the data for slag composition reported by Cicutti *et al.*[22] predicted by FactSage™. The colored markers represent the slag compositions at various time steps. The nose shaped curves with corresponding color represent the stability of C_2S phase field (Slag+ CaO+ C_2S) while the region below the straight lines represent the phase field where free lime exists. For example the addition of undissolved CaO to the slag results in moving from stable slag phase field to the boundary of silicate phase field or "C_2S Nose" and leads to saturation of slag with C_2S in the early part of the blow. In other words, the dissolution mechanism of lime is limited by the saturation level of C_2S (in addition tri-calcium silicate may be present in certain cases), as C_2S is thermodynamically stable. This is referred as *the silicate controlled mechanism* for lime dissolution. In Figure 6.2, the silicate control is observed in the first half of the blow where the ratio of CaO to SiO_2< 2. Saturation with di-calcium silicate occurs at high silica concentration in the slag phase. This finding is consistent with previous studies[8,41].

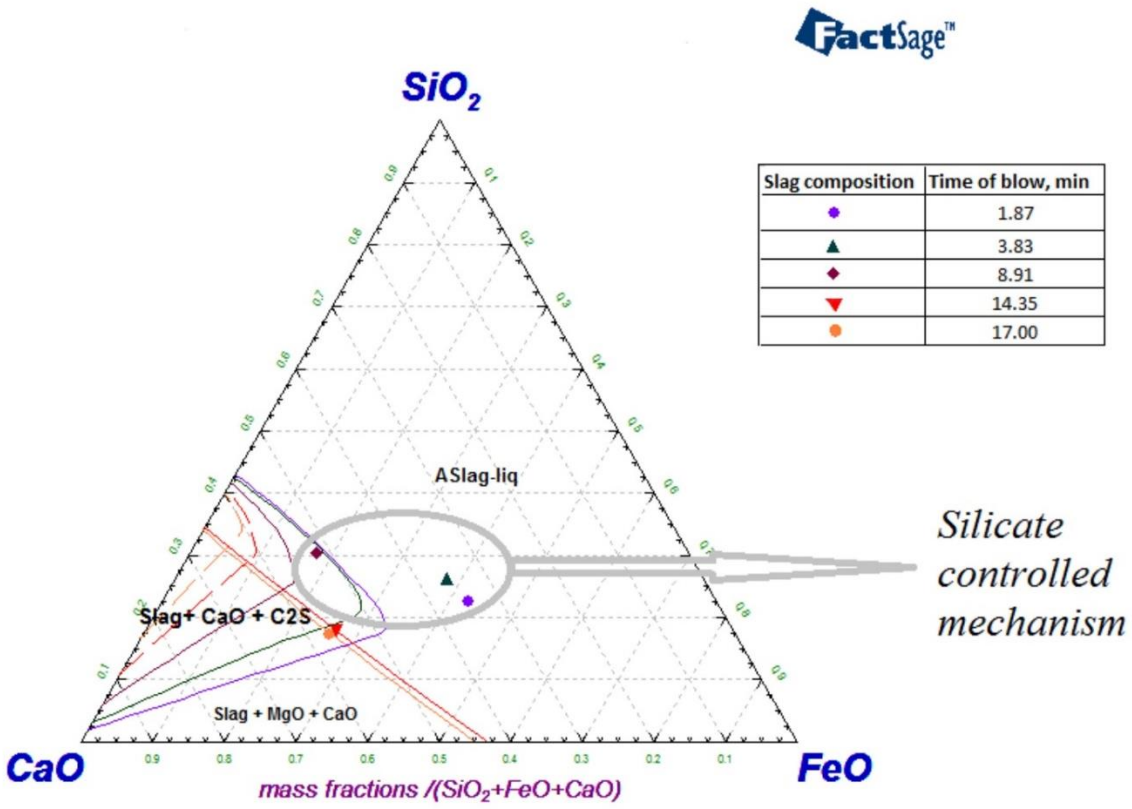

Figure 6.2: Silicate controlled mechanism for lime dissolution predicted by FactSage using the industrial data obtained from Cicutti et al.[22] assuming temperature profile 1. The markers represent the slag compositions at various time steps whereas the correspond

Towards the end of the blow there was an increase in the concentration of CaO and the slag composition encounters the "free lime" phase field. The silicate phase field becomes smaller, and the dissolution mechanism of lime is limited by the saturation level of free lime in equilibrium with the slag. This is refered as *free lime controlled mechanism* and this control mechanism was predicted for certain slag paths at higher temperatures (above 1823K (1550 ^{o}C). Figure 6.3 illustrates the free lime control mechanism for lime dissolution using the data of the slag path (Heat 1840) reported by Millman *et al.*[25]. Through addition of undissolved lime, the slag composition moves towards the CaO end of the ternary

diagram, the "free lime" phase field was encountered without going through the silicate phase field during the entire blow.

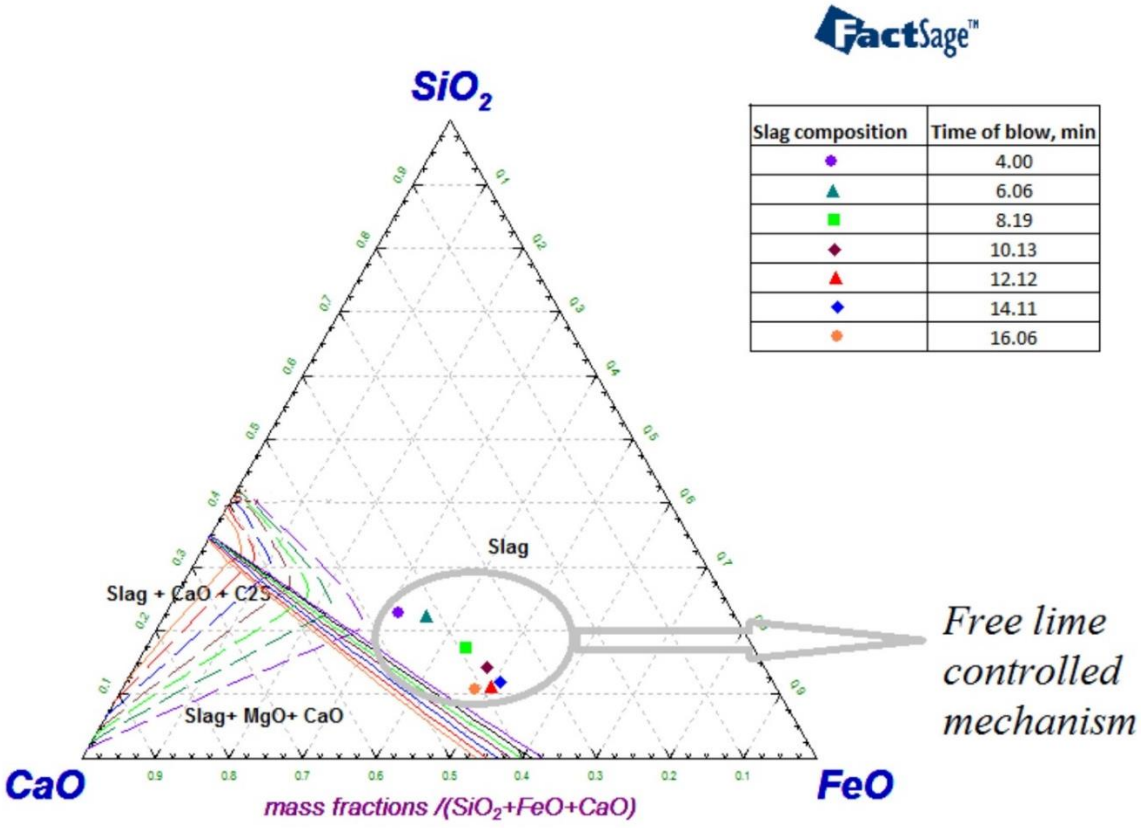

Figure 6.3: Free lime controlled dissolution of lime calculated by FactSage using the industrial data obtained from Millman et al.[25] (Heat S1840) assuming temperature profile 1. The markers represent the slag compositions at various time steps, whereas the corresponding colored solid lines represent the phase field leading to the control mechanism.

6.5.2 **Predictions for the Saturation Concentration of CaO**

Figure 6.4 compares the saturation concentration of CaO predicted by three thermodynamic models using the data reported by Cicutti *et al.*[24] In this comparison, the sub-figures "a" represent the predictions based on an assumption of slag temperature profile 1 whereas the sub-figures "b" represent those using temperature profile 2 as described in section 6.2.3. In

Figure 6.4-6.7, solid markers represent the values based on silicate control mechanism whereas hollow markers represent the values based on free lime control mechanism.

The predictions of saturation concentration of CaO using FactSage™, Thermo-Calc™ and Cell Model are quite close to each other except at the start of the blow as shown in Figure 6.4 (a) and (b). In the early part of the blow the values for the saturation concentration of CaO is higher using temperature profile 2 compared to the temperature profile 1. This is due to the fact that slag temperature is 150K higher using temperature profile 2. Alternatively similar values were found during the rest of the blow. The increase in the values predicted using temperature profile 2 is much lower compared to the values using temperature profile 1. The highest value was predicted at the end of the blow and equal to 52 wt %.

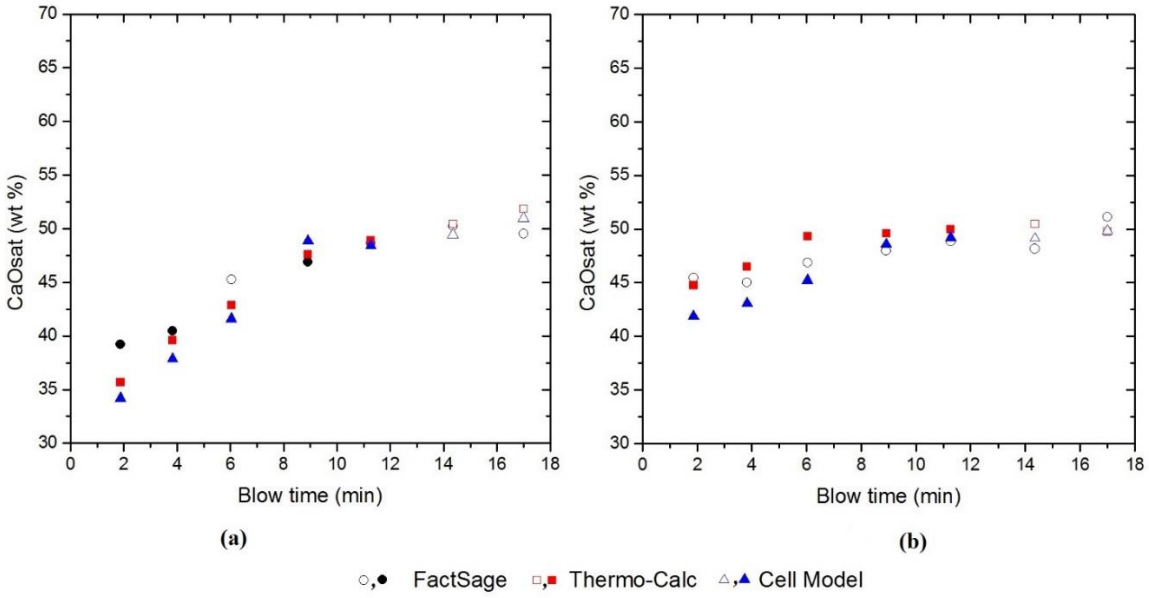

Figure 6.4: Comparison of saturation concentration of CaO predicted by FactSage, Thermo-Calc™ and Cell Model using the data for slag compositions reported by Cicutti et al.[22] with respect to (a) temperature profile 1 (b) temperature profile 2 (Solid markers: Silicate control mechanism, Hollow markers: Free lime control mechanism).

Figure 6.4(a) predicted that slag is saturated by either di- or tri-calcium silicate and silicate control mechanism dominates the flux dissolution between 2-12 min. Towards the end of the blow, the free lime control mechanism governs the flux dissolution. Regardless of temperature profile selected, the predictions of control mechanism by Thermo-Calc™ and Cell Model are consistent with experimental observations of silicate layer formation when the ratio of $CaO/SiO_2 < 2$ in literature.

The predictions of the saturation concentration of CaO using the industrial data (Heat S1835) reported by Millman *et al.*[25] were compared in Figure 6.5. It was found that silicate control mechanism dominates the flux dissolution during the entire blowing period regardless of temperature profile selected. The suggested stable product is C_2S for FactSage™ for both temperature profiles. The Thermo-Calc™ and Cell Model predict either C_2S or C_3S as a stable product during the blow and the predictions are close to those by FactSage™ when the predicted stable product is C_2S. The saturation concentration of CaO increases steadily as the blow progresses with respect to the temperature profile 1. At higher tempertures there is a slight increase found as given in Figure 6.5(b). There are some deviations observed for Thermo-Calc™ calculations due to the change in the predictions of C_2S and C_3S.

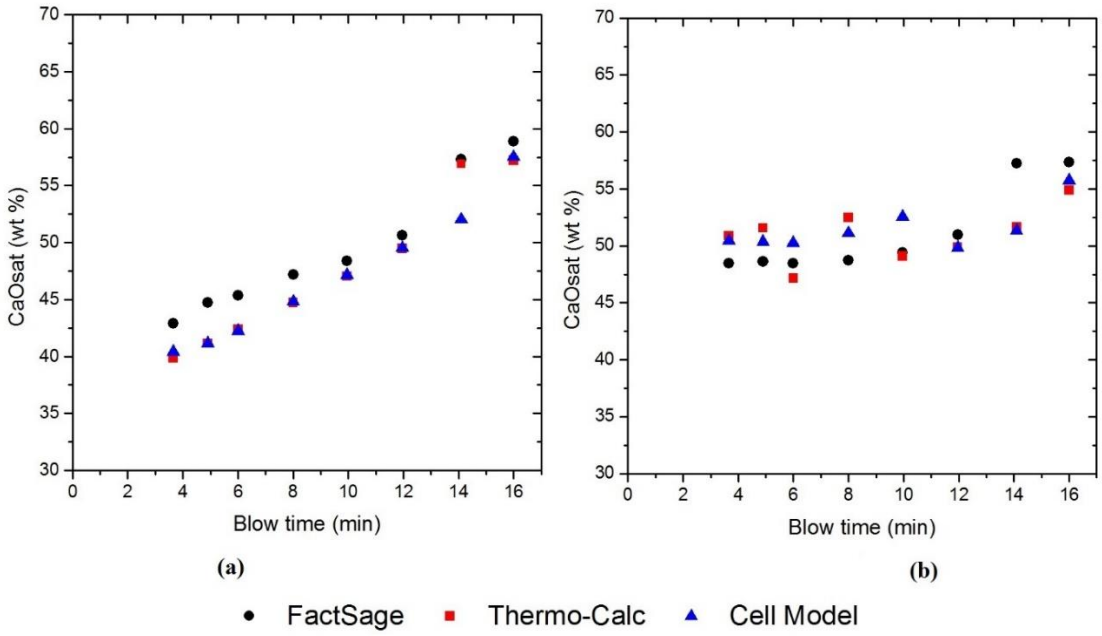

Figure 6.5: Comparison of saturation concentration of CaO predicted by FactSage, Thermo-Calc™ and Cell Model using the data for slag compositions reported by Millman et al. (Heat S1835) with respect to (a) temperature profile 1 (b) temperature profile 2. (Solid markers: Silicate control mechanism, Hollow markers: Free lime control mechanism)

The predicted values for the saturation concentration of CaO for Heat S1840 (slag path presented in Figure 6.3) were compared in Figure 6.6. Figure 6.6(a) shows that the values predicted by FactSage are higher than those predicted by other two thermodynamic models in the early part of the blow. This is due to prediction of C_2S as the stable product by FactSage™ contrary to C_3S by other models. FactSage predicts an earlier onset of the free lime control mechanism of lime dissolution (~3 min) as compared to Thermo-Calc™ (10 min) and Cell Model (8 min), which is a reason for deviations in the subsequent predictions. The silicate layer is expected to be unstable with respect to the ratio of $CaO/SiO_2>2$ for slag compositions provided for Heat 1840. Therefore FactSage is able to predict the suggested stable product by the previous studies. For the second temperature profile, similar dissolution mechanisms were predicted. The saturation concentrations steadily

increase and get plateaued using the first temperature profile, but the saturation concentrations actually decrease for the second temperature profile with the progress of the blow.

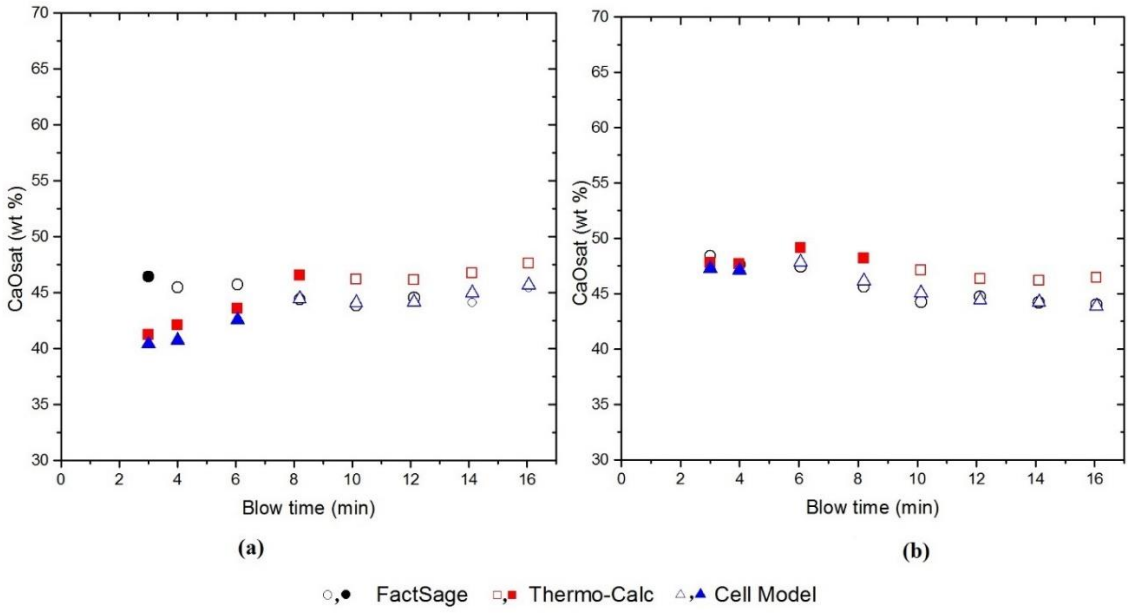

Figure 6.6: Comparison of saturation concentration of CaO predicted by FactSage, Thermo-Calc™ and Cell Model using the data for slag compositions reported by Millman et al.[25,26] (Heat S1840) with respect to (a) temperature profile 1 (b) temperature profile 2 (Solid markers: Silicate control mechanism, Hollow markers: Free lime control mechanism)

Figure 6.7 compares the saturation concentration of CaO predicted by three different models for Heat S1845. For the temperature profile 1, the predictions of Cell Model and Thermo-Calc™ are lower than those reported by FactSage, between 2nd and 5th minute. The difference in the values becomes insignificant as the blow progresses. It is shown that there is only a slight deviation using the second temperature profile except between 8 and 14 min in Figure 6.7(b) . With regards to the control mechanism, FactSage predicts earlier onset of free lime dissolution mechanism for both profiles as compared to the other two models.

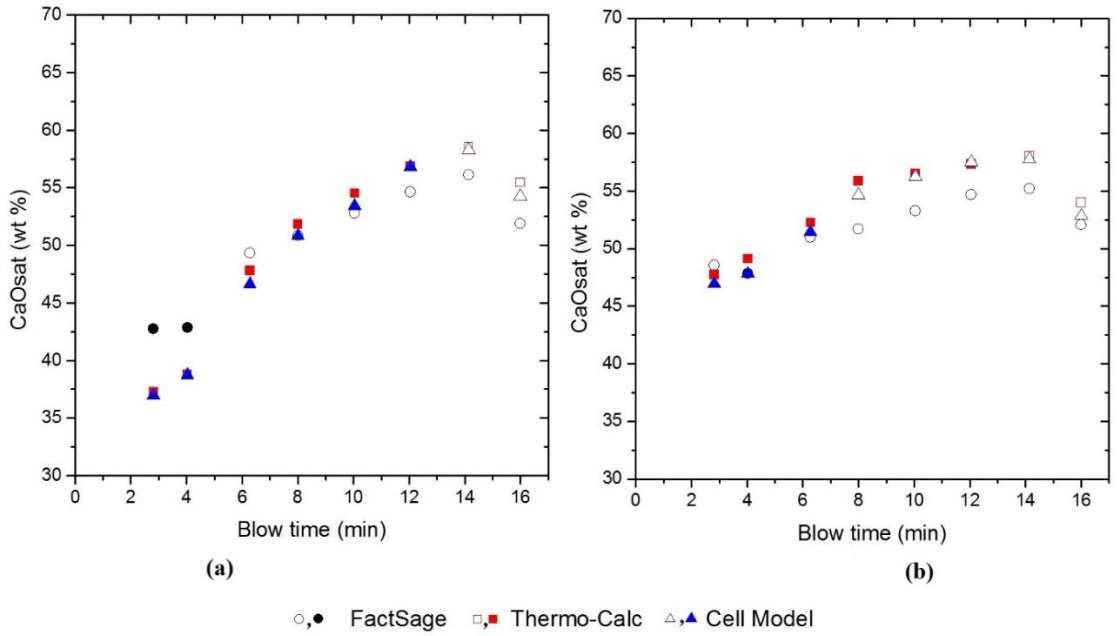

Figure 6.7: Comparison of saturation concentration of CaO predicted by FactSage, Thermo-Calc™ and Cell Model using the data for slag compositions reported by Millman et al.[25,26] (Heat S1845) with respect to (a) temperature profile 1 (b) temperature profile 2 (Solid markers: Silicate control mechanism, Hollow markers: Free lime control mechanism)

The saturation concentration of CaO steadily increased with the progress of the blow and reached to 57 weight % at 14th min of the blow followed by a decrease towards the end of the blow. This might be due to the blowing regime for Heat S1845. Amongst three heats reported by Millman *et al.*[26] Heat S1845 has the hardest blow regime with a lance pattern given in Table 1. The hard blow towards the end of blow causes a sudden increase in FeO content of slag (from 12 to 21.5 wt %), which would move the slag composition away from the CaO rich part of the phase diagram.

Some general observations of the predictions of the thermodynamic tools are as follows:

1. The saturation concentration of CaO increases with the progress of the blow. The rate of increase is much steeper for the first temperature profile compared to the

second temperature profile. There is a slight change in the saturation concentrations in most cases using temperature profile 2.

2. Similar trend for the values of saturation concentration of CaO were predicted by all models regardless of the temperature profile. However the values predicted by Cell Model and Thermo-Calc™ are lower than those predicted by FactSage™ for silicate control mechanism. This prediction was particularly observed when C_3S is predicted as a stable product by Cell Model and Thermo-Calc™ contrary to C_2S by FactSage™. The difference between the values becomes insignificant as the blow progresses. In the case of free lime control mechanism, the saturation concentrations predicted by all thermodynamic models are close to each other.
3. It is established that the silicate film formed in slags of high FeO content and low SiO_2 content are unstable and discontinuous and have a small retarding effect on the dissolution of the lime. Thermo-Calc™ and Cell Model were able to better predict the silicate formation under various blowing conditions except early part of the blow for Heat S1840. It should be noted that the predictions using Thermo-Calc™ (Slag 2 database) and Cell Model were expected to be close to each other as both are based on the Kapoor-Frohberg-Gaye Quasichemical model.
4. One of the major challenges in a thermodynamic model of steelmaking is the determination of an appropriate solution model for each phase particularly for slag phase in the steelmaking processes. The interactions between different species in a phase at different concentrations and temperatures are complex, and particularly in the case of phases where the basic molecular forms in the phase vary with

concentration and temperature, it is hard to find a solution model that works well for all conditions. What determines the actual saturation may be more complicated as shown by Deng[11], where the available concentration of the slag is shown to be different depending on the penetration depth into the lime particles.

6.5.3 Predictions for Lime Dissolution

Flux dissolution model is coupled with thermodynamic models using various methods explained in section 6.3. Accordingly, different thermodynamic models have been used to determine the saturation concentrations of CaO for the calculation of dissolution rate of lime and dolomite particles in the slag. The flux dissolution model is validated against various industrial data. The results for the weight of undissolved lime were compared with those reported by Cicutti *et al.*[22] given in Figure 6.8 . The effect of two assumptions for temperature profile of slag is compared in Figure 6.8 (a) and (b).

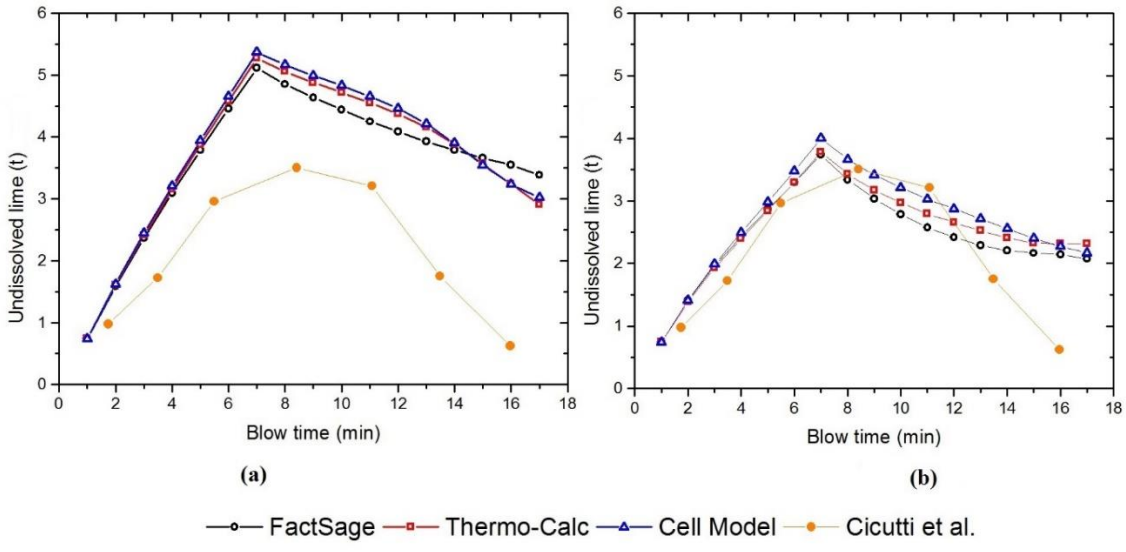

Figure 6.8: Comparison of undissolved lime using industrial data from the study of Cicutti et al. using (a) temperature profile 1(b) temperature profile 2

There is an increase in the amount of undissolved lime in the early part of the blow because there is a constant addition of lime to the oxygen steelmaking process till end of 7th min, followed by a gradual decrease as the blow progresses. Regardless of temperature profile selected, the dissolution path and the values for undissolved lime predicted by all models are close to each other. However the measured values reported by Cicutti *et al.*[22,24] agreed well with those predicted using temperature profile 2 as shown in Figure 6.8(b). Therefore, the authors suggest that the dissolution rate of lime particles can be reasonably predicted using any of the models with the assumption of temperature profile 2.

Figure 6.9 compares the amount of undissolved lime with respect to blowing time using industrial data Heat S1835 from the study of Millman et al[25]. There is an increase in the amount of undissolved lime until lime is added. Slag is saturated with di-calcium or tri-calcium silicate and thermodynamic force for dissolution is very limited particularly in the early part of the blow (2-6 min) and towards the end of the blow (12-16 min). This may be due to the presence of low concentration of FeO in the slag (<15 wt %) and low ratio of CaO/SiO_2. High concentration of FeO in slag is found to lower the stability of the di-calcium silicate. However the effect is not evident for the second temperature profile as relatively higher temperatures decrease the stability of the silicates and nullify the effect of low concentration of FeO in slag. The dissolution of lime progresses gradually at the end of 6th min after the blow starts.

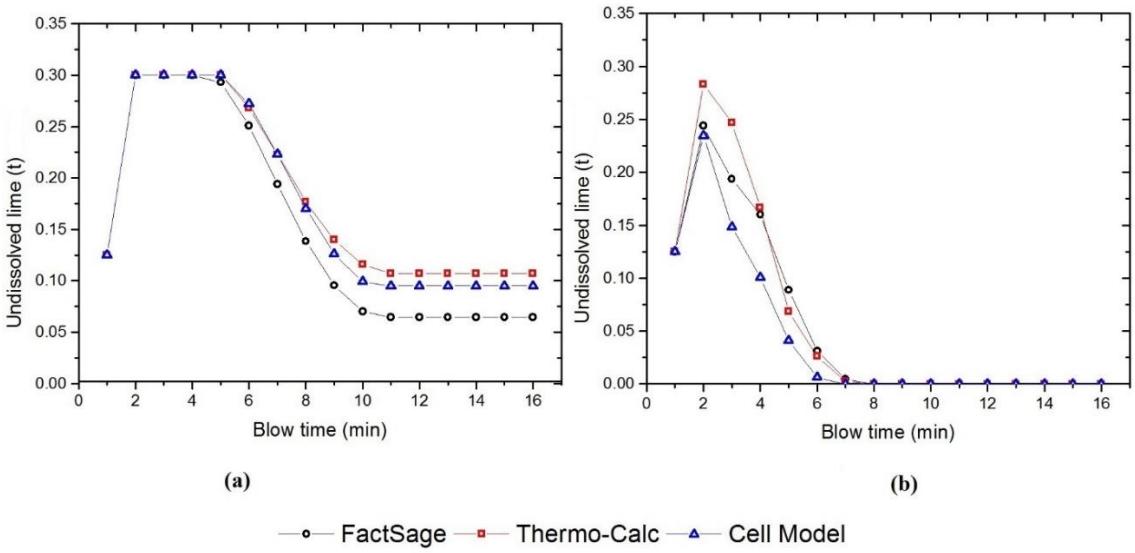

Figure 6.9: Comparison of undissolved lime using industrial data S-1835 from the study of Millman et al. using (a) temperature profile 1 (b) temperature profile 2

The amount of undissolved lime and the dissolution path predicted by Cell Model and Thermo-Calc™ are close to each other and lower than those predicted by FactSage™ as shown in Figure 6.9(a). Moreover the values of undissolved lime simulated with two temperature profiles are significantly different. Based on temperature profile 2, the dissolution of lime progresses simultanously as soon as lime is added to the process. The dissolution rate is faster and all lime added is dissolved by 6-7 minutes into the blow. A possible reason for this is the higher saturation values predicted by the second temperature profile during the early part of the blow. This causes rapid dissolution contrary to the temperature profile 1, where there is no significant dissolution occurred up to 5 minutes (slags being saturated with CaO).

Figure 6.10 compares the amount of lime undissolved with respect to blowing time using industrial data Heat S1840 from the study of Millman *et al.*[26] It is shown that total amount of lime added to the process is completely dissolved and the dissolution path is almost

similar regardless of thermodynamic models selected. The time required for total dissolution is the only difference between temperature profile 1 and 2. The dissolution time varies from 7-9 mins for temperature profile 1 while it is 5 min for temperature profile 2.

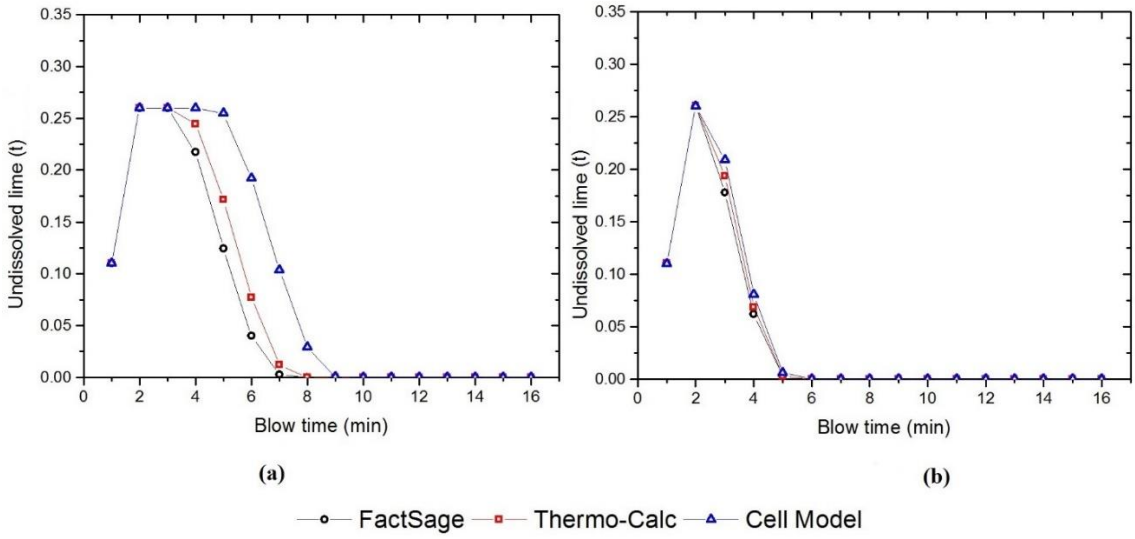

Figure 6.10: Comparison of undissolved lime using industrial data Heat S1840 from the study of Millman et al. using (a) temperature profile 1 (b) temperature profile 2

Figure 6.11 depicts the change in the amount of undissolved lime for two different temperature profiles. Similar results were found regarding to the dissolution pattern and time with respect to various models using both temperature profiles. There was some delay on the dissolution rate of lime predicted by Thermo-Calc™ and Cell Model due to the low values of saturation concentration of CaO in the early part of the blow.

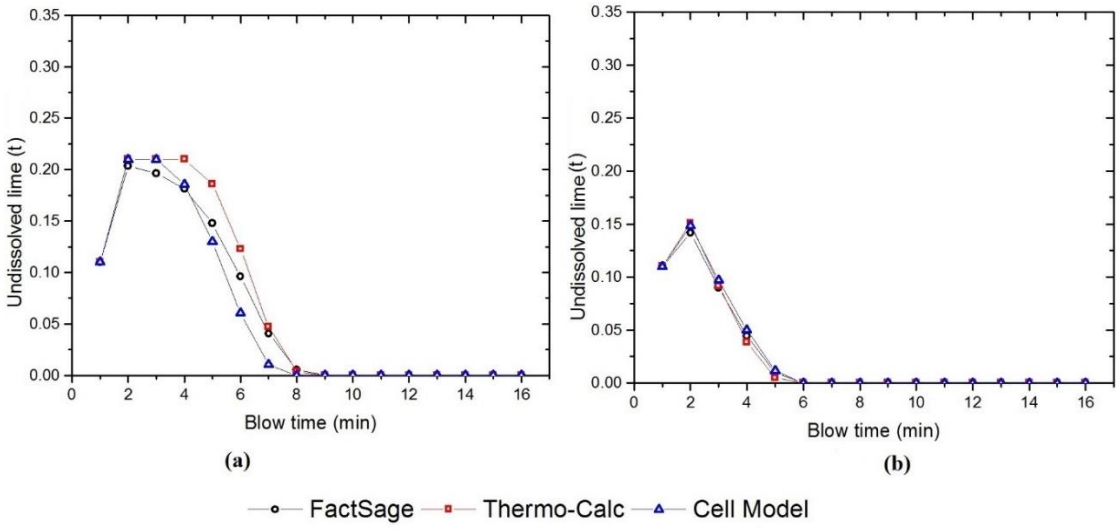

Figure 6.11: Comparison of undissolved lime using industrial data Heat S1845 from the study of Millman et al. using (a) temperature profile 1 (b) temperature profile 2

These findings are important for oxygen steelmaking process because the modified model enables to predict the progress of flux dissolution simultaneously under various flux addition rates and blowing conditions that affects the refining reactions and also the physical properties of slag. Accordingly, this model can be used for better process control of top blowing oxygen steelmaking process.

6.6 **Conclusion**

The kinetic model for lime dissolution as a function of temperature and slag composition was successfully linked with various thermodynamic models at high temperatures. The model provides better predictions of dissolution mechanism and dissolution rate of fluxes under various operating conditions. The following conclusions can be drawn from the present study:

1. A new mechanism for lime dissolution (free lime controlled mechanism) is proposed, which is previously not considered in lime dissolution models. For

certain slag paths, ignoring this mechanism would lead to inaccurate lime dissolution predictions.

2. Even though there were some differences in the performance of thermodynamic models (Cell Model, Thermo-Calc™, FactSage™) with respect to the predictions of control mechanism or saturation concentration of CaO, the coupled model successfully projected the lime dissolution behavior regardless of thermodynamic model selected during oxygen steelmaking process.
3. The values for undissolved lime predicted using temperature profile 2 was consistent with industrial data. Temperature profile 2 will be applied to calculate the slag temperature in future studies.
4. The dynamic linking of the kinetic and thermodynamic models would lead to a comprehensive understanding of the flux dissolution phenomenon under various industrial conditions.

Acknowledgements: The financial support by the Steel Research Center, McMaster University in gratefully acknowleged by the authors. The authors also wish to thank Mr.Alan Galindo for his help with regards to the Cell Model calculations.

6.7 Appendix

Calculation procedure of saturation concentration of CaO using Cell Model [34]

a. Cell Fraction Determination

In this step, for a given slag composition, the combination of cells (R_{ii}^{k} and R_{ij}^{k}) is determined such that the partition coefficient is maximized and hence yields the minimum value of free energy while satisfying the mass balance equations.

b. Calculation of Free energy

The free energy of liquid slag may be approximated from the partition function as:

$$G^M = -RTln\Omega \tag{6.A1}$$
$$= -RT\left(-\frac{E_{tot}}{RT} + \ln g\right)$$
$$= (E_{tot} + E_{int}) - RT(\ln(P) + \ln(U) + \ln(U^+))$$

where G^M is the free energy of mixing, R the ideal gas constant, T the temperature, E_{form} is the energy necessary for the formation of asymmetric cells from symmetric ones, E_{int} is the parameter introduced to describe the energy of interaction between different cells, P the total number of possible permutations of anions and cations, U the total number of randomly distinguishable permutations and U^* the maximum number of randomly distinguishable permutations. The partition coefficient, Ω, in the above equation is a measure of the number of states accessible to the system at a given temperature was defined as,

$$\Omega = \sum_i g_i e^{-\frac{e_i}{k_B T}} \tag{6.A2}$$

g_i is the degeneracy factor and refers to the number of states having energy e_i. The above equation is simplified by considering the 'most probable' energetic arrangement that maximizes the partition function

$$\Omega = g(E)e^{-\left(\frac{E}{RT}\right)} \tag{6.A3}$$

c. Component Activity Determination

Component activities referred to their pure liquid standard states are determined by computing the partial molar free energy of mixing for each slag component as

$$RTln(a_i) = G^M + \sum_{j=2}^{m}\left(\delta_{ij} - X_j\right)\left(\frac{\partial G^M}{\partial X_j}\right) \tag{6.A4}$$

where δ_{ij} is Kronecker's symbol (δ_{ij} = 1 for i=j and δ_{ij} = 0 for i≠ j).

d. Calculation of saturation concentration:

The saturation of CaO is calculated by iteratively calculating the activities of a system at different compositions until one of the stoichiometric components had precipitated as a solid phase. At initial upper and lower saturation points for a component (WT_{high} = 100wt% ; WT_{low} =0 wt%) the cell fractions (R_{ij}^k), free energy (G^M), and slag activities were recursively calculated until the upper and lower bounds have converged to within 0.01wt%. CaO saturation was assumed at a component activity (solid reference) of 0.9995 in order to ensure algorithm convergence at the true saturation point.

NOMENCLATURE:

W_L	Mass of dissolved lime (kg),
ρ_L	Density of lime (kg/m^3),
n_L	Number of lime particles
S	Surface area of particle (m^2),
t_i	Time (min)
dr/dt	Decrease radius of lime particles due to dissolution during a given time step (m/min)
Re	Reynold's number (dimensionless)
Sc	Schmidt number (dimensionless)
Sh	Sherwood number (dimensionless)
u_p	Settling velocity of particles, (m/s)
d_p	Diameter of solid particle, (m)
μ_s	Viscosity of slag, (kg/m.s)
ρ_s	Density of slag,(kg/m^3)
β	Modifying factor for settling velocity of flux particle (dimensionless)
t	Weight/Capacity of LD converter, Metric tonnes
R_{ii}^k and R_{ij}^k	Number of symmetric (i-k-i) and asymmetric (i-k-j) cells respectively
v_{ik}	Anion stoichiometric index of the component
x_{ik}	Mole fraction of cation-i and anion-k
m, p	Number of cations and anions respectively.
W_{ij}	Formation energy of an asymmetric cell
E_{ij}	Interaction energy between symmetric and asymmetric cells
G^M	Free energy of mixing
Ω	The partition coefficient
a_i	Activity of a slag component

6.8 References

1 Y. Satyoko and W.E. Lee: *Br. Ceram. Trans.*, 1999, vol. 98, pp. 261–5.

2 T. Hamano, M. Horibe, and K. Ito: *ISIJ Int.*, 2004, vol. 44, pp. 263–7.

3 T. Hamano, S. Fukagai, and F. Tsukihashi: *ISIJ Int.*, 2006, vol. 46, pp. 490–5.

4 J. Liu, M. Guo, P.T. Jones, F. Verhaeghe, B. Blanpain, and P. Wollants: *J. Eur. Ceram. Soc.*, 2007, vol. 27, pp. 1961–72.

5 S.H. Amini, M.P. Brungs, S. Jahanshahi, and O. Ostrovski: *Metall. Mater. Trans. B*, 2006, vol. 37, pp. 773–80.

6 S.H. Amini, M. Brungs, S. Jahanshahi, and O. Ostrovski: *ISIJ Int.*, 2006, vol. 46, pp. 1554–9.

7 S.H. Amini, O. Ostrovski, and M.P. Brungs: *VII Int. Conf. Molten Slags Fluxes Salts*, 2004, pp. 595–600.

8 M. Matsushima, S. Yadoomaru, K. Mori, and Y. Kawai: *Trans. ISIJ*, 1977, vol. 17, pp. 442–9.

9 H.Y. Sohn: *Metall. Trans. B*, 1978, vol. 9, pp. 89–96.

10 N. Maruoka, A. Ishikawa, H. Shibata, and S. Kitamura: *High Temp. Mater. Process.*, 2013, vol. 32, pp. 15–24.

11 T. Deng: Royal Institute of Technology (KTH), 2012.

12 S. Kitamura, H. Shibata, and N. Maruoka: *Steel Res. Int.*, 2008, vol. 79, p. 586.

13 I. Muchi, S. Asai, and M. Miwa: in *International Conference on Science and Technology of Iron and Steel*, Tokyo, 1970, pp. 347–51.

14 N. Dogan, G.A. Brooks, and M.A. Rhamdhani: *ISIJ Int.*, 2009, vol. 49, pp. 1474–82.

15 E. Graveland-Gisolf, P. Mink, A.B. Snoeijer, E. Barker, R. Boom, D. Dixit, and B. Deo: *Steel Res.*, 2003, vol. 74, pp. 125–30.

16 Y. Lytvynyuk, J. Schenk, M. Hiebler, and A. Sormann: *Steel Res. Int.*, 2014, vol. 85, pp. 537–43.

17 E. Graveland-Gisolf, P. Mink, A. Overbosch, R. Boom, G. de Gendt, and B. Deo: *Steel Res. Int.*, 2003, vol. 74, pp. 125–30.

18 N. Dogan, G. Brooks, and M.A. Rhamdhani: *ISIJ Int.*, 2009, vol. 49, pp. 1474–82.

19 F. Oeters: *Metallurgy of Steelmaking, Verlag Stahleisen GmbH*, Dusseldorf, 1994.

20 B.J. Keene and Mills K.C.: *Density of Molten Slags, Verlag Stahleisen GmbH*, Dusseldorf, 1995.

21 R. Clift, J. Grace, and M. Weber: *Bubbles, Drops and Particles*, 1st edn., New York, 1978.

22 C. Cicutti, M. Valdez, T. Pérez, R. Donayo, and J. Petroni: *Lat. Am. Appl. Res.*, 2002, vol. 32, pp. 237–40.

23 M. Umokoshi, M. Katsumi, and Y. Kawai: *Trans. ISIJ*, 1984, vol. 24, pp. 532–9.

24 C. Cicutti, M. Valdez, T. Perez, J. Petroni, A. Gomez, R. Donayo, and L. Ferro: in *6th International Conference on Molten Slags, Fluxes and Salts*, Stockholm-Helsinki, 2000, p. 367.

25 M.S. Millman, A. Overbosch, A. Kapilashrami, D. Malmberg, and M. Brämming: *Ironmak. Steelmak.*, 2011, vol. 38, pp. 499–509.

26 M.S. Millman, A. Kapilashrami, M. Bramming, and D. Malmberg: *Imphos : Improving Phosphorus Refining*, Luxemborg, 2011.

27 I.H. Jung, S.A. Decterov, and A.D. Pelton: *J. Eur. Ceram. Soc.*, 2005, vol. 25, pp. 313–33.

28 Y.B. Kang and I.H. Jung: in *International Symposium of Molten Salts and Slags*, Santiago, 2009.

29 S.A. Decterov, I.-H. Jung, and A.D. Pelton: *J. Am. Ceram. Soc.*, 2004, vol. 85, pp. 2903–10.

30 www.factsage.com.

31 www.thermocalc.com.

32 M. Kapoor and M. Frohberg: in *Chemical Metallurgy of Iron and Steel*, Iron and Steel Institute., London, 1973, pp. 17–22.

33 H. Gaye and Welfringer: in *2nd International Symposium on Metallurgical Slags and Fluxes*, Metallurgical Society of AIME, Warrendale, PA, 1984, p. 357.

34 K. Graham: Ph.D Thesis, McMaster university, 2008.

35 H. Gaye, J. Lehmann, T. Matsumiya, and W. Yamada: in *4th International Conference on Molten Slags and Fluxes*, 1992, pp. 103–8.

36 H. Lehmann, J., and Gaye: *Rev. Int. des Hautes Temp. des Refract.*, 1992, vol. 28, pp. 81–90.

37 Y. Chen, G. a. Brooks, and S. a. Nightingale: *Can. Metall. Q.*, 2005, vol. 44, pp. 323–30.

38 A. Masui, K. Yamada, and K. Takahashi: in *The role of slag in Basic oxygen steelmaking processes, McMaster Symposium on Iron and Steelmaking No.4*, 1976, pp. 3.1-3.28.

39 S. Asai and I. Muchi: *Trans. ISIJ*, 1970, vol. 10, pp. 250–63.

40 F. Bardenheuer, H. vom Ende, and K.G. Speith: *Blast Furn. Steel Plant*, 1970, vol.

58, pp. 401–6.

41 P. Williams, M. Sunderland, and G. Briggs: *Ironmak. Steelmak.*, 1982, vol. 9, pp. 150–62.

Chapter 7

Concluding remarks

The current study aims to improve the reliability of dynamic modelling of oxygen steelmaking. This was accomplished through development of new process sub-models which were mechanistic, extensively relied on operational parameters and incorporated new insights developed from the experimental studies. Accordingly, the reaction models were developed for the emulsion, impact, slag-metal bulk and cavity zones along with dynamic flux dissolution model. The results for each sub-model have been validated against the experimental data and predictions made for the industrial heat of Cicutti et al.[27,100]. The aim was achieved as demonstrated in Chapter 3, Chapter 4, Chapter 5, Chapter 6.

7.1 Key Findings and Contributions

Chapter 3 presents a new mechanistic model for the impact zone, considering the role of oxygen jets and bottom stirring and quantifies the contribution of the reaction zone to the overall refining.

Chapter 4 presents a rigorous model for metal droplet behavior in the emulsion zone, based on insights derived from experimental studies. Further predictions are made with regards to the contribution of the reaction zone to decarburization under industrial operating conditions.

Chapter 5 proposes the cavity droplets as a new reaction zone. The refining behavior of ‘cavity-droplets’ splashed in oxygen jets is modelled, and its contribution is quantified.

Chapter 6 presents a new dynamic model for the flux dissolution model with the aid of thermodynamic models.

The specific findings of the current study are as follows:

1. In Chapter 3, it has been demonstrated that the impact zone (i.e., the surface of smooth cavities) and the slag-metal bulk have an insignificant contribution to the overall refining. Contrary to previously held belief, the proposed model finds that the momentum of the top-jets does not aid in the surface renewal and has a negligible impact on the refining reactions. Also, an increase in bottom stirring gas flow rate increases the circulation within the bath but does not significantly increase in the rate of surface renewal at the cavities. Even if the temperature at the impact zone is considered to be high (> 2000 ^{o}C), the limitation imposed by low metal circulation (at the cavity surface) on the reaction rate still prevails.
2. Chapter 4 describes the behavior of a single droplet in the slag based on observations from experiments recently conducted at McMaster University. This includes modelling of external and internal CO gas generation and the escape rate of CO gas. It has been found that the emulsion zone contributes to at least 20 % of the overall decarburization, even if a relatively low rate of droplet generation suggested by Subagyo et al.[97] is considered. The maximum residence time of droplets in the emulsion zone is 7.5 s, which is lower than that prescribed by previous studies. However, the suggested residence time is sufficient to achieve the refining of droplets. The bloating of droplets thereby the decarburization rate are primarily dependent on the initial carbon content of the metal droplet. The effects

of droplet size and the temperature are analyzed. The droplet size doesn't affect the decarburization rate, but the refining rates of other elements are affected by the change in (A/V) ratio as the refining takes place at the droplet-slag interface rather than inside the droplet, as in the case of decarburization.

3. In Chapter 5, the cavity zone, i.e. the droplets splashed in the oxidizing jets, is proposed as a site for refining reaction zone. The cavity zone is demonstrated to be a primary source of rapid refining of silicon and manganese in the early blow. Also, it explains the FeO formation throughout the blow and which is the primary source of oxygen to sustain refining reactions in the emulsion zone. Additionally, it has been found that the contribution of carbon refining increases with the progress of the blow.

4. Chapter 6 demonstrates the dynamic linking of thermodynamic tools with a kinetic model for flux dissolution. It leads to a comprehensive understanding of the flux dissolution phenomenon under various industrial conditions. A new mechanism for lime dissolution (a free lime-controlled mechanism) is proposed, which would be prevalent in certain slag paths and will lead to more accurate lime dissolution predictions.

7.2 Limitations of the current study and future work

1. A thorough investigation of the generation of CO bubbles within the metal droplets in emulsion zone is necessary, as classical nucleation theory cannot adequately explain the various aspects of internal CO generation like nucleation, growth and escape rate of CO.

2. Another limitation related to the emulsion zone model is that the slag density is calculated, assuming a constant volume fraction of CO gas = 0.8 in the emulsion zone. The volume fraction of gas varies during the blow and may affect the density of the foamy slag in the emulsion zone and in turn, affect the residence time of droplets in the emulsion zone. The dynamic variation of the slag-density needs to be better addressed in subsequent studies.
3. The temperature of the droplets in the emulsion and cavity zones is assumed to be equal to the bath temperature at a particular ejection time. While the excessively high temperature is less likely, a more definitive phenomenological study is required to identify the heat generation (through refining reactions) and distribution between gas, slag and hot-metal during different times of the blow.
4. The droplet generation rate and the distribution of these droplets within the cavity and emulsion zone are worth of further studies.
5. A chaotic environment exists in jet cavities formed in the oxygen steelmaking. Hence it is difficult to estimate the various model parameters like droplet ejection angles and residence times, droplet size distribution, oxidizing gas composition. More clarity is required on the dynamic variation of these parameters during the blow.
6. More investigation is required for better understanding the formation of FeO layer on the droplet surface with respect to droplet size. Experimental efforts must be directed towards ascertaining the time instant when the FeO formation on the droplet will be hindered.

7. For the flux dissolution model, homogenous liquid slag is assumed while calculating the saturation concentration of CaO and MgO. However, there is a likelihood of prevalence of inhomogeneity in slag, leading irregular distribution of components between solid and liquid components of slag, subsequently a different composition of liquid slag. A more detailed investigation is necessary in this regard.

References

1 A. Chatterjee, C. Mariqne, and N. Page: *Ironmak. Steelmak.*, 1984, vol. 11, p. 117.

2 T.W. Miller, J. Jimenez, A. Sharan, and D.A. Goldstein: *The Making, Shaping and Treating of Steel, 11th Edition Steelmaking and Refining Volume.*, 1998.

3 B. Deo and R. Boom: *Fundamentals of Steel Making Metallurgy*, Pretince Hall International, 1993.

4 K. Nakanishi, K. Saito, T. Nozaki, Y. Kato, K. Suzuki, and T. Emi: in *65th Steelmaking Conference Proceedings*, 1982, pp. 101–8.

5 X. Zhou, M. Ersson, L. Zhong, and P. Jönsson: *Metall. Mater. Trans. B Process Metall. Mater. Process. Sci.*, 2016, vol. 47, pp. 434–45.

6 R.D. Pehlke: *Metall. Trans. B*, 1980, vol. 11, pp. 539–62.

7 N. Dogan: Ph.D Thesis, Swinburne University, 2011.

8 K. Koch, W. Fix, and P. Valentin: *Arch. für das Eisenhüttenwes.*, 1976, vol. 47, p. 659.

9 K. Koch, W. Fix, and P. Valentin: *Arch. für das Eisenhüttenwes.*, 1978, vol. 49, p. 63.

10 A. Chatterjee, N.O. Lindfors, and J.A. Wester: *Ironmak. Steelmak.*, 1976, vol. 21, pp. 21–32.

11 V.S. Kocho: *Steel USSR*, 1971, vol. 1, p. 614.

12 S.K. Sharma, J.W. Hlinka, and D.W. Kern: in *NOH-BOSC Proceedings*, 1977, pp. 187–97.

13 W.G. Davenport, D.H. Wakelin, and A.V. Bradshaw: in *Heat andMass Transfer in*

ProcessMetallurgy, London, 1967, pp. 207–45.

14 H.W. Meyer, W.F. Porter, G. Smith, and J. Szekely: *J. Met.*, 1968, vol. 20, pp. 35–42.

15 J. Schoop, W. Resch, and G. Mahn: *Ironmak. Steelmak.*, 1978, vol. 2, pp. 72–9.

16 R.C. Urquhart and W.G. Davenport: *Can. Metall. Q.*, 1973, vol. 12, pp. 507–16.

17 M. Ersson, A. Tilliander, and P. Jonsson: in *Sohn Int. Symp. Advanced Processing of Metals and Materials, Vol. 2, , TMS, Warrendale, PA*, F. Kongoli and R.G. Reddy, eds., 2006, p. 271.

18 N. Dogan, G.A. Brooks, and M.A. Rhamdhani: *ISIJ Int.*, 2011, vol. 51, pp. 1102–9.

19 B.K. Rout, G. Brooks, M. Akbar Rhamdhani, Z. Li, F.N.H. Schrama, and A. Overbosch: *Metall. Mater. Trans. B*, 2018, vol. 49, pp. 1022–33.

20 F. Oeters: *Metallurgy of Steelmaking*, Verlag Stahleisen mbH., Berlin, 1994.

21 K. Koch, J. Falkus, and R. Bruckhaus: *Steel Res. Int.*, 1993, vol. 64, pp. 15–21.

22 D.J. Price: in *Process Engineering of Pyrometallurgy Symposium*, The Institution of Mining and Metallurgy, London, 1974, pp. 8–15.

23 Z. Han and L. Holappa: *ISIJ Int.*, 2003, vol. 43, pp. 292–7.

24 Z. Han and L. Holappa: *Metall. Mater. Trans. B*, 2003, vol. 34, pp. 525–32.

25 S. Kobayashi: *ISIJ Int.*, 1993, vol. 33, pp. 577–82.

26 A.I. van Hoorn, J.T. van Konynenburg, and P.J. Kreyger: in *The role of slag in Basic oxygen steelmaking processes, McMaster Symposium on Iron and Steelmaking No.4*, W.-K. Lu, ed., Hamilton, Ontario, 1976, pp. 2: 1-26.

27 C. Cicutti, M. Valdez, T. Pérez, R. Donayo, and J. Petroni: *Lat. Am. Appl. Res.*,

2002, vol. 32, pp. 237–40.

28 M.S. Millman, A. Kapilashrami, M. Bramming, and D. Malmberg: *Imphos : Improving Phosphorus Refining*, Luxemborg, 2011.

29 E.T. Turkdogan: *Fundamentals of Steelmaking*, The Institute of Materials, 1996.

30 K. Balajiva, A.G. Quarrell, and P. Vajragupta: *J. Iron Steel Inst.*, 1946, vol. 153, pp. 115–50.

31 A. Ghosh and A. Chatterjee: *Ironmaking and Steelmaking: Theory and Practice*, .

32 Y. Satyoko and W.E. Lee: *Br. Ceram. Trans.*, 1999, vol. 98, pp. 261–5.

33 S.H. Amini, O. Ostrovski, and M.P. Brungs: *VII Int. Conf. Molten Slags Fluxes Salts*, 2004, pp. 595–600.

34 T. Hamano, M. Horibe, and K. Ito: *ISIJ Int.*, 2004, vol. 44, pp. 263–7.

35 J. Liu, M. Guo, P.T. Jones, F. Verhaeghe, B. Blanpain, and P. Wollants: *J. Eur. Ceram. Soc.*, 2007, vol. 27, pp. 1961–72.

36 T. Hamano, S. Fukagai, and F. Tsukihashi: *ISIJ Int.*, 2006, vol. 46, pp. 490–5.

37 S.H. Amini, M.P. Brungs, S. Jahanshahi, and O. Ostrovski: *Metall. Mater. Trans. B*, 2006, vol. 37, pp. 773–80.

38 S.H. Amini, M. Brungs, S. Jahanshahi, and O. Ostrovski: *ISIJ Int.*, 2006, vol. 46, pp. 1554–9.

39 M. Matsushima, S. Yadoomaru, K. Mori, and Y. Kawai: *Trans. ISIJ*, 1977, vol. 17, pp. 442–9.

40 N. Maruoka, A. Ishikawa, H. Shibata, and S. Kitamura: *High Temp. Mater. Process.*, 2013, vol. 32, pp. 15–24.

41 T. Deng: Royal Institute of Technology (KTH), 2012.

42 I. Muchi, S. Asai, and M. Miwa: in *International Conference on Science and Technology of Iron and Steel*, vol. 11, Iron and Steel Institute, Tokyo, 1971, pp. 347–51.

43 N. Dogan, G. Brooks, and M.A. Rhamdhani: *ISIJ Int.*, 2009, vol. 49, pp. 1474–82.

44 E. Graveland-Gisolf, P. Mink, A. Overbosch, R. Boom, G. de Gendt, and B. Deo: *Steel Res. Int.*, 2003, vol. 74, pp. 125–30.

45 Y. Lytvynyuk, J. Schenk, M. Hiebler, and A. Sormann: *Steel Res. Int.*, 2014, vol. 85, pp. 537–43.

46 E.T. Turkdogan: *Physicochemical Properties of Molten Slags and Glasses*, 1983.

47 K.I. Naito, Y. Ogawa, T. Inomoto, S.Y. Kitamura, and M. Yano: *ISIJ Int.*, 2000, vol. 40, pp. 23–30.

48 M. Lee, V. Whitney, and N. Molloy: *Scand. Jounal Metall.*, 2001, vol. 30, pp. 330–6.

49 R. Banks and D.V. Chandrashekara: *J. Fluid Mech.*, 1963, vol. 15, pp. 13–34.

50 S.C. Koria and K.W. Lange: *Steel Res.*, 1987, vol. 58, pp. 421–6.

51 Q. He: Ph.D Thesis, University of Wollongong, 1990.

52 S. Sabah and G.A. Brooks: *Metall. Mater. Trans. B*, 2014, vol. 46, pp. 863–72.

53 H.Y. Hwang and G.A. Irons: *Metall. Mater. Trans. B Process Metall. Mater. Process. Sci.*, 2012, vol. 43, pp. 302–15.

54 H.Y. Hwang and G.A. Irons: *Metall. Mater. Trans. B Process Metall. Mater. Process. Sci.*, 2011, vol. 42, pp. 575–91.

55 M. Alam, J. Naser, G. Brooks, and A. Fontana: *ISIJ Int.*, 2012, vol. 52, pp. 1026–35.

56 Q. Li, M. Li, S. Kuang, and Z. Zou: *Metall. Mater. Trans. B Process Metall. Mater. Process. Sci.*, 2015, vol. 46, pp. 1494–509.

57 N.A. Molloy: *J. Iron Steel Inst.*, 1970, vol. 216, p. 943.

58 T. Fabritius, M. Luomala, E. Virtanen, H. Tenkku, T. Fabritius, T. Siivola, and J. Härkki: *ISIJ Int.*, 2002, vol. 42, pp. 861–867.

59 M.J. Luomala, T.M.J. Fabritius, and J.J. Härkki: *ISIJ Int.*, 2004, vol. 44, pp. 809–16.

60 M. Hino and K. Ito: *Thermodynamic Data for Steelmaking*, Tohoku University Press, Sendai, 2010.

61 G.K. Sigworth and J.F. Elliot: *Met. Sci.*, 1974, vol. 3, pp. 298–310.

62 Y. Kashiwaya, M. Hasegawa, H. Niitani, T. Kakinuma, and M. Iwase: *Steel Res. Int.*, 2010, vol. 81, pp. 333–6.

63 H. Sakao and T. Fujisawa: *Recommended Equilibrium Value of Steel-Making, 19th Committee, No. 1059*, 5th edn., Japan Society for Promotion of Science and Technology, Tokyo, 1982.

64 E.W. Mulholland, G.S. Hazeldean, and M. Davies: *J. Iron Steel Inst.*, 1973, vol. 211, pp. 632–9.

65 T. Gare and G.S.F. Hazeldean: *Ironmak. Steelmak.*, 1981, vol. 4, pp. 169–81.

66 H. Gaye and Riboud.P.V: *Metall. Trans. B*, 1977, vol. 8, pp. 409–15.

67 D.J. Min and R.J. Fruehan: *Metall. Trans. B*, 1992, vol. 23, pp. 29–37.

68 C.L. Molloseau and R.J. Fruehan: *Metall. Mater. Trans. B*, 2002, vol. 33, pp. 335–44.

69 E. Chen: Ph.D Thesis, McMaster University, 2011.

70 E. Chen and K.S. Coley: *Ironmak. Steelmak.*, 2010, vol. 37, pp. 541–5.

71 M.D. Pomeroy: MASc Thesis, McMaster University, 2011.

72 K.S. Coley, E. Chen, and M. Pomeroy: in *Proceedings of the Extraction and Processing Division Symposium on Pyrometallurgy in Honor of David G.C. Robertson*, P.J. Mackey, E.J. Grimsey, R.T. Jones, and G.A. Brooks, eds., 2014, pp. 289–302.

73 A. Paul, B. Deo, and N. Sathyamurthy: *Steel Res.*, 1994, vol. 65, pp. 414–28.

74 D.J. Min, J.W. Han, and W.S. Chung: *Metall. Mater. Trans. B Process Metall. Mater. Process. Sci.*, 1999, vol. 30, pp. 215–21.

75 M. Barati and K.S. Coley: *Metall. Mater. Trans. B*.

76 G.R. Belton and D.R. Sain: *Metall. Mater. Trans. B*, 1976, vol. 7B, pp. 235–44.

77 W. Cramb, W.R. Graham, and G.R. Belton: *Metall. Trans. B*.

78 F.J. Mannion and R.J. Fruehan: *Metall. Trans. B*, 1989, vol. 20, pp. 853–61.

79 L.A. Baker, N.A. Warner, and A.E. Jenkins: *Trans. Metall. Soc. AIME*, 1967, vol. 239, pp. 857–64.

80 L.A. Baker and R.G. Ward: *J. Iron Steel Inst*, 1967, vol. 205, pp. 714–7.

81 H. Sun: *ISIJ Int.*, 2006, vol. 46, pp. 1560–9.

82 S. Jahanshahi: Ph.D Thesis, Imperial College of Science and Technology, 1980.

83 K. Gao, V. Sahajwalla, H. Sun, C. Wheatley, and R. Dry: *ISIJ Int.*, 2000, vol. 40,

pp. 301–8.

84 G. Brooks, Y. Pan, Subagyo, and K.S. Coley: *Metall. Mater. Trans. B*, 2005, vol. 36, pp. 525–35.

85 K. Gu, N. Dogan, and K.S.K.S. Coley: *Metall. Mater. Trans. B Process Metall. Mater. Process. Sci.*, 2017, vol. 48, pp. 1–18.

86 H. Sun and G. Zhang: in *ICS Proceedings*, 2005, pp. 257–68.

87 R. Higbie: *Trans. Am. Inst. Chem. Eng.*, 1935, vol. 35, pp. 36–60.

88 B.K. Rout: Ph.D Thesis, Swinburne University, 2018.

89 H. Sun, K. Gao, V. Sahajwalla, and R.D. Pehlke: *ISIJ Int.*, 1999, vol. 39, pp. 25–33.

90 H. Sun and G. Zhang: in *3rd International Congress on Science ans Technology of Steelmaking*, 2005, pp. 257–68.

91 K. Gu, N. Dogan, and K.S. Coley: *Metall. Mater. Trans. B*, 2018, vol. 49, pp. 1119–35.

92 G.G. Krishna Murthy, Y. Sawada, and J.F. Elliott: *Ironmak. Steelmak.*, 1993, vol. 20, pp. 179–90.

93 G.M. Whitesides: *Adv. Mater.*, 2004, vol. 16, pp. 1375–7.

94 Q.L. He and N. Standish: 1990, vol. 30, pp. 356–61.

95 Q.L. He and N. Standish: *ISIJ Int.*, 1990, vol. 30, pp. 305–9.

96 R. Li and R.L. Harris: in *Pyrometallurgy 95 Conference Proceedings*, IMMM, London, 1995, p. 107.

97 Subagyo, G. a. Brooks, K.S. Coley, and G. a. Irons: *ISIJ Int.*, 2003, vol. 43, pp.

983–9.

98 B.K. Rout, G. Brooks, Subagyo, M.A. Rhamdhani, and Z. Li: *Metall. Mater. Trans. B*, 2016, vol. 47, pp. 3350–61.

99 T. Haas, A. Ringel, V.V. Visuri, M. Eickhoff, and H. Pfeifer: *Steel Res. Int.*, 2019, vol. 1900177, pp. 1–10.

100 C. Cicutti, M. Valdez, T. Perez, J. Petroni, A. Gomez, R. Donayo, and L. Ferro: in *6th International Conference on Molten Slags, Fluxes and Salts*, Stockholm-Helsinki, 2000, p. 367.

101 M.S. Millman, A. Overbosch, A. Kapilashrami, D. Malmberg, and M. Brämming: *Ironmak. Steelmak.*, 2011, vol. 38, pp. 499–509.

102 B. Trentini: *Trans. Metall. Soc. AIME*, 1968, vol. 242, pp. 2377-2388.

103 S.C. Koria and K.W. Lange: *Metall. Trans. B*, 1984, vol. 15, pp. 109–16.

104 K.D. Peaslee: in *Electric furnace conference proceedings*, 1993, p. 403.

105 N. Standish and Q.L. He: *ISIJ Int.*, 1989, vol. 29, pp. 455–61.

106 P. Kozakevitch: *J. Miner. Met. Metarials Soc.*, 1969, vol. 22, pp. 57–68.

107 B.K. Rout, G.A. Brooks, Z. Li, M.A. Rhamdhani, F.N.H. Schrama, and A. Overbosch: in *AISTech*, 2018, pp. 981–91.

108 B. Rout, G. Brooks, M.A. Rhamdhani, Z. Li, F.N. Schrama, and J. Sun: *Metall. Mater. Trans. B*, 2018, vol. 49, pp. 537–57.

109 P.A. Distin, G.D. Hallett, and F.D. Richardson: *J. Iron Steel Inst.*, 1968, vol. August, pp. 821–33.

110 D.G.C. Robertson and A.E. Jenkins: in *Heterogenous Kinetics at Elevated*

Temperatures, Proceedings of International conference in Materials and Process Metallurgy, G.R. Belton and W.L. Worell, eds., Philadelphia, 1969, pp. 393–408.

111 H.G. Lee and Y.K. Rao: *J. Electron. Mater.*, 1982, vol. 13, pp. 403–9.

112 H. Sun and R.D. Pehlke: *Metall. Mater. Trans. B*, 1995, vol. 26, pp. 335–44.

113 H. Sun and R.D. Pehlke: *Metall. Trans. B*, 1996, vol. 27, pp. 854–64.

114 M. Hayer and S.G. Whiteway: *Can. Metall. Q.*, 1973, vol. 12, pp. 23–34.

115 J.H. Swisher and E.T. Turkdogan: *Trans. Metall. Soc. AIME*, 1967, vol. 239, pp. 602–9.

116 S. Kitamura and K. Okohira: *Tetsu-to-Hagane*, 1990, vol. 76, pp. 199–206.

117 A. Nordqvist, A. Tilliander, K. Grönlund, G. Runnsjö, and P. Jönsson: *Ironmak. Steelmak.*, 2009, vol. 36, pp. 421–31.

118 D. Widlund, D.S. Sarma, and P.G. Jönsson: *ISIJ Int.*, 2006, vol. 46, pp. 1149–57.

119 E. Shibata, H. Sun, and K. Mori: *Metall. Mater. Trans. B Process Metall. Mater. Process. Sci.*, 1999, vol. 30, pp. 279–86.

120 K. Gu: Ph.D Thesis, McMaster University, 2017.

121 C. Chigwedu, J. Kempken, and W. Pluschkell: *Stahl und Eisen*, vol. 126, pp. 25–31.

122 A. Kruskopf and V.V. Visuri: *A Gibbs Energy Minimization Approach for Modeling of Chemical Reactions in a Basic Oxygen Furnace*, vol. 48, 2017.

123 M. Järvinen, V.V. Visuri, E.P. Heikkinen, A. Kärnä, P. Sulasalmi, C. De Blasio, and T. Fabritius: *ISIJ Int.*, 2016, vol. 56, pp. 1543–52.

124 L. Vos, I. Bellemans, C. Vercruyssen, and K. Verbeken: *Metall. Mater. Trans. B*,

DOI:10.1007/s11663-019-01677-y.

125 H. Jalkanen and L. Holappa: in *VII International Conference on Molten Slags Fluxes and Salts, The*, 2004, pp. 71–6.

126 S. Asai and I. Muchi: *Trans. ISIJ*, 1970, vol. 10, p. 250.

127 S. Ohguchi, D.G.C. Robertson, B. Deo, P. Grieveson, and J.H.E. Jeffes: *Ironmak. Steelmak.*, 1984, vol. 11, pp. 202–13.

128 B. Deo, P. Ranjan, and A. Kumar: *Process Metall.*, 1987, vol. 58, pp. 427–31.

129 W. v. d. Knoop, B. Deo, A.B. Snoijer, G. v. Unen, and R. Boom: in *4th International Conference on Molten Slags and Fluxes*, Sendai, 1992, pp. 320–307.

130 F. Pahlevani, S. Kitamura, H. Shibata, and N. Maruoka: *Steel Res. Int.*, 2010, vol. 81, pp. 617–22.

131 Y. Lytvynyuk, J. Schenk, M. Hiebler, and A. Sormann: *Steel Res. Int.*, 2014, vol. 85, pp. 544–63.

132 N. Dogan, G.A. Brooks, and M.A. Rhamdhani: *ISIJ Int.*, 2011, vol. 51, pp. 1086–92.

133 N. Dogan, G.A. Brooks, and M.A. Rhamdhani: *ISIJ Int.*, 2011, vol. 51, pp. 1093–101.

134 R. Sarkar, P. Gupta, S. Basu, and N.B. Ballal: *Metall. Mater. Trans. B*, 2015, vol. 46, pp. 961–76.

135 N. Dogan, G. a Brooks, and M. a Rhamdhani: in *Chemeca 2011-39th Australasian Chemical Engineering Conference*, 2011, pp. 1–14.

136 H. Jalkanen: *Sohn Int. Symp. Adv. Process. Met. Mater.*, 2006, vol. 2, pp. 541–54.

137 H. Jalkanen: *Acta Metall. Slovaca*, 2007, vol. 13, pp. 434–6.

138 I.H. Jung, P. Hudon, M.A. van Ende, and W.Y. Kim: in *AISTech Proceedings*, 2014, pp. 1257–68.

139 M.A. van Ende and I.H. Jung: in *Asia Steel Conference*, 2015.

140 M.A. van Ende and I.-H. Jung: in *Computational Materials System Design*, 2017, pp. 47–66.

141 www.factsage.com.

142 C. Chigwedu, J. Kempken, and W. Pluschkell: *Stahl und Eisen*, 2006, vol. 126, pp. 25–31.

143 Ankit and T.K. Kundu: *IOP Conf. Ser. Mater. Sci. Eng.*, 2016, vol. 115, pp. 1–10.

144 Ankit and T.K. Kundu: *IOP Conf. Ser. Mater. Sci. Eng.*, 2015, vol. 75, pp. 1–7.